Electronic, Spin and Valley Transport in Two Dimensional Dirac Systems

by

Hongya Xu

A Dissertation Presented in Partial Fulfillment
of the Requirements for the Degree
Doctor of Philosophy

Approved November 2016 by the
Graduate Supervisory Committee:

Ying-Cheng Lai, Chair
Daniel Bliss
Hongbin Yu
Tingyong Chen

ARIZONA STATE UNIVERSITY

May 2017

ABSTRACT

This dissertation aims to study and understand relevant issues related to the electronic, spin and valley transport in two-dimensional Dirac systems for different given physical settings. In summary, four key findings are achieved.

First, studying persistent currents in confined chaotic Dirac fermion systems with a ring geometry and an applied Aharonov-Bohm flux, unusual whispering-gallery modes with edge-dependent currents and spin polarization are identified. They can survive for highly asymmetric rings that host fully developed classical chaos. By sustaining robust persistent currents, these modes can be utilized to form a robust relativistic quantum two-level system.

Second, the quantized topological edge states in confined massive Dirac fermion systems exhibiting a remarkable reverse Stark effect in response to an applied electric field, and an electrically or optically controllable spin switching behavior are uncovered.

Third, novel wave scattering and transport in Dirac-like pseudospin-1 systems are reported. (a), for small scatterer size, a surprising revival resonant scattering with a peculiar boundary trapping by forming unusual vortices is uncovered. Intriguingly, it can persist in arbitrarily weak scatterer strength regime, which underlies a superscattering behavior beyond the conventional scenario. (b), for larger size, a perfect caustic phenomenon arises as a manifestation of the super-Klein tunneling effect. (c), in the far-field, an unexpected isotropic transport emerges at low energies.

Fourth, a geometric valley Hall effect (gVHE) originated from fractional singular Berry flux is revealed. It is shown that gVHE possesses a nonlinear dependence on the Berry flux with asymmetrical resonance features and can be considerably enhanced by electrically controllable resonant valley skew scattering. With the gVHE, efficient valley filtering can arise and these phenomena are robust against thermal fluctuations and disorder averaging.

To my parents

ACKNOWLEDGMENTS

I would like to express my most sincere gratitude to my advisor, Dr. Ying-Cheng Lai, for his guidance, mentoring, and continuous great support that made everything that I have achieved possible. At the scientific level his open mind, great insights and advice together with the enormous trust and freedom that he gave me along these years made me a more professional researcher.

I am also extremely grateful to Dr. Liang Huang, the former research scientist of our group, who have helped me in so many aspects and inspired me with his solid physics background and deep understanding of physical problems. I owe a lot of thanks to him for his admirable dedication and initial guidance that are of fundamental importance to my research.

I always value the research atmosphere built by our Chaos group members Dr. Riqi Su, Dr. Yuzhong Chen, Dr. Lei Ying, Guanglei Wang, Lezhi Wang, Junjie Jiang, and Zhidan Zhao. I owe a lot of thanks to Guanglei Wang for the fruitful discussions and collaborations that broadened the scope of my knowledge. I owe my gratitude to all those people who have made this dissertation possible and because of whom my graduate experience has been one that I will cherish forever.

I am really thankful to Dr. Celso Grebogi for his great encouragement, instructive suggestions, and disscussions on my research.

My special thanks to the committee members, Dr. Daniel Bliss, Dr. Tingyong Chen, and Dr. Hongbin Yu for their precious time as well as invaluable comments or advice. Also, I owe many thanks to my previous exams' committee members Dr. Yu Yao, Dr. Cun-Zheng Ning and Dr. Dragica Vasileska.

Finally, I would like to express deepest thankfulness to my parents and brothers for their love and support.

TABLE OF CONTENTS

CHAPTER Page

CHAPTER Page

LIST OF FIGURES

Figure Page

1 . INTRODUCTION

1.1. Prototypical Two Dimensional Dirac Fermion Systems

1.1.1. Monolayer Graphene

Consisting of one-atom-thick layer of carbon atoms tightly packed into a honeycomb crystal lattice, monolayer graphene can be thought of as a single layer of graphite and has become one of the most intriguing two dimensional materials since its surprising experimental discovery. Most of its unusual properties are associated with the particular band-structure and lattice configuration, which make the low-energy excitations behaving as massless spin-$1/2$ particles governed by the two-dimensional (2-D) Dirac-Weyl equation. In this regard, the monolayer graphene represents a standard condensed-matter realization of the 2-D Dirac fermion system. On the other hand, we should keep in mind that the "massless Dirac fermions" in graphene are quasi-particles originating from a $k \cdot p$ expansion around the so-called Dirac points in its energy-momentum dispersion, traveling at the Fermi velocity about two orders of magnitude smaller than the speed of light, with the spinor structure encoded by its two non-equivalent sublattices, and the massless feature being subject to discrete lattice symmetries. To shed light on such relevant differences, we shall present a brief derivation of the underlying effective Hamiltonian in the following.

As displayed in Fig. 1 (a), the crystal structure of graphene can be viewed as a bipartite lattice composed of two interpenetrating triangular sublattices denoted by "A" and "B". From Figs. 1 (b) and (c), we have $\mathbf{a} = (\sqrt{3}a/2, -a/2), \mathbf{b} = (\sqrt{3}a/2, a/2), \mathbf{G}_1 = (2\pi/\sqrt{3}a, -2\pi/a)$, and $\mathbf{G}_2 = (2\pi/\sqrt{3}a, 2\pi/a)$ with $a = |\mathbf{a}| = |\mathbf{b}|$, the corners of the Brillouin zone $\mathcal{K}_i$ expressed as $\mathbf{K}_1 = (\mathbf{G}_2 - \mathbf{G}_1)/3, \mathbf{K}_2 = (2\mathbf{G}_2 + \mathbf{G}_1)/3$, and $\mathbf{K}_3 = (2\mathbf{G}_1 + \mathbf{G}_2)/3$. Noticing that $\mathbf{K}_3 = \mathbf{K}_1 + \mathbf{K}_2$, one can show among the six corners only two of them are non-equivalent. The "A" and "B" sublattices are related with each other by a translation vector $\tau = -(\mathbf{a} + \mathbf{b})/3$ in real

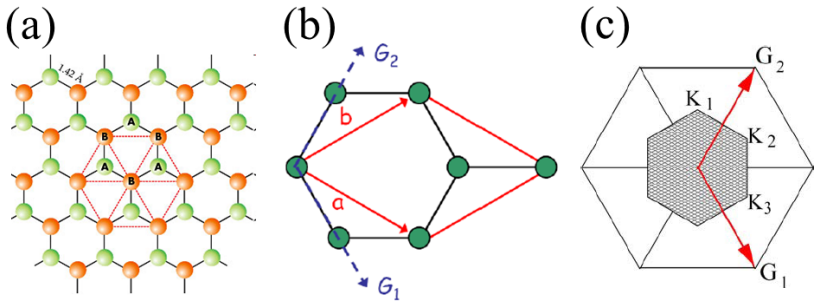

Fig. 1. (a) Honeycomb lattice of monolayer graphene, (b) primitive unit cell with translation vectors $\mathbf{a}$ and $\mathbf{b}$ in the real space, (c) the 1st Brillouine zone and the primitive vectors $\mathbf{G}_1$ and $\mathbf{G}_2$ in the corresponding reciprocical space.

position space, i.e. if let $\mathbf{R} = n_1\mathbf{a} + n_2\mathbf{b}$ be an abitrary lattice point a position belonging to the "A" sublattice, then the one in the "B" sublattice can be defined as $\mathbf{R} = \mathbf{R} + \tau$. As such, the tight-binding Hamiltonian for graphene is obtained as

$$\hat{H} = -t \sum_{\mathbf{R}} \left(|\mathbf{R}\rangle\langle \mathbf{R} + \tau| + |\mathbf{R}\rangle\langle \mathbf{R} + \mathbf{a} + \tau| + |\mathbf{R}\rangle\langle \mathbf{R} + \mathbf{b} + \tau| + \text{H.c.} \right), \tag{1.1}$$

where $\langle \mathbf{r}|\mathbf{R}\rangle = \Psi(\mathbf{R} - \mathbf{r})$ denotes a wave function on the sublattice "A" at site $\mathbf{R}$. Similarily, $\langle \mathbf{r}|\mathbf{R} + \tau\rangle$ represents a state on the "B" sublattice, and t is the hopping from a state to an adjacent state. Since there are two atoms in the unit cell and according to the Bloch theorem, we can define two Bloch states as $|\mathbf{k}A\rangle = \frac{1}{\sqrt{N}} \sum_{\mathbf{R}} e^{i\mathbf{k}\cdot\mathbf{R}} |\mathbf{R}\rangle, |\mathbf{k}B\rangle = \frac{1}{\sqrt{N}} \sum_{\mathbf{R}} e^{i\mathbf{k}\cdot\mathbf{R}} |\mathbf{R} + \tau\rangle$. Therefore, the eigenstates of the Hamiltonian Eq. (1.1) can be expressed as $|\mathbf{k}\rangle = \alpha|\mathbf{k}A\rangle + \beta|\mathbf{k}B\rangle$. By projecting it onto this sublattices space, we obtain

$$H(\mathbf{k}) = \begin{pmatrix} \langle \mathbf{k}A|\hat{H}|\mathbf{k}A\rangle & \langle \mathbf{k}A|\hat{H}|\mathbf{k}B\rangle \\ \langle \mathbf{k}B|\hat{H}|\mathbf{k}A\rangle & \langle \mathbf{k}B|\hat{H}|\mathbf{k}B\rangle \end{pmatrix} = \begin{pmatrix} 0 & e(\mathbf{k}) \\ e(\mathbf{k})^* & 0 \end{pmatrix}, \tag{1.2}$$

where $e(\mathbf{k}) \equiv \langle \mathbf{k}A|\hat{H}|\mathbf{k}B\rangle = \frac{1}{N} \sum_{\mathbf{R}\mathbf{R}'} e^{i\mathbf{k}\cdot(\mathbf{R}' - \mathbf{R})} \langle \mathbf{R}|\hat{H}|\mathbf{R} + \tau\rangle = -t\left(1 + e^{i\mathbf{k}\cdot\mathbf{a}} + e^{i\mathbf{k}\cdot\mathbf{b}}\right)$. The single particle eigenenergies are obtained as

$$\varepsilon(k_x, k_y) = \pm|e(\mathbf{k})| = \pm t\sqrt{1 + 4\cos\left(\frac{\sqrt{3}k_x a}{2}\right)\cos\left(\frac{k_y a}{2}\right) + 4\cos^2\left(\frac{k_y a}{2}\right)}. \tag{1.3}$$

It is straightforward that at the corners of the Brillouin zone, i.e. $\mathbf{k} = \mathbf{K}_i$, $\varepsilon(\mathbf{k}) = 0$. In the vicinity of the zone corner, say K_1, defining $\delta\mathbf{k} = \mathbf{k} - \mathbf{K}_1$ and expanding $e(\mathbf{k})$ up to the first order in $\delta\mathbf{k}$ give

$$-\frac{e(\mathbf{k})}{t} = 1+e^{(\mathbf{K}+\delta\mathbf{k})\cdot\mathbf{a}}+e^{(\mathbf{K}+\delta\mathbf{k})\cdot\mathbf{b}} \approx -\frac{1}{2}i\delta\mathbf{k}\cdot(\mathbf{a}+\mathbf{b})+\frac{\sqrt{3}}{2}i\delta\mathbf{k}\cdot(\mathbf{a}-\mathbf{b}) = -i\frac{\sqrt{3}}{2}|\delta\mathbf{k}|ae^{-i\pi/2}e^{-i\theta},$$

with $\theta = \arctan(\delta k_y/\delta k_x)$. Substituting this back into the Eq. (1.2), we have

$$H(\delta\mathbf{k}) = \frac{\sqrt{3}at}{2\hbar}\begin{pmatrix} 0 & \hbar(\delta k_x - i\delta k_y) \\ \hbar(\delta k_x + i\delta k_y) & 0 \end{pmatrix} = v_F\boldsymbol{\sigma}\cdot\mathbf{p}, \tag{1.4}$$

with the Fermi velocity $v_F = \frac{\sqrt{3}at}{2\hbar}$, and the energy dispersion $\varepsilon(\delta\mathbf{k}) = \pm v_F\hbar\sqrt{\delta k_x^2 + \delta k_y^2}$. Therefore, we arrive at a quasiparticle Hamiltonian around the "Dirac point" K_1 that shares the same form with the standard 2-D Dirac-Weyl Hamiltonian for massless Dirac fermions.

1.1.2. Surface States of Three Dimensional Topological Insulators

Another prototype 2-D Dirac fermion system can be surface states of three dimensional (3-D) topological insulators (TIs). Since their theoretical predictions, many materials have been experimentally demonstrated to be 3-D TIs characterized by a gapped insulating bulk yet a conducting surface that hosts topologically protected gapless surface states, in which carriers are turned out to be well described as 2-D massless (helical) Dirac fermions. One of the most promising materials is the bismuth selenide (Bi_2Se_3), which has robust gapless Dirac surface states and a large bulk band gap up to 0.3 eV that is equivalent to 3000 K much higher than room temperatures. Distinguished from the graphene case, the states here are from a single Dirac cone at the Γ point with a real spin representation. For the sake of clarity and concreteness, a general procedure to obtain the low-energy effective Hamiltonian for the surface states is given based on the electronic $k\cdot p$ model for the bulk of 3-D TIs Bi_2Se_3, Bi_2Te_3 and Sb_2Te_3 [1] obtained in the basis of

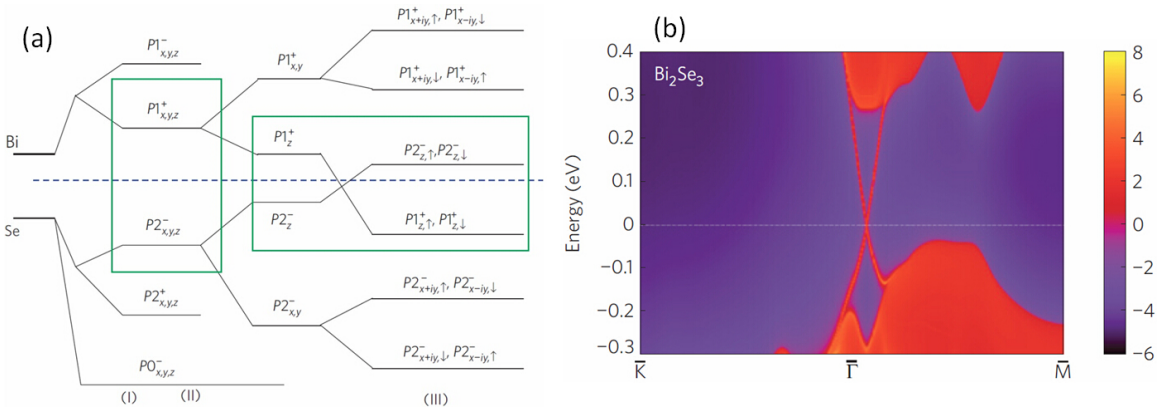

Fig. 2. (a) Schematic diagram of the evolution from the atomic orbitals of Bi and Se into the conduction and valence bands of Bi_2Se_3 at the Γ point. (b) Calculated surface states for Bi_2Se_3. From Ref. [1]

$|P1_z^+,\uparrow\rangle, |P1_z^+,\downarrow\rangle, |P2_z^-,\uparrow\rangle, |P2_z^-,\downarrow\rangle$ [c.f. Fig. 2] up to the quadratic order in $\boldsymbol{p} = (p_x, p_y, p_z)$ as

$$H(\boldsymbol{p}) = \epsilon(\boldsymbol{p}) + \sum_{i=x,y,z} v_i p_i \alpha_i + \mathcal{M}(\boldsymbol{p})\beta + o(\boldsymbol{p}^3), \tag{1.5}$$

with $\alpha_i = \sigma_x \otimes \sigma_i$, $\beta = \sigma_z \otimes \sigma_0$, $v_x = v_y = v_\parallel$, $v_z = v_\perp$, $B_x = B_y = B_\parallel$, $B_z = B_\perp$ and $\mathcal{M}(\boldsymbol{p}) = M - B_\parallel(p_x^2 + p_y^2) - B_\perp p_z^2$. Except for the indentity term $\epsilon(\boldsymbol{p}) = C + D_\parallel(p_x^2 + p_y^2) + D_\perp p_z^2$ and the second-order term $\sum_{i=x,y,z} B_i p_i^2 \beta$, the Eq. (1.5) is nothing but the 3-D Dirac Hamiltonian with uniaxial anisotropy along the z-direction and $\boldsymbol{p}$-dependent mass terms. We note that the bands $|P1_z^+\rangle$ and $|P2_z^-\rangle$ can be inverted around $\boldsymbol{p} = 0$ compared with large $\boldsymbol{p}$, which will give rise to the topologically non-trivial nature of the system.

Following the same method adopted in the study of the 2-D quantum spin Hall insulator, we consider a surface perpendicular to the z-direction in an $x - y$ plane at $z = 0$, where p_x and p_y are still good quantum numbers but p_z is replaced by $-i\hbar\partial_z$. The basic idea to obtain an effective Hamiltonian for the surface states is thinking of the p_x and p_y dependent part as a perturbation, then figuring out the surface-state solutions on the half infinite space $z > 0$ for $p_x = p_y = 0$ by solving $H(z)|\psi_0\rangle = E|\psi_0\rangle$ with $H(z) = C - D_\perp \hbar^2 \partial_z^2 - i v_\perp \hbar \partial_z \alpha_z + (M + B_\perp \hbar^2 \partial_z^2)\beta$, and

finally using the solutions $|\psi_0\rangle$ as the basis to project the bulk Hamiltonian Eq. (1.5) to a surface Hamiltonian defined in the $x-y$ plane that reads $H_{surf}(p_x,p_y) = \langle\psi_0|H(\boldsymbol{p})|\psi_0\rangle$. Under the conditions of $D_\perp^2 < B_\perp^2$ and $MB_\perp > 0$, we obtain two physically relevant surface-state solutions given by $|\psi_{0,1}\rangle = [a_1,0,b_1,0]^T(e^{\lambda_+ z}-e^{\lambda_- z})$ and $|\psi_{0,2}\rangle = [0,-a_1,0,b_1]^T(e^{\lambda_+ z}-e^{\lambda_- z})$ with $\lambda_\pm = \sqrt{v_\perp^2/4(B_\perp^2-D_\perp^2)} \pm \sqrt{v_\perp^2/4(B_\perp^2-D_\perp^2)-M/B_\perp}$, $a_1/b_1 = iA\lambda_+/(B_\perp+D_\perp)(\lambda_+^2+M/B_\perp) = iA\lambda_-/(B_\perp+D_\perp)(\lambda_-^2+M/B_\perp)$, and $|a_1|^2+|b_1|^2 = [(\lambda_++\lambda_-)/2\lambda_+\lambda_- - 2/(\lambda_++\lambda_-)]^{-1}$. As such, the effective surface Hamiltonian projected out to the leading order of p_x, p_y reads

$$H_{surf}(p_x,p_y) = \epsilon_0 + v_{eff}(\boldsymbol{p}\times\boldsymbol{\sigma})_z, \tag{1.6}$$

where $v_{eff} = \text{sgn}(B_\perp)\sqrt{1-D_\perp^2/B_\perp^2}v_\parallel$ and $\epsilon_0 = E_0 + D_\parallel(p_x^2+p_y^2)$. The resulting Hamiltonian for the surface states given in Eq. (1.6) is reminiscent of the one for the 2-D massless Dirac fermions and characterizes the key features of the topological surface states. One key feature from this model is the spin-momentum lock-in relation that makes the surface states promising in TI-based spintronics applications. We note that such an effective Hamiltonian is only valid for a small $\boldsymbol{p}$ and including the higher-order term up to $\boldsymbol{p}^3$ it has the following deformed form

$$H = \epsilon_0 + v_{eff}(p_x\sigma_y - p_y\sigma_x) + \frac{\lambda}{2}(p_+^3+p_-^3)\sigma_z,$$

with $p_\pm = p_x \pm ip_y$.

1.2. Remarkable Basic Properties

Based on the genuine Dirac equation, we review several remarkable features associated with Dirac fermions living in flat low-dimensional, especially 2-D, space by taking into account relevant perturbations.

1.2.1. Time Reversal Symmetry Breaking Without Magnetic Fields

Firstly, we show that for single flavor massless Dirac fermions in 2-D free space described by the Hamiltonian $H_0 = v(\sigma_x p_x + \sigma_y p_y)$, a massive type perturbation $H_1 = mv^2\sigma_z$ itself will break the

time reversal $\mathcal{T}$ symmetry regardless of whether applied magnetic fields are turned on or not, which means that Dirac's mass generation in 2-D space or $(2+1)$ dimensional time-space accompanies $\mathcal{T}$-breaking, i.e. $\mathcal{T}H_0\mathcal{T}^{-1} = H_0$, while $\mathcal{T}\mathcal{H}\mathcal{T}^{-1} \neq \mathcal{H}$ with $\mathcal{H} = H_0 + H_1$. Noticing that the $\mathcal{T}$ operation in quantum mechanics corresponds to an antiunitary operator, we look for a representation of $\mathcal{T}$ having the form

$$\mathcal{T} = UK, \tag{1.7}$$

where U is a position-independent unitary operator acting on the relevant internal degrees of freedom and K denotes complex conjugation. Physically, in time-reversed state $\mathcal{T}|\phi\rangle$, all velocities including momentums should have opposite directions to those in state $|\phi\rangle$. For a spin-$1/2$ system, the time reversal should also flip the spin, i.e. $\mathcal{T}\sigma_i\mathcal{T}^{-1} = -\sigma_i$. Noting that $K\sigma_y = -\sigma_y K, K\sigma_{x,z} = \sigma_{x,z}K$ and $\sigma_y\sigma_{x,z}\sigma_y = -\sigma_{x,z}$, we can explicitly express the time reversal operator as

$$\mathcal{T} = i\sigma_y K, \tag{1.8}$$

for a spin-$1/2$ system and as well as the Dirac fermions concerned. Under this operation, $\mathcal{H}$ transforms to $\mathcal{H}' = \mathcal{T}\mathcal{H}\mathcal{T}^{-1} = H_0 - H_1$, which will not be equal to $\mathcal{H}$ if the massive perturbation exists. In recognition of the classical counterpart is $\mathcal{T}$ symmetry, we thus encounter a subtle situation where the massive Dirac particle system loses the $\mathcal{T}$ symmetry when quantized in $(2+1)$-D time-space. In terms of a confined geometry called neutrino billiard [], Sir M. Berry proposed an instructive semi-calssical explanation/origin of this $\mathcal{T}$-breaking by showing the existence of chiral closed (periodic) orbits with odd time bounces. Remarkably, it was turned out that such a discontinuity correspondence is associated with the parity anomaly in $(2+1)$-D relativistic quantum field theory that is a failure of the parity symmetry of a classical action to be that of the quantum counterpart.

Investigating such basic concepts in condensed matter systems e.g. graphene and TIs has led to very intriguing consequences and phenomena such as anomalous Hall effect, spin/valley Hall effect and a quantum Hall effect without Landau levels. We note that the unusual spinor-wave analog of whispering gallery modes and their great robustness uncovered in Chapter 2 are also attributed to such a $\mathcal{T}$-symmetry-breaking feature.

1.2.2. Jackiw-Rebbi Solution and Chiral Edge State

Further peculiarities associated with Dirac equation can be obtained when the constant in space mass term is replaced by an inhomogeneous term that varies with position from negative to positive at two ends or regions. In addition to be mathematically fascinating, their physical realization and interpretation reveal novel excitations, which underlie unusual charge fractionalization and lead to great insights for the formation of the chiral (helical) edge and surface states in topological insulators. In particular, we consider a one-dimensional case with the Hamiltonian given by

$$H_{1D} = -iv\hbar\frac{d}{dx}\sigma_x + m(x)v^2\sigma_z, \tag{1.9}$$

where $m(x) = m_0 x/|x|$. Solving the corresponding eigenvalue equation $H_{1D}\psi = E\psi$ with relevant boundary conditions of continuity at $x = 0$ and vanishing at $x = \pm\infty$, one obtains an interesting solution of zero energy $E = 0$ and the wave-function as

$$\psi(x) = \sqrt{\frac{m_0 v}{2\hbar}} \begin{pmatrix} 1 \\ i \end{pmatrix} e^{-\frac{|m_0 v x|}{\hbar}}. \tag{1.10}$$

It is obvious that this solution dominantly distributes near the interface at $x = 0$ and exponentially decay away from it. We note that such a solution was first obtained by Jackiw and Rebbi and has been a theoretical basis of topological excitations or solitons in 1-D space. Extending this issue into the 2-D case, one will encounter a similar such solution but with the dispersion $E = \text{sgn}(m_0)vp_y$. Therefore, an oriented current exists along the interface with its density decaying exponentially

away from it and orientation depending on the sign of m_0. Such a behavior underlies the intriguing helical anomalous Hall edge states in graphene or TIs.

1.2.3. Chiral, Klein Tunneling and Negative Refractive Index

According to the 2-D massless Dirac equation with its stationary form given by

$$\hat{H}_D\psi(\boldsymbol{r}) = -i\hbar v\hat{\boldsymbol{\sigma}}\cdot\boldsymbol{\nabla}\psi(\boldsymbol{r}) = E\psi(\boldsymbol{r}), \tag{1.11}$$

we review several another interesting properties in terms of the wave scattering from scalar type perturbations. Some basic properties of Eq. (3.1) are the following. First, in free space, the plane-wave solutions have the form:

$$\psi_s(\boldsymbol{r}) = \frac{1}{\sqrt{2}}\begin{pmatrix} e^{-i\theta_{\boldsymbol{k}}/2} \\ se^{i\theta_{\boldsymbol{k}}/2} \end{pmatrix}\exp\left(i\boldsymbol{k}\cdot\boldsymbol{r}\right), \tag{1.12}$$

where $\boldsymbol{k} = (k_x, k_y)$ is the wavevector that makes an angle $\theta_{\boldsymbol{k}} = \arctan(k_y/k_x)$ with the x axis. The corresponding energy-momentum relationship is

$$E_s(\boldsymbol{k}) = s\hbar v|\boldsymbol{k}| = s\hbar v\sqrt{\boldsymbol{k}\cdot\boldsymbol{k}}, \tag{1.13}$$

where $s = \pm$ denotes the sign of E that acts as the band-index of the Dirac cone with $s = +$ being the conduction band and $s = -$ for the valence band. It then follows from the Eq. (1.13) that a band-dependent relative direction between the group velocity and the wavevector, i.e.

$$\boldsymbol{v}_s^g = \frac{\mathrm{d}E_s}{\mathrm{d}(\hbar\boldsymbol{k})} = sv\frac{\boldsymbol{k}}{|\boldsymbol{k}|}. \tag{1.14}$$

Second, we have an unconventional definition of the local current operator $\boldsymbol{j} = v\hat{\boldsymbol{\sigma}}$ and a physical observable of chirality $\hat{h} = \hat{\boldsymbol{\sigma}}\cdot\boldsymbol{k}/|\boldsymbol{k}|$ associated with the first order differential feature and the spinor representation of the wave Eq. (3.1) respectively. The chirality is conserved in free space (i.e. $[\hat{h}, \hat{H}_D] = 0$) with its eigenvalues $\Lambda = \pm 1$ corresponding to the conduction ($\Lambda = +1$)

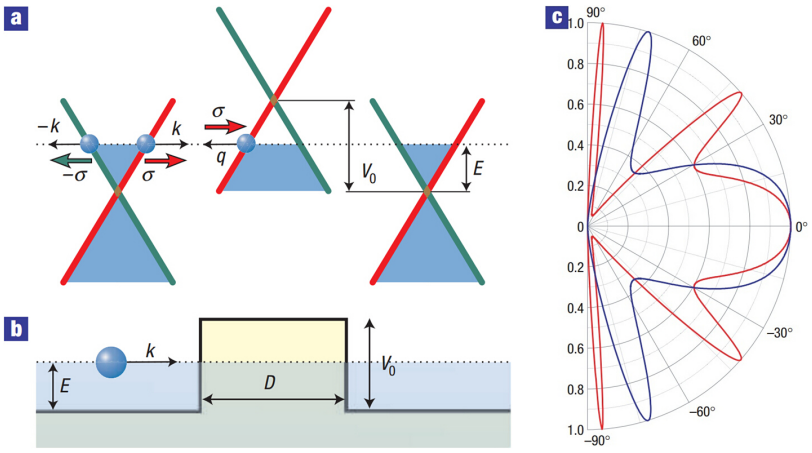

Fig. 3. (a) Schematic the dispersion diagrams of a Dirac cone. (b) Potential barrier profile with height V_0 and width D. (c) Transmission probability as a function of the incident angle. From Ref. [2]

and valence ($\Lambda = -1$) bands of the Dirac cone. As such, there is also a definite band-dependent relative direction of the spin and the wavevector: for the conduction band ($s = +$), $\boldsymbol{\sigma}$ is parallel to $\boldsymbol{k}$ ($\Lambda = +1$); while, for the valence band ($s = -$), $\boldsymbol{\sigma}$ is antiparallel to the $\boldsymbol{k}$ ($\Lambda = -1$). Based on the key points noted above, two particular unusual features of massless Dirac fermions can be deduced as below.

Klein tunneling and absense of backscattering. Considering a textbook wave scattering problem defined by the wave equation (3.1) with a straight gate potential barrier as schetched in Fig. 3 (b), one will finally obtain the transmission probability as $V_0 \gg E$, [2]

$$T = \frac{\cos^2\phi}{1 - \cos^2(q_x D)\sin^2\phi}. \tag{1.15}$$

In contrast to the conventional situations, where an exponential damping behavior follows generally in the barrier region with the decay exponent being propotional to the square root of the difference of the barrier hight and incident energy, we see from Eq. (1.15) that there can be a total transmission regardless of the barrier hight. Historically, such a weird phenomenon was first discovered by Oskar

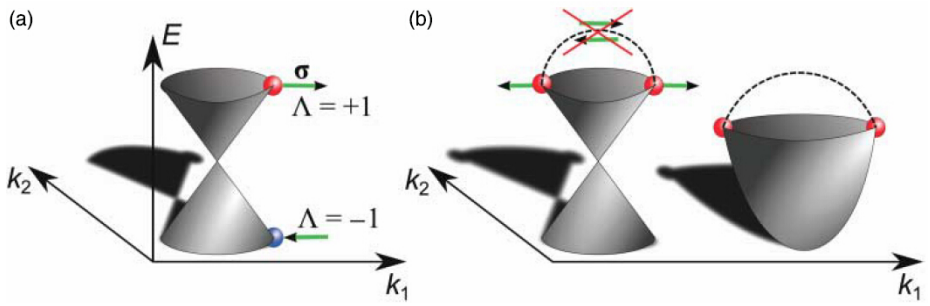

Fig. 4. (a) A cartoon picture of the Drac cone. (b) Diagram explaination of the absense of backscattering. From Ref. [3]

Klein — a Swedish theoretical physicist — in 1929 and hence named Klein paradox/tunneling. From the Eq. (1.15) and Fig. 3 (c), we see that one more significantly point is that there is always a perfect transmission for the normal incident case, i.e., $\phi = 0$.

According to the following arguments on the group velocity and chirality

- for the conduction band ($s = +, \Lambda = +1$): both $\boldsymbol{v}^g$ and $\boldsymbol{\sigma}$ are parallel to $\boldsymbol{k}$,
- for the valence band ($s = -, \Lambda = -1$): both $\boldsymbol{v}^g$ and $\boldsymbol{\sigma}$ are antiparallel to $\boldsymbol{k}$,

one can figure out a clear physical picture underlying this abnormal behavior that: given a normal incident state denoted by $|s = +; \boldsymbol{k}, \boldsymbol{\sigma}, \Lambda = +1\rangle$ as indicated on the left side of the barrier in Fig. 3 (a)-(b), the corresponding backscattering state will be $|s = +; -\boldsymbol{k}, -\boldsymbol{\sigma}, \Lambda = +1\rangle$. Therefore, if the scattering potential V cannot flip the spin direction from $\boldsymbol{\sigma} \to -\boldsymbol{\sigma}$ such that a conservation in the chirality, the backscattering process will be suppressed as illustrated in Fig. 4. On the other hand, in the barrier region, there is a well-defined traveling state given by $|s = -; -\boldsymbol{k}, \boldsymbol{\sigma}, \Lambda = -1\rangle$ that can be available. Noting that the associated group velocity is the same as the incident one, we thus obtain a total transmission independent on the barrier hight (strength). We remark that such an absence of backscattering phenomenon is promising in applications of wave transport when the backscattering is undesirable.

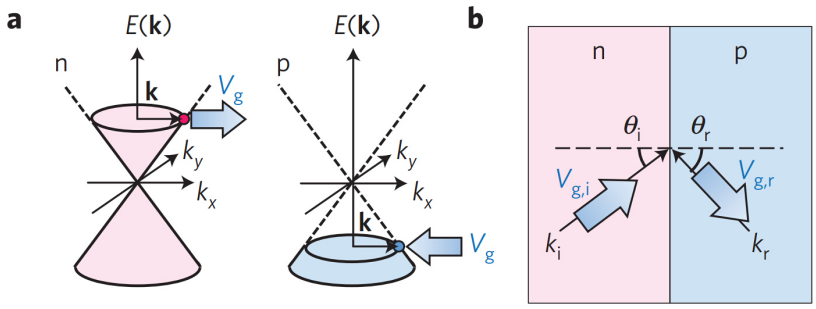

Fig. 5. (a) Dirac cone band dispersion. (b) Negative refraction across a flat junction. From Ref. [4]

Negative refractive index. Another remarkable feature is the negative refractive index. To see why this can happen, let us consider a similar scattering process for a straight interface with states residing two sides of it belonging to different bands respectively as shown in Fig. 5. Two definite points can be concluded from the previous analysis that

- at the incident region (n side: $s = +$), the group velocity $\boldsymbol{v}_i^g$ should be parallel to the incident wavevector $\boldsymbol{k}_i$; while, at the refractive region (p side: $s = -$), $\boldsymbol{v}_r^g$ should be antiparallel to the refractive wavevector $\boldsymbol{k}_r$;

- the normal component of the group velocity should be the same on both sides, which thus implies a direction reversal in that of the corresponding wavevectors.

Moreover, because of the translation-invarient along the interface, we have an additional constrain that the tangential component of the wavevector should be conserved. In particular, for an incident configuration denoted in Fig. 5 (b), we finally obtain the following geometric relation

$$|\boldsymbol{k}_i| \sin\theta_i = -|\boldsymbol{k}_r| \sin\theta_r, \tag{1.16}$$

which therefore defines an effective negative refractive index

$$n = \frac{\sin\theta_i}{\sin\theta_r} = -\frac{|\boldsymbol{k}_r|}{|\boldsymbol{k}_i|}. \tag{1.17}$$

We note that such an analogue of the Snell's law underlying the Dirac cones was theoretically predicted in 2007 [7], and has been observed in a very recent graphene-based experiment [4]. There are several interesting applications associated with the negative refractive index, such as caustics, super-lens and cloaking.

1.3. Dirac-Like Systems with Gapless Bosonic Excitations and Beyond

Since the underlying new physics and intriguing physical properties, tremendous interest has been aroused for exploring physical implementations or analogues of such Dirac systems in rather different research fields such as condensed matter physics, cold atom physics, photonics, acoustics and even classical mechanics. Apart from the standard ones like monolayer graphene, surface states of TIs, many systems actually host quasiparticles or excitations governed by the deformed or generalized Dirac equations and are hence named Dirac-like systems.

1.3.1. Emerging Dirac-Like Pseudospin-1 Systems

Of particular interest recently are the ones with gapless bosonic excitations by forming a pseudospin-1 conical intersection in their energy-momentum spectrum. In practice, they can be created in variety of physical systems that are either electronic or optical ranging from centimeter to nanometer as displayed in Fig. 6, which is based on two general ideas: specific lattice symmetries and accidental degeneracies. For instance, in a common dielectric photonic lattice, the pseudospin-1 conical intersection can be induced at the center of the Brillouin zone as accidental degeneracies via tuning relevant system parameters. Alternatively, configuring an array of evanescently coupled optical waveguides into a Lieb lattice can also make it at the corner of the Brillouin zone. Loading cold atoms into an optical Lieb lattice provides another experimental realization at a smaller scale with greater dynamical controllability of the system parameters. Moreover, many electronic materials such as transition-metal oxide $SrTiO_3/SrIrO_3/SrTiO_3$ trilayer heterostructures, 2-D carbon or

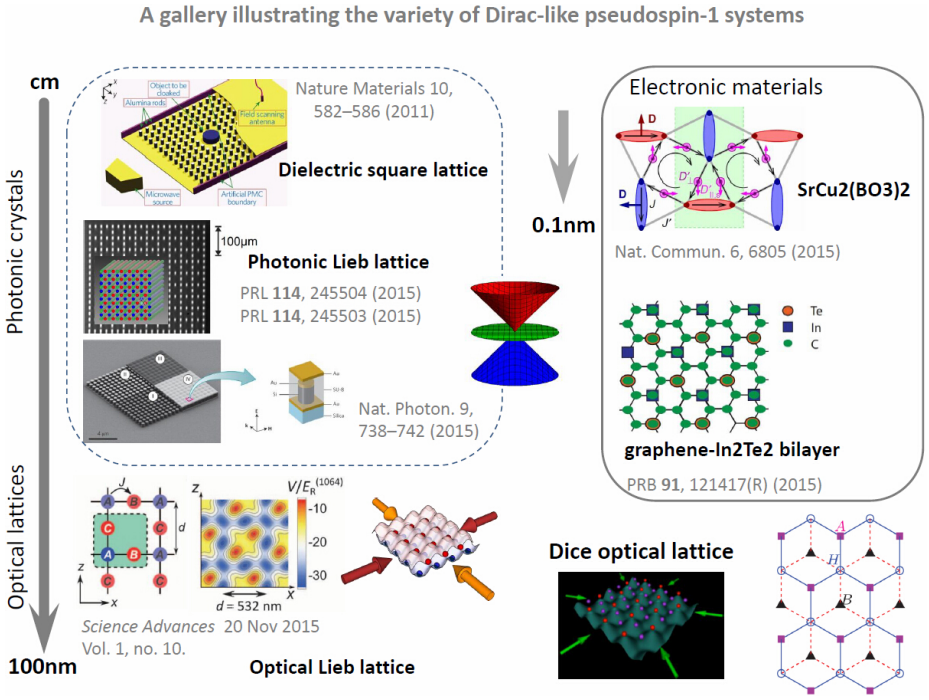

Fig. 6. A Gallery Illustrating the Variety of Dirac-Like Pseudospin-1 Systems.

MoS_2 allotropes with a square symmetry, $SrCu_2(BO_3)_2$ and graphene-In_2Te_2 bilayer etc. have been turned out to host such a gapless bosonic excitation.

In spite of the diversity and the broad scales in realization, there is a unified underlying theoretical framework: generalized Dirac-Weyl equation for the massless pseudospin-1 excitations. As such, we call the related systems Dirac-like pseudospin-1 systems.

1.3.2. Dirac-Like Hybrid Quasiparticles of Fermionic and Bosonic Excitations

Going beyond the prototypical Dirac fermion systems further, we will encounter more peculiarities that would contradict the conventional wisdoms or even well-established textbook knowledge. As concrete examples, we introduce two systems hosting exotic gapless Dirac-like quasiparticles that are rare hybrid ones of massless fermionic and bosonic excitations with a fractional Berry phase.

$\alpha - \mathcal{T}_3$ *lattice.* As shown in Fig. 7, the $\alpha - \mathcal{T}_3$ lattice can be viewed as a simple extention of the

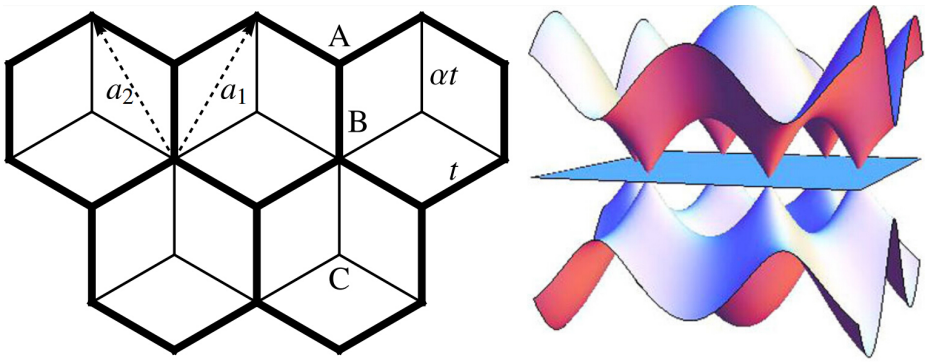

(a) (b)

Fig. 7. (a) Schematic representation of the $\alpha - \mathcal{T}_3$ lattice. (b) Energy band structure in momentum space for any value of α. From [5].

graphene lattice by adding an additional sublattice "C" at the center of each hexagon that connects to one of the other sublattices with a different hopping αt. By varying α, it interpolates between graphene ($\alpha = 0$) and the Dice lattice ($\alpha = 1$). The former represents a typical 2-D Dirac fermions system while the latter is the standard so-called Dirac-like pseudospin-1 system. Interestingly, for $0 < \alpha < 1$, we shall see that the system has unusual low-energy excitations but with the same zero field energy spectrum (band-structure). Note that the $\alpha - \mathcal{T}_3$ lattice has three sites/atoms per unit cell and shares the same shaped 1st Brillouin zone with the graphene. Following the similar procedure as did in the monolayer graphene, one obtains the Bloch Hamiltonian expressed in sublattices space as

$$H(\boldsymbol{k}) = \begin{pmatrix} 0 & f_{\boldsymbol{k}} \cos\phi & 0 \\ f_{\boldsymbol{k}}^* \cos\phi & 0 & f_{\boldsymbol{k}} \sin\phi \\ 0 & f_{\boldsymbol{k}}^* \sin\phi & 0 \end{pmatrix} \tag{1.18}$$

where $\tan\phi \equiv \alpha$ and $f(\boldsymbol{k}) = -t(1 + e^{-i\boldsymbol{k}\cdot\boldsymbol{a_1}} + e^{-i\boldsymbol{k}\cdot\boldsymbol{a_2}})$ with $\boldsymbol{a}_1 = a(\sqrt{3}/2, 3/2), \boldsymbol{a}_2 = a(-\sqrt{3}/2, 3/2)$ and a being the intersite distance. Linearization around the hexagonal Brillouin zone corners $\tau\boldsymbol{K}$ yields $f_{\boldsymbol{k}} \approx v(\tau\delta k_x - i\delta k_y)$ with $\tau = \pm$ denoting the valley index and

$\boldsymbol{\delta k} = \boldsymbol{k} - \tau \boldsymbol{K} = (\delta k_x, \delta k_y)$. Therefore, when $\alpha \neq 0, 1$, the resulting low energy Hamiltonian near $\tau \boldsymbol{K}$ points involves more than a single pseudospin operator [5]. In chapter 6, we will see that this model possesses α-dependent fractional Berry phase in general, which underlies very unusual physics.

Massless Kane fermions. Recently, it has been shown that bulk gapless excitations in $Hg_{1-x}Cd_xTe$ at a critial doping concentration and Cd_3As_2 can be exotic Dirac-like quasiparticles named massless Kane fermions beyond any other relativistic particles, which obey the following Dirac-like low-energy Hamiltonian

$$H_{Kane} = v \sum_{i=x,y,z} \tilde{\alpha}_i p_i + mv^2 \tilde{\beta}, \tag{1.19}$$

where $\tilde{\beta} = \sigma_0 \otimes U$ and $(\tilde{\alpha}_x, \tilde{\alpha}_y, \tilde{\alpha}_z) = (\sigma_z \otimes J_x, \sigma_0 \otimes J_y, \sigma_x \otimes J_z)$, with $U = \text{diag}[1, -1, -1]$ and the matrices J_i given by

$$J_x = \begin{pmatrix} 0 & \sqrt{3}/2 & -1/2 \\ \sqrt{3}/2 & 0 & 0 \\ -1/2 & 0 & 0 \end{pmatrix}, J_y = \begin{pmatrix} 0 & -i\sqrt{3}/2 & -i/2 \\ i\sqrt{3}/2 & 0 & 0 \\ i/2 & 0 & 0 \end{pmatrix}, J_z = \begin{pmatrix} 0 & 0 & -1 \\ 0 & 0 & 0 \\ -1 & 0 & 0 \end{pmatrix}.$$

Note that J_i do not satisfy the algebra of angular momentum one nor any other closed algebra. Consequently, H_{Kane} does not follow any well-known case for relativistic particles, while it actually describes a Dirac-like system with a hybrid of massless spin-1 and spin-$1/2$ particles. Remarkably, as disscussed in Chapter 6, there can be a map between the massless Kane fermion system and the $\alpha - \mathcal{T}_3$ lattice model.

1.4. Outline of This Thesis

In the preceding Chapters, we shall theoretically address relevant issues related to the electronic, spin and valley transport in the 2-D Dirac or Dirac-like systems reviewed above by considering given physical settings. In Chapter 2, we investigate the Aharonov-Bohm oscillations and persistent

currents in confined 2-D chaotic Dirac fermion systems with a ring geometry and an applied line magnetic flux. In Chapter 3, we eluciate a robust relativistic quantum two level system based on a family of unusual Dirac whispering gallery modes with edge-dependent currents and spin polarization. In Chapter 4, we study the response of the quantized helical (anomalous Hall) edge states to an applied electric field and identify a reverse quantum-confined Stark effect and electrically or optically controllable spin switching behavior. In Chapter 5, we investigate the basic scattering and transport properties of the Dirac-like pseudospin-1 systems based on the simplest possible setting while retaining the essential physics. In Chapter 6, taking the $\alpha - \mathcal{T}_3$ lattices as concrete examples, we semiclassically address the bulk valley and charge transports in novel systems with the Dirac-like hybrid quasiparticles of gapless fermionic and bosonic excitations.

2 . SUPERPERSISTENT CURRENTS AND WHISPERING GALLERY MODES IN RELATIVISTIC QUANTUM CHAOTIC SYSTEMS

2.1. Background

A remarkable phenomenon in the quantum world is persistent currents (PCs), permanent currents without any external source [8], which are generated by the Aharonov-Bohm (AB) effect [9] in non-superconducting systems. PCs have been observed experimentally in metallic [10–14] and semiconductor [15–17] rings in the mesoscopic regime. Theoretical efforts have been focused on the effects of bulk disorders [18–20], electron-electron interactions [21–23], spin-orbital interactions [24, 25], and electromagnetic radiation [26, 27] on PCs, typically studied in the diffusive regime using idealized circular-symmetric rings and cylinders. Rapid advances in nanotechnology have made it feasible to fabricate mesoscopic devices with mean free path larger than their sizes at sufficiently low temperatures (the ballistic transport regime) [28]. The AB system can thus be modeled as a quantum ballistic billiard in which the particles are scattered at the boundaries of the domain. As a result, the boundary shape becomes highly relevant. In experiments, uncontrollable boundary imperfections are inevitable [29, 30] even when there are no bulk disorders. It is thus of interest to study the effects of boundaries, e.g., those that generate chaos in the classical limit, on PCs. In general, an asymmetric boundary destroys angular momentum conservation and introduces irregular scattering. Theoretical [31–36] and experimental [29] studies have shown that, similar to the effects of bulk disorder, symmetry breaking of the boundary can result in opening of gaps at the degeneracy points of the energy levels, leading to level repulsion, a typical manifestation of classical chaos. Energy gap opening can diminish AB oscillations through pinning of the corresponding states, leading to vanishing PCs. Since fully chaotic domains are associated with a strong degree of symmetry breaking, PCs are not expected to arise [37, 38]. In nonrelativistic quantum systems

governed by the Schrödinger equation, PCs are thus *fragile*.

In this paper, we address the question of whether, in relativistic quantum systems, PCs can arise and sustain in the presence of symmetry-breaking perturbations. Besides the importance of this question to fundamental physics, our work was motivated by the tremendous recent research on two-dimensional Dirac materials [39] such as graphene [40–46], topological insulators [47], molybdenum disulfide (MoS_2) [48, 49], HITP [$Ni_3(HITP)_2$] [50], and topological Dirac semimetals [51, 52]. The physics of these materials is governed by the Dirac equation. This is thus interest in investigating relativistic PCs in Dirac fermion systems [53–64]. Existing theoretical works on relativistic PCs, however, assumed idealized circular-symmetric rings in the ballistic limit. Whether AB oscillations and consequently relativistic PCs can exist in asymmetric rings that exhibit chaos in the classical limit is a fundamental question. Our finding is that, even in the presence of significant boundary deformations so that the classical dynamics becomes fully chaotic, robust PCs can occur in relativistic quantum, Dirac fermion systems, henceforth the term *superpersistent currents* (SPCs). A more striking finding is that SPCs are generated by localized states at the domain boundaries, which are effectively chaotic Dirac whispering gallery modes (WGMs) that carry larger angular momenta. While WGMs are common in photonic systems [65–68], its emergence in electronic systems [69], especially in relativistic quantum systems, is rare and surprising. We develop a physical understanding of the counterintuitive phenomenon of SPCs by analytically exploiting the properties of the spinor wavefunctions in an idealized relativistic quantum system.

The significance of our results lies in the perspective of observing SPCs in the presence of strong random scattering, implying that they may occur in systems of size beyond the mesoscopic limit. This can potentially be a relativistic quantum phenomenon occurring at relatively large scales. We note that, previous experimental studies of AB oscillations in graphene [70] and topological

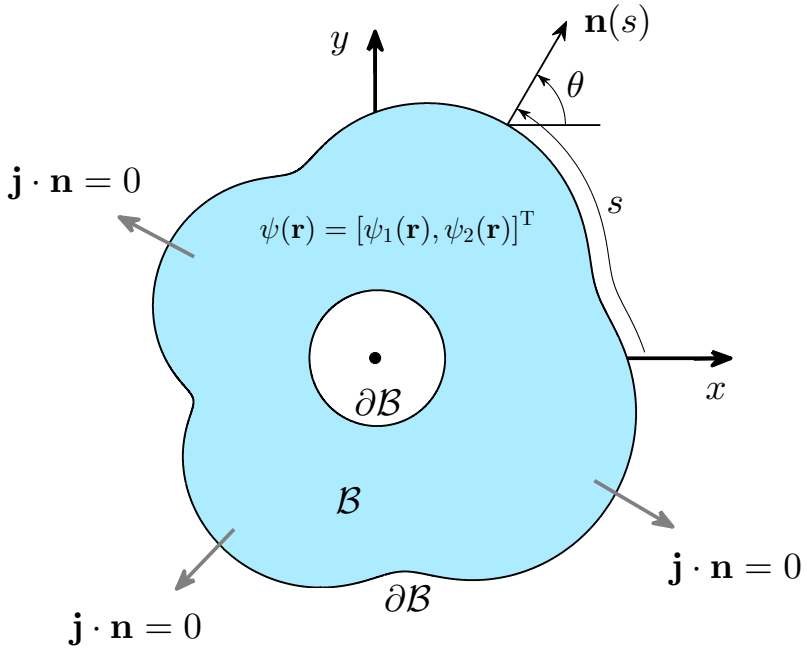

Fig. 8. Illustration of a chaotic ring domain with boundary parameterized by the arc length s. For motion of massless Dirac fermion inside the domain, the boundary condition is of the zero-flux type, i.e., no outward current at any point s: $\boldsymbol{j}\cdot\boldsymbol{n}=0$.

insulators [71,72] make it possible to experimentally test the phenomena of Dirac WGMs and SPCs that we predict in this paper. To motivate experimental verification, we propose a feasible scheme using three-dimensional topological insulators.

2.2. Theoretical Model of the Relativistic AB System

Consider a single massless spin-half particle of charge $-q$ confined by hard walls in a domain $\mathcal{B}$ with a ring topology in the plane $\boldsymbol{r}=(x,y)$, as shown in Fig. 8. Applying a single line of magnetic flux (AB flux) Φ at its origin and utilizing an infinite mass term outside the domain to model the confinement, we obtain the following Hamiltonian in the position representation:

$$\hat{H}=v\hat{\boldsymbol{\sigma}}\cdot(-i\hbar\boldsymbol{\nabla}+q\boldsymbol{A})+M(\boldsymbol{r})\hat{\sigma}_z,$$

where v is the Fermi velocity, $\hat{\boldsymbol{\sigma}} = (\hat{\sigma}_x, \hat{\sigma}_y)$ and $\hat{\sigma}_z$ are the Pauli matrices, and $M = 0$ in the ring domain but $M = \infty$ otherwise (for hard-wall confinement - used previously, e.g., in the study of graphene rings [73], graphene quantum dots [74], and topological insulator quantum dots [75]). The vector potential $\boldsymbol{A}(\boldsymbol{r})$ can be chosen as any vector field satisfying $\boldsymbol{\nabla} \times \boldsymbol{A}(\boldsymbol{r}) = \hat{\boldsymbol{e}}\alpha\Phi_0\delta(\boldsymbol{r})$, where $\hat{\boldsymbol{e}}$ is the unit vector perpendicular to $\mathcal{B}$ and $\alpha \equiv \Phi/\Phi_0$ is the dimensionless quantum flux parameter, with $\Phi_0 = 2\pi\hbar/q$ being the flux quantum. The Hamiltonian $\hat{H}$ acting on the two-component spinor wave-function $\psi(\boldsymbol{r}) = [\psi_1, \psi_2]^{\mathrm{T}}$ has eigenvalue E:

$$[-i\hbar v\hat{\boldsymbol{\sigma}} \cdot \boldsymbol{D} + M(\boldsymbol{r})\hat{\sigma}_z]\,\psi(\boldsymbol{r}) = E\psi(\boldsymbol{r}), \tag{2.1}$$

where $\boldsymbol{D} = \boldsymbol{\nabla} + i\boldsymbol{a}$ is a compact notation for the covariant derivative with $\boldsymbol{a} \equiv 2\pi\boldsymbol{A}/\Phi_0$.

In Eq. (2.1), $M\sigma_z$ represents the mass potential that takes into account the Klein tunneling effect, which can confine massless Dirac fermions in a finite domain. Such a confinement itself will break the time-reversal symmetry (T-breaking) in absence of any external magnetic field. However, the T-breaking due to mass potential confinement is different from that due to magnetic field in a classical picture in which no Lorentz force acts on particles so that the geodesic motions are still characterized by straight lines within the confined domain. In relativistic quantum theory of electrons, magnetic field is introduced through the form of minimal coupling in the corresponding vector potential that is different from the mass term. As a result, in the conventional $(3 + 1)$-dimensional spacetime, the mass itself cannot break the time-reversal symmetry. However, in $(2 + 1)$-dimensional systems studied in this paper (as for two-dimensional Dirac materials such as graphene and topological insulators), the mass term will induce chiral anomaly and hence T-breaking. Thus the T-breaking caused by mass confinement also has a different feature from that due to the magnetic field [76, 77].

To better understand the physical origin of the mass confinement term $M\sigma_z$, we consider a single particle in absence of magnetic field and compare the following two situations: (a) the particle is

in a Dirac ring with hard-wall confinement of mass potential and (b) the particle is in a Schrödinger ring with the conventional, electrical potential (hard-wall) confinement. We assume that the classical orbits are identical for both cases. Apparently, in case (a), the T-breaking is intrinsic but there is no T-breaking in case (b). In fact, as indicated by Sir Berry [78], the semiclassical origin of T-breaking induced by mass confinement is quite intriguing. One aim of our work is to uncover new and interesting phenomena caused by the mass confinement $M\sigma_z$ in $(2+1)$-dimensional Dirac systems. As we argue and demonstrate later, this type of confinement can be experimentally realized by exploiting the surface states of three-dimensional topological insulators, where the mass term in the Dirac equation is originated from a Zeeman term induced by local exchange coupling.

Some basic properties of Eq. (2.1) are the following. Firstly, the confinement condition of imposing infinite mass outside $\mathcal{B}$ naturally takes into account the Klein paradox for relativistic quantum particles and thus guarantees that our study is conducted in the single-particle framework, which is relevant to the *intrinsic* physics of a single Dirac cone in graphene or topological insulator. Secondly, both reduced spatial dimension together with mass confinement and applied magnetic flux can break the time-reversal symmetry of $\hat{H}$: $[\hat{T},\hat{H}]\neq 0$ if $M\neq 0$ or $\alpha\neq 0$, where $\hat{T}=i\sigma_y\hat{K}$ and $\hat{K}$ denotes complex conjugate. Thirdly, for $M=0$ and $\boldsymbol{A}=0$ in Eq. (2.1) (i.e. free massless particle), there exist plane wave solutions whose positive energy part has the following form:

$$\psi_{\boldsymbol{k}}(\boldsymbol{r})=\frac{1}{\sqrt{2}}\begin{pmatrix}\exp(-i\frac{\theta}{2})\\ \\ \exp(i\frac{\theta}{2})\end{pmatrix}\exp(i\boldsymbol{k}\cdot\boldsymbol{r}), \tag{2.2}$$

where $\boldsymbol{k}$ is a wave vector that makes an angle θ with the x axis. Fourthly, by using the Dirac equation $i\partial_t\psi=\hat{H}\psi$ and defining $\rho=\psi^\dagger\psi$ as the local probability density, we have the following continuity equation $\partial_t\rho+\boldsymbol{\nabla}\cdot[\psi^\dagger v\hat{\boldsymbol{\sigma}}\psi]=0$. It is therefore natural to define $v\hat{\boldsymbol{\sigma}}$ as the local current operator, so the local current density in state $\psi(\boldsymbol{r})$ is given by $\boldsymbol{j}(\boldsymbol{r})\equiv v\psi^\dagger\psi=2v\,[\mathrm{Re}(\psi_1^*\psi_2),\mathrm{Im}(\psi_1^*\psi_2)]$.

To obtain solutions of Eq. (2.1), a proper treatment of the boundary condition is necessary. As done in previous works, we use the infinite mass (also called Berry-Mondragon [78] or chiral-bag [79–81]) boundary condition

$$\frac{\psi_2}{\psi_1}\Big|_{\partial\mathcal{B}} = \mathrm{sgn}(M) i \exp[i\theta(s)], \tag{2.3}$$

where $\mathrm{sgn}(\cdot)$ stands for the signum function and $\theta(s)$ denotes the angle made by the outward unit normal $\boldsymbol{n}$ with the x axis at an arbitrary boundary point s, as shown in Fig. 8. Substituting Eq. (3.2) into the current density formula, one can show that the boundary current $\boldsymbol{j}(s) = 2v|\psi_1|^2(-\sin\theta, \cos\theta)$ is polarized along the boundary: *clockwise* and *counterclockwise* for the inner and outer edges, respectively. It is remarkable that this polarized property is independent of the shape of the confinement potential $M(\boldsymbol{r})$ and is thus *topologically protected* from irregular boundary scatterings, even though the magnitude of the edge current can be affected.

An analysis of the general properties of the α (magnetic flux) dependent relativistic quantum spectrum $\{E_j(\alpha)\}$, as determined by Eq. (2.1) under the boundary condition Eq. (3.2), reveals that the first "Brillouin zone" is given by $-1/2 \leq \alpha \leq 1/2$ (Supplementary Note 1). To calculate a large number of relativistic eigenvalues and eigenstates with high accuracy, we use the conformal-mapping method [6, 82, 83] (Supplementary Note 2).

2.3. Results

2.3.1. Whispering Gallery Modes and Superpersistent Currents.

To demonstrate our findings, we deform a circular ring domain $\xi = 0.5 \leq r \leq 1$, using the mapping $w(z) = h[z + 0.05az^2 + 0.18a\exp(i\omega)z^5]$, where $\omega = \pi/2$, $a \in [0, 1]$ is the deformation parameter that controls the classical dynamics. Specifically, when increasing a from zero to unity the deformed ring will undergo a transition from being regular to mixed and finally to being fully chaotic. The normalization coefficient $h = 1/\sqrt{1 + \frac{a^2}{200}(1+\xi^2) + \frac{81a^2}{500}(1+\xi^2+\xi^4+\xi^6+\xi^8)}$

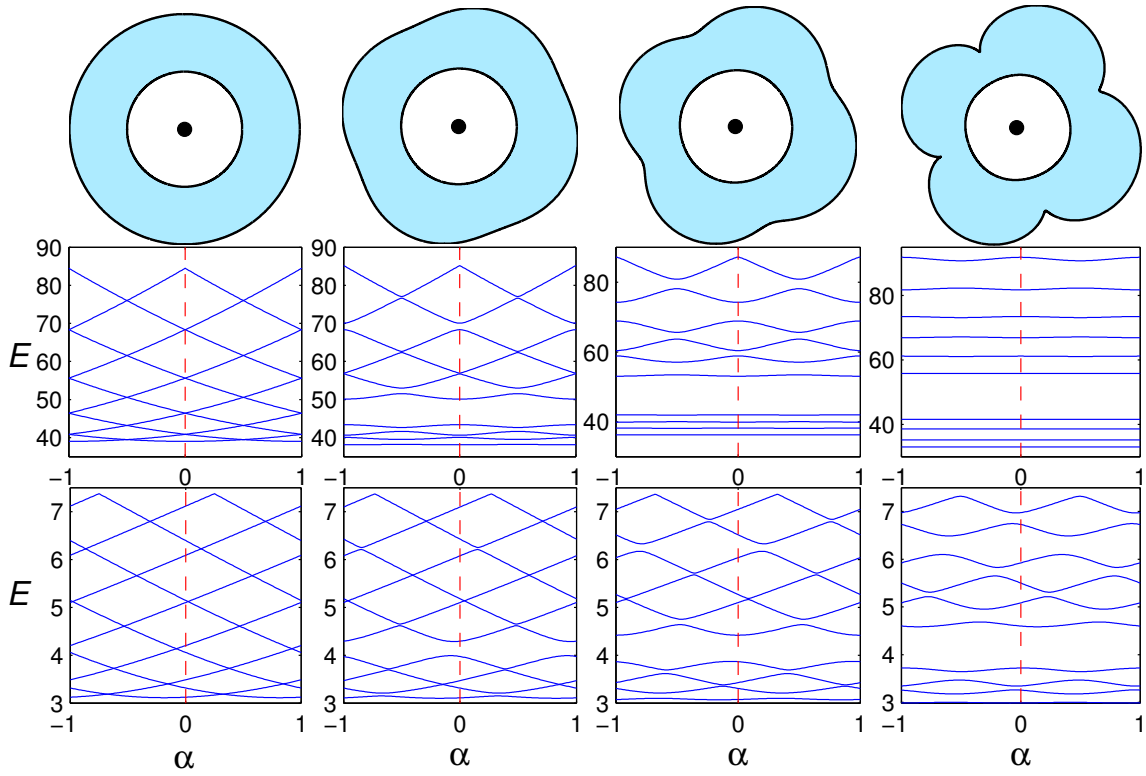

Fig. 9. Top panels: domain shape with classical dynamics ranging from integrable ($a = 0$; left most panel) and mixed ($a = 0.25$ and 0.5; middle two panels) to chaotic ($a = 1.0$; right most panel). Middle panels: nonrelativistic AB oscillations (energy-flux dispersions). Bottom panels: relativistic AB oscillations.

guarantees that the domain area is invariant for arbitrary values of the deformation parameters $\{a, \omega, \xi\}$. Four representative domains are shown in the top row in Fig. 9 where, classically, the left most domain is integrable, the right most domain is fully chaotic, and the two middle domains have mixed phase space. The middle and bottom rows of Fig. 9 show the lowest 10 energy levels as functions of the quantum flux parameter α, i.e., energy-flux dispersions, for Schrödinger and Dirac particles, respectively. We see that $E_j(\alpha) = E_j(-\alpha)$ holds for the Schrödinger particle, but for the Dirac fermion, the symmetry is broken: $E_j(\alpha) \neq E(-\alpha)$. However, for both nonrelativistic and relativistic spectra, we have $E_j(\alpha) = E_j(\alpha + 1)$. For the circular-symmetric ring ($a = 0$), AB oscillations in the energy levels have the period Φ_0 (i.e., $\alpha = 1$) and there are level crossings. Making the domain less symmetric by tuning up the value of the deformation parameter a leads to classical mixed phase space (regular and chaotic), and eventually to full chaos ($a = 1$). We see that, for the Schrödinger particle, emergence of a chaotic component in the classical space leads to opening of energy gaps, generating level repulsion and flattening the AB oscillations associated with the corresponding energy levels. Surprisingly, for the Dirac fermion, the AB oscillations are much more robust against asymmetric deformations. In particular, for the fully chaotic case, AB oscillations for the Schrödinger particle disappear almost entirely while those for the Dirac fermion persist with amplitudes of the same order of magnitudes as the integrable case.

We now present evidence of Dirac WGMs for the case of fully chaotic AB ring domain. By examining the eigenstates, we note that, for low energy levels, the Schrödinger particle is strongly localized throughout the domain, as shown in Figs. 10(a-c), leading to a flat energy-flux dispersion. However, the Dirac fermion typically travels around the ring's boundaries, forming relativistic WGMs that persist under irregular boundary scattering due to chaos and are magnetic-flux dependent, as shown in Fig. 10(d-f). Conventional wisdom for Schrödinger particle stipulates that asym-

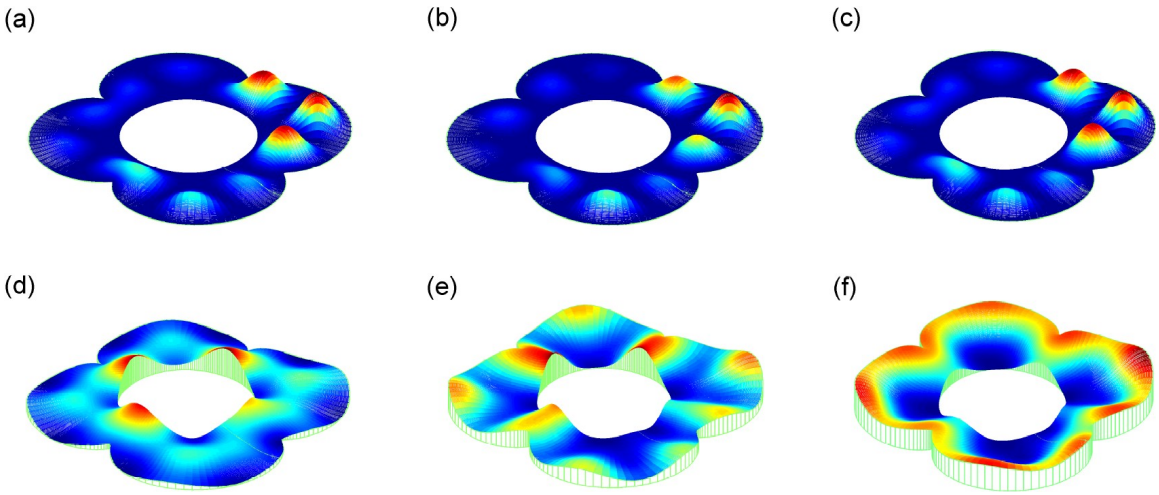

Fig. 10. Probability distribution of the 10th eigenstate for (a-c) nonrelativistic and (d-f) relativistic AB chaotic billiard for $\alpha = -1/4, 0, 1/4$, respectively.

metry in the domain geometry can mix/couple well-defined angular momentum states, opening energy gaps and leading to localization of lower states in the entire domain region, so AB oscillations would vanish, as demonstrated both theoretically and experimentally [29, 31]. However, for Dirac fermion, this picture breaks down - there are robust AB oscillations even in the fully chaotic domain and the particle tends to execute motions corresponding to WGMs.

The robust AB oscillations in chaotic Dirac rings lead to SPCs. The total persistent current can be calculated at zero temperature through [8,73] $I(\alpha) = -\sum_j (\partial E_j/\partial\alpha)$, where the sum runs over all occupied states with $E_j > 0$. Due to periodicity in the energy: $E_j(\alpha) = E_j(\alpha+1)$, the current is also periodic in α with the fundamental period $\alpha = 1$. Figure 11 shows, for the nonrelativistic (top panels) and relativistic (bottom panels) cases, PCs resulted from the lowest three states (including spin) in regular (left column) and chaotic (right column) rings. We see that, for classical integrable dynamics, PC oscillations display a common sawtooth form. However, at zero flux, PC is zero for the nonrelativistic case [Fig. 11 (a)], while it has a finite value for the relativistic case due to breaking of the time-reversal symmetry. In the chaotic case, the oscillations become smooth due

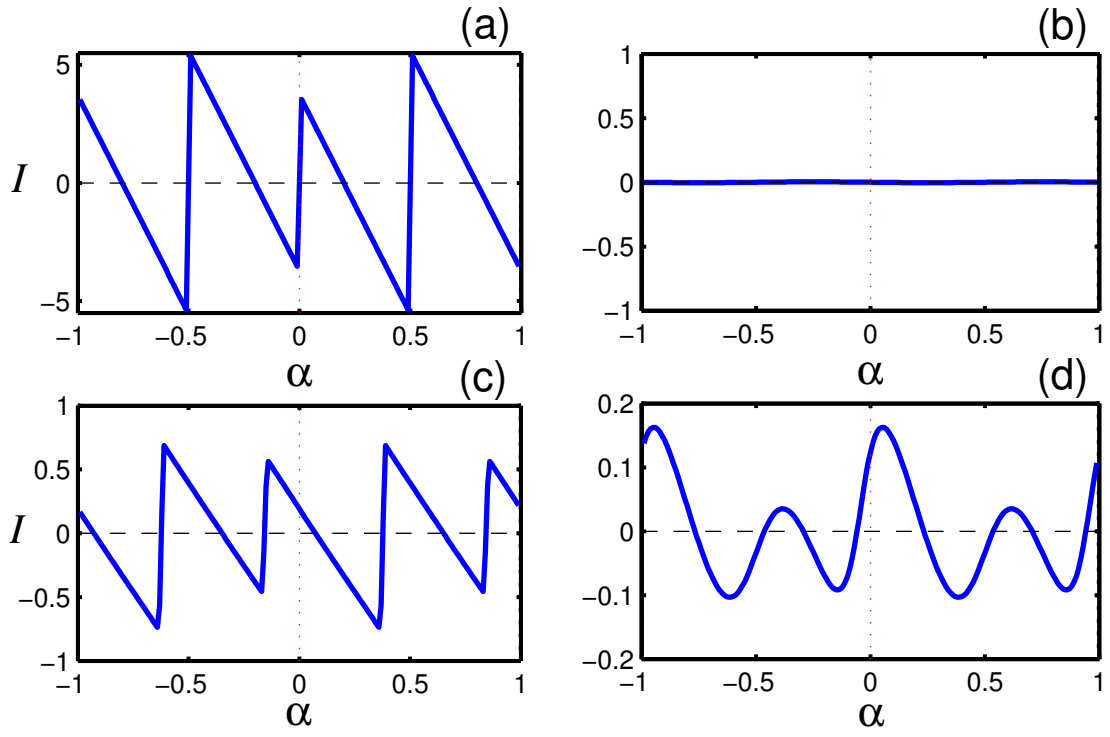

Fig. 11. Persistent current (PC) as a function of the quantum flux parameter α from five lowest states (including spin) for nonrelativistic (a,b) and relativistic (c,d) cases. The domain is integrable for (a,c) and chaotic for (b,d).

to level repulsion in the corresponding energy-flux dispersion pattern. As a result, PCs carried by the Schrödinger particle practically vanish as compared with the integrable case but, strikingly, the Dirac fermion still carries a persistent current with amplitude of the same order of magnitude as that for the integrable case - SPCs. Intuitively, SPCs carried by the Dirac fermion as an "exceptional" magnetic response are associated with the chaotic Dirac WGMs exemplified in Fig. 10.

2.3.2. Origin of WGMs and SPCs.

The origin of the "exceptional" magnetic response of the chaotic Dirac fermion can be understood through the behavior of the current carried by the particle at the boundary interface. We have developed an analytic understanding to predict the occurrence of Dirac WGMs and, consequently, SPCs. In particular, we consider the following problem: a plane wave incident obliquely on a straight potential jump $M(x, y)$ given by

$$M(x,y) = \begin{cases} 0, & x < 0 \\ \\ V_0, & x > 0, \end{cases}, \tag{2.4}$$

as shown in Fig. 12. Without loss of generality, we let the incident wave ψ^i be described by the wave vector

$$\boldsymbol{k}_0 = (k\cos\theta_0, k\sin\theta_0),$$

the reflected wave ψ^r by

$$\boldsymbol{k}_1 = (k\cos\theta_1, k\sin\theta_1),$$

and the transmitted wave ψ^t by

$$\boldsymbol{u} = (iq, K),$$

where $\theta_1 = \pi - \theta_0$ and $K \equiv k\sin\theta_0$. We focus on the situation where the energy of the incident wave satisfies $E < V_0$, which corresponds to the total reflection case.

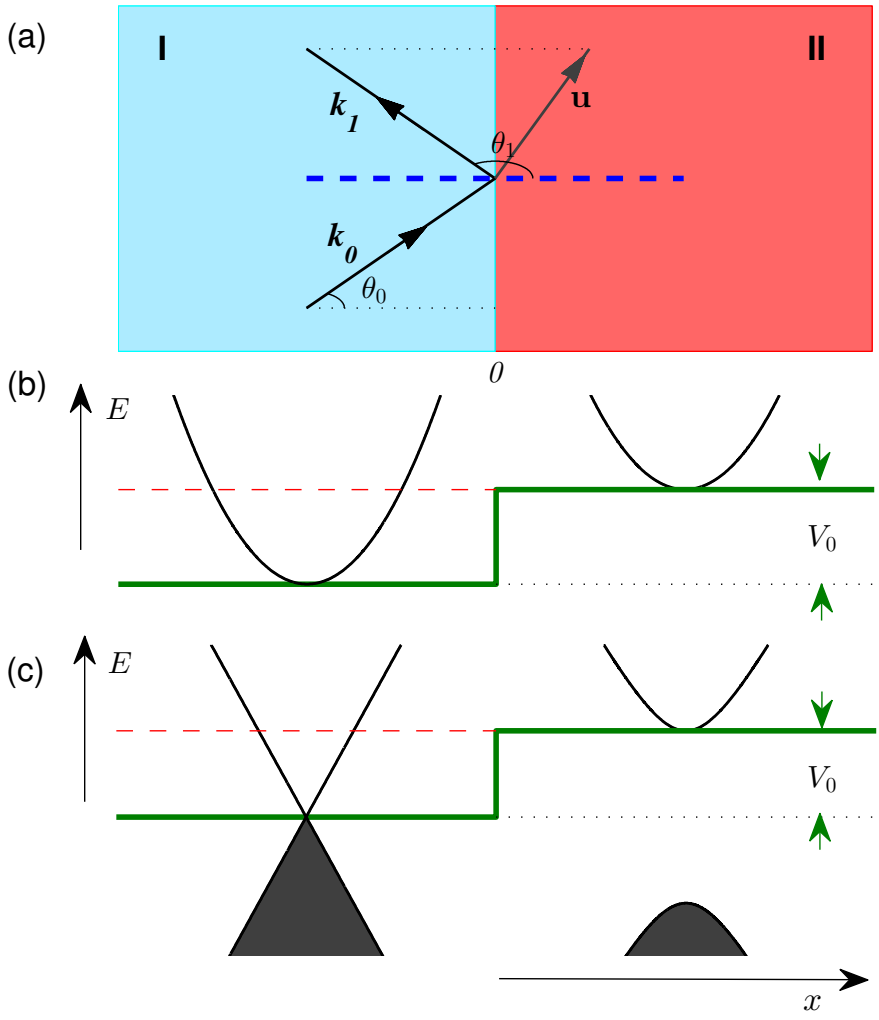

Fig. 12. Incident, Reflected and Transmitted Local Plane Waves At a Potential Jump.

Referring to Fig. 12, we have that the wave in region I ($x < 0$) can be written as

$$\Psi^{\rm I}(\boldsymbol{r}) = \psi^i(x,y) + R\psi^r(x,y),$$

and the wave in region II is

$$\Psi^{\rm II}(\boldsymbol{r}) = T\psi^t(x,y),$$

where the coefficients R and T are to be determined by matching the waves at $x = 0$. In the following, we treat the Schrödinger scalar wave and Dirac spinor wave separately.

Schrödinger scalar plane wave. For the nonrelativistic quantum case as shown in Fig. 12(b), we have, in region I ($x < 0$),

$$\Psi_S^{\rm I} = \left(e^{ikx\cos\theta_0} + Re^{-ikx\cos\theta_0}\right) e^{iky\sin\theta_0},$$

and in region II ($x > 0$),

$$\Psi_S^{\rm II} = Te^{-qx}e^{iKy},$$

where q and K are related to each other through

$$q = \sqrt{\frac{2\mu(V_0 - E)}{\hbar^2} + K^2};\;\; E = \frac{\hbar^2 k^2}{2\mu},$$

with μ denoting the mass of the particle. Matching the waves and their derivatives at $x = 0$, we obtain

$$R = \frac{k\cos\theta_0 - iq}{k\cos\theta_0 + iq} = e^{-2i\beta};\;\; T = \frac{2k\cos\theta_0}{k\cos\theta_0 + iq} = 2\cos\beta e^{-i\beta},$$

where the parameter β is defined through

$$\tan\beta = \frac{q}{k\cos\theta_0};\;\; 0 \le \beta \le \frac{\pi}{2}.$$

Given the wave function $\Psi_S(\boldsymbol{r})$, the associated probability current density is

$$\boldsymbol{J}_S(\boldsymbol{r}) = \frac{\hbar}{2\mu i}\left[\Psi_S^\dagger(\boldsymbol{r})\boldsymbol{\nabla}\Psi_S(\boldsymbol{r}) - \text{c.c.}\right],$$

where c.c. denotes complex conjugate. We therefore obtain, in region I,

$$\boldsymbol{J}_S^{\mathrm{I}} \begin{cases} (J_S^{\mathrm{I}})_x = \dfrac{\hbar k \cos\theta_0}{\mu}[1 - |R|^2] = 0; \\ (J_S^{\mathrm{I}})_y = \dfrac{\hbar k}{\mu} \sin\theta_0 \left[2 + 2\cos(2kx\cos\theta_0 + 2\beta)\right]; \end{cases} \tag{2.5}$$

and in region II,

$$\boldsymbol{J}_S^{\mathrm{II}} \begin{cases} (J_S^{\mathrm{II}})_x = 0; \\ (J_S^{\mathrm{II}})_y = \dfrac{\hbar K}{\mu}|T|^2 e^{-2qx} = \dfrac{\hbar k \sin\theta_0}{\mu} 4\cos^2\beta e^{-2qx}. \end{cases} \tag{2.6}$$

In region I, the y component of the probability current is the sum of two terms: (1) the term resulting from the sum of the currents associated with the incident and reflected waves, and (2) the term containing the factor $\cos(2kx\cos\theta_0 + 2\beta)$ that accounts for the interference between the incident and reflected waves. In region II, the probability current is also parallel to the y-axis, and it decays exponentially as an evanescent wave. Note that $(J_S^{\mathrm{II}})_y \to 0$ as $q \to \infty$ (i.e., $V_0 \to \infty$).

Planar Dirac spinor wave. The relativistic case is shown in Fig. 12(c). We proceed in the same manner as for the nonrelativistic case. Expressing the wave in terms of massless spinor planar waves that are solutions of the Dirac equation, we have, in region I ($x < 0$),

$$\Psi_D^{\mathrm{I}} = \frac{1}{\sqrt{2}} \left\{ \begin{pmatrix} e^{-\frac{1}{2}i\theta_0} \\ e^{\frac{1}{2}i\theta_0} \end{pmatrix} e^{ikx\cos\theta_0} + \; R \begin{pmatrix} e^{-\frac{1}{2}i\theta_1} \\ e^{\frac{1}{2}i\theta_1} \end{pmatrix} e^{-ikx\cos\theta_0} \right\} e^{iky\sin\theta_0},$$

and in region II ($x > 0$),

$$\Psi_D^{\mathrm{II}} = \frac{T}{\sqrt{2}} \begin{pmatrix} -i\lambda_1 \\ \lambda_2 \end{pmatrix} e^{-qx} e^{iKy},$$

where

$$\lambda_1 = \sqrt{\frac{(V_0 + E)(q - K)}{V_0 q - EK}}; \;\; \lambda_2 = \sqrt{\frac{(V_0 - E)(q + K)}{V_0 q - EK}},$$

and

$$q = \sqrt{\frac{V_0^2 - E^2}{\hbar^2 v^2} + K^2}; E = v\hbar k,$$

with v being the Fermi velocity.

Matching boundary conditions at $x = 0$, we obtain

$$R = \frac{i\lambda - e^{i\theta_0}}{i - \lambda e^{i\theta_0}} = e^{i(2\gamma+\theta_0-\frac{\pi}{2})},$$

where the parameters γ and λ are defined through

$$\tan\gamma = \frac{\lambda_1 - \lambda_2 \sin\theta_0}{\lambda_2 \cos\theta_0} = \frac{1 - \lambda \sin\theta_0}{\lambda \cos\theta_0},$$

$$\lambda = \frac{\lambda_2}{\lambda_1} = \sqrt{\frac{(V_0 - E)(q + K)}{(V_0 + E)(q - K)}} = \frac{V_0 - E}{\hbar v(q - K)} = \frac{\hbar v(q + K)}{V_0 + E},$$

and

$$T = \frac{1}{\lambda_2}\left[e^{\frac{1}{2}i\theta_0} + Rie^{-\frac{1}{2}i\theta_0}\right] = \frac{2\cos\gamma}{\lambda_2} e^{i(\gamma+\frac{\theta_0}{2})}.$$

For the spinor wave $\Psi_D(\boldsymbol{r})$ describing a Dirac fermion in two dimensions, the corresponding probability current density is

$$\boldsymbol{J}_D(\boldsymbol{r}) \equiv v\Psi_D^\dagger(\boldsymbol{r})\hat{\boldsymbol{\sigma}}\Psi_D(\boldsymbol{r}) = 2v\left(\Re[\psi_1^*\psi_2], \Im[\psi_1^*\psi_2]\right),$$

where $\hat{\boldsymbol{\sigma}} = (\sigma_x, \sigma_y)$ and $\Psi_D = [\psi_1, \psi_2]^{\mathrm{T}}$. We have, in region I,

$$\boldsymbol{J}_D^{\mathrm{I}} \begin{cases} (J_D^{\mathrm{I}})_x = v(1 - |R|^2)\cos\theta_0 = 0; \\ \\ (J_D^{\mathrm{I}})_y = v\left[2\sin\theta_0 + 2\sin\left(-2kx\cos\theta_0 + 2\gamma + \theta_0\right)\right]; \end{cases} \tag{2.7}$$

and in region II,

$$\boldsymbol{J}_D^{\mathrm{II}} \begin{cases} (J_D^{\mathrm{II}})_x = 0; \\ \\ (J_D^{\mathrm{II}})_y = v|T|^2\lambda_1\lambda_2 e^{-2qx} = v\dfrac{4\cos^2\gamma}{\lambda} e^{-2qx}. \end{cases} \tag{2.8}$$

From Eqs. (2.5)-(2.6) and Eqs. (2.7)-(2.8), we observe identical behaviors in the normal current densities (i.e., the x-component) for both nonrelativistic and relativistic cases, but there is a significant difference in the transverse current densities (i.e., the y-component). In particular, as $E/V_0 \to 0$ (the hard-wall limit), we have $(J_S^{\mathrm{I}})_y|_{x=0} \equiv (J_S^{\mathrm{II}})_y|_{x=0} \to 0$ for the nonrelativistic case,

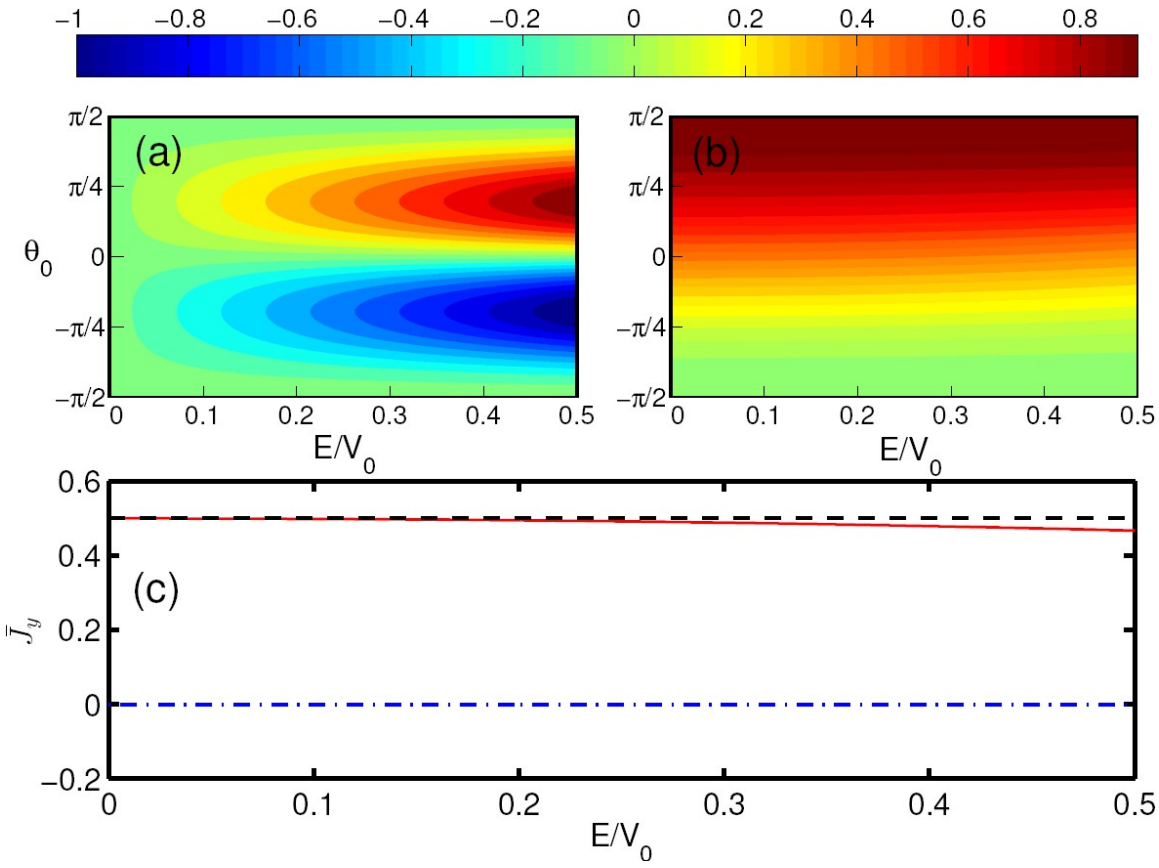

Fig. 13. Comparison of the y-component of the current density (coded by colors) as a function of the incident angle θ_0 and the height of the reduced potential barrier E/V_0 between the nonrelativistic (a) and relativistic (b) cases at the interface ($x = 0$). (c) The y-component of the current density averaged over all possible incident angles θ_0 as a function of E/V_0: blue dash-dotted (red) curve is for the nonrelativistic (relativistic) case and the dash black line denotes the theoretical estimation of the relativistic case based on Eq. (2.8) with the assumption $E/V_0 \ll 1$. In both cases, the values of the current density have been normalized by the respective maxima.

while $(J_D^{\rm I})_y|_{x=0} \equiv (J_D^{\rm II})_y|_{x=0} \to 2(1+\sin\theta_0)$ for the relativistic case. In addition, it is apparent from Eqs. (2.5)-(2.6) that $(J_S)_y$ is antisymmetric (odd function) with respect to θ_0 so that its average over all possible incident angles, $\bar{J}_S^y \equiv \int_{-\pi/2}^{\pi/2} {\rm d}\theta_0 (J_S)_y$, is zero. The averaged transverse current density $\bar{J}_D^y$ in the relativistic case, however, tends to a finite value in the hard-wall limit. A schematic comparison of the y component of the probability current density $\boldsymbol{J}$ at the interface ($x = 0$) as a function of the incident angle θ_0 and the magnitude of the reduced incident energy E/V_0 between the Schrödinger and Dirac cases is shown in Fig. 13. We see that the nonrelativistic transverse current density $(J_S)_y$ is antisymmetric with respect to θ_0, leading to zero contribution to $\bar{J}_S^y$, while the relativistic transverse current density $(J_D)_y$ is a nonnegative monotonic function of θ_0 so that there exists a finite transverse current even for a fully chaotic ring when all possible incident angles are taken into account. Such a finite averaged transverse current density $\bar{J}_D^y$ with magnitude one half the maximum makes it possible to form chaotic Dirac whispering gallery modes that carry considerable directional currents. This is the fundamental mechanism for the phenomenon of SPCs.

Note that, although Eqs. (2.7) and (2.8) appear different in form, at the interfact ($x = 0$) they give exactly the same current density (see Supplementary Note 3). For $V_0 \to \infty$, the hard-wall boundary condition is restored (the infinity-mass boundary condition). Physically the counterintuitive phenomenon can be understood, as follows. The incoming wave from the metal region (mass term $M = 0$) is spin polarized along its momentum (current) direction. After entering the insulator region, a finite mass term acting on σ_z will change the direction of the spin and hence affect the current via the spin-momentum locking term $\mathbf{k} \cdot \sigma$. The relevant Hall-like phenomenon associated with the T-breaking mass potential has been uncovered in a very recent work [84]. In addition, we note that the results do not depend on the special form of the wave function in region II (although such a symmetric form is convenient for analysis). In fact, we obtain the same results [45] when

choosing the wavefunction to have the form $\sim [1, C(E)]^T$.

2.3.3. Experimental Scheme.

A possible experimental scheme to observe and characterize Dirac WGMs and SPCs is, as follows. A 3D topological insulator supports a (2D) gapless state on its surface, with low-energy excitations described by the massless Dirac Hamiltonian [47, 85] $\hat{H}_{\rm surface} = -i\hbar v_F \hat{\boldsymbol{\sigma}} \cdot \boldsymbol{\nabla}$, where $\hat{\boldsymbol{\sigma}}$ characterizes the spin. The surface electronic structure is similar to that of graphene, except that there is only a single Dirac point. Different from graphene, the Dirac surface states of a topological insulator are associated with strong spin-orbit interactions. In spintronics applications of topological insulators, it is desirable to introduce a gap into the surface states. This can be done by breaking the time-reversal symmetry using a ferromagnet insulator (FMI) deposited on the top of a topological insulator [75]. The exchange coupling induced due to proximity to the ferromagnet insulator will give rise to a local exchange field that lifts the Kramers degeneracy at the surface Dirac point and introduces a mass term into the Dirac Hamiltonian. Thus, generally, we have $\hat{H} = v\hat{\boldsymbol{\sigma}}\cdot(\hat{\boldsymbol{p}} + e\boldsymbol{A}) + M(\boldsymbol{r})\hat{\sigma}_z + \gamma_z B\hat{\sigma}_z$, where the vector potential $\boldsymbol{A}$ accounts for the effect of the external magnetic field $\boldsymbol{B} = \boldsymbol{\nabla} \times \boldsymbol{A} = B\hat{z}$, with an additional Zeeman splitting correction in the last term. The controllable mass term $M\hat{\sigma}_z$, responsible for the local exchange coupling with a FMI cap layer, makes 3D topological insulators a potential experiment platform for observing and characterizing Dirac WGMs and SPCs.

2.4. Conclusions

We formulate a relativistic version of AB chaotic billiards to study PCs in Dirac rings. We find that, in contrast to the nonrelativistic quantum counterpart where PCs vanish for chaotic rings, the currents continue to exist in the relativistic chaotic AB rings and, in this sense, they are superpersistent. We demonstrate that SPCs are a consequence of Dirac WGMs, and we develop an analytic

understanding of their emergence in relativistic quantum systems. We also propose that, experimentally, chaotic rings patterned by magnetic domain heterostructures deposited on the surface of a 3D topological insulator can be a feasible scheme to observe and characterize chaotic Dirac WGMs and SPCs. To investigate the magnetic response of chaotic Dirac fermions is not only fundamental to the emerging field of relativistic quantum chaos, but also relevant to device applications based on Dirac materials.

2.5. Methods

Before solving the Dirac equation with vector potential, we investigate some general properties of the magnetic flux (characterized by parameter α) dependent relativistic quantum spectrum $\{E_j(\alpha)\}$ as determined by Eq. (1) in the main text, under the boundary condition [Eq. (3) in the main text]. Since the vector potential $\boldsymbol{A}$ depends on the gauge while the Dirac equation is gauge-invariant, we can choose a proper gauge transformation to eliminate explicitly $\boldsymbol{A}$ from the Dirac Hamiltonian $\hat{H} = v\hat{\boldsymbol{\sigma}}\cdot(-i\hbar\boldsymbol{\nabla} + q\boldsymbol{A}) + V(\boldsymbol{r})\hat{\sigma}_z$. An example of such transformation is

$$\phi(\boldsymbol{r}) \equiv \begin{pmatrix} \phi_1 \\ \\ \phi_2 \end{pmatrix} = \psi(\boldsymbol{r}) \times \exp\left[-i\frac{2\pi}{\Phi_0}\int_{\boldsymbol{r}_0}^{\boldsymbol{r}} \boldsymbol{A}(\boldsymbol{r'})\cdot \mathrm{d}\boldsymbol{r'}\right]. \tag{2.9}$$

Substituting Eq. (5.37) into the Dirac equation and taking into account the boundary conditions [Eq. (3) in main text], we obtain

$$\hat{H}_0\phi(\boldsymbol{r}) \equiv \left[-i\hbar v\hat{\boldsymbol{\sigma}}\cdot\boldsymbol{\nabla} + V(\boldsymbol{r})\hat{\sigma}_z\right]\phi(\boldsymbol{r}) = E\phi(\boldsymbol{r}), \tag{2.10}$$

with the following complex boundary condition:

$$\frac{\phi_2}{\phi_1}\Big|_{\partial\mathcal{B}} = \mathrm{sgn}(V) i \exp[i\theta(s)], \tag{2.11}$$

which is equivalent to the original boundary condition [Eq. (3) in main text]. The nontrivial point here is that, because ψ is single valued, ϕ must be multivalued. As a result, for any circuit C about

the flux line, ϕ will acquire a phase factor:

$$\hat{c}\phi = \exp\left[-i\frac{2\pi}{\Phi_0}\oint_C \boldsymbol{A}\cdot \mathrm{d}\boldsymbol{r}\right]\phi = \exp\left(-2\pi i W_C \alpha\right)\phi, \tag{2.12}$$

where the operator $\hat{c}$ denotes the circuit operation acting on ϕ and W_C ($= \pm 1, \pm 2, \cdots$) is the winding number of C. From Eqs. (2.10)-(2.12), we can conclude that, because the complex boundary condition does not depend on α, it is not possible to generate the so-called "false T-breaking" only by tuning the quantum flux parameter α, in contrast to the nonrelativistic case [78]. If boundary $\mathcal{B}$ is chosen to be geometrically asymmetric so that there is chaotic dynamics in the classical limit, contrary to nonrelativistic quantum systems, the relativistic quantum spectral statistics are characterized by those of the Gaussian unitary ensemble (GUE), regardless of the value of α. Furthermore, the spectrum $\{E_j(\alpha)\}$ does not possess symmetry with respect to flux reversal ($\alpha \to -\alpha$), in contrast to nonrelativistic quantum spectra as determined by the Schrödinger equation where the symmetry is preserved. This can be shown explicitly, as follows.

For our Dirac ring system, the flux-reversal operator $\hat{f}$ can be represented as

$$\hat{f} = \hat{U}\hat{K}, \tag{2.13}$$

where $\hat{U}$ is unitary and commutes with $\hat{c}$:

$$[\hat{f}, \hat{c}] = 0. \tag{2.14}$$

We see that ϕ transforms to

$$\phi' \equiv \left[\phi_1', \phi_2'\right]^{\mathrm{T}} = \hat{f}\phi = \hat{U}\phi^*,$$

and

$$\hat{c}\phi' = \exp[-2\pi i W_C(-\alpha)]\phi'. \tag{2.15}$$

Thus, in order that $E_j(\alpha) = E_j(-\alpha)$, $\hat{f}$ must satisfy

$$[\hat{f}, \hat{H}_0] = 0, \tag{2.16}$$

and ϕ' must follow the same boundary condition as Eq. (2.11). It was pointed out by Berry and Mondragon [78] that, if $V(\boldsymbol{r})$ possesses no geometric symmetry, no operator would exist which satisfies Eq. (2.13) and Eq. (2.16) simultaneously, but it may be possible to find an operator with the form given by Eq. (2.13) that commutes with $\hat{H}_0$ if $V(\boldsymbol{r})$ does possess any geometric symmetry. In our system, however, any such possible operator would not satisfy the pre-condition Eq. (2.14) at the same time. Consequently, the energy spectrum $\{E_j(\alpha)\}$ does not possess the flux-reversal symmetry, i.e., $E_j(\alpha) \neq E_j(-\alpha)$.

By considering the specific situation of $\hat{U} = i\hat{\sigma}_y$, we see that the flux-reversal symmetry emerges if the sign of the potential V is changed simultaneously, i.e., $\{\alpha \to -\alpha, V \to -V\}$. That is the primary reason that the energy spectrum in graphene is symmetric with respect to $\alpha = 0$ when both valleys are included [73]. From Eqs. (2.10)-(2.12), we have

$$E_j(\alpha) = E_j(\alpha + 1). \tag{2.17}$$

Studying the relativistic AB quantum billiard spectrum in the range $-1/2 \leq \alpha \leq 1/2$ thus suffices, which corresponds to the first "Brillouin zone."

2.5.1. Magnetic Flux Dependent Relativistic Quantum Energy Spectrum

2.5.1.1. Conformal-Mapping Method

The idea of employing conformal mapping to calculate quantum eigenenergies and eigenstates was proposed by Robnik and Berry [6, 82] for non-relativistic quantum billiard systems. In a recent work [83], we adopted the method to relativistic quantum billiards governed by the Dirac equation. Here, we further extend the method to relativistic quantum chaotic billiards subject to AB magnetic flux as given by Eq. (2.10). The basic idea is that, while the Dirac equation together with the boundary condition is generally not separable in the Cartesian coordinates, for circularly symmetric ring domains analytic solutions can be written down. Given a closed domain with an analytic

boundary, we can identify a proper conformal mapping that transforms the domain into a circular ring. The analytic solutions of the Dirac equation in the circular ring can then be transformed back to the original domain to yield a large number of eigenvalues and eigenstates with high accuracy.

We begin by choosing the gauge

$$\boldsymbol{A}(\boldsymbol{r}) = \frac{\alpha}{2\pi}\Phi_0 \left(\frac{\partial F}{\partial y}, -\frac{\partial F}{\partial x}, 0\right); \;\; F = -\ln|\boldsymbol{r}| \tag{2.18}$$

and writing the Dirac equation [Eq. (1) in the main text] in the polar coordinates $\boldsymbol{r} = (r, \theta)$ for the closed circular ring domain defined by $V(\boldsymbol{r}) = 0$:

$$\begin{pmatrix} 0 & \exp(-i\phi)\left(\frac{\partial}{\partial r} - \frac{i}{r}\frac{\partial}{\partial \phi} + \frac{\alpha}{r}\right) \\ \exp(i\phi)\left(\frac{\partial}{\partial r} + \frac{i}{r}\frac{\partial}{\partial \phi} - \frac{\alpha}{r}\right) & 0 \end{pmatrix} \times \psi(\boldsymbol{r}) = i\mu\psi(\boldsymbol{r}), \tag{2.19}$$

where $\mu \equiv E/\hbar v$. For a circularly symmetric ring boundary, we have $[\hat{J}_z, \hat{H}] = 0$, where

$$\hat{J}_z = -i\hbar\partial_\phi + \hbar/2\hat{\sigma}_z$$

is the total angular momentum operator. The solutions of Eq. (2.19) can thus be written as

$$\psi(\boldsymbol{r}) = \exp[i(l-1/2)\theta] \begin{pmatrix} \phi(r) \\ i\chi(r)\exp(i\theta) \end{pmatrix}, \tag{2.20}$$

where $l = \pm 1/2, \pm 3/2, \cdots$ denotes the eigenvalues of $\hat{J}_z$. Substituting Eq. (3.4) into Eq. (2.19) yields the following radial equation:

$$\hat{H}_r \begin{pmatrix} \phi(r) \\ \chi(r) \end{pmatrix} = \mu \begin{pmatrix} \phi(r) \\ \chi(r) \end{pmatrix}, \tag{2.21}$$

with the radial 'Hamiltonian' given by

$$\hat{H}_r = i\hat{\sigma}_y\left(\frac{\mathrm{d}}{\mathrm{d}r} + \frac{1/2}{r}\right) + \hat{\sigma}_x\frac{l+\alpha}{r} = \begin{pmatrix} 0 & \frac{\mathrm{d}}{\mathrm{d}r} + \frac{1/2}{r} + \frac{l+\alpha}{r} \\ -\frac{\mathrm{d}}{\mathrm{d}r} - \frac{1/2}{r} + \frac{l+\alpha}{r} & 0 \end{pmatrix}. \tag{2.22}$$

Under the similarity transformation: $\hat{\mathcal{P}} = (\hat{\sigma}_x + \hat{\sigma}_z)/\sqrt{2}$, the radial Hamiltonian $\hat{H}_r$ is transformed to

$$\hat{H}_r' = \hat{\mathcal{P}}\hat{H}_r\hat{\mathcal{P}}^\dagger = \begin{pmatrix} -\frac{l+\alpha}{r} & \frac{\mathrm{d}}{\mathrm{d}r} + \frac{1/2}{r} \\ -\frac{\mathrm{d}}{\mathrm{d}r} - \frac{1/2}{r} & \frac{l+\alpha}{r} \end{pmatrix} = i\hat{\sigma}_y \left(\frac{\mathrm{d}}{\mathrm{d}r} + \frac{1/2}{r} \right) + \hat{\sigma}_z \frac{-(l+\alpha)}{r}, \tag{2.23}$$

with an equivalent mass term $-(l+\alpha)/r$ that is both position and state dependent. Although either the AB flux (α) or the mass (V) can lead to T-breaking, quantitatively their roles in the solutions of the Dirac equation are generally different. As a result, in a Dirac fermion system the effects of fixed T-breaking due to the mass confinement V cannot be completely compensated by those induced by the tunable AB flux α.

From Eqs. (2.21) and (2.22), we see that $\phi(r)$ is a solution of the Bessel's equation of order $\bar{l} - 1/2$, i.e.,

$$\frac{\mathrm{d}^2\phi}{\mathrm{d}R^2} + \frac{1}{R}\frac{\mathrm{d}\phi}{\mathrm{d}R} + \left[1 - \frac{(\bar{l} - 1/2)^2}{R^2} \right] \phi = 0, \tag{2.24}$$

where $\bar{l} \equiv l + \alpha$ and $R = \mu r$ is the dimensionless radial coordinate. For the ring geometry, $\phi(r)$ can be written as

$$\phi(r) = N \left(H^{(1)}_{\bar{l}-1/2}(\mu r) + \beta H^{(2)}_{\bar{l}-1/2}(\mu r) \right), \tag{2.25}$$

where $H^{(1,2)}_\nu$ denote the ν-th order Hankel functions of the (first, second) kind, N and β are undetermined coefficients. Substituting Eq. (2.25) back into Eq. (2.21) and using the relations

$$H^{(1,2)'}_\nu(x) - \nu H^{(1,2)}_\nu(x)/x = -H^{(1,2)}_{\nu+1}(x),$$

we obtain the second radial component

$$\chi(r) = N \left(H^{(1)}_{\bar{l}+1/2}(\mu r) + \beta H^{(2)}_{\bar{l}+1/2}(\mu r) \right). \tag{2.26}$$

Without loss of generality, we assume that the outer radius of the ring is unity and the inner radius is $\xi \in (0, 1)$. Imposing the boundary condition [Eq. (3) in main text] on the wavefunction $\psi(\boldsymbol{r})$ with

the expressions of Eqs. (3.4), (2.25), and (2.26), and taking into account their orthonormal property, we get

$$\beta = -\frac{\mathcal{H}_+^{(1)}(\mu_j\xi)}{\mathcal{H}_+^{(2)}(\mu_j\xi)} = -\frac{\mathcal{H}_-^{(1)}(\mu_j)}{\mathcal{H}_-^{(2)}(\mu_j)}, \tag{2.27}$$

with the compact notations $j \equiv (\bar{l}, n)$ and

$$\mathcal{H}_\pm^{(m)}(x) \equiv H_{\bar{l}+1/2}^{(m)}(x) \pm H_{\bar{l}-1/2}^{(m)}(x); \text{ for } m = 1, 2,$$

as well as the normalization constants

$$|N|^{-2} = 2\pi \int_\xi^1 \mathrm{d}rr \left[\left| H_{\bar{l}-1/2}^{(1)}(\mu_j r) + \beta H_{\bar{l}-1/2}^{(2)}(\mu_j r) \right|^2 + \left| H_{\bar{l}+1/2}^{(1)}(\mu_j r) + \beta H_{\bar{l}+1/2}^{(2)}(\mu_j r) \right|^2 \right]. \tag{2.28}$$

The quantity μ_j in Eqs. (2.27) and (2.28) satisfies the (compact) energy eigenvalue equation

$$\begin{vmatrix} \mathcal{J}_-(\mu) & \mathcal{Y}_-(\mu) \\ \mathcal{J}_+(\mu\xi) & \mathcal{Y}_+(\mu\xi) \end{vmatrix} = 0, \tag{2.29}$$

$$\begin{aligned} \mathcal{J}_\pm(x) &\equiv J_{\bar{l}+1/2}(x) \pm J_{\bar{l}-1/2}(x), \\ \mathcal{Y}_\pm &\equiv Y_{\bar{l}+1/2}(x) \pm Y_{\bar{l}-1/2}(x), \end{aligned}$$

with J and Y being the Bessel functions of the first and second kind, respectively.

We have so far obtained the complete (positive-energy part) solutions $\{\psi_j, \mu_j\}$ to Eq. (2.19) in the circular ring domain under the boundary condition. The eigenfunctions $\psi_j \equiv \langle \boldsymbol{r}|j\rangle$ satisfy

$$\langle i|j\rangle \equiv \iint_{\mathcal{B}} \mathrm{d}\boldsymbol{r}^2 \langle i|\boldsymbol{r}\rangle\langle \boldsymbol{r}|j\rangle = \iint_{\mathcal{B}} \mathrm{d}\boldsymbol{r}^2 \psi_i^\dagger(\boldsymbol{r})\psi_j(\boldsymbol{r}) = \delta_{ij},$$

and thus form an orthonormal complete basis for the operator $-i\hat{\boldsymbol{\sigma}} \cdot \boldsymbol{D}$ and its positive integral power $[-i\hat{\boldsymbol{\sigma}} \cdot \boldsymbol{D}]^n$ defined in the same domain under the same boundary condition.

The billiard domain $\mathcal{B}$ in which the Dirac equation is to be solved is defined as a conformal transformation of the circular ring domain in the $w-$plane, as shown in Fig. 14, i.e.,

$$u(x, y) + iv(x, y) = w(z) \equiv w(re^{i\phi}), r \in [\xi, 1], \tag{2.30}$$

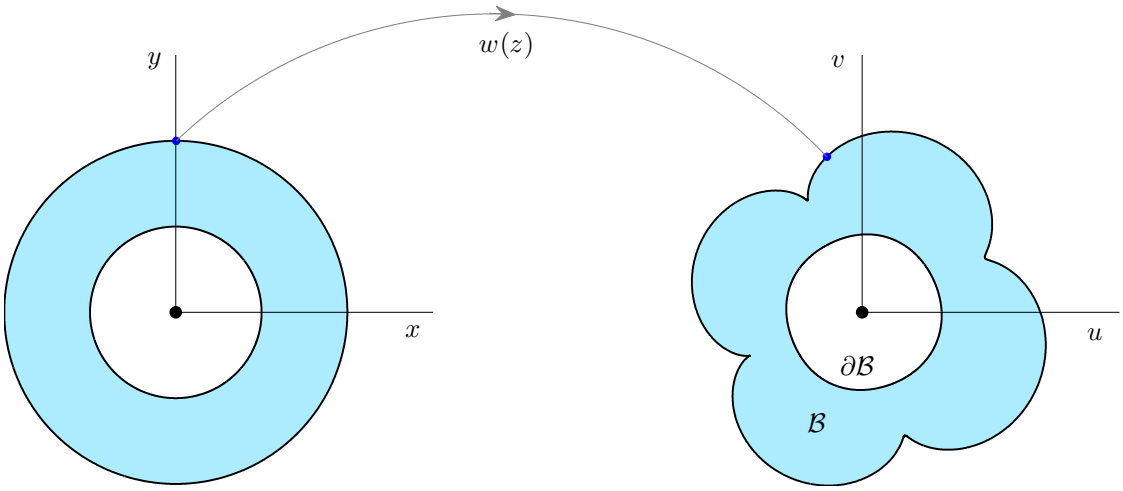

Fig. 14. Conformal transformation from the unit disc in $z = x + iy$ (z-plane) to the billiard domain in $w = u + iv$ (w-plane). The boundary is generated by the mapping function Eq. (2.38) with parameters $a = 1, \omega = \pi/2$, and $\xi = 0.5$. (Adapted from Ref. [6]).

where $w(z)$ is an analytic function with non-vanishing derivative in $\mathcal{B}$. The outer boundary can be defined parametrically by $u = \mathrm{Re}[w(e^{i\phi})], v = \mathrm{Im}[w(e^{i\phi})]$. We aim to solve the following stationary Dirac equation:

$$-i\hat{\boldsymbol{\sigma}} \cdot \boldsymbol{D}_{uv}\Psi(u,v) = k\Psi(u,v), \tag{2.31}$$

together with the boundary condition

$$\Psi_2/\Psi_1|_{\partial_{\mathcal{B}}} = \mathrm{sgn}(V) i e^{i\theta},$$

where $k \equiv E/\hbar v$, $\Psi = [\Psi_1, \Psi_2]^{\mathrm{T}}$ denotes the spinor wave-function, $\boldsymbol{D}_{uv} = \boldsymbol{\nabla}_{uv} + \boldsymbol{a}(u,v)$, and $\boldsymbol{a} = 2\pi\boldsymbol{A}/\Phi_0$ denotes the normalized magnetic vector potential, with

$$\boldsymbol{a}(u,v) = \alpha(\partial g/\partial v, -\partial g/\partial u, 0)$$

being the contours of the scalar function $g(u,v)$ given by $\Delta_{uv} g = -2\pi\delta(u,v)$. Under the operator $-i\hat{\boldsymbol{\sigma}} \cdot \boldsymbol{D}_{uv}$, Eq. (2.31) becomes

$$\left[-\boldsymbol{D}_{uv}^2 \mathbf{1} + 2\pi\alpha\delta(u,v)\hat{\sigma}_z\right] \Psi(u,v) = k^2 \Psi(u,v), \tag{2.32}$$

where

$$\boldsymbol{D}_{uv}^2 = \Delta_{uv} + 2i\alpha \left(\frac{\partial g}{\partial v}\partial_u - \frac{\partial g}{\partial u}\partial_v\right) - \alpha^2 \left[\left(\frac{\partial g}{\partial u}\right)^2 + \left(\frac{\partial g}{\partial v}\right)^2\right]. \tag{2.33}$$

Using the conformal mapping

$$\begin{pmatrix} \Delta \\ \frac{\partial F}{\partial y}\partial_x - \frac{\partial F}{\partial x}\partial_y \\ \left(\frac{\partial F}{\partial x}\right)^2 + \left(\frac{\partial F}{\partial y}\right)^2 \\ \delta(\boldsymbol{r}) \end{pmatrix} = \left|\frac{\mathrm{d}w}{\mathrm{d}z}\right|^2 \begin{pmatrix} \Delta_{uv} \\ \frac{\partial g}{\partial v}\partial_u - \frac{\partial g}{\partial u}\partial_v \\ \left(\frac{\partial g}{\partial u}\right)^2 + \left(\frac{\partial g}{\partial v}\right)^2 \\ \delta(u,v) \end{pmatrix}$$

to transform Eq. (2.32) to the circular ring domain in the z-plane, together with the definitions $F(\boldsymbol{r}) \equiv f(u,v)$ and $\Psi'(\boldsymbol{r}) = \Psi(u,v)$, we obtain the following form of Eq. (2.31):

$$\left[\boldsymbol{D}^2 \mathbf{1} - 2\pi\alpha\delta(\boldsymbol{r})\hat{\sigma}_z\right] \Psi'(\boldsymbol{r}) + k^2 \left|\frac{\mathrm{d}w}{\mathrm{d}z}\right| \Psi'(\boldsymbol{r}) = 0. \tag{2.34}$$

The ring topology guarantees that any singular solutions that are divergent at the origin [86–88] arising from the singular Zeeman-like term introduced in Eqs. (2.32) and (2.34) can be avoided.

To solve Eq. (2.34), we expand Ψ' in terms of the eigenfunctions $\{\psi_j(r,\theta), j = 1, \cdots\}$ of the circular ring domain in the presence of a central flux line:

$$\Psi'(r,\theta) = \sum_{j=1}^{\infty} c_j \psi_j(r,\theta), \tag{2.35}$$

where c_j's are the expansion coefficients. Substituting Eq. (2.35) into Eq. (2.34), together with the orthogonality of ψ_j, we obtain

$$\frac{\nu_i}{k^2} - \sum_j M_{ij}\nu_j = 0, \tag{2.36}$$

where $\nu_i = \mu_i c_i$,

$$M_{ij} = \frac{1}{\mu_i} \langle i|T(r,\theta)|j\rangle \frac{1}{\mu_j}, \tag{2.37}$$

and $T(r,\theta) = |\mathrm{d}w/\mathrm{d}z|^2$. Once the eigenvalues λ_n and eigenvectors $\boldsymbol{\nu}$ of the matrix (M_{ij}) are obtained, we get the complete solutions of Eq. (2.31) through the relations $k_n = 1/\sqrt{\lambda_n}$ and $c_i = \nu_i/\mu_i$. In actual computations, a truncated basis $\{\psi_j(r,\phi), j_{\min} \leq j \leq j_{\max}\}$ can be used, where $j_{\min}$ denotes the first eigenstate. The conformal mapping based method can yield a large number of energy levels and the corresponding eigenstates with high accuracy [83].

2.5.1.2. Energy Level Statistics

To demonstrate the working of our conformal-mapping based method to calculate the eigenenergies and eigenstates of the Dirac equation subject to AB flux, we set $\xi = 0.5$ for the circular ring domain $|z| \in [\xi, 1]$. We choose the following complex function $w(z)$ as a polynomial conformal map for the confinement domain:

$$w(z) = h[z + 0.05az^2 + 0.18a\exp(i\omega)z^5], \tag{2.38}$$

where $\omega \in [0, 2\pi)$ is a constant (we choose, somewhat arbitrarily, $\omega = \pi/2$), and $a \in [0, 1]$ is the deformation parameter, which is also a control parameter to generate different types of classical dynamics. In particular, when a is increased from zero to unity, the deformed ring system will undergo a transition from being regular, mixed to fully chaotic. The normalization coefficient

$$h = \frac{1}{\sqrt{1 + \frac{a^2}{200}(1+\xi^2) + \frac{81a^2}{500}(1+\xi^2+\xi^4+\xi^6+\xi^8)}}$$

guarantees that the domain area is invariant for arbitrary values of the deformation parameters $\{a, \omega, \xi\}$. Justifications for choosing this particular transformation to generate ring domains with distinct types of classical dynamics are as follows. Firstly, to our knowledge, the form of $w(z)$ presented in Eq. (2.38) is the simplest conformal map that can result in classically chaotic bil-

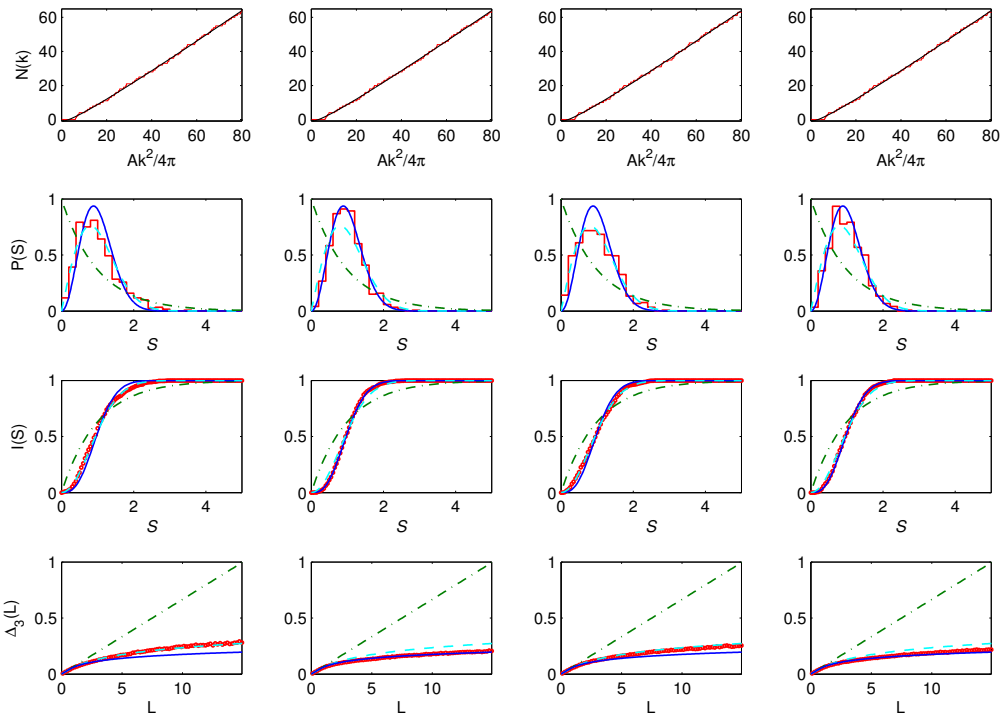

Fig. 15. Spectral statistics for the nonrelativistic AB chaotic billiard, where panels in columns 1-4 show, for quantum flux parameter $\alpha = 0, 1/4, 1/2, (\sqrt{5}-1)/2$, respectively, the unfolded level-spacing distribution $P(S)$, the cumulative level-spacing distribution $I(S)$, and the spectral rigidity Δ_3. In all panels, numerical data are represented by red line (or circle) and theoretical distribution curves for Poisson, GOE, and GUE statistics are plotted using green dash-dotted, cyan dashed, and blue solid curves, respectively.

liards with the topology of a ring but without any geometric symmetries. For example, choosing $\{a = 1, \omega = \pi/2, \xi = 0.5\}$ fulfills this requirement [89]. Secondly, the conformal map also has the advantage of being analytically amenable. Thirdly, since the matrices (M_{ij}) are nearly diagonal, the associated computational cost is minimal. Fourthly, as classical dynamics is concerned, this family of deformed rings is especially appealing as transitions from regular to mixed and finally to fully chaotic motions can be realized by tuning a single parameter, a, from 0 to 1.

To validate our method, we calculate the level-spacing statistics, which are believed to exhibit universal characteristics for quantum systems, nonrelativistic [90,91] or relativistic [92], that exhibit chaos in the classical limit. In particular, let $\{k_n | n = 0, 1, 2, \cdots\}$ denote the non-decreasing positive wave-number sequence of a quantum billiard system. According to the Weyl formula [90, 91] that has the same form regardless of presence or absence of a magnetic flux, the smoothed wave-vector staircase function is given by

$$\langle \mathcal{N}(k) \rangle = \frac{\mathcal{A}k^2}{4\pi} + \gamma \frac{\mathcal{L}k}{4\pi} + \cdots , \tag{2.39}$$

where $\mathcal{A}$ and $\mathcal{L}$ are the area and the perimeter of the billiard, respectively, $\gamma = -1$ (or 1) holds for Dirichlet (or Neumann) boundary conditions, and $\gamma = 0$ holds for massless Dirac fermion billiards [78]. Define $x_n \equiv \langle \mathcal{N}(k_n) \rangle$ as the unfolded spectra scaled in units of the mean-level spacing. Let $S_n = x_{n+1} - x_n$ be the nearest-neighbor spacing and $P(S)$ be the probability distribution of S [i.e., $P(S)dS$ is the probability that a spacing S lies between S and $S + dS$]. It has been known that, for classically integrable systems, the level spacing distribution is Poisson: $P(S) \sim \exp(-S)$. For classically chaotic systems that possess time-reversal symmetry but no geometrical symmetry, the level-spacing distributions follow the GOE (Gaussian orthogonal ensemble) statistics: $P(S) = (\pi/2)S \exp(-\pi S^2/4)$. For chaotic systems without time-reversal symmetry, $P(S)$ obeys the GUE (Gaussian unitary ensemble) statistics: $P(S) = (32/\pi)S^2 \exp(-4S^2/\pi)$. Given $P(S)$,

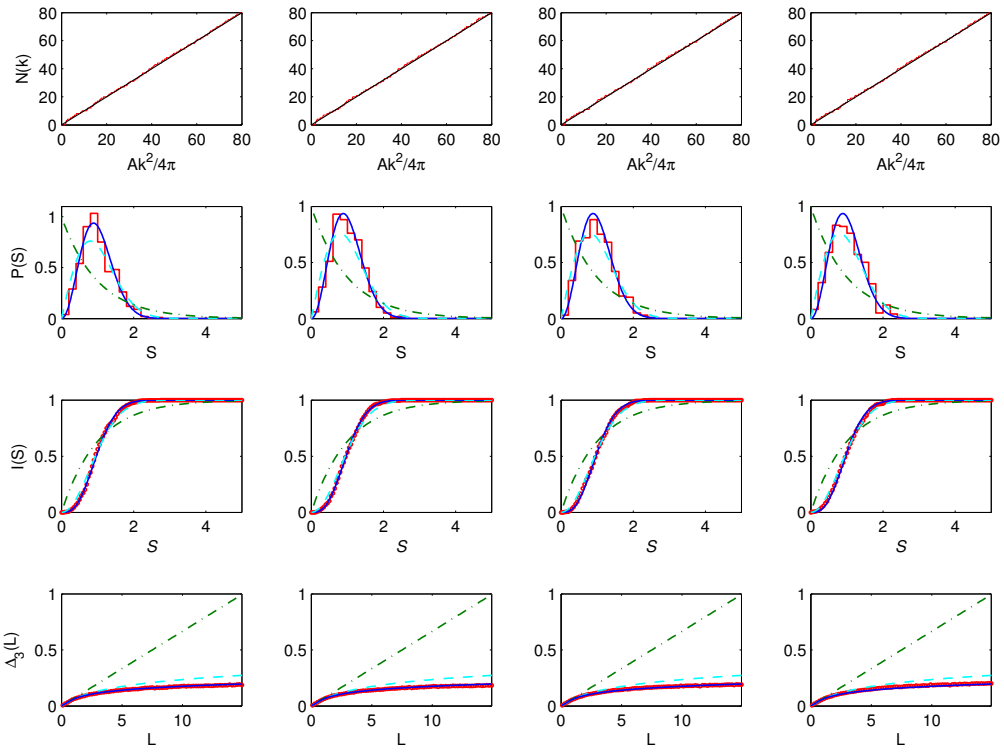

Fig. 16. Spectral statistics for the *relativistic* AB chaotic billiard. The legends are the same as in Fig. 15.

the corresponding cumulative level-spacing distribution can be obtained from $I(S) = \int_0^S \mathrm{d}S' P(S')$. Different types of level-spacing statistics can also be distinguished by using the Δ_3 statistics [90,91].

To give an example, we choose the parameters $a = 1, \omega = \pi/2, \xi = 0.5$. Diagonalizing the matrix (M_{ij}) gives about 2000 levels for each of the four values of the magnetic flux $\alpha = 0, 1/4, 1/2, (\sqrt{5}-1)/2$. We use the lowest 600 levels to calculate the spectral statistics. Figures 15 and 16 show the statistics from the non-relativistic (Schrödinger) and relativistic (Dirac) AB chaotic billiards, respectively. As predicted, we observe GUE statistics for the relativistic quantum billiard because of the persistent T-breaking by the confinement (Fig. 16). Deviations from the

GUE statistics are observed for the zero-flux case (the 1st column) and the "false T-breaking" case with $\alpha = 1/2$ (the 3th column) for nonrelativistic quantum billiard (Fig. 15).

2.5.2. Equality of Interfact Current Density From Eqs. (2.7) and (2.8)

The analyzable model in the main text is a metal-insulator step junction (which is relevant to the closed rings case), where the insulator region is denoted as II and the metal region as I. Physically, the Hall-like current at the interface can be attributed to the T-breaking mass potential in the insulator region.

At $x = 0$, Eqs. (7) and (8) are identical, which can be seen, as follows. In the main text, we have

$$\tan\gamma = \frac{\lambda_1 - \lambda_2 \sin\theta_0}{\lambda_2 \cos\theta_0} = \frac{1 - \lambda \sin\theta_0}{\lambda \cos\theta_0}. \tag{2.40}$$

Setting $x = 0$, we have

$$\begin{aligned} (J_D^I)_y &= v[2\sin\theta_0 + 2\sin(2\gamma + \theta_0)], \\ (J_D^{II})_y &= v\frac{4\cos^2\gamma}{\lambda} \equiv v\frac{4\cos^2\gamma\cos\theta_0}{\lambda\cos\theta_0}. \end{aligned}$$

From Eq. (2.40), we have

$$\frac{1}{\lambda\cos\theta_0} = \tan\gamma + \tan\theta_0.$$

Substituting this into the expression for $(J_D^{II})_y$, we obtain

$$\begin{aligned} (J_D^{II})_y &= 4v(\tan\gamma + \tan\theta_0)\cos^2\gamma\cos\theta_0 \\ &= 4v(\sin\gamma\cos\theta_0 + \cos\gamma\sin\theta_0)\cos\gamma \\ &= v[2\sin(2\gamma + \theta_0) + 2\sin\theta_0] \\ &= (J_D^I)_y. \end{aligned}$$

3 . ROBUST RELATIVISTIC TWO LEVEL SYSTEM WITH EDGE-DEPENDENT CURRENTS AND SPIN POLARIZATION

3.1. Background

Two level systems are the fundamental building blocks of quantum information processing and computing [93]. Uncovering and exploiting various physical systems for two level system implementation has been an active area of research for a few decades [94–96]. Among various types of two level system systems, solid state devices such as superconducting and semiconductor-based qubits are of particular interest [97]. A basic requirement for qubits is an effective two-state system that provides two controllable degrees of freedom such as the direction of the circulating currents on a ring, the charge states in a double quantum dot, and the electron spin. The performance of the two level system device is affected by the coupling of these degrees with the environment and by their robustness against material defects or various types of random interactions. For example, charge qubits in double quantum dots are sensitive to charge noise and electrostatic fluctuations induced by interface roughness or bulk defects [98]. It is thus of general interest to articulate and develop two level system systems that are robust against random scattering and weak direct environmental coupling.

Recent years have witnessed a rapid growth of interest in Dirac materials [39] such as graphene [40–46], topological insulators (TIs) [47], molybdenum disulfide (MoS_2) [48, 49], HITP [$Ni_3(HITP)_2$] [50], and topological Dirac semimetals [51,52]. A common feature of these materials is that the electronic motions can be approximately described by the Dirac equation, with physical properties that are not usually seen in conventional semiconductor materials. Appealing features of these materials include the emergence of topologically protected quantum states and long-range phase coherence [99], making them potential candidate for solid state qubits. Theoretical schemes

have been proposed for graphene [100, 101], topological insulators [75], and more recently the monolayer transitional metal dichalcogenides [102].

In this work, we present a two level system system based on a class of relativistic quantum modes, the Dirac spinor-wave analog of the whispering galley modes (WGMs). In particular, we consider the setting where a massless Dirac fermion is confined within a finite domain of ring topology, subject to a perpendicular magnetic flux at the center [100]. The confinement can be generated from a mass potential, which can be experimentally realized using ferromagnetic insulators [103]. A remarkable feature of the WGM type of spinor waves in the ring geometry is that they appear in pairs: one along the inner and another near the outer boundaries with oppositely circulating currents and spin polarizations, effectively forming a two-state relativistic two level system. This Dirac two level system has peculiar spin textures as the coupling between the spin and current (momentum) constrains the spin directions into the plane transverse to the interface. The current and spin orientations can be changed through tuning of the strength of the external magnetic field. The relativistic two level system is extremely robust against random scattering caused by boundary roughness and/or bulk electric disorders. Due to the breaking of the time-reversal symmetry (TRS) by the mass term, an insulator region is created. Based on the metal-insulator step junctions formed by spatially dependent mass potential in 2D Dirac fermion systems, we present an analytic argument to understand the origin of the robustness and the edge-dependent current/spin polarizations. A counter-intuitive feature is that, the inevitable boundary roughness and/or bulk defects are in fact desired, as they serve to introduce a finite coupling between the states, which is necessary for generating coherent oscillations through non-adiabatic sweeping of the external magnetic flux. We address the issue of decoherence and propose an experimental realization using 3D topological insulators (TIs). Our decoherence analysis based on a spin-boson model indicates that, for exam-

ple, for a ring size of 100 nm, the quantum quality factor can be on the order of 10^4. Moreover, due to the TRS-breaking confinement, our two level system system is less sensitive to electrostatic fluctuations than those based on conventional split-gate electrodes.

The paper is organized as follows: in Sec. 4.2, we formulate the theoretical model and present the proposal of relativistic two level system based on Dirac WGMs. In Sec. 3.3, we demonstrate robustness and coherence of the two level system states against random scatterings, and provide a physical explanation. In Sec. 3.4, we address the issue of decoherence. In Sec. 4.5, we conclude the work by articulating a feasible scheme for experimental realization.

3.2. Dirac Hamiltonian and Relativistic Two Level System

We consider a 2D Dirac ring threaded by a magnetic flux Φ, as shown in Fig. 17(a). The Hamiltonian (in units $\hbar = c = 1$) is

$$\hat{H}_D = v\hat{\boldsymbol{\sigma}}\cdot(-i\boldsymbol{\nabla} + e\boldsymbol{A}) + M(\boldsymbol{r})\hat{\sigma}_z, \tag{3.1}$$

where v is the Fermi velocity, $\hat{\boldsymbol{\sigma}} = (\hat{\sigma}_x, \hat{\sigma}_y)$ and $\hat{\sigma}_z$ are the Pauli matrices. The vector potential is $\boldsymbol{A}(\boldsymbol{r}) = (\Phi/2\pi r)\hat{\boldsymbol{e}}_\theta$ in the polar coordinates, with the magnetic field given by $\boldsymbol{B} = \alpha\Phi_0\delta(\boldsymbol{r})\hat{\boldsymbol{e}}_z$. The dimensionless quantum flux parameter is $\alpha = \Phi/\Phi_0$ with $\Phi_0 = 2\pi/e$ being the flux quantum. The mass confinement term $M(\boldsymbol{r})$ is zero inside the ring domain and infinity elsewhere, giving rise to the hard-wall boundary conditions [78, 104]:

$$[\mathbb{1} - \mathrm{sgn}(M)\hat{\boldsymbol{n}}_\perp\cdot\hat{\boldsymbol{\sigma}}]\psi = 0, \tag{3.2}$$

where $\hat{\boldsymbol{n}}_\perp$ denotes the unit tangent vector at the boundaries and $\psi = [\psi_1, \psi_2]^{\mathrm{T}}$ is the eigenspinor.

In the polar coordinates, the kinetic part of the Hamiltonian Eq. (3.1) reads

$$v\hat{\boldsymbol{\sigma}}\cdot(-i\boldsymbol{\nabla} + e\boldsymbol{A}) = -iv\left[\hat{\sigma}_r\partial_r + \hat{\sigma}_\theta\frac{1}{r}(\partial_\theta + i\alpha)\right], \tag{3.3}$$

where $\hat{\sigma}_r = \hat{\sigma}_x \cos\theta + \hat{\theta}_y \sin\theta$ and $\hat{\sigma}_\theta = -\hat{\sigma}_x \sin\theta + \hat{\sigma}_y \cos\theta$. For a circularly symmetric ring, $\hat{H}_D$ commutes with the the total angular momentum ($\hat{J}_z = -i\partial_\theta + \hat{\sigma}_z/2$). The corresponding eigenspinors ψ thus have the following form

$$\psi_l(\boldsymbol{r}) = \exp[i(l-1/2)\theta] \begin{pmatrix} \varphi_l(r) \\ i\varphi_{l+1}(r)\exp(i\theta) \end{pmatrix}, \tag{3.4}$$

with

$$\varphi_l(r) = \mathcal{N}\left(H^{(1)}_{\bar{l}-1/2}(\kappa r) + \beta H^{(2)}_{\bar{l}-1/2}(\kappa r)\right),$$

where $\mathcal{N}$ denotes the normalization constants, $\bar{l} = l + \alpha$ ($l = \pm 1/2, \pm 3/2, \cdots$ are the eigenvalues of $\hat{J}_z$), $H^{(1,2)}_\nu$ are Hankel functions of the (first, second) kind and $\kappa = |E|R/v$. The eigenstates and eigenvalues are determined by imposing the boundary condition Eq. (3.2).

Using the local charge current density $\boldsymbol{j} = v\psi^\dagger \hat{\boldsymbol{\sigma}}\psi$, we can show that the edge current $\boldsymbol{j}(\boldsymbol{r}_B) = 2v|\psi_1|^2 \mathrm{sgn}(M)\hat{\boldsymbol{n}}_\perp$ is polarized along the edges, *clockwise* for the inner and *counterclockwise* for the outer boundaries. Adopting the spin operator in the Hamiltonian as [75] $\hat{\boldsymbol{S}} = 1/2(\hat{\sigma}_y, -\hat{\sigma}_x, \hat{\sigma}_z)$ we obtain that the edge spin direction $\boldsymbol{S}(\boldsymbol{r}_B) = |\psi_1|^2 \mathrm{sgn}(M)\hat{\boldsymbol{n}}_\parallel$ is parallel to the outer normal vector $\hat{\boldsymbol{n}}_\parallel$, where $\boldsymbol{r}_B$ specifies the coordinates of the boundary points. The detailed form of the confinement potential $M(\boldsymbol{r})$ and disorders in the system will affect the magnitude of the edge charge current/spin but not the polarization properties. This current/spin polarization characteristic makes the system a potential candidate for relativistic qubits.

For two level system operation, in addition to the well defined current/spin polarization characteristic, it is necessary to lift the state degeneracy in the circular symmetric ring [100]. Intuitively, this can be accomplished via boundary roughness of the ring or defects in the bulk, with the current/spin polarization characteristic well maintained. Without loss of generality, we consider a class of deformed Dirac rings with shape being a conformal image of the circular-symmetric ring so that

the eigenstates can be determined efficiently and accurately [83, 105]. The conformal mapping of the circular ring domain z is given by $w(z) = \sum_n c_n z^n$ where $n = 5$ and the coefficient vector is given by $\boldsymbol{c} = [1, 0.05g, 0, 0, 0.18g\exp(i\delta)]$, $\delta \in [0, 2\pi)$, and $g \in [0, 1]$ is the deformation parameter that opens the gap at anti-level crossing. For relatively large deformation, e.g., $g \gtrsim 0.5$, bottlenecks along the boundary occur, leading to chaotic behavior in the classical ray dynamics and random scattering in the quantum regime. Conventional wisdom stipulates that the current/spin polarizations along the inner and outer boundaries would be suppressed or even eliminated.

Remarkably, we find that the (deformed) Dirac ring system and the associated polarized properties in the charge current and spin texture can persist in an extremely robust manner, as shown in Fig. 17. In particular, Fig. 17(b) shows the lowest few energy levels versus α, Figs. 17(c) and 17(d) show, for the two energy values indicated in Fig. 17(b), the associated spinor eigenstates. The states are radially localized at the ring edges with opposite propagating edge currents, forming the spinor-wave-analog of the WGMs. The coupling between the spin and current (momentum) constrains the spatial spin texture into the $S_r - S_z$ plane with $S_r = \sigma_y \cos\theta - \sigma_x \sin\theta$. From Figs. 17(c) and 17(d), we see that, at the boundaries, the spinors are planar with opposite polarization for the inner and outer states. Further, the oppositely circulating currents lead to opposite magnetic response in that the inner and outer WGM-like states are *diamagnetic* and *paramagnetic*, respectively. In absence of coupling between these WGM states (e.g., in absence of any random boundary scattering or bulk disorder), a level-crossing structure will arise as the magnetic flux is varied.

A pair of WGM-like states traveling along the inner and outer boundaries define a two level system. For simplicity, we use the symbols $|\circlearrowleft\rangle$ and $|\circlearrowright\rangle$ to denote the two states, with the respective energy levels $E_{\curvearrowleft}(\alpha)$ and $E_{\curvearrowright}(\alpha)$. About the level anti-crossing point [i.e., minimal-gap position in Fig. 17(b)], the states $|\circlearrowleft\rangle$ and $|\circlearrowright\rangle$ are coupled and superposed with approximately equal

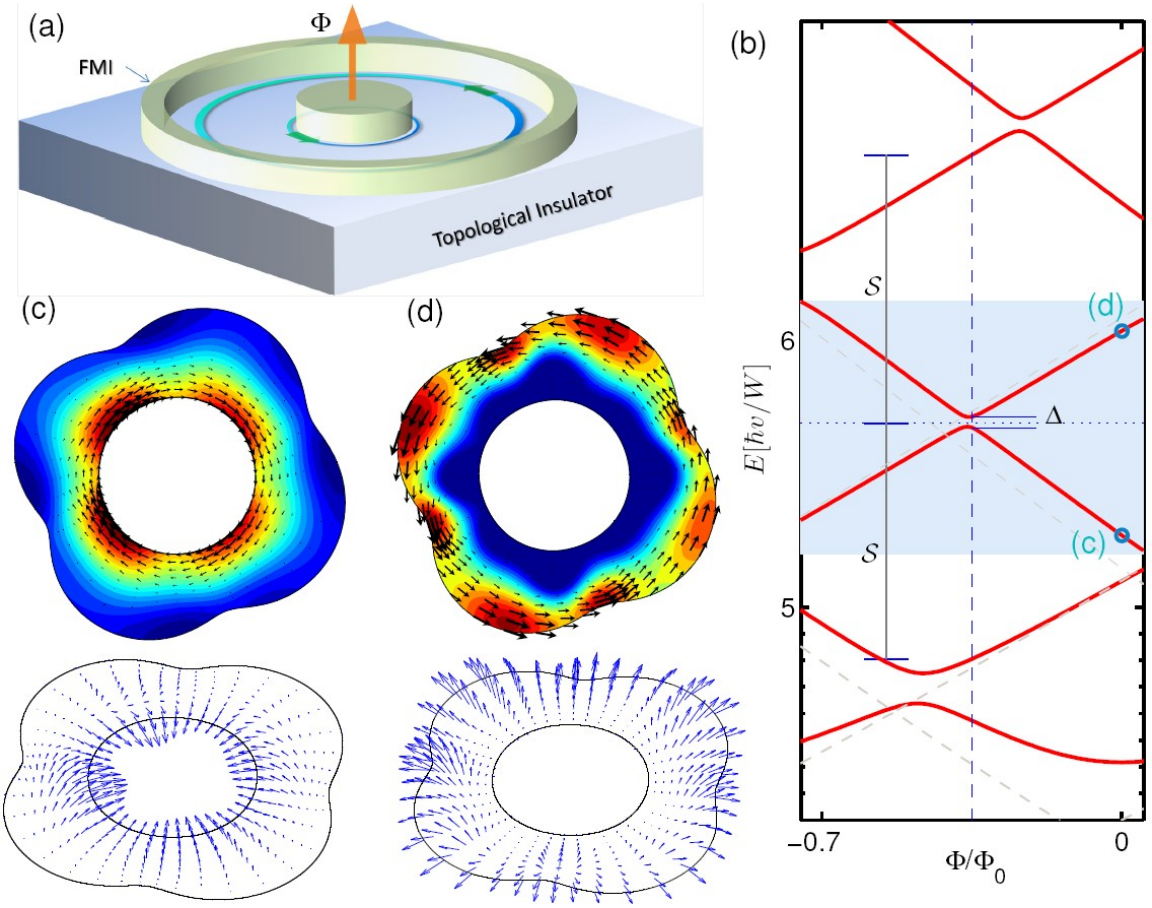

Fig. 17. (a) Proposed scheme of two level system patterned as a ring domain through the deposition of a ferromagnetic insulator (e.g., EuS) on the surface of the 3D TI, where a controllable mass potential is created through local exchange coupling (the proximity effect). (b) For $g = 0.5$, energy levels versus α, where the dashed lines show the circularly symmetric case for comparison. (c,d) The corresponding electronic densities and the associated charge current distribution (upper panels) and spin texture (lower panels) of the two adjacent Dirac WGMs indicated by the open circles in (b).

amplitude. An example of the "on-off" curves is shown in Fig. 18(a). Rabi oscillations can be generated by varying the magnetic flux non-adiabatically. Specifically, our single flux-tunable two level system system can be described by the following 2×2 effective Hamiltonian in the pseudo-spin representation as

$$\hat{H}_{\text{two level system}} = -(\tilde{\varepsilon}/2)\hat{\tau}_z - (\Delta/2)\hat{\tau}_x, \tag{3.5}$$

where $\hat{\tau}_{x,z}$ are Pauli matrices in the pseudo-spin base of $|\circlearrowleft\rangle$ and $|\circlearrowright\rangle$, and $\varepsilon = |E_{\curvearrowleft}(\alpha) - E_{\curvearrowright}(\alpha)|$. The level detuning $\tilde{\varepsilon} = \varepsilon - \varepsilon_0$ can be adjusted by changing α, where ε_0 characterizes the displacement with respect to the uncoupled situation. The tunnel coupling parameter Δ is the anti-crossing energy, which can be tuned by varying the boundary deformation parameter g or the bulk disorder strength. Non-adiabatic transitions between $|\circlearrowleft\rangle$ and $|\circlearrowright\rangle$ can be realized through non-adiabatic tuning of α such that the level detuning changes from $|\tilde{\varepsilon}| \gg \Delta$ to $\tilde{\varepsilon} = 0$ (i.e. $\varepsilon = \varepsilon_0$), driving the system from a pure $|\circlearrowleft\rangle$ (or $|\circlearrowright\rangle$) state to the minigap position. This induces Rabi oscillations between $|\circlearrowleft\rangle$ and $|\circlearrowright\rangle$ at the angular frequency of $\Delta/2$: $\cos(\Delta t/2)|\circlearrowleft\rangle - i\sin(\Delta t/2)|\circlearrowright\rangle$.

We note that the effect of additional mass term (dynamical gap) generation induced by such a dynamical flux is irrelevant in practice, as that requires an *off-resonant* circularly polarized irradiation (laser) or a high-frequency analog driving signal input [e.g., about 100 meV ($\sim 10^{15}$ Hz) - see the work [**?**], and references therein]. In our proposal, the time-dependent gauge potential induced by the applied dynamic magnetic flux has a different form from that generated by the circularly polarized laser field, and the relevant operation (driving) frequency is on the same order of magnitude of the energy spacing between the two adjacent WGM states. The energy requirement is 1 meV for a real ring size (say 100 nm). As a result, the additional mass term can be neglected. The $\delta(r)$ field adopted in our work is for theoretical simplicity only. Insofar as the applied magnetic flux is confined within the inner ring boundary, there is no essential difference in the final results. In ex-

perimental implementation, it is more convenient to generate a magnetic flux of finite size confined within the inner ring boundary.

To make such a two level system proposal be convinced, one need the two-state approximation above can be effectively fulfilled in the present system, i.e. the level spacing to the next lower and higher lying states should be much larger than the two level system splitting energy to avoid the leakage of quantum information [New J. Phys. 7, 219 (2005)]. Based on a direct calculation of the present system, we conclude that the proposed two level system fulfill this requirement quite well. In particular, considering a two level profile consisting of a pair of WGM-like states as indicated in Fig. 17(b) by empty circles, we obtain the level splitting $\Delta \sim 0.04\hbar v/W$, while the level spacing $\mathcal{S} \sim \hbar v/W$ is about 25 the expected two level system splitting. For a real sample size, say $W = 100$ nm, we get $\mathcal{S} \sim 5$ meV $\simeq 60$ K and $\Delta \sim 0.2$ meV [2.5 K] $\ll \mathcal{S}$, which means the concerned two-level profile can be effectively decoupled from the other levels. We remark that the splitting energy Δ, on the other hand, defines an effective temperature T under that the dephasing effect of thermal noise can be ruled out primarily. In this sense, by tuning the fermi energy near a desired position as indicated by the dotted blue horizontal line in Fig. 17(b), and assumed working under a lower temperature such that $k_B T \ll \Delta$, the system can be effectively reduced to a two-state system and behave quantum mechanically around a certain magnetic flux. Noting that the theoretical proposal above is based on the low-energy effective model of the 3D TIs, we only focus on the low-lying states throughout the present work.

3.3. Robustness Against Random Scattering

The two level system states in our system, which are the Dirac spinor-wave analog of WGMs with opposite circulating currents and spin polarizations, are far superior to the same two level system setup in nonrelativistic, semiconducting rings. This can be argued, as follows. Say we calculate

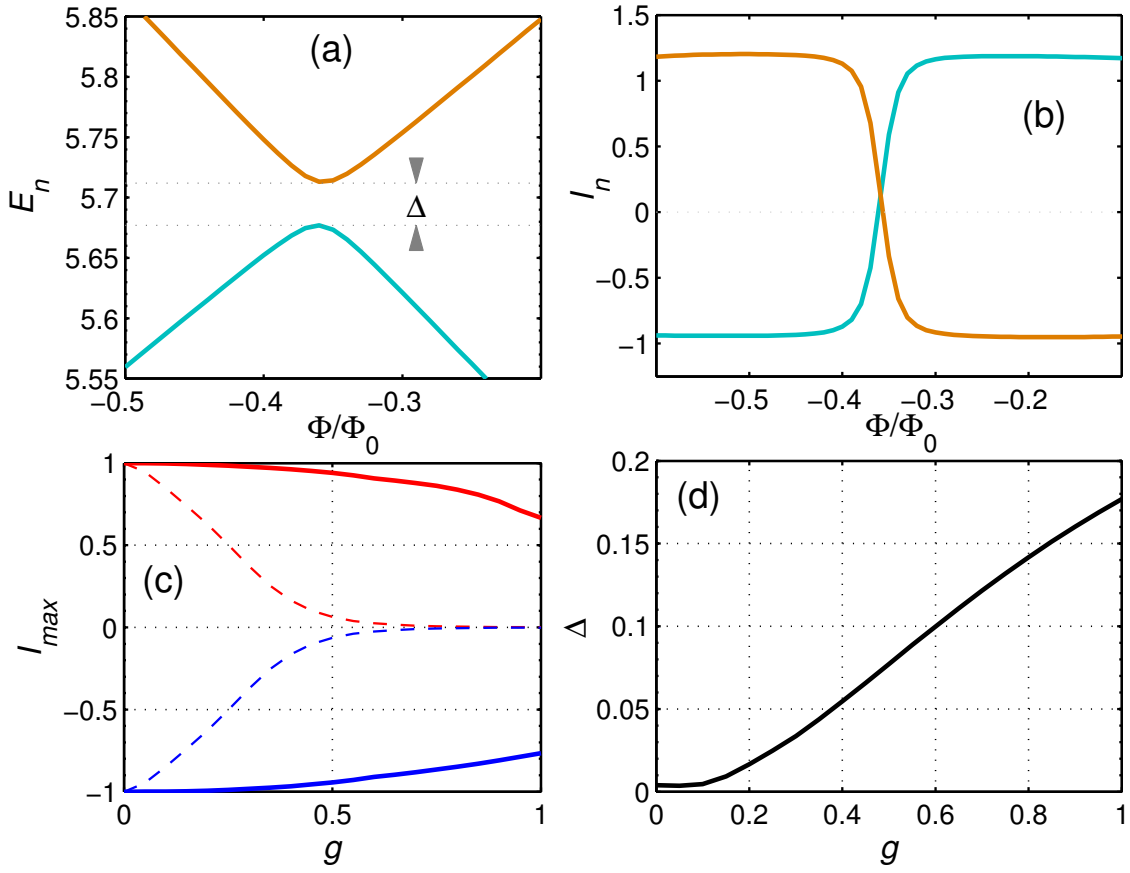

Fig. 18. Illustration of a flux-tunable two level system based on a pair of Dirac WGMs: (a,b) "on-off" curves, and (c,d) the circulating current amplitudes and the anti-crossing energy as a function of the deformation parameter g, respectively. The dashed lines in (c) are for the non-relativistic counterpart of our system.

the slope of the states $I_n = -\partial E_n/\partial\alpha$ (the persistent current [10–27, 106]), which measures the degree of coherence in terms of the states' ability to maintain circulation. The slope will have large and near zero values for circulating and angularly localized states, respectively. From Fig. 18(b), we see that the Dirac WGMs have quite large circulating currents. Remarkably, as the deformation strength g is increased, the corresponding current amplitudes denoted by the solid thick lines in Fig. 18(c) decrease much more slowly. For comparison, we have calculated the corresponding behaviors for the non-relativistic counterpart of our system [the thin dashed lines in Fig. 18(c)], where the current amplitude decays much faster. Figure 18(d) shows that the mingap Δ increases with the deformation strength g, which is reasonable as gap opening is typically more pronounced as some symmetry-breaking parameter is increased.

In terms of the persistent currents, we can analyze the two level system more explicity for a specific two level profile as shown in Fig. 18(a) by expressing the two level system parameter

$$\tilde{\varepsilon} \sim 2I_m(\alpha - \alpha_c), \tag{3.6}$$

where α_c is the position of the anti-crossing and I_m denotes the maximum absoulute amplitude of the persistent current carried by the two level system states. For a promising two level system implementation, one expect that I_m is robust against perturbations, which hence leads to a stable two level system parameter. Modeling the perturbations through the irregular boundary deformations in general, we demonstrate that the present two level system possesses a remarkable stability with the two level system states being the roubust relativistic WGM-like states, which makes it competitive with its nonrelativistic counterparts. Concerning the fact that the bundary deformation modeling of the perturbations is obtained by a set of general conformal map of the circular-symmetric ring, we may think of the random scatterings from the irregular ring boundary as those from an equivalent complex "potential" on the regular ring. In this sence, it is fair to argue that the present two level

system could be robust against random perturbations, even indcued by the time-reversal breaking disorders. Interestingly, such a great robustness of the proposed two level system states enables one introduce coupling between them by the irregular boundary deformation and hence give the other two level system parameter Δ as a function of deformation degree g. Form Figs. 18(a)-(d), we can estimate that, for the strongest deformation case, i.e. $g = 1$, the maximum level detuning $\tilde{\varepsilon}_M \sim 0.88\hbar v/W$ is still about five times the two level system energy splitting $\Delta \sim 0.18\hbar v/W$, which suggests the effective two-level approximation still work.

To understand the physical mechanism of robust Dirac WGMs, we analyze the relativistic quantum behaviors of a particle in a 2D step junction system with metal-insulator (MI) and insulator-metal (IM) configurations formed by a spatial-dependent mass potential, as shown in Fig. 19(a). The insulator region can be created experimentally with a finite constant mass potential $M = M_0$ (since we only consider the lowest few levels), while the metal region with zero band gap hosts massless Dirac fermions. An incoming plane wave $|k^i\rangle$ from the metal to the insulator regions with the incident angle θ and energy $E = v|k|$ inside the mass gap $|M_0| > E$ is reflected to state $|k^r\rangle$, together with an evanescent state $|k^t\rangle$ in the insulator region. Solving the Dirac equation together with the boundary conditions (Appendix **??**), we obtain the associated local charge current density and spin orientation as

$$\begin{aligned} j_x &= 0, \\ j_y &= v\frac{4\tau\cos^2\gamma}{\tan\beta} \times \exp\left(-2qx\right), \end{aligned} \tag{3.7}$$

and

$$\begin{aligned} S_x &= \frac{2\tau\cos^2\gamma}{\tan\beta} \times \exp\left(-2qx\right), \\ S_y &= 0, \\ S_z &= \frac{\cos^2\gamma}{\sin^2\beta}\cos\left(2\beta\right) \times \exp\left(-2qx\right), \end{aligned} \tag{3.8}$$

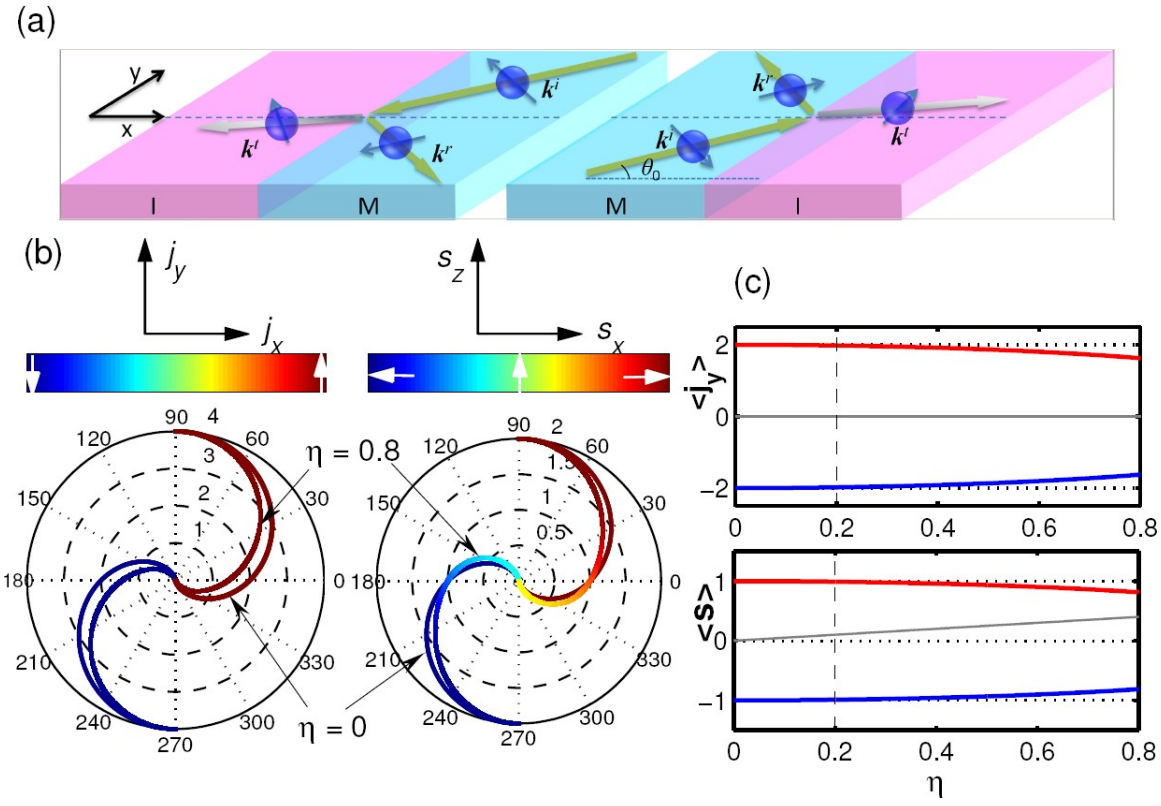

Fig. 19. Physical mechanism of robust Dirac WGMs: (a) a 2D step junction with IM (left) and MI (right) configurations, where the junction interface is located at $x = 0$, (b) interface current orientation (j_x, j_y) (left panel) and spin texture (S_x, S_z) (right panel) versus the incident angle θ_0 and the relative energy η, where $\theta_0 \in [-\pi/2, \pi/2]$ and $\theta_0 \in [\pi/2, 3\pi/2]$ for MI and IM, respectively. The results for different values of η are indicated. (c) Averaged transverse electric current (top panel) and spin (bottom panel) versus the incident relative energy η.

where

$$\begin{aligned}
\tan\beta &= |(vq + E\sin\theta_0)/(M_0 + E)|\,, \\
\tan\gamma &= (1 - \tau\tan\beta\sin\theta_0)/(\tau\tan\beta\cos\theta_0), \\
\tau &= \mathrm{sgn}(M_0 q), \\
vq &= \pm\sqrt{M_0^2 - (E\cos\theta_0)^2},
\end{aligned}$$

with the $\pm$ signs denoting the propagating directions of the incident wave from the metal region (corresponding to the MI and IM configurations, respectively). We see that spin is perpendicular to the current direction, which is responsible for the strong spin-orbit coupling associated with the surface states of 3D TIs. The transverse current j_y and the constrained spin orientation (S_x, S_z) are both functions of the relative incident energy ratio $\eta = E/M_0$ and the incident angle θ_0 with respect to the x-axis. An interesting feature is that the signs of j_y and S_x are simply determined by those of mass M_0 and q. Restricting our consideration to $M_0 > 0$, we see that both j_y and S_x are anti-symmetric with respect to the transformation of $q \to -q, \theta_0 \to \theta_0 + \pi$. As a result, j_y and S_x are positive/negative for the MI/IM junction, leading to persistent positive/negative transverse current and left/right spin polarization at the junction interfaces when all possible incident angles are taken into account. This is the situation where there are transverse Hall currents *without* external magnetic fields, and the directions of the currents can be controlled by changing the configuration of the junction. More physical insights into these peculiar currents can be gained by considering the case of hard wall confinement: $\eta \ll 1$. At the interface, we have

$$\begin{aligned}
j_y &\to 2v(\tau + \sin\theta_0), \\
S_x &\to (\tau + \sin\theta_0), \\
S_z &\to 0.
\end{aligned}$$

That is, the spin becomes fully in-plane polarized ($\leftarrow$ or $\rightarrow$), as shown in Fig. 19(b). Averaging over all the incident angles $\theta_0 \in [-\pi/2, \pi/2]$ for MI ($[\pi/2, 3\pi/2]$ for IM), we obtain

$$\langle j_y \rangle = \frac{1}{\pi} \lim_{\eta \to 0} \int_{-\pi/2}^{\pi/2} d\theta_0 j_y(\eta, \theta_0) = 2v\tau, \tag{3.9}$$

and

$$\langle S_x \rangle = \frac{1}{\pi} \lim_{\eta \to 0} \int_{-\pi/2}^{\pi/2} d\theta_0 s_x(\eta, \theta_0) = \tau. \tag{3.10}$$

As shown in Fig. 19(c), both average values are half of their maximum values in magnitude but the currents and spins are opposite in direction for the MI and IM configurations.

3.4. Decoherence

For a two level system to be practically useful, the dephasing time τ_φ and the relaxation time τ_r need to be much larger than the Rabi period (operation time scale) $\tau_{op} = 4\pi/\Delta$. Our two level system states are spin polarized WGMs, so they are less sensitive to nonmagnetic perturbations, such as electrostatic fluctuations, than those based on conventional split-gate electrodes [107]. For our two level system operated under low temperature $k_B T \ll \Delta$, decoherence mainly comes from the measurement process. We use the standard spin-boson model (SBM) to calculate the decoherence time caused by the coupling to the measurement device (e.g., a superconducting quantum interference device - SQUID), which has been used to assess decoherence in conventional flux qubits in mesoscopic semiconducting [108] or superconducting rings [109]. For a system at bath temperature T, the energy relaxation time is

$$\tau_r^{-1} = 0.5J \left(\frac{\mu}{\hbar}\right) \coth\left(\frac{\mu}{2k_B T}\right) \sin^2 \Omega, \tag{3.11}$$

and the phase-decoherence time is

$$\tau_\varphi^{-1} = \frac{\tau_r^{-1}}{2} + 2\pi\xi k_B T \cos^2 \Omega/\hbar, \tag{3.12}$$

where the two level system level spacing is $\mu = \sqrt{\tilde{\varepsilon}^2 + \Delta^2}$, $\Omega = \tan^{-1}(\Delta/\mu)$ is the mixing angle, $J(\omega)$ is a spectral density function characterizing the environment, and the dimensionless dissipation parameter is defined as

$$\xi = \lim_{\omega \to 0} J(\omega)/2\pi\omega.$$

For $\mu \gg k_B T$ and assuming that the environment can be treated as an Ohmic bath [i.e., $J(\omega) \propto \omega$], we have

$$\tau_r^{-1} \simeq \pi \xi \mu \sin^2 \Omega/\hbar,$$

with the damping parameter given by

$$\xi \simeq (2\pi/\hbar)(\mathcal{M}I/\Phi_0)^2 I_{sq}^2 \tan^2 [f(L_J^2/R_l)k_B T],$$

where $\mathcal{M}$ is the mutual inductance coefficient between the two level system and the measuring SQUID, I and I_{sq} are the respective circulating currents. The SQUID is effectively an inductor of inductance

$$L_J = (\hbar/2e)/\sqrt{4I_c^2 \cos^2 f - I_{sq}^2}$$

and is driven by a magnetic flux f with the flux-tunable critical current I_c. The quantity R_l is used to model the real part of the impedance resulted from non-ideal wirings to the SQUID. Adopting the same parameters for the measuring device as in Ref. [110], we obtain $\tau_r \sim 45$ ns and $\tau_\varphi \sim 59$ ns at 300 mK for our Dirac ring of size ~ 100 nm. In realistic situations the Ohmic environment assumption cannot adequately describe all sources of decoherence, but these estimates provide a meaningful assessment of the operation of our two level system. In particular, level spacing in our two level system sets the operation time to be $\tau_{op} \sim 4$ ps, which is much less than τ_φ. The corresponding quantum quality factor can thus be quite large: on the order of 10^4, suggesting strongly our two level system system as a promising candidate for experimental test and applications [111, 112].

3.5. Conclusions

We conclude by presenting a potential experimental scheme to realize our robust relativistic two level system. The key lies in the implementation of mass confinement, which can be accomplished using graphene or 3D TIs. For example, a controllable mass term can be created by depositing a ferromagnetic insulator (FMI) layer on the surface of a 3D TI [103]. Differing from graphene, the surface states of a 3D TI host Dirac fermions originated from a single Dirac cone, which is the case treated in this work. One possible scheme based on 3D TIs (Bi_2Se_3, $Pb_xSn_{1-x}Te$) is sketched in Fig. 17(a), where the material EuS (GdN or $Cr_2Ge_2Te_6$) can be used for the FMI cap layer and patterned to generate a ring geometry. two level system readout can be realized by measuring the sign of the flux generated by the circulating currents, using a separate SQUID magnetometer inductively coupled to the two level system. In practice, the current scanning SQUID technique allows one to filter the applied controlling flux from the one induced by the two level system states [**?**]. Two or more qubits can also be coupled by means of the induced flux, making it possible to develop multi-two level system gates or even a network of Dirac qubits. We emphasize the surprising feature of our two level system: during various stages of the fabrication process boundary imperfections and/or bulk disorders are inevitable, but they are counter-intuitively beneficial for our two level system because they provide the necessary coupling between the two oppositely circulating boundary states. A key merit of our proposal lies in its relativistic quantum nature, due to the strong current interest in Dirac materials and their unconventional electronic properties.

4 . REVERSE STARK EFFECT AND CONTROL OF SPIN IN FERROMAGNET-TOPOLOGICAL INSULATOR HETEROSTRUCTURES

4.1. Background

In systems exhibiting the conventional quantum-confined Stark effect (QCSE), e.g., a semiconducting quantum well, an external electrical field shifts the electronic states in the conduction band to lower energies and the hole states in the valence band to higher energies [113]. As a result, the energy gaps between the electronic and hole states are narrowed, reducing the frequencies of the permitted photon absorption or emission. In this paper, we report the intriguing phenomenon of reverse Stark effect: in topological Dirac materials an applied electrical field tends to *widen* the energy gaps and consequently *increase* the light absorption or emission frequencies.

Uncovering, understanding, and exploiting exotic quantum phases are frontier problems in physics [114]. Recent years have witnessed a great deal of effort in phase phenomena of a topological origin [47, 85]. For example, 2D gapless topological phases were predicted and realized at the interface between bulk Bi_2Se_3 crystal and the vacuum [115], where a change in the Z_2 invariant from the former to the latter occurs. Inducing an energy gap by breaking the time-reversal symmetry in the vicinity of a magnetic material can lead to exotic phases of broken symmetry with dramatic physical phenomena [47, 103] such as zero-field half-integer quantum Hall effect [85], topological magnetoelectric effect [116], and magnetic monopole [117]. Topological effects in gapped Dirac materials are thus quite intriguing, where topologically protected chiral interfacial states carrying dissipationless currents can arise, which share the same mechanism as that for the Jackiw-Rebbi modes [118]. More recently, it was demonstrated that tuning the topological behaviors through an electric field can lead to quantum spin Hall effect, bringing field-effect topological transistor closer to reality [119].

We investigate the response of the topological states in a confined geometry, e.g., a quantum dot formed on the surface of a 3D topological insulator via a closed magnetic domain heterostructure, to an applied electric field. The system can be described by the Dirac equation subject to proper mass confinement. With an inverted mass profile, a branch of quantized topological edge states can emerge [75]. We find that, when an external electric field is applied, the under-gap topological states exhibit quite unusual alignments: the positive (negative) energy electronic states follow (aligh against) the direction of the field. As a result, a reverse QCSE occurs in that the frequencies of permitted light absorption or emission *increase*. Remarkably, these states possess spin textures of ring-like in-plane polarization, which can be effectively controlled electrically or optically. We provide an analysis based on solutions of the Dirac equation to explain these counterintuitive phenomena. The findings can have potential applications in Dirac material based optoelectronics and spintronics.

This paper is organized as follows: in Sec. 4.2, we formulate the theoretical model and show the emergence of quantized topological edge states. In Sec. 5.2.2, we investigate their response to an external electric field, and present two relevant consequences of reverse electric alignments and electrically controllable spin and optical transitions. In order to make such a theoretical study be accessible in practice, in Sec. 4.4, we discuss feasible experimental schemes and applicabilities. Finally, we conclude the work by articulating our primary discoveries and related potential applications.

4.2. Hamiltonian and Quantized Topological States

Consider a dot geometry formed on the surface of a 3D TI through a nanoscale magnetic heterostrucutre, as schematically shown in Fig. 20(a). For low energies, the system is described by the

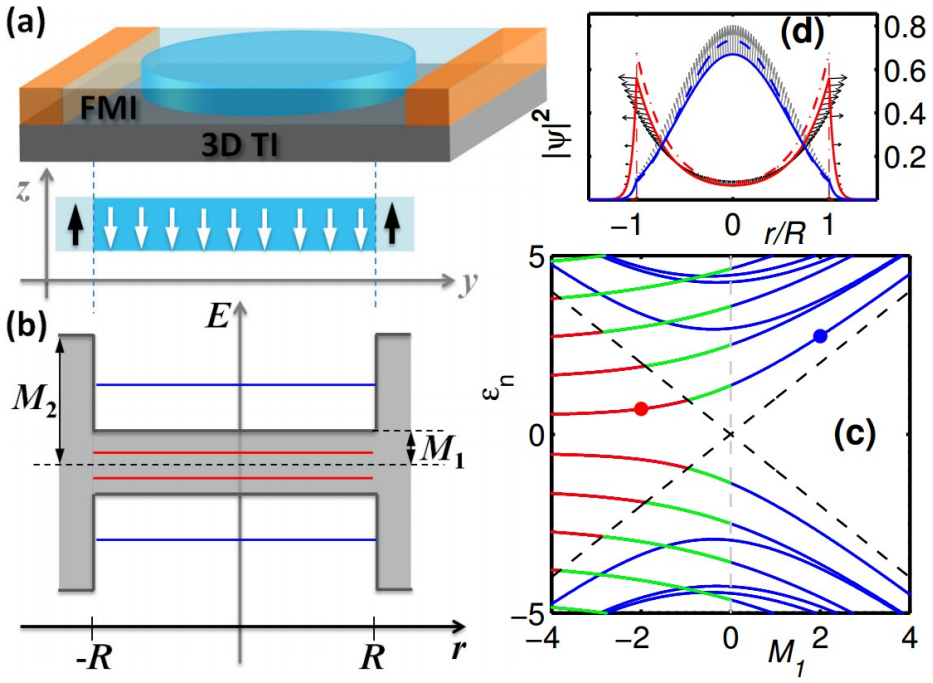

Fig. 20. (a) Schematic illustration of a quantum dot formed on the surface of a 3D topological insulator through a closed magnetic domain heterostructure of ferromagnetic insulators (e.g., EuS). (b) Schematic energy diagram of the dot system with mass confinement for zero applied field (R: dot radius; M_1 and M_2: dimensionless masses of the inner and outer regions, respectively). (c) Energy spectra of the dot structure in (b) as a function of M_1 for fixed $M_2 = 10$, where the blue curves denote the normal states and the black dash lines specify the insulating gap boundaries defined by M_1. The emergent edge states through a topological mechanism are divided into the under-gap and over-gap ones, denoted by red and green curves, respectively. (d) Sectional view of the density distributions of the lowest positive energy states for $M_1 = \mp 2$ as indicated by red and blue dots in (c). The red and blue curves are for the topological and normal states, respectively. Arrows denote the local spin orientation in the $S_x - S_z$ plane. The dashed/dot-dashed lines correspond to the case of hard-wall confinement, i.e. $M_2 \to +\infty$.

following 2D Dirac Hamiltonian [47, 120]:

$$\hat{H} = v_F \hat{\boldsymbol{\sigma}} \cdot \hat{\boldsymbol{p}} - e\varphi + \mathcal{M}(\boldsymbol{r})\hat{\sigma}_z, \tag{4.1}$$

where v_F is the Fermi velocity, $\hat{\boldsymbol{\sigma}}$ is the vector of Pauli matrices, $\boldsymbol{p} = (p_x, p_y, 0)$, $\boldsymbol{r} = (x, y, 0)$, the potential φ comes from the applied electric field $\boldsymbol{E} = -\boldsymbol{\nabla}\varphi$, and $-e < 0$ is the charge of an electron. The position dependent "mass" term $\mathcal{M}$ is responsible for the confinement through a time-reversal symmetry breaking mechanism. To be concrete, we assume that the confined region is circularly symmetric with potential jumps at the boundary: $\mathcal{M}(r) = \mathcal{M}_1\Theta(R-r) + \mathcal{M}_2\Theta(r-R)$, where R is the dot radius, as shown in Fig. 20(b), the corresponding energy diagram for the confinement. A constant electric field is applied in the x direction: $\mathcal{E} = \mathcal{E}_0\boldsymbol{e_x}$. In the polar coordinates, the Hamiltonian can be written as $\hat{H} = \hat{H}_0 + \hat{H}_1$, where

$$\hat{H}_0 = \begin{pmatrix} \mathcal{M} & \hat{\mathcal{L}}_- \\ \hat{\mathcal{L}}_+ & -\mathcal{M} \end{pmatrix}; \hat{H}_1 = e\mathcal{E}_0 r\cos\theta, \tag{4.2}$$

and $\hat{\mathcal{L}}_\pm = -i\hbar v_F e^{\pm i\theta}\left(\partial_r \pm i\frac{\partial_\theta}{r}\right)$. For zero field ($\mathcal{E}_0 = 0$), the z component of the total angular momentum, $\hat{J}_z = -i\hbar\partial_\theta + \hbar/2\hat{\sigma}_z$, commutes with $\hat{H}$. As a result, the eigenstates take on the following general form [121]:

$$\langle \boldsymbol{r}|\nu\rangle = \psi_\nu(r,\theta) = \frac{1}{\sqrt{N_\nu}}\exp(il\theta)\begin{pmatrix} f_l(\kappa_\nu r) \\ i\xi_\nu f_{l+1}(\kappa_\nu r)e^{i\theta} \end{pmatrix}, \tag{4.3}$$

where $\xi_\nu = \hbar v_F\kappa_\nu/(\epsilon_\nu + \mathcal{M})$, $\kappa_\nu = \sqrt{\epsilon_\nu^2 - \mathcal{M}^2}/\hbar v_F$, and the radial distribution function is $f_l(\kappa_\nu r) = J_l(\kappa_\nu r)$ for $r < R$, and $f_l = \mathcal{C}H_l^{(1)}$ otherwise (J_l and $H_l^{(1)}$ are respectively the Bessel and the Hankel functions of the first kind). Introducing the compact index $\nu = [\tau, ln]$, we can use the integers l and n to specify the orbital angular momentum and discrete bound states due to the radial confinement, respectively, and $\tau = \pm 1$ to denote the

sign of the bound states energies. The eigenvalues $\epsilon_\nu = \varepsilon_\nu \hbar v_F/R$ can be determined by imposing the continuity of wavefunction $\psi_\nu(r,\theta)$ at $r = R$, and the associated unknown coefficients can be calculated through $\mathcal{C} = J_l(\sqrt{\epsilon_\nu^2 - M_1^2}R/\hbar v_F)/H_l^{(1)}(\sqrt{\epsilon_\nu^2 - M_2^2}R/\hbar v_F)$, and $N_\nu = 2\pi \int_0^\infty r \left[|f_l(\kappa_\nu r)|^2 + |\xi_\nu f_{l+1}(\kappa_\nu r)|^2\right] \mathrm{d}r = R^2 A_\nu^2$.

Figure 20(c) shows, for the zero field case, the dependence of the eigenenergies on the inner region mass (in units of energy) $\mathcal{M}_1 = M_1 \hbar v_F/R$ for one fixed value of the outer region mass $\mathcal{M}_2 = 10\hbar v_F/R$. As $\mathcal{M}_1$ changes from positive to negative (in the sense that a sign change in the mass occurs between the inner and outer domains, i.e., $\mathcal{M}_1\mathcal{M}_2 < 0$), a class of new electronic states arise, which are localized at the dot edge. The mechanism behind the formation of these edge states is the Jackiw-Rebbi modes, which are protected by topological changes due to a sign change in the band masses between the two sides of a boundary. The edge states are quantized version of the modes (henceforth the term *quantized Jackiw-Rebbi states*). For the configuration shown in Fig. 20(a), it is thus possible to engineer quantum (electronic) states topologically by tuning the sign of $\mathcal{M}_1$ for a fixed $\mathcal{M}_2$ value, as demonstrated in Fig. 20(c). It is remarkable that the emergent topological states have special spin polarization and carry a dissipationless current. Along with the definition of the spin operator $\hat{\boldsymbol{S}} = \hbar/2(\hat{\sigma}_y, -\hat{\sigma}_x, \hat{\sigma}_z)$, we show the density distribution and spin texture of a representative topological state [one marked by the red dot in Fig. 20(c)] in Fig. 20(d). For comparison, we also display the normal state as marked by the blue dot in Fig. 20(c), which is localized within the inner dot domain and exhibits conventional spin polarization due to the given inner region mass. Our goal is to study and understand the response of these quantized topological states to an external electric field.

4.3. Results

Say the external electric field is along the x direction. Due to lack of a circular symmetry in $\hat{H}$, the eigenstates and eigenenergies can be calculated numerically through an expansion of the state vector: $|\tau, n\rangle = \sum_\nu c_\nu |\nu\rangle$, in terms of the eigenstates $|\nu\rangle$ of the circularly symmetric case ($\mathcal{E}_0 = 0$), where c_ν's are the expanding coefficients. Note that the particle-hole symmetry (i.e., symmetry between the positive and negative energies) is preserved even in the presence of an external electric field [122]. This can be seen by transforming $\hat{H}$ in the Hamiltonian with $\varphi = -\mathcal{E}_0 x$ to $\hat{H}' = U\hat{H}U^\dagger = -\hat{H}$ through the unitary transformation $\hat{U} = \hat{\sigma}_x \mathcal{R}_x$, with $\mathcal{R}_x$ denoting the reflection operation with respect to $x = 0$, provided that the confinement potential $\mathcal{M}(\boldsymbol{r})$ is an even function of x. For the disk geometry considered, the resulting bounded energies occur in symmetric pairs with respect to the zero energy line. For simplicity, we adopt the hard-wall confinement to explicitly generate a set of complete orthogonal basis $\{\epsilon_\nu, |\nu\rangle\}$ and then determine the bound states $\{E_n, |\tau, n\rangle\}$ for a given electric field $\mathcal{E}_0$ through numerical diagonalization of the matrix Hamiltonian $[H_{\mu\nu}]$ of elements $H_{\mu\nu} = \delta_{\mu\nu}\epsilon_\nu + \langle\mu|\hat{H}_1|\nu\rangle$. For convenience, we use the dimensionless parameter $\lambda = \mathcal{E}_0 R|e|/(\hbar v_F/R)$ to characterize the applied electric field and set $\mathcal{M}_2$ to be $+\infty$. The mass potential inside is set as $\mathcal{M}_1 = \pm 2\hbar v_F/R$, which characterize the normal and topological quantum dot systems, respectively. We use a basis of size about 800 to calculate approximately 50 pairs of bound states with a maximum convergence accuracy of 10^{-6} for any λ within the range of $[-5, 5]$.

4.3.1. Reverse Electric Alignments

The bound-state energies as a function of the dimensionless electric field strength λ are shown in Figs. 21(a) and 21(b) for the normal ($\mathcal{M}_1 = 2\hbar v_F/R$) and the topological ($\mathcal{M}_1 = -2\hbar v_F/R$) cases, respectively. As expected, for both cases, the spectra exhibit the particle-hole symmetry.

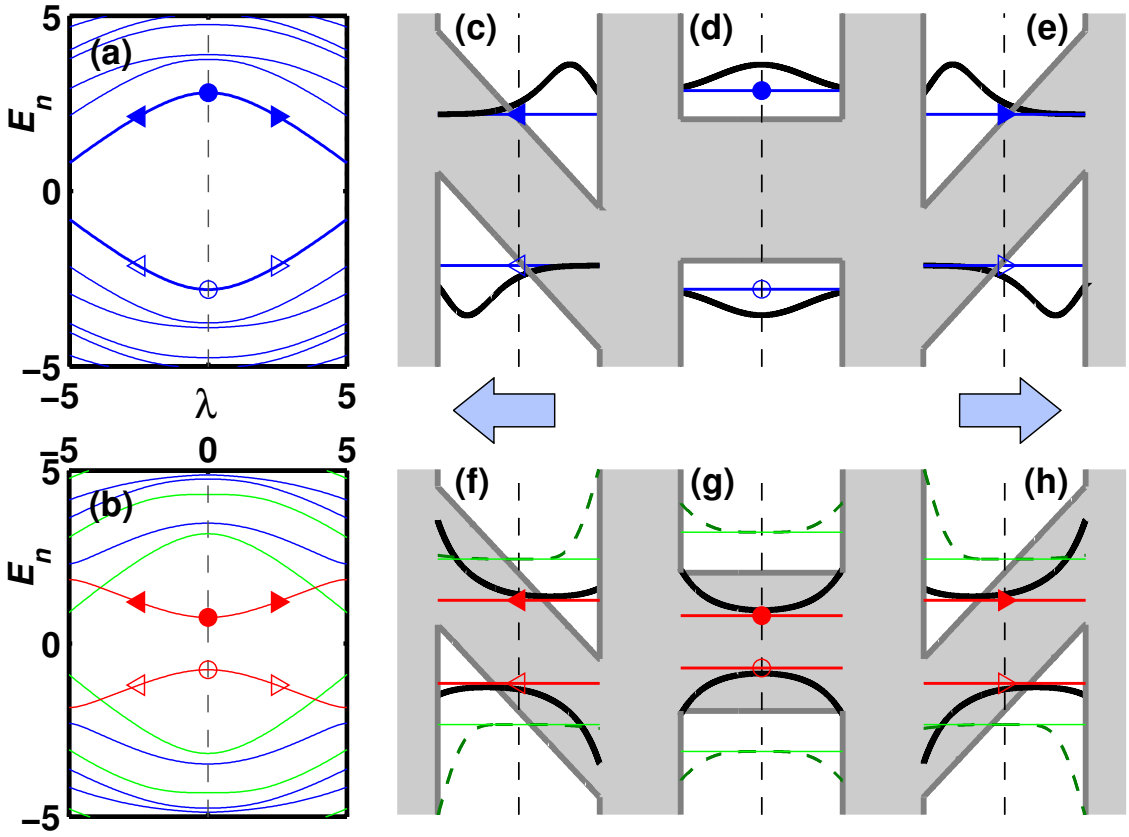

Fig. 21. (a,b) Dependence of the bound state energies on the applied electric field strength λ for $M_1 = \pm 2$, respectively. (c-e) Sectional view of the evolution of the normal electronic states [triangles and circles in (a)] for $\lambda = -2.5, 0, 2.5$, respectively. (f-h) Similar to (c-e) but for the topological electronic states indicated in (b) and their adjacent over-gap topological bound states [green (gray) dashed lines]. In (c-h), all the probability density distributions of the indicated electronic states are displaced with solid horizontal lines defining $\langle n, \tau | \tau, n \rangle = 0$ for each curve, while those of the negative energy electronic states are rescaled by -1 at the same time.

In addition, there is a Stark shift between levels that have approximate equal energies (quasi-degeneracy), and a stronger field generates a larger shift. A striking phenomenon is that, as λ is increased, the dependence of the under-gap topological bound-state energies on λ (the red curves) exhibits a pattern that is *squarely opposite* to those for the normal bound states [blue curves, Figs. 21(a) and 21(b)] and for the over-gap topological bound states [green curves, Fig. 21(b)]. We note that the under-gap topological states are in fact the QAHE (quantized anomalous Hall effect) states with the absolute values of energies less than $|\mathcal{M}_1|$ that defines a basic insulating gap for the inner region of the dot. In spite of the fact that these states originate from the same topological mechanism as and share similar edge-localized density distributions with other topological bound states, the effects of an applied electric field can be quite different. This can be further seen from Figs. 21(c-h), where the responses of the corresponding electronic states to the external electric field are shown. For the normal bound states [thick solid lines, Figs. 21(c-e)] and over-gap topological bound states [dashed green lines, Figs. 21(f-h)], we observe the usual alignment behavior: the positive energy electronic states move against the direction of the applied field while the negative energy states move towards the direction of the field. The under-gap topological bound states [thick solid black lines, Figs. 21(f-h)], however, follow the opposite pattern, which is consistent with the behavior observed from the energy spectrum.

To understand the abnormal electric response behavior exhibited by the under-gap topological bound states, we develop a perturbation based analysis by treating λ as a small parameter. From the standard time-independent nondegenerate perturbation theory [123], we calculate the perturbed energy for a given unperturbed bound state $|\nu\rangle$ up to second order in λ through the expansion $E_\nu = E_\mu^{(0)} + \lambda E_\nu^{(1)} + \lambda^2 E_\nu^{(2)}$. We obtain the corresponding corrections (expressed in dimensionless

form):

$$E_\nu^{(0)} = \langle\nu|\hat{H}_0|\nu\rangle = \varepsilon_\nu, \lambda E_\nu^{(1)} = H_1^{\nu\nu},$$

and

$$\lambda E_\nu^{(2)} = \sum_{\mu\neq\nu} \frac{|H_1^{\mu\nu}|^2}{\varepsilon_\nu - \varepsilon_\mu}, \tag{4.4}$$

where the matrix element $H_1^{\mu\nu}$ is given by

$$H_1^{\mu\nu} \equiv \lambda\langle\mu|\rho\cos\theta|\nu\rangle = \lambda\pi\left[\delta_{l,l'-1} + \delta_{l,l'+1}\right] A_\mu^{-1} A_\nu^{-1} \times$$
$$\int_0^1 \rho^2 \left[J_{l'}^*(k_\mu\rho) J_l(k_\nu\rho) + \xi_\mu^* \xi_\nu J_{l'+1}^*(k_\mu\rho) J_{l+1}(k_\nu\rho)\right] \mathrm{d}\rho,$$

and $\rho \equiv r/R$, $k_\nu \equiv R\kappa_\nu$. We see that $H_1^{\nu\nu} = 0$ and hence the first order energy correction $E_\nu^{(1)}$ is zero. To analyze the second order effect and relate it to the numerical results, we focus on the lowest (highest) positive (negative) unperturbed electronic state, i.e., $|1, 01\rangle$ ($|-1, -11\rangle$). From

$$E_\nu^{(2)} = \sum_{\mu\neq\nu} \frac{|\langle\mu|\rho\cos\theta|\nu\rangle|^2}{\varepsilon_\nu - \varepsilon_\mu},$$

we can conclude that the leading term is restricted into two nearest-neighbor states in the energy domain with the angular momentum difference ±1 relative to the given state $|\nu\rangle$, e.g., for $|\nu\rangle = |1, 01\rangle$, $|\mu\rangle \in \{|-1, -11\rangle, |1, \pm11\rangle | \varepsilon_{-1,-11} < 0 < \varepsilon_\nu < \varepsilon_{1,\pm11}\}$. As a result, we can calculate the second order correction to the lowest positive bound-state energy using the approximation

$$E_\nu^{(2)} = \pi\left[\frac{|\mathcal{I}_{\mu_1\nu}|^2}{\varepsilon_\nu - \varepsilon_{\mu_1}} - \frac{|\mathcal{I}_{\mu_2\nu}|^2}{\varepsilon_{\mu_2} - \varepsilon_\nu}\right]. \tag{4.5}$$

We obtain

$$\begin{aligned} \mathcal{I}_{\mu_1\nu} &= \frac{1}{A_{\mu_1} A_\nu} \int_0^1 \rho^2 \mathcal{F}_1(\rho) \mathrm{d}\rho, \\ \mathcal{I}_{\mu_2\nu} &= \frac{1}{A_{\mu_2} A_\nu} \int_0^1 \rho^2 \mathcal{F}_2(\rho) \mathrm{d}\rho, \end{aligned} \tag{4.6}$$

where

$$\mathcal{F}_1(x) \equiv J_{-1}^*(k_{\mu_1} x) J_0(k_\nu x) + \xi_{\mu_1}^* \xi_\nu J_0^*(k_{\mu_1} x) J_1(k_\nu x),$$

and

$$\mathcal{F}_2(x) \equiv J^*_{\pm 1}(k_{\mu_2}x)J_0(k_\nu x) + \xi^*_{\mu_2}\xi_\nu J^*_{\pm 1+1}(k_{\mu_2}x)J_1(k_\nu x),$$

the sub-indices $\mu_1 = [-1, -11]$, $\nu = [1, 01]$ and $\mu_2 = [1, \pm 11]$ denote the relevant states, and the corresponding energies satisfy the relation $\varepsilon_{\mu_1} = -\varepsilon_\nu < 0 < \varepsilon_\nu < \varepsilon_{\mu_2}$. Specifically, for the normal case ($\mathcal{M}_1 = 2\hbar v_F/R$), we have $\mu_2 = [1, 11]$, $M_1 < \varepsilon_\nu = -\varepsilon_{\mu_1} \lesssim \varepsilon_{\mu_2}$ and, hence, $(\varepsilon_{\mu_2} - \varepsilon_\nu) \ll (\varepsilon_\nu - \varepsilon_{\mu_1}) = 2\varepsilon_\nu$, $\xi^*_{\mu_1}\xi_\nu = -1$ and $\xi^*_{\mu_2}\xi_\nu \ll 1$. Using these relations, we obtain $|\mathcal{I}_{\mu_2\nu}| \sim 2|\mathcal{I}_{\mu_1\nu}|$. It is thus straightforward to conclude $E^{(2)}_\nu < 0$ and, consequently, a decreasing energy-field strength relation. For the topological case of $\mathcal{M}_1 = -2\hbar v_F/R$, we see that the states $|\mu_1\rangle$ and $|\nu\rangle$ are the highest negative and lowest positive under-gap topological states, respectively, while the state $|\mu_2\rangle = |1, -11\rangle$ is an adjacent positive over-gap normal state. Finally, we have $(\varepsilon_{\mu_2} - \varepsilon_\nu) > (\varepsilon_\nu - \varepsilon_{\mu_1})$ and $|\mathcal{I}_{\mu_2\nu}| \sim |\mathcal{I}_{\mu_1\nu}|/3$, leading to $E^{(2)}_\nu > 0$ and hence a reverse dependence of the energies on the strength of the applied field.

4.3.2. Optical Transition and Spin Control

The phenomenon of reverse field alignments for the under-gap topological bound states and our perturbation analysis suggest the occurrence of abnormal QCSE in our mass confined Dirac system, with potential applications in Dirac material-based optoelectronic and spintronic devices. As a concrete demonstration, we calculate the electric field dependent optical absorption intensity α between the highest negative $|g\rangle$ and the lowest positive $|f\rangle$ energy states, which is determined by dipole matrix element $\boldsymbol{d}_{gf}$ by

$$\alpha \propto |\boldsymbol{v} \cdot \boldsymbol{d}_{gf}|^2, \tag{4.7}$$

with

$$\boldsymbol{d}_{gf} = \frac{ie\hbar v_F}{E_f - E_g}\langle g|\hat{\boldsymbol{\sigma}}|f\rangle,$$

and $\boldsymbol{v} = (\boldsymbol{e}_x + \boldsymbol{e}_y)/\sqrt{2}$, the polarization vector of the incident light [124, 125].

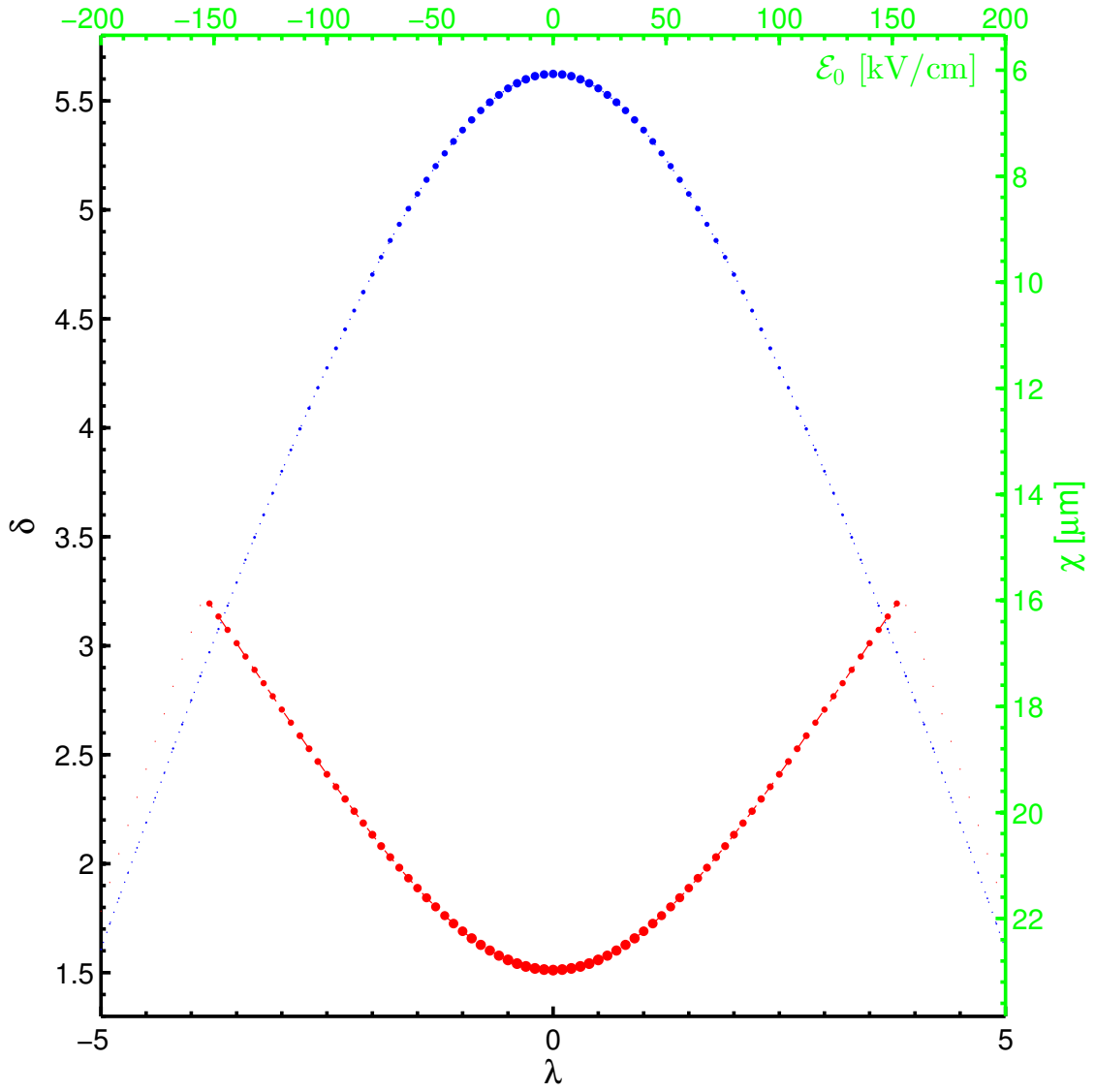

Fig. 22. Dipole-induced optical transition rate between states $|g\rangle$ and $|f\rangle$ as a function of the applied electric field strength λ and the transition energy $\Delta E \equiv E_f - E_g = \delta\hbar v_F/R$, where blue and red dots are for the normal ($\mathcal{M}_1 = 2\hbar v_F/R$) and topological ($\mathcal{M}_1 = -2\hbar v_F/R$) cases, respectively, with the dot size being proportional to the optical absorption intensity α.

Fig. 22 shows the calculated absorption spectra for the normal (blue dots) and topological (red dots) cases, where the sizes of the dots are scaled by the values of the corresponding optical absorption intensity. We see that, in contrast to the normal case where increasing the electric field strength can significantly reduce the transition energy and hence the optical absorption as with conventional QCSE [126], the under-gap topological states generate a small electric field modulated optical absorption rate but, within a certain range of the field strength, lead to an opposite dependence of the transition energy on the field strength.

A remarkable phenomenon is that the spin texture of the topological states [c.f., Fig. 20(d)] renders possible control of spin (and hence the associated magnetic properties) through modulation of the electrical field. To demonstrate this, we calculate the expectation values of the in-plane spin for the topological states, $\langle S_{x,y}\rangle = \pm\hbar/2\langle j|\hat{\sigma}_{y,x}|j\rangle$ ($j = g, f$). Figure 23(a) shows the dependence of $\langle S_{x,y}\rangle$ on the electric field strength λ, where the dashed and solid lines are for the state $|g\rangle$ and $|f\rangle$, respectively, and the results for the normal states are included in the inset. Compared with the normal states, the topological states have the intriguing feature that the applied in-plane polarized electric field can modulate the in-plane spins effectively, which is highly desired in spintronics applications. This feature can be further seen in Figs. 23(b) and 23(c), where the evolutions of the spin texture of the state $|f\rangle$ (i.e., the lowest positive energy state) under the applied field in both cases are shown, with the middle and bottom panels corresponding to the topological and normal cases, respectively. The robust optical transition between the under-gap topological states $|g\rangle$ and $|f\rangle$ shown in Fig. 22 indicates that, for a given applied electrical field, it is also possible to control the spin polarizations optically. In fact, Fig. 23(b) indicates unequivocally the reversal alignment behavior of the under-gap topological states as analyzed.

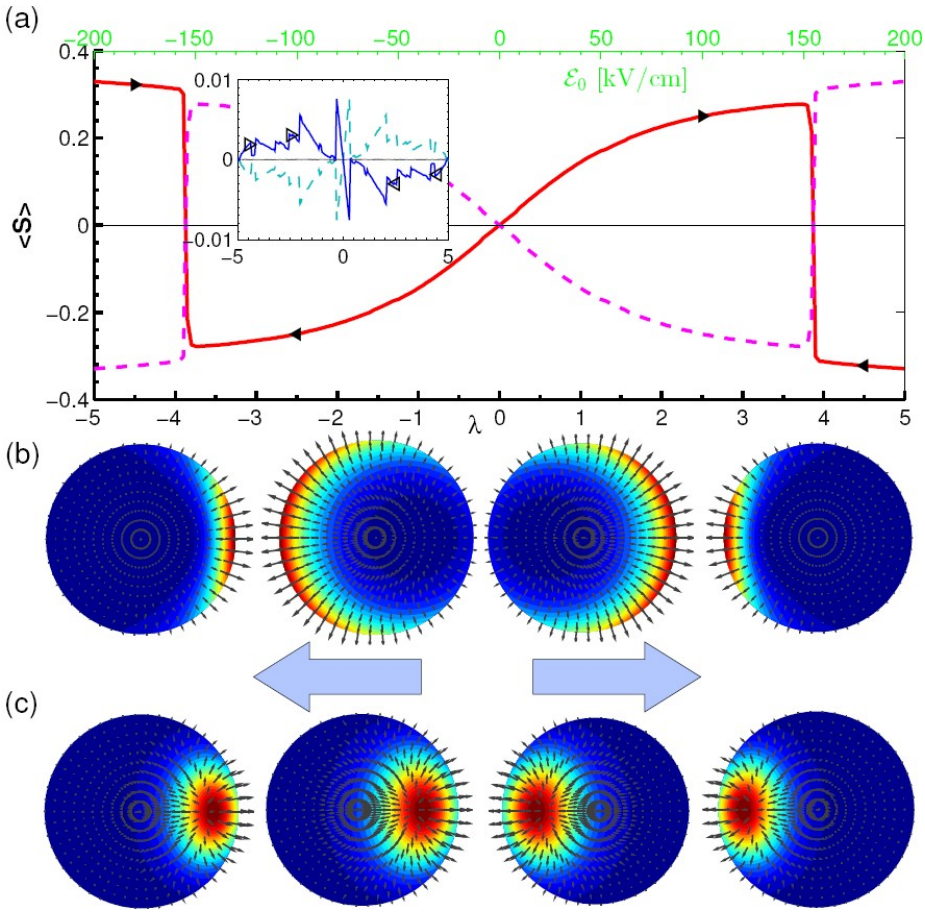

Fig. 23. (a) Expectation values of the in-plane spin projection $\langle S_{x,y} \rangle$ of the electronic states $|g\rangle$ and $|f\rangle$ as a function of λ, where the solid-red and dashed-pink lines are $\langle S_x \rangle$ and the gray lines represent $\langle S_y \rangle$. The inset denotes the normal case, where the solid-blue and dashed-cyan lines are for $\langle S_x \rangle$ and gray lines correspond to $\langle S_y \rangle$. In both cases, the solid lines are for the lowest positive energy electronic state $|f\rangle$, while the dashed lines correspond to the highest negative energy electronic state $|g\rangle$. (b,c) Density distributions and spin textures of the state $|f\rangle$ for different values of λ: $-4.5, -2.5, 2.5, 4.5$, from left to right as marked by the solid triangles for the topological case in (b) and by the open triangles for the normal case in the inset of (b), respectively. In both, the color code represents the local probability density, and the gray arrows denote the local in-plane spin orientations.

4.4. Discussion of Experimental Schemes and Application Issues

In order to validate and characterize the phenomena presented above, we need a feasible experimental scheme to realize the proposed setup as schematized in Fig. 20 (a). Referring to the existing experiments [103, 127–131], we note that the non-uniform mass confinement can be implemented via a closed magnetic heterostructure of ferromagnetic insulators (such as EuS, GdN, YIG or $Y_3Fe_5O_{12}$, $Cr_2Ge_2Te_6$ etc.) with different magnetizations of each side that is deposited on the surface of a 3D topological insulator. Depending on the local exchange coupling of the topological insulator and ferromagnetic insulator and the interface quality between them, the magnitude of the induced mass potential can be several to hundred meV [127, 129, 131]. Intriguingly, the sign of the induced mass is also tunable in reality by changing the direction of the magnetization in the ferromagnetic insulator caper layer, which can be achieved by means of the anisotropic feature of the materials [103, 130]. The gate electrode could be attached to the topological insulator to account the external electric field [132].

To be relevant in practice, it is convenient to restore the physical units of the related dimensionless quantities according to certain material parameters. In particular, we obtain $\hbar v_F \sim 400$ meV nm for typical materials [115], say Bi_2Se_3 or $Pb_xSn_{1-x}Te$. For sake of being comparable with existing related investigations on the conventional InAs/GaAs self-assembled quantum dots [126] and the HgTe quantum dots [133], we consider the similar dot size $R = 10$ nm as a specific case, where the concerned bound states energies lay within the range of $[-120, 120]$ meV for the mass potential magnitude $|\mathcal{M}_1| \sim 80$ meV, and the applied electric field $\mathcal{E}_0 \sim 40\lambda$ kV/cm, i.e. ranging from -200 kV/cm to 200 kV/cm for $\lambda \in [-5, 5]$. Correspondingly, we obtain the transition energy $\Delta E \sim 40\delta$ meV with the associated wavelength $\chi \sim \frac{hc}{40\delta} = \frac{30.996}{\delta}$ μm. For clarity, we also include these quantities with the related physical units in the resulting figures as shown in Fig. 22 and Fig. 23

(a). By doing this, one will apparently figure out that the electric field dependent optical transitions for both the conventional and topological cases happen at the mid-infrared (mid-IR) regime in the present system, which could be potentially promising to achieve the QCSE and reversal QCSE mid-IR optical modulators. Interestingly, for the latter case, one can be also allowed to control the in-plane spin texture effectively at the same time when varying the applied electric field, thanks to their unusual ring-like spin orientation of the associated topological modes. In addition, we remark that the electric field strength applied here is actually the same order of magnitude as that used for the conventional situation [126]. Noting that the bulk band gap of the typical material Bi_2Se_3 being about 300 meV [47, 115] is indeed much larger than the energy scales concerned/considered above, we conclude that the present study, in principle, could be accessible in experiments.

4.5. Conclusions

To summarize, we uncover a striking reverse Stark effect in TI based quantum dot systems that permit a class of quantized topological states. With an in-plane electric field, the under-gap topological states exhibit a reverse electric alignment, leading to a reverse QCSE phenomenon. We show that the counterintuitive phenomenon can be fully explained by using a second-order perturbation theory. The phenomenon is not only fundamental to relativistic quantum mechanics of Dirac materials, but also practically significant. For example, the reverse Stark effect leads to an inverted optical absorption spectrum, and this anomalous feature can be exploited to develop Dirac material-based optoelectronic devices, e.g. the reversal QCSE mid-IR optical modulators. In addition, due to their special spin textures, the in-plane spin degree of freedom of the under-gap topological states can be effectively controlled electrically or optically, opening an avenue for spintronics applications. To make these arguments convinced, we further discuss feasible experimental validation schemes and applicabilities in practice. Of course, we note that the present study is based on an ideal theoretical

model of the proposed system, and it would be one's future interest to generally investigate such unusual phenomena by including the symmetry breaking effects, different kinds of impurity scattering etc..

5 . UNUSUAL WAVE SCATTERING AND TRANSPORT OF MASSLESS PSEUDOSPIN-1 PARTICLES

5.1. Revival Resonant Scattering, Perfect Caustics, and Isotropic Transport

5.1.1. Background

Solid state materials whose energy bands contain a Dirac cone structure have been an active area of research since the experimental realization of graphene [40, 41]. From the standpoint of quantum transport, the Dirac cone structure and the resulting pseudospin characteristic of the underlying quasiparticles can lead to unconventional physical properties/phenomena such as high carrier mobility, anti-localization, chiral tunneling, and negative refractive index, which are not usually seen in traditional semiconductor materials. Moreover, due to the underlying physics being effectively governed by the Dirac equation, relativistic quantum phenomena such as Klein tunneling, Zitterbewegung, and pair creations can potentially occur in solid state devices and be exploited for significantly improving or even revolutionizing conventional electronics. Uncovering/developing alternative materials with a Dirac cone structure has also been extremely active [3, 134]. In this regard, the discovery of topological insulators [135, 136] indicates that Dirac cones with a topological origin can be created, leading to the possibility of engineering materials to generate remarkable physical phenomena such as zero-field half-integer quantum Hall effect [137], topological magneto-electric effect [138], and topologically protected wave transport [139, 140].

A parallel line of research has focused on developing photonic materials with a Dirac cone structure, due to the natural analogy between electromagnetic and matter waves. For example, photonic graphene [141, 142] and photonic topological insulators [143–148] have been realized, where novel phenomena of controlled light propagation have been demonstrated. Due to the much larger wavelength in optical materials as compared with the electronic wavelength, synthetic photonic de-

vices with a Dirac cone structure can be fabricated at larger scales with greater tunabilities through modulations. The efforts have led to systems with additional features in the energy band together with the Dirac cones, opening possibilities for uncovering new and "exotic" physics with potential applications that cannot even be conceived at the present.

The materials assumed in our work are those whose energy bands consist of a pair of Dirac cones and a topologically flat band, electronic or optical. For example, in a dielectric photonic crystal, Dirac cones can be induced through accidental degeneracy that occurs at the center of the Brillouin zone. This effectively makes the crystal a zero-refractive-index metamaterial at the Dirac point where the Dirac cones intersect with another flat band [149–153]. Alternatively, configuring an array of evanescently coupled optical waveguides into a Lieb lattice [154–157] can lead to a gapless spectrum consisting of a pair of common Dirac cones and a perfectly flat middle band at the corner of the Brillouin zone. As demonstrated more recently, loading cold atoms into an optical Lieb lattice provides another experimental realization of the gapless three-band spectrum at a smaller scale with greater dynamical controllability of the system parameters [158]. With respect to creating materials whose energy bands consist of a pair of Dirac cones and a topologically flat band, there have also been theoretical proposals on Dice or $\mathcal{T}_3$ optical lattices [5, 159–163] and electronic materials such as transition-metal oxide $SrTiO_3$/$SrIrO_3$/$SrTiO_3$ trilayer heterostructures [164], 2D carbon or MoS_2 allotropes with a square symmetry [165, 166], $SrCu_2(BO_3)_2$ [167] and graphene-In_2Te_2 bilayer [168].

In spite of the diversity and the broad scales to realize the band structure that consists of two conical bands and a characteristic flat band intersecting at a single point in different physical systems, there is a unified underlying theoretical framework: generalized Dirac-Weyl equation for massless spin-1 particles [161]. For convenience, we call such systems pseudospin-1 Dirac cone systems.

Comparing with the conventional Dirac cone systems with massless pseudospin/spin-$1/2$ quasiparticles (i.e., systems without a flat band), pseudospin-1 systems can exhibit quite unusual physics such as super-Klein tunneling for the two conical (linear dispersive) bands [153, 162, 169, 170], diffraction-free wave propagation and novel conical diffraction [154–157], flat band rendering divergent dc conductivity with a tunable short-range disorder [171], unconventional Anderson localization [172, 173], flat band ferromagnetism [158, 174, 175], and peculiar topological phases under external gauge fields or spin-orbit coupling [164, 176–178]. Especially, the topological phases arise due to the flat band that permits a number of degenerate localized states with a topological origin (i.e., "caging" of carriers) [179]. Most existing works, however, focused on the physics induced by the additional flat band, and the scattering/transport dynamics in pseudospin-1 systems remains largely unknown (except the super-Klein tunneling behavior). Our main question is the following: what types of transport properties can arise form pseudospin-1 systems whose band structure is characterized by coexistence of a pair of Dirac cones and a flat band? To address this question in the simplest possible setting while retaining the essential physics, we study ballistic wave scattering against a circularly symmetric potential barrier. We note that for conventional Dirac cone systems with pseudospin or spin-$1/2$ quasiparticles, there has been extensive work on scattering [180–182] with phenomena such as caustics [183], Mie scattering resonance [184], birefringent lens [185], cloaking [186], spin-orbit interaction induced isotropic transport and skew scattering [187, 188], and electron whispering gallery modes [189]. To our best knowledge, prior to our work there were no corresponding studies for pseudospin-1 Dirac cone systems.

Our main findings are three: revival resonant scattering, super-Klein tunneling induced perfect caustics, and universal low-energy isotropic transport without broken symmetries for massless quasiparticles. First, for small scatterer size, the effective three-component spinor wave exhibits re-

vival resonant scattering as the incident wave energy is varied continuously - a phenomenon that has not been reported in any known wave systems. Strikingly, the underlying revival resonant modes show a peculiar type of boundary trapping profile in their intensity distribution. While the profile resembles that of a whispering gallery mode, the underlying mechanism is quite different: these modes occur in the wave dominant regime through the formation of fusiform vortices around the boundary in the corresponding local current patterns, rather than being supported by the gallery type of orbits through total internal reflections. Second, for larger scatterer size where the scattering dynamics are semiclassical, a perfect caustic phenomenon arises when the incident wave energy is about half of the barrier height, as a result of the super-Klein tunneling effect. A consequence is that the scatterer behaves as a lossless Veselago lens with effective negative refractive index resulting from the Dirac cone band structure. Compared with conventional Dirac cone systems for pseudospin-$1/2$ particles, the new caustics possess remarkable features such as significantly enhanced focusing, vanishing of the second and higher order caustics, and a well-defined static cusp. Third, in the far scattering field, an isotropic behavior arises at low energies. Considering that there is no broken symmetry so the quasiparticles remain massless, the phenomenon is quite surprising as conventional wisdom would suggest that the scattering be anisotropic. By analyzing the characteristic ratio of the transport to the elastic time as a function of the scatterer size, we find that the phenomenon of scattering isotropy can be attributed to vanishing of the Berry phase for massless pseudospin-1 particles that results in constructive interference between the time-reversed backscattering paths. Because of the isotropic structure, the emergence of a Fano-type resonance structure in the function of the ratio versus the scatterer size can be exploited to realize effective switch of wave propagation from a forward dominant state to a backward dominant one, and vice versa. We develop an analytic theory with physical reasoning to understand the three novel phenomena, and

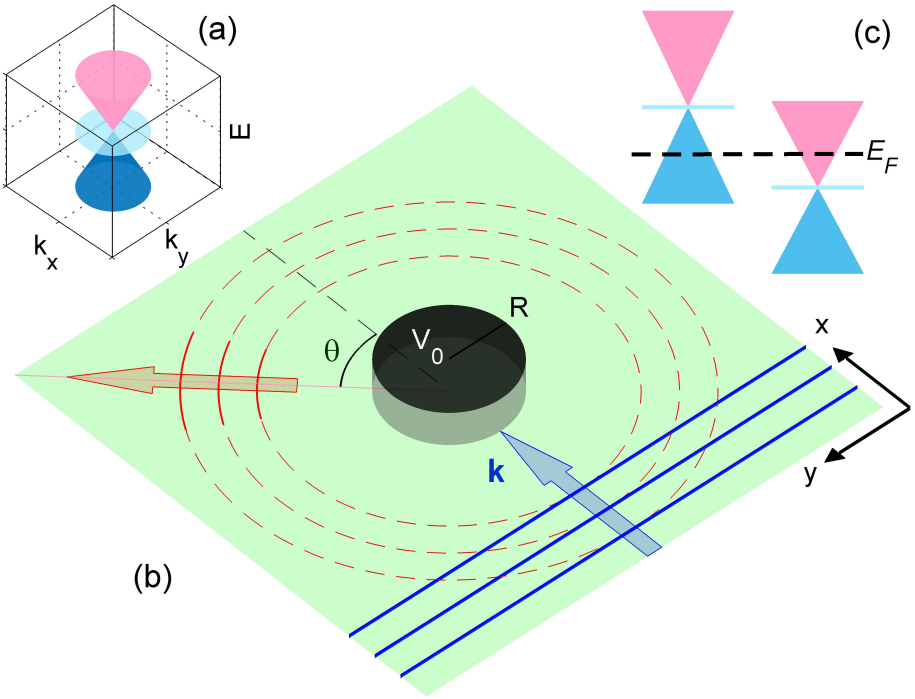

Fig. 24. Scattering configuration of a pseudospin-1 particle. (a) The energy-momentum $E - k$ relation, (b) schematic illustration of plane wave scattering from a circularly symmetric step like potential, and (c) illustration of the energy dispersion profiles in the regions inside and outside the potential.

articulate experimental verification schemes with photonic or electronic systems.

5.1.2. Results

Our setting of ballistic wave scattering of a pseudospin-1 particle is illustrated in Fig. 24. The scattering is from a circularly symmetric scalar potential barrier of height V_0 defined by $V(r) = V_0\Theta(R - r)$, where R is the scatterer radius and Θ denotes the Heaviside function. The band structure for the particle consists of a pair of Dirac cones and a flat band, as shown in Fig. 24(a). Incident plane wave and scattered wave are illustrated in Fig. 24(b), and the energy dispersion profiles in and outside the scattering potential are demonstrated in Fig.24(c).

A comprehensive description of the Hamiltonian, its properties, the boundary conditions, and

detailed solutions of the scattering waves is given in Appendix A. To characterize the scattering dynamics quantitatively, we use the scattering efficiency, defined as a ratio of the scattering to the geometric cross sections [184]:

$$Q = \frac{\sigma}{2R}, \tag{5.1}$$

where the scattering cross section σ can be calculated through the far field radial reflected current, as detailed in Appendix 5.1.4.2.

5.1.2.1. Near-Field Behavior 1: Revival Resonant Scattering

To uncover unusual physics, we calculate and analyze the scattering efficiency Q as a function of the reduced barrier strength V_0R (normalized by the group velocity v_g associated with the Dirac cone) and the relative incident energy E/V_0. In order to highlight the unique manifestations of the unconventional band structure, we focus on the under barrier scattering process in which the particle energy is below the barrier height: $0 < E/V_0 < 1$. To be concrete, we choose $E/V_0 = 0.01, 0.1, 0.9$ and, for each fixed value of E/V_0, we calculate the scattering efficiency Q versus the barrier strength V_0R. For the three chosen values of E/V_0, the results are shown by the respective red curves in Figs. 25(a-c). We see that there are well-separated sharp resonances in Q for small values of E/V_0 [e.g., Fig. 25(a)], while broadened and overlapping ripple structures occur for larger values of E/V_0 [e.g., Figs. 25(b) and 25(c)]. Using the characteristic size parameter kR, we can generally classify two distinct scattering regimes: $kR \ll 1$ and $kR \gg 1$. In the former case ($kR \ll 1$), the incident wavelength $2\pi/k$ is much larger than the range R of the scattering potential. In this case, the wave effects dominate the scattering dynamics with a remarkable resonance characteristic, as shown in Figs. 25(a) and 25(b). The case $kR \gg 1$, and $(1 - E/V_0)/(E/V_0)kR \gg 1$, corresponds to the semiclassical limit where the classical ray picture is applicable. In this case, the scatterer acts essentially as a Veselago reflector/lens due to an equivalent negative refractive index arising from

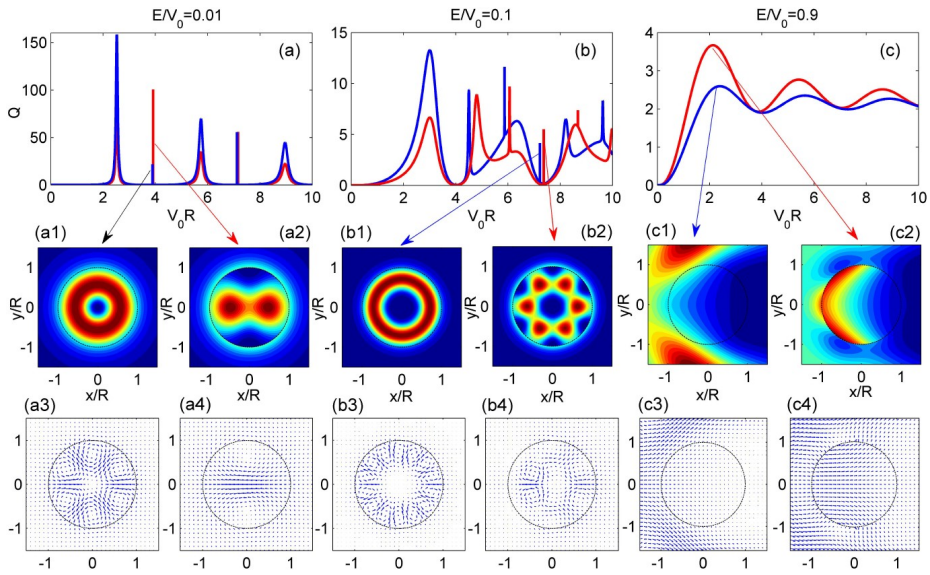

Fig. 25. General behaviors of the scattering efficiency versus the scatterer strength. Scattering efficiency Q as a function of the scatterer strength V_0R for a number of representative values of the relative incident energy: (a) $E/V_0 = 0.01$, (b) $E/V_0 = 0.1$, and (c) $E/V_0 = 0.9$. The middle and bottom panels show the corresponding probability density and local current density profiles, respectively. In (a-c), the blue curves are for the conventional massless pseudospin/spin-$1/2$ case while the red ones are for the massless pseudospin-1 wave system. Certain features can be understood by referring to the resonance width expressions $\Gamma_1 \propto (kR)^3$ for the resonances associated with the $|l| = 1$ channel and $\Gamma_0 \propto (kR) \gg \Gamma_1$ for those with the $l = 0$ channel. For example, in (a), the second and fourth modes belong to the normal excitations of the $|l| = 1$ channel, which are located about the first ($V_0R \sim 3.8$) and the second ($V_0R \sim 7$) zeros of the Bessel function J_1 in the domain of V_0R, while the first, third and fifth modes are the excitations of normal modes belonging to the $l = 0$ channel, which are located about the first (~ 2.4), the second (~ 5.5) and the third (~ 8.7) zeros of the Bessel function $J_0(V_0R)$. This is why the long lifetime (corresponding to narrow resonance width) appears in the fourth mode but not in the third and fifth modes. This argument holds in the regime $kR \ll 1$ and $E/V_0 \ll 1$.

the particular band structure of Dirac cones with a flat band.

From the explicit summation form of Q and the reflection coefficients A_l (labeled by the angular momentum l) obtained within the generalized partial-wave decomposition formalism in Appendix B, we see that the size parameter kR provides a general estimate of the maximum number of angular momentum channels contributing to the scattering process. Accordingly, we can obtain a closed form of Q in the limit of $kR \ll 1$, where only a few lowest channels dominate in a given range of the barrier strength, say $V_0R \in [0.01, 10]$. Specifically, using the short-range ($x \ll 1$) behavior of the Bessel functions appearing in the solutions of the scattering problem, we get a closed expression for the dependence of the scattering efficiency Q on the effective barrier strength V_0R for $kR \ll 1$ and $E/V_0 \ll 1$, which reads

$$Q \approx \frac{2}{kR}\left[\frac{\Gamma_0^2}{\Gamma_0^2 + \left(V_0R - x_0 + kR\ln\left(\gamma_E kR/2\right)\right)^2} + 2 \times \frac{\Gamma_1^2}{\Gamma_1^2 + \left(V_0R - x_1 - kR\right)^2}\right], \tag{5.2}$$

where γ_E is the constant appearing in the small value approximation of the Bessel function: $Y_0(x) \approx (2/\pi)\ln(\gamma_E x/2)$for $x \ll 1$ and the lowest $|l| = 0, 1$ channels give the leading contribution to and hence dominate the scattering process with well-separated symmetric sharp resonances around $V_0R = x_0, x_1$, which correspond to the zeros of the Bessel functions J_0 and J_1. The respective lifetimes are given by

$$\frac{1}{\Gamma_0} = \frac{2}{\pi kR} \quad \text{and} \quad \frac{1}{\Gamma_1} = \frac{2}{\pi(kR)^3}.$$

From Eq. (5.2), we see that, for $kR \ll 1$ and $E/V_0 \ll 1$, the resonances exhibit a Lorentzian shape (also known as the Breit-Wigner distribution). Due to their longer lifetime: $1/\Gamma_1 \gg 1/\Gamma_0$, the resonances associated with the $|l| = 1$ channel are much narrower than those with $l = 0$. In the limit $kR \to 0$, the resonant excitations are typically positioned at the zeros of $J_l(V_0R)$ with an infinite lifetime (i.e., zero resonant widths) that physically correspond to a bound state in the

antidot potential profile without an incident wave. Further insights can be gained by considering the local probability and current density distributions of one particular excitation of the normal modes, e.g., the first resonance associated with the $|l| = 1$ channel, as indicated in Figs. 25(a2) and 25(a4). Analytically, we obtain the probability density inside the scattering region ($r < R$) as

$$\begin{aligned}\rho_< \approx & |B_1|^2 \left[J_1^2(V_0 r) + \frac{J_0^2(V_0 r) + J_2^2(V_0 r)}{2} \right. \\ & \left. + \left(J_1^2 - J_0 J_2 \right) \cos\left(2\theta\right) \right],\end{aligned} \tag{5.3}$$

together with the local current distribution

$$\begin{aligned}\boldsymbol{j}_< \approx & - \Re(B_1^* B_0) \left[2J_1^2(V_0 r) + J_0^2(V_0 r) - J_0(V_0 r) J_2(V_0 r) \right] \cos\theta \hat{e}_r \\ & + \Re(B_1^* B_0) J_0(V_0 r) \left[J_0(V_0 r) + J_2(V_0 r) \right] \sin\theta \hat{e}_\theta,\end{aligned} \tag{5.4}$$

where $\Re(B_1^* B_0)$ denotes the real part of $(B_1^* B_0)$, and B_l are the transmission coefficients (Appendix B). When a scattering resonance emerges, the magnitude of the transmission coefficient behaves as

$$|B_1| \sim \frac{1}{kRJ_1(V_0 R)} \gg 1,$$

leading to a noticeable probability density concentration inside the scatterer, indicating the occurrence of wave trapping/confinement. Moreover, it follows from Eq. (5.4) that, accompanying the confinement, a vortex pattern symmetric with respect to the $x-$axis is formed. In general, in the resonant scattering regime, the incident wave is confined/trapped in vortices (as demonstrated in the bottom panel of Fig. 25) rather than through the conventional total internal reflection mechanism.

Comparing with the conventional pseudospin-$1/2$ Dirac cone systems [cf., Figs. 25(a1) and 25(a3), as well as the blue curve in Fig. 25(a)], we see that there are common features in the scattering curve and trapping mechanism but with different resonant wave/current patterns. In particular, the trapping intensity distribution is radially symmetric for the pseudospin-$1/2$ case, but for a pseudospin-1 particle, there is an angular dependence of the scattering amplitude with a well-defined rotational symmetry, which can be analyzed for a specific resonant mode using Eq. (5.3).

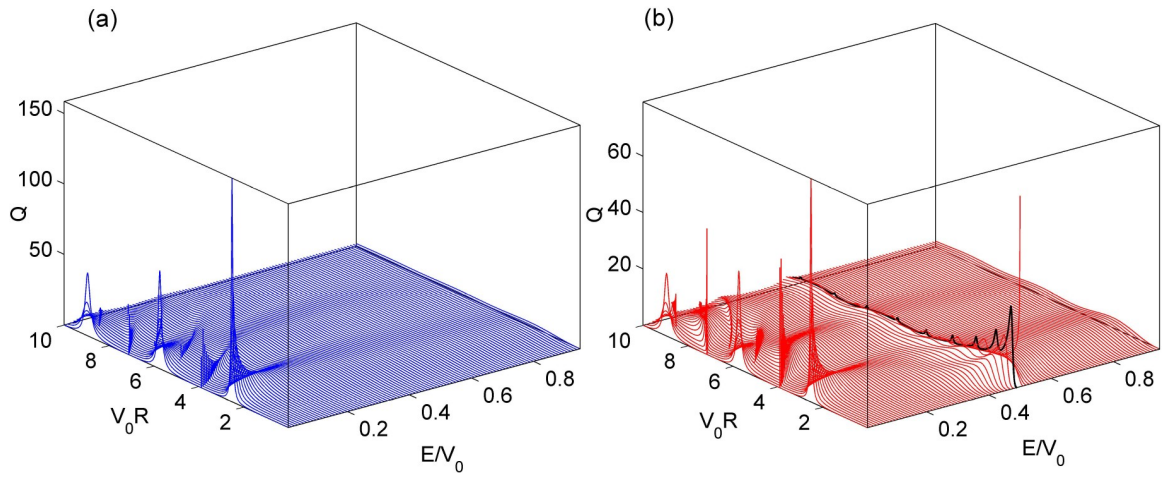

Fig. 26. Scattering efficient Q versus the scatterer strength V_0R and the relative incident energy E/V_0 for (a) massless pseudospin-$1/2$ and (b) massless pseudospin-1 wave systems. The black curve is for $E/V_0 = 0.49$ with a highlighted visual effect.

Given the particular range of the scattering strength V_0R as set in Figs. 25(a-c), we see that increasing E/V_0 leads to larger values of kR and hence the scattering process involves higher angular momentum channels. As a result, more quasi-bound modes can be excited, generating overlapping and broadened resonances, as shown in Figs. 25(b) and 25(c). In the limit of $kR \gg 1$, say $V_0R \gg 1$ for $E/V_0 \sim 1$, we enter the semiclassical regime where the ray picture is applicable. We obtain $Q \approx 2\,[1 - \pi\cos(2V_0R - \pi/4)/4V_0R]$ as a damped oscillatory function of the scattering strength V_0R about a constant value. Distinct from the resonant scattering regime dominated by wave interference/diffraction, in the semiclassical regime the scatterer acts as a Veselago reflector due to its effective negative refractive index. The associated local probability density and current density patterns in typical situations for both conventional massless pseudospin-$1/2$ and massless pseudospin-1 cases are shown in Figs. 25(b1-b4) and 25(c1-c4), respectively.

To gain further insights into the scattering behaviors, we plot Q as a function of V_0R and E/V_0, as shown in Figs. 26(a) and 26(b), respectively. As expected, for the pseudospin-$1/2$ Dirac cone

system, the curve of Q versus V_0R tends to be smooth as E/V_0 is increased [Fig. 26(a)]. However, for the pseudospin-1 Dirac cone system shown in Fig. 26(b), the remarkable phenomenon of revival resonant scattering emerges: the sharp resonances disappear, reappear unexpectedly, and then disappear again with continuous increase in E/V_0. We emphasize that this revival phenomenon is quite exceptional which, to our knowledge, has not been reported in any other known wave systems. In the limit of $V_0R \ll 1$ ($V_0R > kR$), we obtain

$$Q \simeq \frac{2}{kR}\left[\frac{P_0^2}{P_0^2+Q_0^2} + 2\times\frac{P_1^2}{P_1^2+(4+Q_1)^2}\right], \tag{5.5}$$

where

$$\begin{aligned} P_0 &= \pi kR, \text{ and} \\ Q_0 &= 2\left[kR\ln(\gamma_E kR/2) - J_0(V_0R-kR)/J_1(V_0R-kR)\right], \end{aligned}$$

with P_1 and Q_1 given by $[P_1, Q_1] = kR[P_0, Q_0]$. The first term of Eq. (5.5),

$$\begin{aligned} \frac{P_0^2}{P_0^2+Q_0^2} &\approx \frac{\pi^2 J_1^2(V_0R-kR)}{4J_0^2(V_0R-kR)}(kR)^2 \\ &\simeq \frac{\pi^2(1-E/V_0)^2}{16}(V_0R)^2(kR)^2 \ll 1, \end{aligned}$$

is off-resonance. Remarkably, the second term generates an additional resonance for $4+Q_1=0$, which corresponds to the emerging revival resonance observed. Explicitly, the associated revival resonant condition can be obtained from $4+kRQ_0=0$ as $E/V_0 \approx 1/2$, which agrees with the numerical results as displayed in Fig. 26(b).

Certain remarkable features of the revival resonances can be revealed through the underlying revival resonant modes (RRMs) defined in terms of the associated local probability and current density patterns, as shown in Figs. 27 and 28 respectively. From Fig. 27, we see that the RRMs exhibit unusual boundary trapping profiles, where the higher the resonance frequency (energy) the more

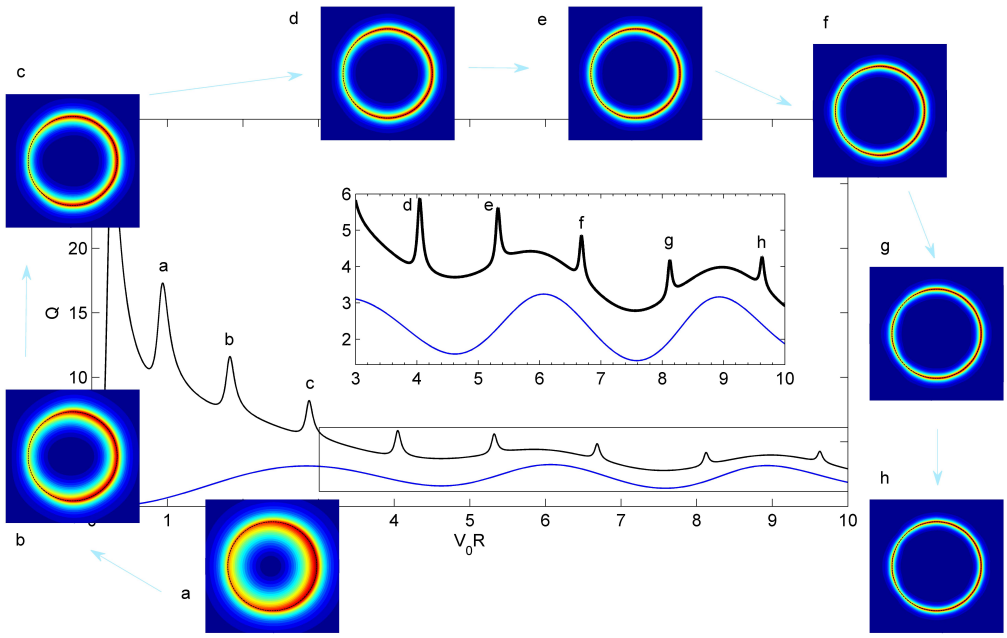

Fig. 27. Revival resonant scattering occurs at $E/V_0 = 0.49$ in the massless pseudospin-1 wave system.

pronounced the trapping. Examining the corresponding local current density distribution of a specific RRM [cf., Figs. 28(a-c)], we find that the incident wave is fed into fusiform vortices about the boundary and is trapped there. In contrast, for the conventional pseudospin-$1/2$ scattering, as indicated by the blue line in Fig. 27, no such trapping phenomenon occurs, giving rise to conventional scattering states as shown in Figs. 28(d-f). Using the general vortex-based trapping mechanism, we can get an intuitive physical picture for the unusual boundary trapping phenomenon through a qualitative analysis of vortex formation in the local current distribution stipulated by the boundary conditions. In particular, for a given local current configuration outside the scattering boundary, as indicated by the light blue arrows in Figs. 29(a-c), we sketch the possible local current patterns inside the boundary, denoted by the blue, green and red arrows, respectively. This can be done with the boundary conditions defined in terms of the spinor wavefunction $\Psi = [\psi_1, \psi_2, \psi_3]^T$ and their effect on the associated local current field $\boldsymbol{j}$ (see Appendix 5.1.4.1). Since continuity is the

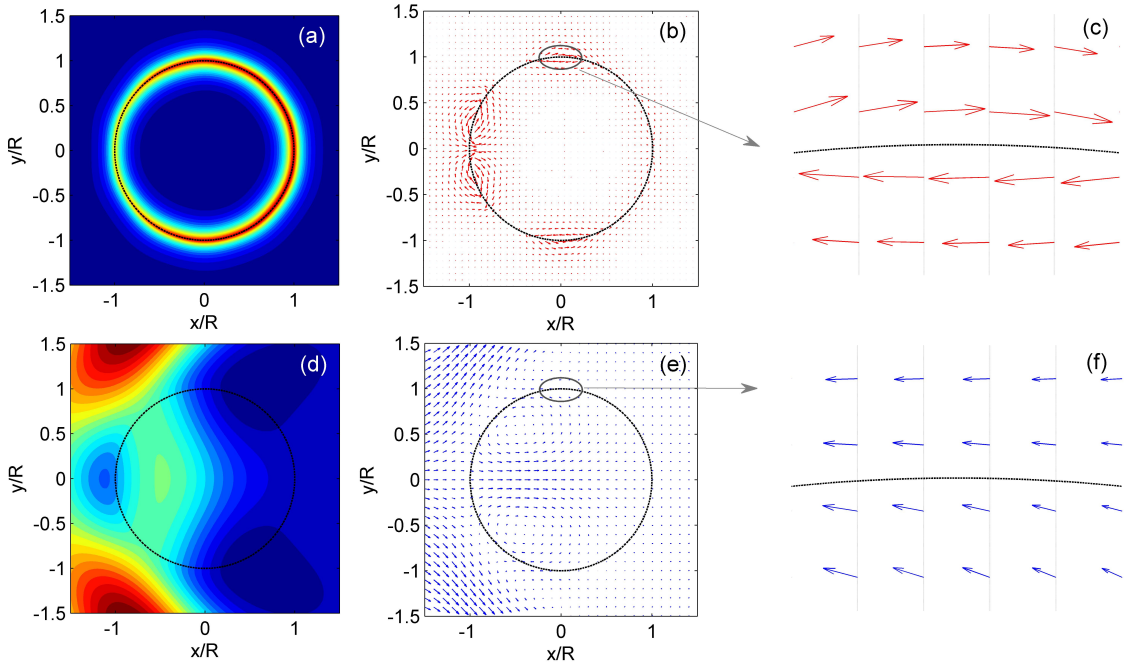

Fig. 28. Scattering modes associated with revival resonant and conventional scattering. (a-c): A typical revival resonant mode for the pseudospin-1 Dirac cone system. (d-f): Conventional scattering state for pseudospin-$1/2$ system. The parameters are the same for both systems.

only constraint on the normal component of the local currents at the boundary (the tangent component is in general discontinuous and can even have opposite directions), there is an additional freedom to configure the corresponding current pattern inside the potential region for a particular pattern outside. This leads to the remarkable fusiform boundary vortices as illustrated in Fig. 29(c) with the dramatic phenomenon of boundary trapping and, consequently, to the resonances in the curve of the scattering efficiency. Note that, for the conventional scalar or spinor wave systems, the current configuration is well-determined in the sense that, given a configuration on one side of the boundary, that on the other side is then determined completely. This is due to the continuity in both components of the local currents at the boundary, as illustrated in Fig. 29(a). As a concrete example, we demonstrate the full local current patterns in Figs. 29(d-f), where the former two represent the typical local current profiles underlying the conventional low-order resonant modes excited in the massless pseudospin-$1/2$ and massless pseudospin-1 wave systems, respectively, while the last one is for that of the RRM that arises only for the massless pseudospin-1 wave system.

For pseudospin-1 Dirac cone systems, a remarkable phenomenon is super-Klein tunneling (see Appendix 5.1.4.1), which occurs when the energy of the incident particle is about one half of the potential height. In this case, forward scattering is maximized. In contrast, the revival scattering resonances are associated with fusiform vortices about the boundary, creating perfect wave trappings there and eliminating any forward scattering. Both super-Klein tunneling and revival resonant scattering depend on the scatterer strength V_0R and the relative incident energy E/V_0. From an applied point of view, it is thus possible to switch the super-Klein-tunneling dominant forward scattering on and off efficiently by tuning the parameters. In fact, the higher pseudospin degree of freedom and the flexible scattering boundary conditions render richer current patterns that can be manipulated through parameter perturbation. This may find applications in novel photonic integrated

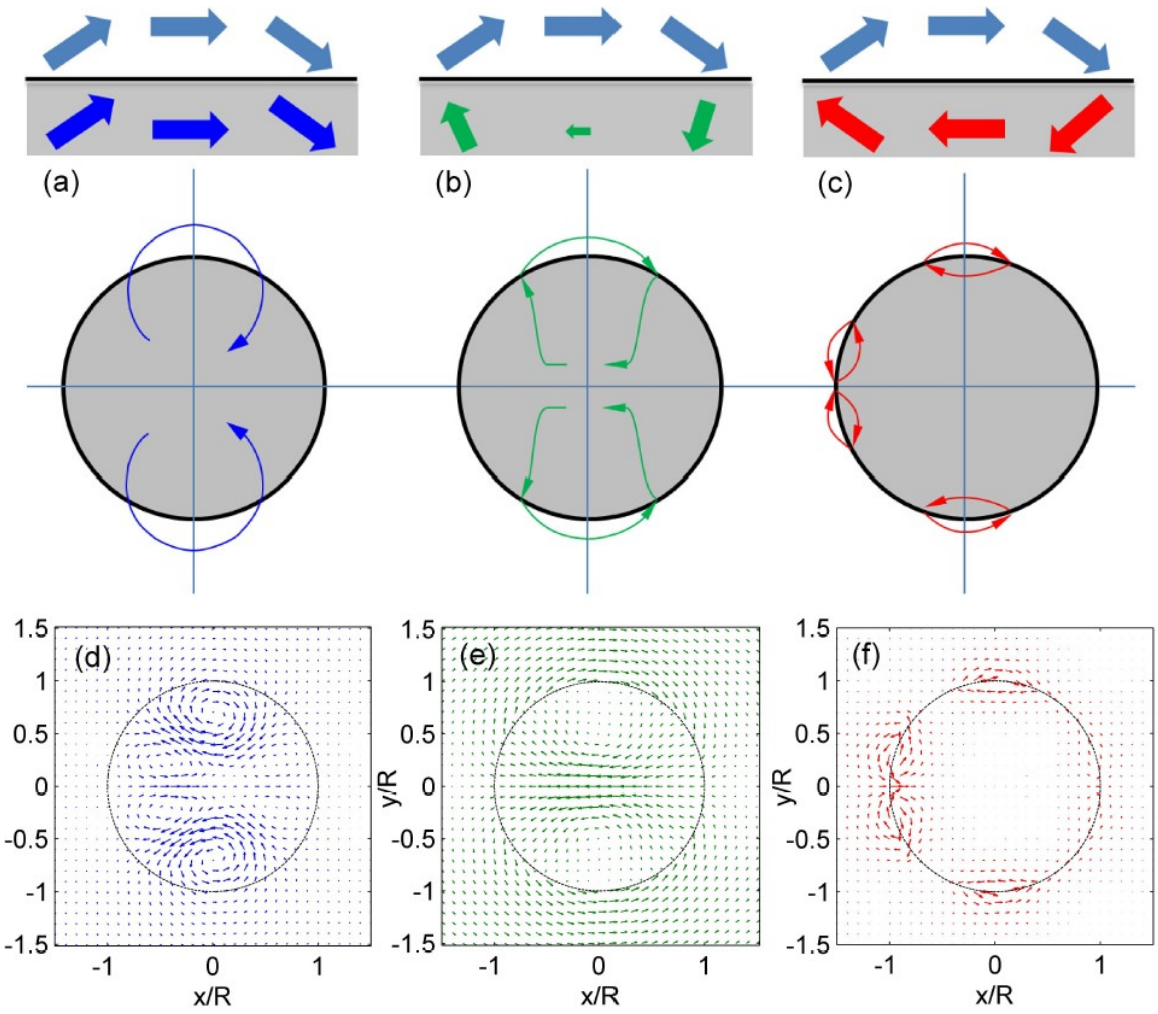

Fig. 29. Vortex-based wave trapping for massless pseudospin-1 scattering. (a-c) Schematic illustration of three types of vortex-based wave trapping. (d) Wave pattern near the boundary for a massless pseudospin-1/2 particle for $E/V_0 = 0.086$. (e,f) Boundary wave patterns for the massless pseudospin-1 case for $E/V_0 = 0.044$ and $E/V_0 = 0.487$, respectively. The value of V_0R is set to be 4.5 for all cases.

circuit design, as pseudospin-1 systems have been realized experimentally in a variety of photonic crystals [149, 150, 153–156, 158].

While the RRMs uncovered appear similar to the well-known whispering gallery modes (WGMs) in terms of the intensity profiles, we emphasize that the underlying mechanisms are quite different. In particular, the WGMs are due to the total internal reflection within an effective semi-classical ray regime, but the RRMs result from the formation of unusual, dominant vortices locally attached to the boundary due to wave interference and can thus occur for much smaller scatterer size kR, a regime in which the semiclassical ray approximation fails. An explicit comparison of conventional resonant, revival resonant and whispering gallery modes for the pseudospin-1 Dirac cone system is presented in Fig. 30.

5.1.2.2. Near-Field Behavior 2: Perfect Caustics

Caustics, a spatial region in which the density of light rays is singular, occur in the semiclassical regime. This phenomenon is quite common in daily life, mostly through geometric optics. For a pseudospin-$1/2$ Dirac cone system, caustics can occur due to the tunable effective negative refractive index and the Klein tunneling effect, as shown in Figs. 31(a) and 31(c). For the pseudospin-1 Dirac cone system, the surprising phenomenon of perfect caustic/lens behavior occurs, as shown in Figs. 31(b) and 31(d) for the same parameter as in Figs. 31(a) and 31(c), which emerges in the regime where the incident wavelength is much smaller than the scatterer radius R. The caustic patterns for the massless pseudospin-1 system are "perfect" in the sense that they are significantly more focused/concentrated than the pseudospin-$1/2$ counterparts. We find that perfect caustics are a result of the super-Klein tunneling effect for massless pseudospin-1 particle, where the transmission coefficient approaches unity for *any* incident angle [153, 162, 169, 170]. Specifically, for a single straight scattering interface, we obtain the transmission coefficient for incident angle θ ($-\pi/2 \leq \theta \leq \pi/2$)

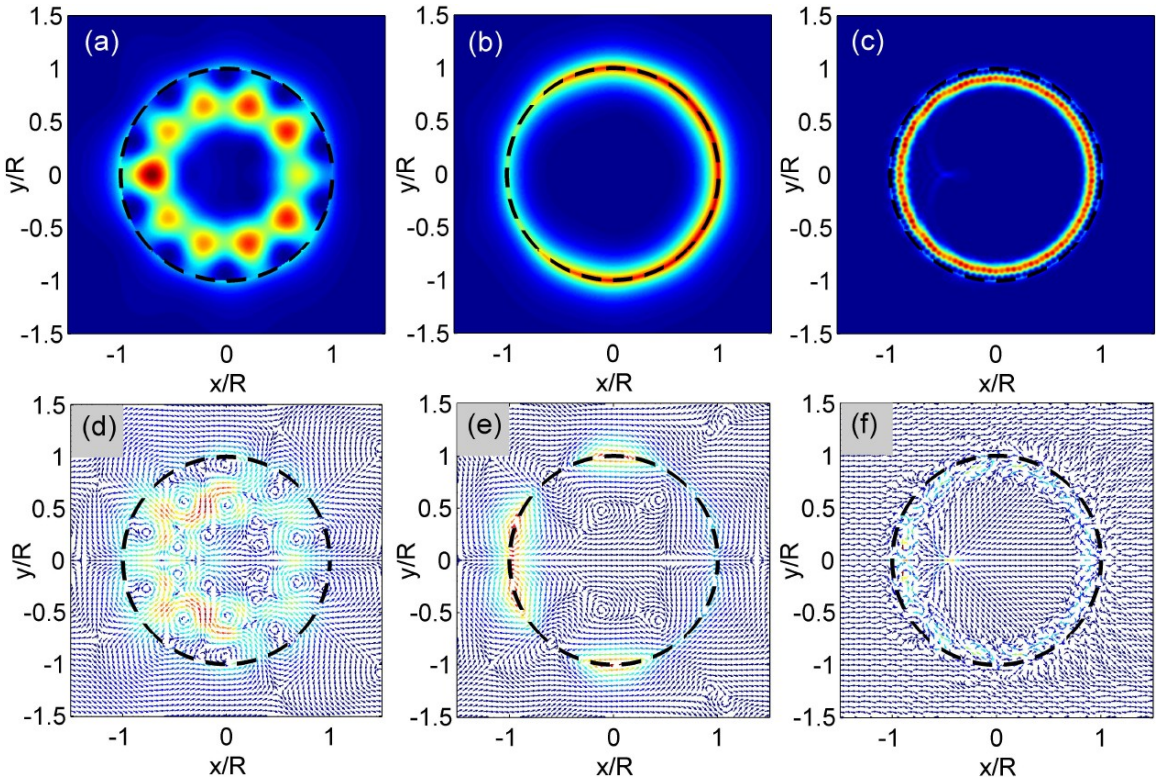

Fig. 30. Comparision of conventional resonant, revival resonant and whispering gallery modes for pseudospin-1 Dirac cone system. (a-c): Typical probability distributions for the conventional resonant mode (CRM), revival resonant mode (RRM) and whispering gallery mode (WGM), respectively, where the scattering parameters [E/V_0,V_0R] are: (a) [0.2, 11.598], (b) [0.487,4.5] and (c) [0.4157, 100]. (d-f) The corresponding current patterns.

as

$$T = \frac{4\tau\tau' \cos\theta' \cos\theta}{\cos^2\theta' + \cos^2\theta + 2\tau\tau' \cos\theta' \cos\theta}, \tag{5.6}$$

with the refractive angle given by

$$\theta' = \pi - \tan^{-1} \frac{|E/V_0| \sin\theta}{\sqrt{(1 - E/V_0)^2 - (E/V_0)^2 \sin^2\theta}},$$

where $\tau = \text{sgn}(E)$ and $\tau' = \text{sgn}(E - V_0)$. It follows from Eq. (5.6) that $T \equiv 1$ for $E/V_0 = 1/2$, regardless of the incident angle, as shown by the thick red curve in Fig. 32, signifying a super-Klein tunneling behavior. For comparison, the incident angle dependent transmission probability for the conventional pseudospin-$1/2$ system is shown as the thick blue line in the same figure.

Within the ray formalism and based on differential geometry [183], we obtain analytically the following caustic envelope equation defining a curve $\boldsymbol{r}_c = (x_c, y_c)$ as

$$\begin{aligned} \frac{\boldsymbol{r}_c(p,\theta)}{R} = (-)^{p-1} \Bigg[& (-\cos\Theta, \sin\Theta) + \cos\beta \frac{1 + 2(p-1)\beta'}{1 + (2p-1)\beta'} \\ & \times (\cos(\Theta + \beta), -\sin(\Theta + \beta)) \Bigg], \end{aligned} \tag{5.7}$$

where $\Theta = \theta + 2(p-1)\beta$, $\sin\beta = \sin\theta/|1 - V_0/E|$, and $\beta' = \cos\theta/\sqrt{(1 - V_0/E)^2 - \sin^2\theta}$ with p being the number of chords inside the scattering region corresponding to $p-1$ internal reflections. Intuitively, the caustics for $p > 1$ are less visible since the ray intensity decreases after each internal reflection. However, for our pseudospin-1 Dirac cone system, the super-Klein tunneling effect for $E/V_0 = 1/2$ will suppress the $p > 1$ caustics completely, leading to a perfect caustic for $p = 1$, which intuitively can be better seen from the corresponding local current patterns in Figs. 31(c,d).

While super-Klein tunneling $T \equiv 1$ occurs exactly for $E/V_0 = 0.5$ for the entire range of the incident angle, even when E/V deviates from the value of 0.5 (e.g., $E/V = 0.4$), $T \approx 1$ still persists for a substantial range of the incident angle, as shown in the top-right corner of Fig. 33. In addition, the phenomenon of perfect caustics holds as well, as shown in Figs. 33(b,d). Because of

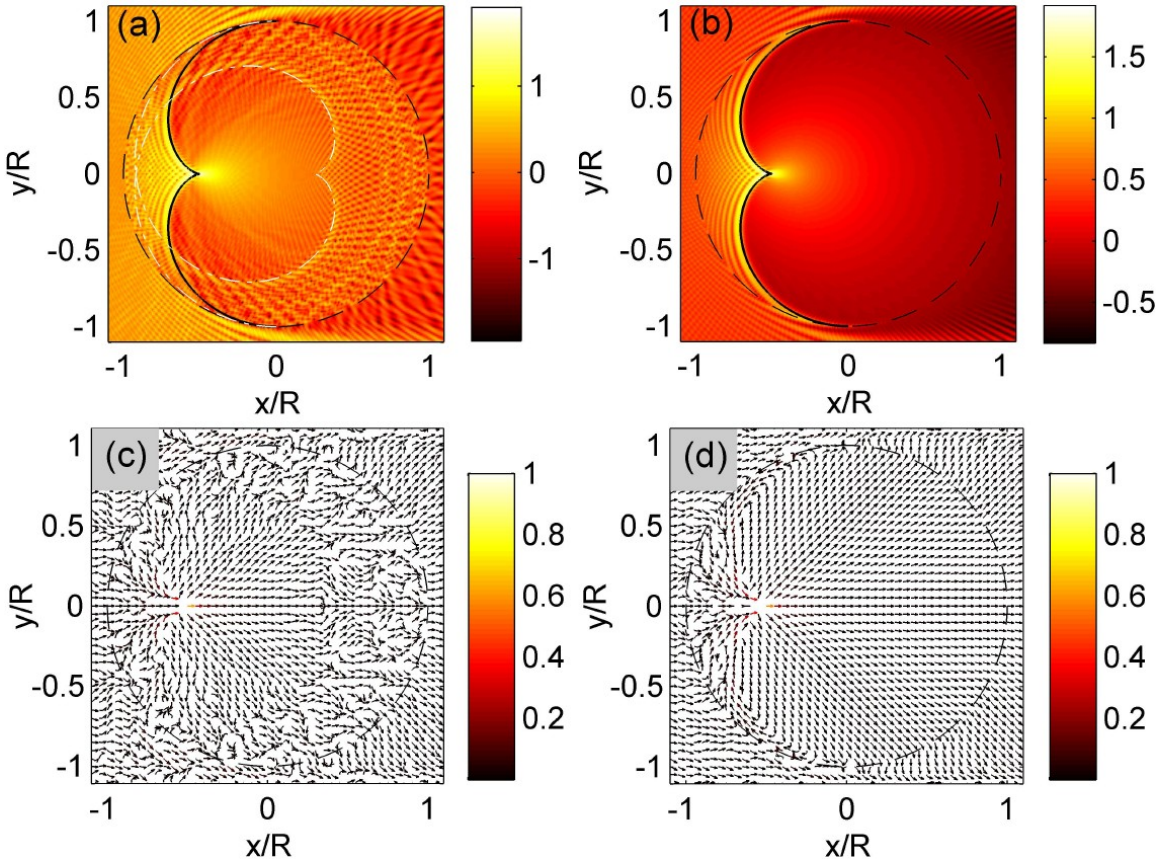

Fig. 31. Caustic behavior in the semiclassical regime and perfect caustics in pseudospin-1 Dirac cone systems. The probability and local current density patterns, respectively, for (a,c) conventional pseudo-$1/2$ and (b,d) pseudospin-1 Dirac cone systems. The probability density patterns in (a) and (b) are plotted on a logarithmic scale. The corresponding local current density patterns in (c) and (d) are color-coded with magnitude normalized by its maximum. The parameters are $kR = 300$ and $E/V_0 = 1/2$.

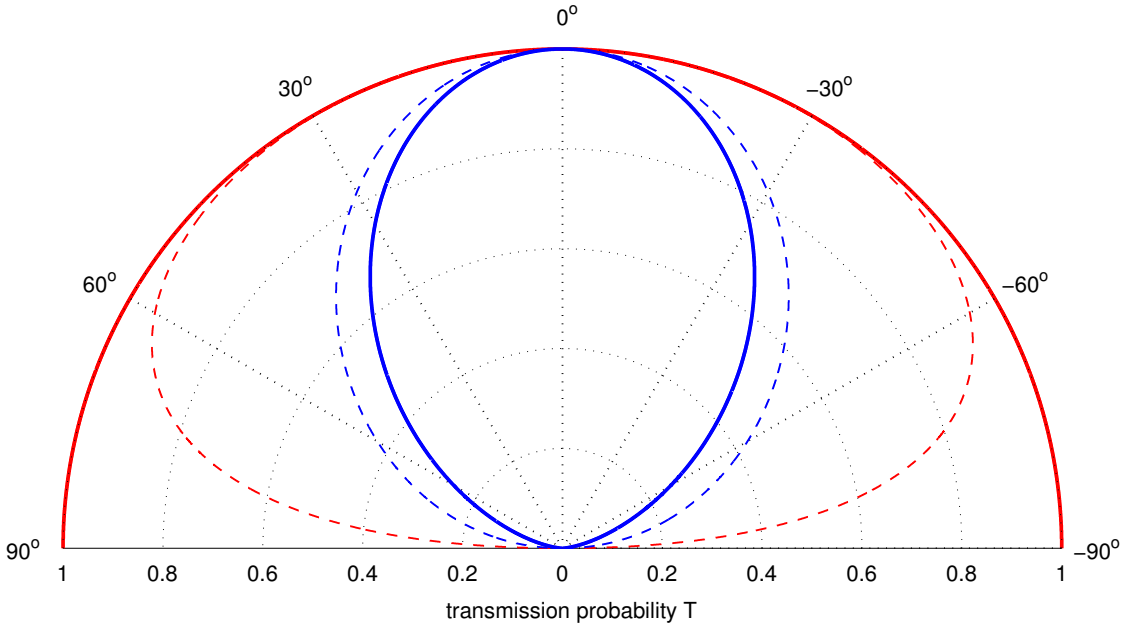

Fig. 32. Super-Klein tunneling in pseudospin-1 Dirac cone systems. Transmission probability: red and blue curves are for the massless pseudospin-1 and pseudospin-$1/2$ particles, respectively, with $E/V_0 = 0.5$ (solid lines) and $E/V_0 = 0.4$ (dash lines). For the former (solid red line) the transmission is unity, regardless of the incident angle.

the flexible energy range for super-Klein tunneling and perfect caustics to occur, it may be feasible to observe these phenomena in experiments.

5.1.2.3. Far-Field Behavior: Isotropic Scattering of Massless Pseudospin-1 Quasiparticles and Control

Far away from the scattering center, i.e., $r \gg R$, for unit incident density, the spinor wavefunction can be written as

$$\Psi_{>}(r,\theta) \approx \frac{1}{2}\begin{pmatrix} 1 \\ \sqrt{2}\tau \\ 1 \end{pmatrix} e^{ikr\cos\theta} + \frac{1}{2}\begin{pmatrix} e^{-i\theta} \\ \sqrt{2}\tau \\ e^{i\theta} \end{pmatrix} \frac{f(\theta)}{\sqrt{r}} e^{ikr}, \tag{5.8}$$

where $f(\theta)$ denotes the 2D far-field scattering amplitude in the direction defined by the angle θ with the x axis. The differential and the total cross sections are given, respectively, by

$$\frac{\mathrm{d}\sigma}{\mathrm{d}\theta} = |f(\theta)|^2, \tag{5.9}$$

and

$$\sigma = \int_0^{2\pi} |f(\theta)|^2 \mathrm{d}\theta. \tag{5.10}$$

In addition, we define the transport or momentum-relaxation cross section as

$$\sigma_{\mathrm{tr}} = \int_0^{2\pi} \mathrm{d}\theta |f(\theta)|^2 (1-\cos\theta). \tag{5.11}$$

The three types of cross sections are experimentally measurable and can be used to quantitatively characterize the basic scattering and transport physics for pseudospin-1 Dirac cone systems. For example, consider such a system with randomly distributed identical scatterers of low concentration, i.e., $n_c \ll 1/R^2$, the conductivity in units of the conductance quantum G_0 can be expressed as (see Appendix 5.1.4.3)

$$\frac{G}{G_0} = \frac{k}{n_c \sigma_{\mathrm{tr}}} = v_g k \tau_{\mathrm{tr}}, \tag{5.12}$$

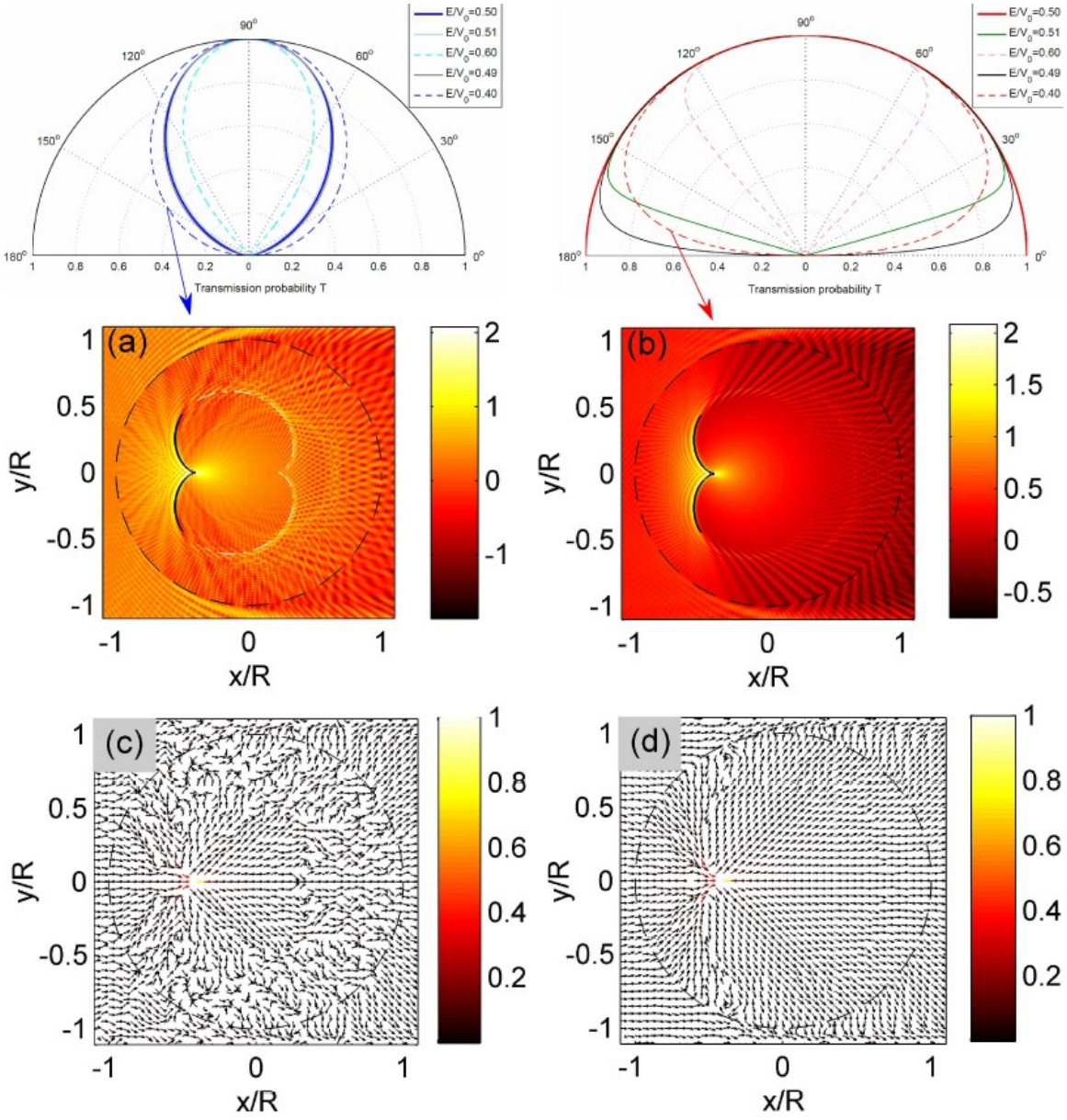

Fig. 33. Robustness of super-Klein tunneling and perfect caustics in pseudospin-1 Dirac cone systems. Top panels: polar plots of the transmission probability for different values of E/V_0 as indicated. The left column is for the pseudospin-$1/2$ system, while the right is for the pseudospin-1 system. Parameters used for generating the caustic patterns are $kR = 300$ and $E/V_0 = 0.4$ (rather than exactly at $E/V_0 = 0.5$).

where the sample size is assumed to be larger than the mean-free path $L = v_g\tau_{\text{tr}}$ with τ_{tr} being the transport mean free time, and v_g is the group velocity. The elastic scattering time (the quantum lifetime) τ_e can be determined from the total cross section through

$$\frac{1}{\tau_e} = n_c v_g \sigma. \tag{5.13}$$

The two time scales define the following characteristic ratio:

$$\xi = \frac{\tau_{\text{tr}}}{\tau_e} = \frac{\sigma}{\sigma_{\text{tr}}} \equiv \frac{\oint \mathrm{d}\theta |f(\theta)|^2}{\oint \mathrm{d}\theta |f(\theta)|^2 (1-\cos\theta)}, \tag{5.14}$$

which can be used to characterize the far-field behavior of the scattering process. Through a detailed analysis, we obtain the following formula (see Appendix 5.1.4.2):

$$\xi = \frac{2\sum_l \sin^2\delta_l}{\sum_l \sin^2(\delta_{l+1}-\delta_l)}, \tag{5.15}$$

where δ_l is the scattering phase shift associated with angular momentum l.

We present our finding of the general isotropic nature of low-energy scattering for massless pseudospin-1 wave. To be concrete, we calculate from Eq. (5.15) the ratio ξ as a function of kR for a given barrier strength $V_0R = 5$. The result is shown as the red curves in Fig. 34, where we see that there is a characteristic constant ratio $\xi \approx 1$ of the transport time to the elastic time for $kR \ll 1$. For comparison, we calculate the corresponding ratio for the massless pseudospin-$1/2$ wave, where low-energy scattering is universally anisotropic as characterized by the constant ratio $\xi \approx 2$ [182, 187]. Our result indicates that, for a massless pseudospin-1 particle, back scattering is as pronounced as forward scattering. This finding is quite counterintuitive as, if the massless nature of the quasiparticles is sustained, they can penetrate through potential barriers of arbitrary strength via the mechanism of Klein tunneling, making forward scattering more pronounced. Since super-Klein tunneling can occur for massless pseudospin-1 quasiparticles but the scattering is isotropic at low energies, the message is that, to generate isotropic transport, it may not be necessary to break

symmetries to alter the massless nature of the quasiparticles through, e.g., additional mechanisms such as spin-orbit interactions. Equivalently, an isotropic ratio ξ for massless quasiparticles does not necessarily imply any symmetry breaking leading to a finite mass.

To gain deeper insights into the physics underlying the counterintuitive phenomenon of isotropic scattering for massless particles, we analyze the characteristic ratio ξ in terms of the scattering cross sections. The reflection coefficient associated with angular momentum l satisfies $A_l = A_{-l}$. Using this relation, we obtain the differential cross section as (Appendix 5.1.4.2)

$$\begin{aligned}\frac{\mathrm{d}\sigma}{\mathrm{d}\theta} &= \frac{2}{\pi k}\{|A_0|^2 + 2\sum_{n=1}^{\infty}|A_n|^2[1+\cos(2n\theta)] + 4\sum_{n=1}^{\infty}\Re(A_0A_n^*)\cos(n\theta) \\ &+ 8\sum_{m>n=1}^{\infty}\Re(A_nA_m^*)\cos(n\theta)\cos(m\theta)\}.\end{aligned} \tag{5.16}$$

In the regime $kR \ll 1$ where the total angular momentum channels ($l = 0, \pm 1$) dominate the scattering process, we have

$$\frac{\mathrm{d}\sigma}{\mathrm{d}\theta} \approx \frac{2}{\pi k}\left\{|A_0|^2 + 2|A_1|^2[1+\cos(2\theta)]\right\}, \tag{5.17}$$

resulting in an isotropic ratio that agrees with the simulation result:

$$\xi \equiv \frac{\oint \mathrm{d}\theta \frac{d\sigma}{d\theta}}{\oint \mathrm{d}\theta \frac{d\sigma}{d\theta}(1-\cos\theta)} \approx 1. \tag{5.18}$$

A remarkable feature associated with the expression of $\mathrm{d}\sigma/\mathrm{d}\theta$ in Eq. (5.17) is the presence of backscattering characterized by a finite differential cross section at $\theta = \pi$:

$$\frac{\mathrm{d}\sigma}{\mathrm{d}\theta}\Big|_{\theta=\pi} = \frac{2}{\pi k}\left[|A_0|^2 + 4|A_1|^2\right], \tag{5.19}$$

which results from the constant term contributed by the $l = 0$ channel and the constructive interference between the time-reversed scattering paths denoted by $l = \pm 1$. The underlying physical picture can then be understood, as follows. Consider the pseudohelicity defined as $\hat{h} = \boldsymbol{S} \cdot \boldsymbol{k}/k$. Its

eigenvalues are conserved during the scattering process because of the commutation $[\hat{h}, \hat{H}] = 0$ for the massless pseudospin-1 system. In general, when time-reversal symmetry is taken into account, a typical backscattering process consists of a pair scattering paths with a 2π relative rotation of the pseudospin between them. This leads to a phase difference determined by the underlying Berry phase $e^{i\Phi_B}$. For a massless pseudospin-1 particle, we have $\Phi_B = 0$. There is thus coherent interference for backscattering, which makes the low-energy scattering isotropic. When this general picture is applied to a conventional pseudospin-$1/2$ Dirac cone system with $\Phi_B = \pi$, it is straightforward to see that, for backscattering there is complete destructive interference and the zero total angular momentum channel is absent [**?**, 180]. In particular, we have, for the differential cross section, $\mathrm{d}\sigma/\mathrm{d}\theta \sim (1 + \cos\theta)$ for $kR \ll 1$. The ratio ξ thus becomes $\xi \approx 2/\oint \mathrm{d}\theta(1 - \cos 2\theta) = 2$. The analysis agrees with the numerical results in Fig. 34.

Another phenomenon is the emergence of Fano-like resonance profile for larger values of kR where higher angular momentum channels can be excited and interfere with the lower ones, as manifested in the behavior of ξ versus kR. This provides a way to manipulate Klein-tunneling based scattering. In particular, for the conventional pseudospin-$1/2$ Dirac cone system (as illustrated by the blue curves in the insets (II) and (III) of Fig. 34), the preferred scattering directions can be controlled through tuning of the quantity kR. However, for such particles, since backscattering is typically totally suppressed, it is not possible to switch between forward and backward scattering. Remarkably, controlled switching in the scattering dynamics from forward to backward and vice versa can be done for our pseudospin-1 system. There are in fact a number of controllable scattering scenarios ranging from the isotropic type ($\xi \approx 1$), the backscattering dominant type ($\xi < 1$), and the forward scattering dominant type ($\xi > 2$), and the switches among them can be realized by tuning the scattering parameter kR. The feasibility of controlled scattering can be seen from the red

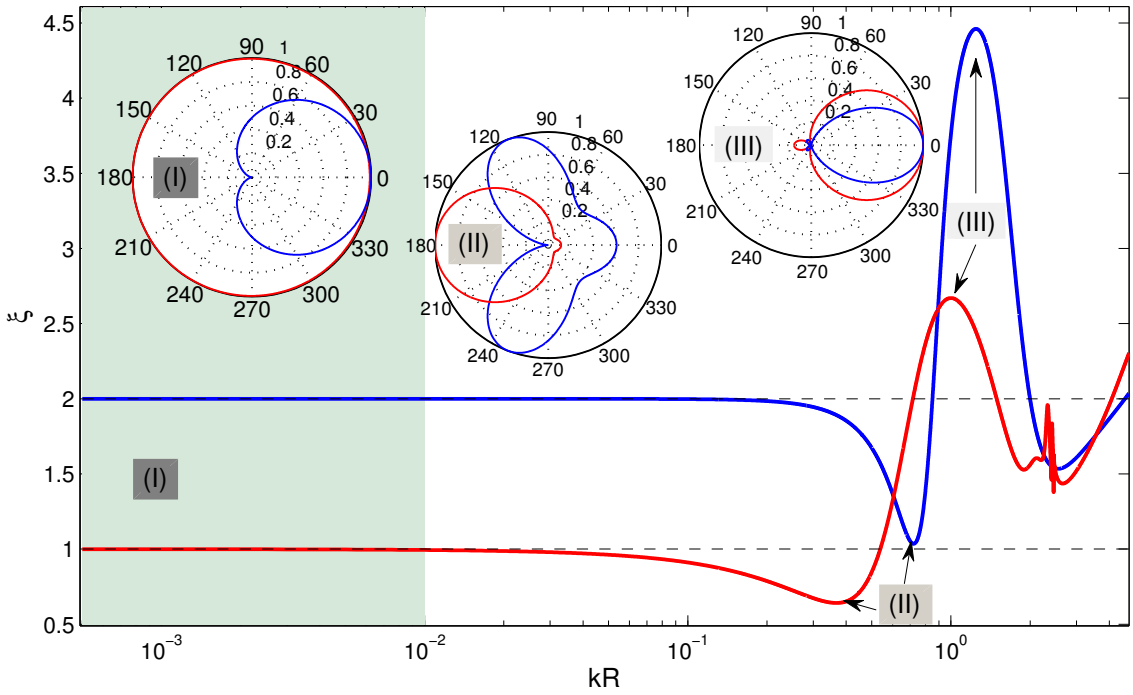

Fig. 34. Isotropic scattering of massless pseudospin-1 quasiparticle. Ratio ξ as a function of kR for $V_0R = 5$: the red and blue lines are for the massless pseudospin-1 and pseudospin-$1/2$ cases, respectively.

curves in the insets of Fig. 34. This capability of scattering control can have potential applications in unconventional photonic/electronic circuit design.

5.1.3. Discussion

Using a general Hamiltonian for pseudospin-1 systems whose energy band structure constitutes a pair of Dirac cones and a topologically flat band, we investigate the basic problem of wave scattering from a circularly symmetric potential barrier. In spite of its simplicity, the system gives unusual and unexpected physics: revival resonant scattering, perfect caustics, and isotropic scattering for massless quasiparticles. In particular, for small scatterer size, the effective three-component spinor wave exhibits revival resonant (Mie) scattering features as the incident wave energy is varied con-

tinuously - a surprising phenomenon which, to our knowledge, has not been reported in any known wave systems. For larger scatter size rendering semiclassical the underlying scattering dynamics, a super-caustic phenomenon arises when the incident wave energy is about half of the barrier height, which is essentially a manifestation of the super-Klein tunneling effect for massless pseudospin-1 particles. Because of Klein tunneling, intuitively wave scattering should be anisotropic due to suppression of backward scattering, which is indeed the case for conventional pseudospin-$1/2$ particles. However, for a pseudospin-1 particle, the associated Berry phase can lead to constructive interference in the backward direction, leading to the counterintuitive phenomenon of isotropic scattering even for massless quasiparticles. We develop an analytic theory and physical understanding with extensive numerical support to substantiate our findings.

It is possible to conduct experimental test of the findings of this paper. For example, in a recent work [153], it was demonstrated for a class of two-dimensional dielectric photonic crystals with Dirac cones induced accidentally [149–152] that the Maxwell's equations can lead to an effective Hamiltonian description sharing the same mathematical structure as that of massless pseudospin-1 particles. Especially, the photonic analogy of the gate potential in the corresponding electronic system can be realized by manipulating the scaling properties of Maxwell's equations. Recent experimental realizations of photonic Lieb lattices consisting of evanescently coupled optical waveguides implemented through the femtosecond laser-writing technique [154–157] make them prototypical for studying the physics of pseudopsin-1 Dirac systems. With a particular design of the refractive index profile across the lattice to realize the scattering configuration, our findings can be experimentally tested. Loading ultracold atoms into an optical Lieb lattice fabricated by interfering counter-propagating laser beams [158] provides another versatile platform to test our findings, where appropriate holographic masks can be used to implement the desired scattering potential bar-

rier [162, 190]. In electronic systems, we note that the historically studied but only recently realized 2D magnetoplasmon system [191] is described by three-component linear equations with the same mathematical structure of massless pseudospin-1 particles, which can serve as a 2D electron gas system to test our results.

From an applied perspective, the phenomenon of revival resonant scattering can be a base for articulating a new class of microcavity lasers based on the principles of relativistic quantum mechanics. It may also lead to new discoveries in condensed matter physics through exploiting the phenomenon in electronic systems. The phenomenon of perfect caustics can have potential applications in optical imaging defying the diffraction limit as well as in optical cloaking.

5.1.4. Methods

5.1.4.1. Hamiltonian and General Properties

The effective low-energy Hamiltonian associated with pseudospin-1 Dirac cones can be written, in the unit $\hbar = 1$, as [153, 154, 169]

$$H_0 = v_g \boldsymbol{S} \cdot \boldsymbol{k}, \tag{5.20}$$

where v_g is the magnitude of the group velocity associated with the Dirac cone, $\boldsymbol{k} = (k_x, k_y)$ denotes the wavevector, and $\boldsymbol{S} = (S_x, S_y)$ is a vector of matrices with components

$$S_x = \frac{1}{\sqrt{2}} \begin{pmatrix} 0 & 1 & 0 \\ 1 & 0 & 1 \\ 0 & 1 & 0 \end{pmatrix} \text{ and } S_y = \frac{1}{\sqrt{2}} \begin{pmatrix} 0 & -i & 0 \\ i & 0 & -i \\ 0 & i & 0 \end{pmatrix}. \tag{5.21}$$

Along with another matrix

$$S_z = \begin{pmatrix} 1 & 0 & 0 \\ 0 & 0 & 0 \\ 0 & 0 & -1 \end{pmatrix},$$

the three matrices form a complete representation of spin-1, which satisfies the angular momentum commutation relations $[S_l, S_m] = i\epsilon_{lmn}S_n$ with three eigenvalues: $s = \pm 1, 0$, where ϵ_{lmn} is the Levi-Civita symbol. It follows from Eq. (5.20) that the energy spectrum consists of three bands that intersect at the Dirac point: a dispersionless flat band $E_0(\boldsymbol{k}) = 0$ and two linearly dispersive bands $E_\tau(\boldsymbol{k}) = \tau v_g|\boldsymbol{k}|$ with $\tau = \pm 1$ being the band index. The corresponding eigenfunctions in the position representation $\boldsymbol{r} = (x, y)$ are

$$\psi_{\boldsymbol{k},\tau}(\boldsymbol{r}) = \langle \boldsymbol{r}|\boldsymbol{k}, \tau\rangle = \frac{1}{2}\left[e^{-i\theta}, \sqrt{2}\tau, e^{i\theta}\right]^T e^{i\boldsymbol{k}\cdot\boldsymbol{r}}, \tag{5.22}$$

for the dispersive bands and

$$\psi_{\boldsymbol{k},0}(\boldsymbol{r}) = \langle \boldsymbol{r}|\boldsymbol{k}, 0\rangle = \frac{1}{\sqrt{2}}\left[-e^{-i\theta}, 0, e^{i\theta}\right]^T e^{i\boldsymbol{k}\cdot\boldsymbol{r}}, \tag{5.23}$$

for the flat band, where $\theta = \tan^{-1}(k_y/k_x)$. The current operator is defined from Eq. (5.20) as

$$\hat{\boldsymbol{j}} = \nabla_{\boldsymbol{k}} H_0 = v_g \boldsymbol{S}. \tag{5.24}$$

The local current in a given state $\psi(\boldsymbol{r}) = [\psi_1, \psi_2, \psi_3]^T$ can thus be expressed as

$$\begin{aligned} \boldsymbol{j}(\boldsymbol{r}) &= v_g \psi^\dagger \boldsymbol{S} \psi \equiv (j_x, j_y) \\ &= \sqrt{2} v_g \left(\Re[\psi_2^*(\psi_1 + \psi_3)], -\Im[\psi_2^*(\psi_1 - \psi_3)]\right), \end{aligned} \tag{5.25}$$

which satisfies the common continuity equation

$$\frac{\partial}{\partial t}\rho + \nabla \cdot \boldsymbol{j} = 0, \tag{5.26}$$

where $\rho = \psi^\dagger\psi$ is the probability density associated with state ψ. From Eqs. (5.22) and (5.23), we see that the associated local current density satisfies $\boldsymbol{j}_0 = \boldsymbol{0}$ for the flat band plane-wave, and

$$\boldsymbol{j}_\tau = v_g(\cos\theta, \sin\theta) = \tau v_g \frac{\boldsymbol{k}}{|\boldsymbol{k}|}, \tag{5.27}$$

for the dispersive band plane-wave. In terms of the Berry phase associated with the band structure, we obtain from Eqs. (5.22) and (5.23) the corresponding Berry connections

$$\begin{aligned}\mathcal{A}^{\tau}_{\boldsymbol{k}} &= \langle \boldsymbol{k}, \tau | i\nabla_{\boldsymbol{k}} | \boldsymbol{k}, \tau \rangle = 0, \\ \mathcal{A}^{0}_{\boldsymbol{k}} &= \langle \boldsymbol{k}, 0 | i\nabla_{\boldsymbol{k}} | \boldsymbol{k}, 0 \rangle = -2\mathcal{A}^{\tau}_{\boldsymbol{k}} = 0\end{aligned}$$

for all three bands. The Berry phase is thus given by

$$\Phi_B^{\tau,0} = \oint_{\mathcal{C}^{\tau,0}_{\boldsymbol{k}_d}} d\boldsymbol{k} \cdot \mathcal{A}^{\tau,0}_{\boldsymbol{k}} = 0, \tag{5.28}$$

for any closed path $\mathcal{C}^{\tau,0}_{\boldsymbol{k}_d}$ encircling the degeneracy point $\boldsymbol{k}_d$ of the momentum space defined in each band. We note that the vanishing or 2π quantized Berry phase is consistent with the fundamental properties of spin-1 particles.

Super-Klein tunneling. A remarkable phenomenon for pseudospin-1 Dirac cone systems, which is not usually seen in conventional Dirac cone systems such as graphene and topological insulators, is super-Klein tunneling [153]. Specifically, following the standard treatment of Klein tunning for graphene systems [2], one can consider the basic problem of wave scattering from a rectangular scalar (electrostatic) potential barrier defined as $V(x, y) = V_0\Theta(x)\Theta(D - x)$ with barrier width D and height V_0. The transmission probability based on the effective Hamiltonian Eq. (5.20) for incident energy $E \neq 0, V_0$ is given by

$$T = \frac{(1-\gamma^2)(1-\gamma'^2)}{(1-\gamma^2)(1-\gamma'^2) + \frac{1}{4}(\gamma+\gamma')^2 \sin^2(q_x D)}, \tag{5.29}$$

where $\gamma = \tau \sin\theta$, $\gamma' = \tau' \sin\theta'$ with $\tau = \text{sgn}(E), \tau' = \text{sgn}(E - V_0)$, $\theta = \tan^{-1}(k_y/k_x)$ is the incident angle, and $\theta' = \arctan(k_y/q_x)$ with

$$q_x = \sqrt{(E - V_0)^2 - k_y^2}.$$

A striking feature of Eq. (5.29) is that, when the incident wave energy is one half of the potential barrier height, i.e., $E = V_0/2$, one has $\tau = -\tau', \theta = \theta'$ and, consequently, perfect transmission with $T \equiv 1$ for *any* incident angle θ - hence the term "super-Klein tunneling."

5.1.4.2. Analysis of Scattering of Massless Pseudospin-1 Wave

Due to the circular symmetry of the scattering potential, it is convenient to formulate the solution in the polar coordinates $\boldsymbol{r} = (r, \theta)$, in which the Hamiltonian is

$$\hat{H} = \hat{H}_0 + V(r)\mathbf{1} = \frac{v_g}{\sqrt{2}} \begin{pmatrix} 0 & \hat{L}_- & 0 \\ \hat{L}_+ & 0 & \hat{L}_- \\ 0 & \hat{L}_+ & 0 \end{pmatrix} + V_0 \Theta(r - R)\mathbf{1}, \tag{5.30}$$

with the compact operator given by

$$\hat{L}_\pm = -ie^{\pm i\theta} \left(\partial_r \pm i \frac{\partial_\theta}{r} \right).$$

The z component of the total angular momentum is $\hat{J}_z = -i\partial_\theta + \hat{S}_z$, and we have $[\hat{H}, \hat{J}_z] = 0$. For a conventional two-dimensional Dirac cone system with massless spin-$1/2$ excitations, we have

$$\begin{aligned} \begin{pmatrix} 0 & \hat{L}_- \\ \hat{L}_+ & 0 \end{pmatrix} \begin{pmatrix} f_l^{(0,1)}(kr) \\ i\tau f_{l+1}^{(0,1)}(kr) e^{i\theta} \end{pmatrix} e^{il\theta} \\ = E \begin{pmatrix} f_l^{(0,1)}(kr) \\ i\tau f_{l+1}^{(0,1)}(kr) e^{i\theta} \end{pmatrix} e^{il\theta}, \end{aligned} \tag{5.31}$$

where the radial function $f_l^{(0)} = J_l$ is the Bessel's function, and $f_l^{(1)} = H_l^{(1)}$ is the Hankel's function of the first kind. Assuming $V_0 = 0$, we obtain solutions to Eq. (5.30):

$$\psi_{lE}^{(0,1)}(r, \theta) = \frac{1}{\sqrt{2\pi}} \begin{pmatrix} f_{l-1}^{(0,1)}(kr) e^{-i\theta} \\ i\tau\sqrt{2} f_l^{(0,1)}(kr) \\ -f_{l+1}^{(0,1)}(kr) e^{i\theta} \end{pmatrix} e^{il\theta}, \tag{5.32}$$

for the dispersive band $E = \tau v_g k$, and

$$\psi_{l0}^{(0,1)}(r,\theta) = \frac{1}{\sqrt{2\pi}} \begin{pmatrix} f_{l-1}^{(0,1)}(kr)e^{-i\theta} \\ 0 \\ f_{l+1}^{(0,1)}(kr)e^{i\theta} \end{pmatrix} e^{il\theta} \tag{5.33}$$

for the flat band $E = 0$. Apparently, ψ_{lE} and ψ_{l0} act as a spinor spherical wave basis for massless spin-1 excitation governed by Hamiltonian (5.20). To reveal and characterize the basic scattering features/mechanisms in a massless pseudospin-1 Dirac cone system, we turn on the circularly symmetric scattering potential $V(r) = V_0\Theta(R - r)$ and launch an incident plane spinor wave of a massless spin-1 particle outside the scattering region ($r > R$). Without loss of generality, we assume that the incident wave propagating along the x axis with a finite incident energy $|E| > 0$ is explicitly given by

$$\psi_{k,\tau}^{I}(r,\theta) = \frac{1}{2} \begin{pmatrix} 1 \\ \sqrt{2}\tau \\ 1 \end{pmatrix} e^{ikr\cos\theta}. \tag{5.34}$$

Making use of the Jacobi-Anger identity

$$e^{iz\cos\theta} \equiv \sum_{l=-\infty}^{\infty} i^l J_l(z) e^{il\theta},$$

we can rewrite the incident wave in the spinor spherical wave basis as

$$\begin{aligned} \psi_{k,\tau}^{I}(r,\theta) &= \frac{1}{2}\sum_l i^{l-1} \begin{pmatrix} J_{l-1}e^{i(l-1)\theta} \\ i\tau\sqrt{2}J_l e^{il\theta} \\ -J_{l+1}e^{i(l+1)\theta} \end{pmatrix} \\ &= \sqrt{\frac{\pi}{2}} \sum_{l=-\infty}^{\infty} i^{l-1}\psi_{lE}^{(0)}(r,\theta). \end{aligned} \tag{5.35}$$

Since the total (pseudo-)angular momentum is conserved during scattering, the reflected wave can be written as ($r > R$)

$$\psi^R_{k,\tau}(r,\theta) = \sqrt{\frac{\pi}{2}} \sum_{l=-\infty}^{\infty} i^{l-1} A_l \psi^{(1)}_{lE}(r,\theta). \tag{5.36}$$

Similarly, we define the transmitted wave inside the scattering region ($r < R$) as

$$\psi^T_{q,\tau'}(r,\theta) = \sqrt{\frac{\pi}{2}} \sum_{l=-\infty}^{\infty} i^{l-1} B_l \psi^{(0)}_{lE'}(r,\theta), \tag{5.37}$$

where $q = |E - V_0|/v_g$ and $E' = E - V_0 = \tau' v_g q$. The total wavefunction outside the scattering region ($r > R$) is given by

$$\Psi_>(r,\theta) = \psi^I_{k,\tau}(r,\theta) + \psi^R_{k,\tau}(r,\theta) = [\psi_1^>, \psi_2^>, \psi_3^>]^T, \tag{5.38}$$

while the wavefunction inside the scattering region ($r < R$) is

$$\Psi_<(r,\theta) = \psi^T_{q,\tau'}(r,\theta) = [\psi_1^<, \psi_2^<, \psi_3^<]^T. \tag{5.39}$$

In order to determine the reflection and transmission coefficients, A_l and B_l, respectively, we need the exact boundary conditions (BCs) imposed on the total wave functions at the scattering interface ($r = R$).

Boundary conditions. Recalling the commutation relation $[\hat{J}_z, \hat{H}] = 0$ (i.e., conservation of the total angular momentum), we define the following wavefunction

$$\Psi(r,\theta) = [\psi_1, \psi_2, \psi_3]^T = \begin{pmatrix} \mathcal{R}_1(r) e^{-i\theta} \\ \mathcal{R}_2(r) \\ \mathcal{R}_3(r) e^{i\theta} \end{pmatrix} e^{il\theta}, \tag{5.40}$$

which satisfies

$$\hat{H}\Psi = E\Psi. \tag{5.41}$$

Substituting Eq. (6.26) into Eq. (6.27) and eliminating the angular components, we obtain the following one-dimensional, first-order ordinary differential equation for the radial component of the wavefunction:

$$\begin{aligned} -i\frac{v_g}{\sqrt{2}}&\begin{pmatrix} 0 & \frac{d}{dr}+\frac{l}{r} & 0 \\ \frac{d}{dr}-\frac{l-1}{r} & 0 & \frac{d}{dr}+\frac{l+1}{r} \\ 0 & \frac{d}{dr}-\frac{l}{r} & 0 \end{pmatrix}\begin{pmatrix} \mathcal{R}_1(r) \\ \mathcal{R}_2(r) \\ \mathcal{R}_3(r) \end{pmatrix} \\ &= [E-V(r)]\begin{pmatrix} \mathcal{R}_1(r) \\ \mathcal{R}_2(r) \\ \mathcal{R}_3(r) \end{pmatrix}. \end{aligned} \tag{5.42}$$

Directly integrating the radial equation over a small interval $r \in [R-\eta, R+\eta]$ defined about the interface at $r = R$ and taking the limit $\eta \to 0$, we obtain

$$\begin{aligned} \mathcal{R}_2(R-\eta) &= \mathcal{R}_2(R+\eta), \\ \mathcal{R}_1(R-\eta)+\mathcal{R}_3(R-\eta) &= \mathcal{R}_1(R+\eta)+\mathcal{R}_3(R+\eta), \end{aligned} \tag{5.43}$$

provided that the potential $V(r)$ and the radial wavefunction components $\mathcal{R}_{1,2,3}(r)$ are all finite. Reformulating the continuity conditions in terms of the corresponding wavefunctions, we obtain the boundary conditions for scattering of massless pseudospin-1 wave as

$$\begin{aligned} \psi_2^<(R,\theta) &= \psi_2^>(R,\theta), \\ \psi_1^<(R,\theta)e^{i\theta}+\psi_3^<(R,\theta)e^{-i\theta} &= \psi_1^>(R,\theta)e^{i\theta}+\psi_3^>(R,\theta)e^{-i\theta}. \end{aligned} \tag{5.44}$$

It follows from Eq. (6.30) that in general there is a discontinuity in the spinor components ψ_1 and ψ_3.

To see the physical meaning underlying the boundary conditions, we calculate the associated local current density in a given state $\Psi = [\psi_1, \psi_2, \psi_3]^T$, which in the polar coordinates reads

$$\begin{cases} j_r = v_g\Psi^\dagger \boldsymbol{S}\cdot\hat{e}_r\Psi = \sqrt{2}v_g\Re\Big[\psi_2^*\left(\psi_1 e^{i\theta}+\psi_3 e^{-i\theta}\right)\Big], \\ j_\theta = v_g\Psi^\dagger \boldsymbol{S}\cdot\hat{e}_\theta\Psi = -\sqrt{2}v_g\Im\Big[\psi_2^*\left(\psi_1 e^{i\theta}-\psi_3 e^{-i\theta}\right)\Big], \end{cases} \tag{5.45}$$

where $\hat{e}_r = (\cos\theta, \sin\theta)$ and $\hat{e}_\theta = (-\sin\theta, \cos\theta)$. We conclude from Eq. (5.45) that the boundary conditions in Eq. (6.30) imply conservation/continuity of the radial (normal) current density j_r across the boundary, but the angular (tangent) current density j_θ needs not to be continuous across the boundary in general. In addition, with respect to the probability density $\rho = |\psi_1|^2 + |\psi_2|^2 + |\psi_3|^2$, we infer from the boundary conditions the following two features: (1) $\rho_< \neq \rho_>$ in general (2) a larger probability density difference $\Delta\rho = \rho_< - \rho_>$ will occur if there is a prominent imbalance in the wavefunction components between ψ_1 and ψ_3 across the boundary. For the closed scattering boundary studied in this paper, we have $\rho_< = |\mathcal{R}_1^<|^2 + |\mathcal{R}_2^<|^2 + |\mathcal{R}_3^<|^2$ and $\rho_> = |\mathcal{R}_1^>|^2 + |\mathcal{R}_2^>|^2 + |\mathcal{R}_3^>|^2$. Making use of the boundary conditions in Eq. (6.29), we obtain

$$\Delta\rho = \left(|\mathcal{R}_1^<|^2 + |\mathcal{R}_3^<|^2\right) - \left(|\mathcal{R}_1^>|^2 + |\mathcal{R}_3^>|^2\right), \tag{5.46}$$

with the constraint $\mathcal{R}_1^< + \mathcal{R}_3^< = \mathcal{R}_1^> + \mathcal{R}_3^> \equiv 2\overline{\mathcal{R}}$. Defining δ as the (radial) wavefunction component imbalance strength and then substituting

$$\mathcal{R}_1^< = \overline{\mathcal{R}} - \delta_<, \mathcal{R}_3^< = \overline{\mathcal{R}} + \delta_<; \mathcal{R}_1^> = \overline{\mathcal{R}} - \delta_>, \mathcal{R}_3^> = \overline{\mathcal{R}} + \delta_>$$

into Eq. (5.46), we obtain

$$\Delta\rho = 2\left(\delta_<^2 - \delta_>^2\right). \tag{5.47}$$

As a result, we see that there is a remarkable increase in the probability density, $\Delta\rho \sim 2\delta_<^2$, from the outer to the interior of the scattering boundary if the scattering potential redistributes the wavefunction components such that $|\delta_<| \gg |\delta_>| \sim 0$, suggesting the emergence of a strong boundary confinement/trapping phenomenon.

Imposing the boundary conditions on the total wavefunctions on both sides of the scattering

region as in Eqs. (5.38) and (5.39), we get

$$\begin{cases} B_l J_l(qR) = \tau\tau' \left[J_l(kR) + A_l H_l^{(1)}(kR) \right], \\ B_l X_l^{(0)}(qR) = X_l^{(0)}(kR) + A_l X_l^{(1)}(kR), \end{cases} \tag{5.48}$$

where

$$X_l^{(0,1)} = f_{l-1}^{(0,1)} - f_{l+1}^{(0,1)}.$$

Solving Eq. (6.33), we obtain the reflection and transmission coefficients, respectively, as

$$A_l = -\frac{J_l(qR)X_l^{(0)}(kR) - \tau\tau' X_l^{(0)}(qR)J_l(kR)}{J_l(qR)X_l^{(1)}(kR) - \tau\tau' X_l^{(0)}(qR)H_l^{(1)}(kR)}, \tag{5.49}$$

$$B_l = \frac{H_l^{(1)}(kR)X_l^{(0)}(kR) - X_l^{(1)}(kR)J_l(kR)}{H_l^{(1)}(kR)X_l^{(0)}(qR) - \tau\tau' X_l^{(1)}(kR)J_l(qR)}. \tag{5.50}$$

The θ-independent expressions of A_l and B_l are consistent with the rotational symmetry of the system. Using the basic relations $J_{-l} = (-)^l J_l$ and $H_{-l}^{(1)} = (-)^l H_l^{(1)}$, we have $A_{-l} = A_l$ and $B_{-l} = B_l$. Once A_l and B_l have been obtained, the resulting probability density $\rho = \Psi^\dagger\Psi$ and the local current density $\boldsymbol{j} = v_g \Psi^\dagger \boldsymbol{S} \Psi$ can be calculated.

Scattering efficiency. To quantify the scattering dynamics of massless pseudospin-1 particle, we use the scattering efficiency in terms of the scattering cross section as $Q = \sigma/(2R)$. In general, the various scattering cross sections can be calculated using the far field radial reflected current. For example, for the incident wave given in Eq. (5.34), we have $\sigma = 1/(\tau v_g)\int_{-\pi}^{\pi} j_\infty^{\text{ref}} r d\theta$ with $j_\infty^{\text{ref}} \equiv \lim_{r\to\infty} j_r^{\text{ref}}(\theta)$ being the far-field radial reflected current. We have

$$j_r^{\text{ref}}(\theta) = \frac{\tau v_g}{2} \Re \left\{ \sum_{l,m} i^{m-l-1} A_l^* A_m H_l^{(2)}(kr) \left[H_{m-1}^{(1)}(kr) - H_{m+1}^{(1)}(kr) \right] e^{i(m-l)\theta} \right\}. \tag{5.51}$$

With the asymptotic expressions of the Hankel functions $H_l^{(1,2)}(kr) \sim \sqrt{[2/(\pi kr)]} e^{\pm i(kr - l\frac{\pi}{2} - \frac{\pi}{4})}$ for $kr \gg 1$, we have

$$j_\infty^{\text{ref}} \sim \frac{2\tau v_g}{\pi kr} \Re \left[\sum_{l,m} A_l^* A_m e^{i(m-l)\theta} \right], \tag{5.52}$$

and finally arrive at

$$\sigma = \frac{4}{k} \sum_{l=-\infty} |A_l|^2, \tag{5.53}$$

and

$$Q = \frac{2}{kR} \sum_{l=-\infty}^{\infty} |A_l|^2 = \frac{2}{kR} \left(|A_0|^2 + 2 \sum_{n=1}^{\infty} |A_n|^2 \right). \tag{5.54}$$

Far-field behavior: general analysis. Far away from the scattering center, i.e., $r \gg R$, for unit incident density, the spinor wavefunction can be written as

$$\Psi_>(r,\theta) \approx \frac{1}{2} \begin{pmatrix} 1 \\ \sqrt{2}\tau \\ 1 \end{pmatrix} e^{ikr\cos\theta} + \frac{1}{2} \begin{pmatrix} e^{-i\theta} \\ \sqrt{2}\tau \\ e^{i\theta} \end{pmatrix} \frac{f(\theta)}{\sqrt{r}} e^{ikr}, \tag{5.55}$$

where $f(\theta)$ denotes the 2D far-field scattering amplitude in the direction defined by angle θ with the x axis. The differential and the total cross sections are given, respectively, by

$$\frac{\mathrm{d}\sigma}{\mathrm{d}\theta} = |f(\theta)|^2, \tag{5.56}$$

and

$$\sigma = \int_0^{2\pi} |f(\theta)|^2 \mathrm{d}\theta. \tag{5.57}$$

In addition, we define the transport or momentum-relaxation cross section as

$$\sigma_{\mathrm{tr}} = \int_0^{2\pi} \mathrm{d}\theta |f(\theta)|^2 (1 - \cos\theta). \tag{5.58}$$

The three types of cross sections are experimentally measurable and can be used to quantitatively characterize the basic scattering and transport physics for pseudospin-1 Dirac cone systems. For example, consider such a system with randomly distributed identical scatterers of low concentration, i.e., $n_c \ll 1/R^2$, the conductivity in units of the conductance quantum G_0 can be expressed as

$$\frac{G}{G_0} = \frac{k}{n_c \sigma_{\mathrm{tr}}} = v_g k \tau_{\mathrm{tr}}, \tag{5.59}$$

where the sample size is assumed to be larger than the mean-free path $L = v_g\tau_{\text{tr}}$ with τ_{tr} being the transport mean free time. The elastic scattering time (the quantum lifetime) τ_e can be determined from the total cross section through

$$\frac{1}{\tau_e} = n_c v_g \sigma. \tag{5.60}$$

The ratio of the two characteristic times defines the following pertinent dimensionless parameter

$$\xi = \frac{\tau_{\text{tr}}}{\tau_e} = \frac{\sigma}{\sigma_{\text{tr}}} \equiv \frac{\oint \mathrm{d}\theta |f(\theta)|^2}{\oint \mathrm{d}\theta |f(\theta)|^2 (1-\cos\theta)}, \tag{5.61}$$

leading to insights into the type and the spatial structure of the impurities presented in the sample. In particular, long-range impurities have a large value of ξ, while a small value implies that the impurities are short-ranged or have sharp boundaries. Equation (5.61) can be used to measure the degree of angular anisotropy of the scattering process. In fact, a recent work [187] demonstrated that there is a general constant $\xi \approx 2$ characterizing the anisotropic feature of low-energy scattering for massless pseudospin-$1/2$ wave in the presence of short-range scatterers, while the spin-orbit interactions that make the quasiparticles massive can dramatically change this scenario, effectively leading to an isotropic ratio of $\xi \approx 1$ - a typical signature of scattering of massive particles at low energies. More recently, the angular scattering feature for a general α-T_3 model was studied [192], and an explicit relation between ξ and the underlying Berry phase Φ_B was obtained with the finding that massless pseudospin-1 wave (i.e., for $\Phi_B = 0$) possesses the much larger ratio of $\xi = 3$. These results imply that scattering of massless pseudospin-1 wave should be much more anisotropic than the massless pseudospin-$1/2$ wave, due to super-Klein tunneling. However, we find that this may not be true for massless pseudospin-1 wave in general. In contrast, the underlying low-energy scattering displays a remarkable isotropic character (i.e., $\xi \approx 1$) even without any symmetry breaking affecting the massless nature of the quasiparticle.

From the exact expression of $\Psi_>$ [Eq. (5.38)], we obtain the scattering amplitude in terms of the reflection coefficients A_l as

$$f(\theta) = e^{-i\frac{\pi}{4}}\sqrt{\frac{2}{\pi k}}\sum_{l=-\infty}^{\infty} A_l e^{il\theta} = \frac{e^{-i\pi/4}}{\sqrt{2\pi k}}\sum_{l=-\infty}^{\infty}(S_l - 1)e^{il\theta}, \tag{5.62}$$

where

$$S_l \equiv 1+2A_l = -\frac{J_l(qR)\left[H_{l-1}^{(2)}(kR) - H_{l+1}^{(2)}(kR)\right] - \tau\tau'\left[J_{l-1}(qR) - J_{l+1}(qR)\right]H_l^{(2)}(kR)}{J_l(qR)\left[H_{l-1}^{(1)}(kR) - H_{l+1}^{(1)}(kR)\right] - \tau\tau'\left[J_{l-1}(qR) - J_{l+1}(qR)\right]H_l^{(1)}(kR)} = e^{2i\delta_l}, \tag{5.63}$$

with δ_l denoting the scattering phase shift associated with angular momentum l. Substituting the expression of $f(\theta)$ into Eqs. (5.56)-(5.58), we obtain the differential cross section as

$$\frac{\mathrm{d}\sigma}{\mathrm{d}\theta} = \frac{1}{2\pi k}\left|\sum_l (S_l - 1)e^{il\theta}\right|^2. \tag{5.64}$$

Similarly, the other two cross sections are given by

$$\sigma = \frac{1}{k}\sum_l |S_l - 1|^2 = \frac{4}{k}\sum_l \sin^2\delta_l, \tag{5.65a}$$

$$\sigma_{\text{tr}} = \sigma - \frac{1}{k}\sum_l \Re\big[(S_l - 1)(S_{l+1}^* - 1)\big], \tag{5.65b}$$

$$= \frac{2}{k}\sum_l \sin^2(\delta_{l+1} - \delta_l). \tag{5.65c}$$

With the definition of $f(\theta)$ [Eq. (5.62)], the underlying optical theorem can be expressed as

$$\sigma = \sqrt{\frac{8\pi}{k}}\Im\Big[e^{-i\frac{\pi}{4}}f(0)\Big], \tag{5.66}$$

where $\Im\cdot$ denotes the imaginary part. We finally obtain the following formula for the characteristic ratio:

$$\xi = \frac{2\sum_l \sin^2\delta_l}{\sum_l \sin^2(\delta_{l+1} - \delta_l)}. \tag{5.67}$$

5.1.4.3. Derivation of Eq. (5.12) or Eq. (5.59)

In two dimensions, it follows from the Boltzmann transport equation that the resulting current $\boldsymbol{i}$ due to an applied electric field $\boldsymbol{E}$ takes the general form given by [193]

$$\boldsymbol{i} = \frac{ge^2}{(2\pi)^2}\int d^2\boldsymbol{k}\tau_{tr}\frac{\partial f(\epsilon)}{\partial\epsilon}(\boldsymbol{v_k}\cdot\boldsymbol{E})\boldsymbol{v}_k, \tag{5.68}$$

where g denotes the degeneracies, $f(\epsilon)$ is the Fermi distribution function, and $\boldsymbol{v_k} = (1/\hbar)\nabla_{\boldsymbol{k}}\epsilon(\boldsymbol{k})$ is the band velocity. The transport relaxation time τ_{tr} can be calculated from Fermi's golden rule, which for our scattering process takes the following form in relation to the transport cross section

$$\frac{1}{\tau_{tr}} = \frac{1}{(2\pi)^2}\int d^2\boldsymbol{k'}(1-\cos\phi)W(\boldsymbol{k'},\boldsymbol{k}) = n_c v_g \sigma_{tr}, \tag{5.69}$$

where n_c is the concentration of impurities and

$$W(\boldsymbol{k'},\boldsymbol{k}) = \frac{4\pi^2\hbar v_g^2 n_c}{k}|f(\phi)|^2\delta(\epsilon_{\boldsymbol{k}} - \epsilon_{\boldsymbol{k'}}) \tag{5.70}$$

is the quantum scattering rate from state $|\boldsymbol{k}\rangle$ to final state $|\boldsymbol{k'}\rangle$ with the scattering angle $\phi = \arccos(\boldsymbol{k}\cdot\boldsymbol{k'}/k^2)$ and the scattering amplitude $f(\phi)$ at the angle ϕ. Comparing with the standard macroscopic equation (Ohm's law) $\boldsymbol{i} = \boldsymbol{G}\cdot\boldsymbol{E}$ with $\boldsymbol{G}$ being the conductivity tensor, we obtain, for $\boldsymbol{E} = E\boldsymbol{e}_x$,

$$G = G^{xx} = \frac{ge^2}{(2\pi)^2}\frac{1}{\hbar^2}\int_0^{2\pi}\cos^2\theta d\theta\int\epsilon d\epsilon\frac{\partial f(\epsilon)}{\partial\epsilon}\tau_{tr}. \tag{5.71}$$

At zero temperature, we have

$$G = \frac{ge^2}{4\pi}\frac{\epsilon}{\hbar^2}\tau_{tr} = G_0 v_g k\tau_{tr} = G_0\frac{k}{n_c\sigma_{tr}}, \tag{5.72}$$

where $g = 4$ is assumed (accounting for spin and valley) and $G_0 = 2e^2/h$ is the conductance quantum or, equivalently, the quantized unit of conductance.

5.2. Superscattering

5.2.1. Background

In wave scattering, a conventional and well accepted notion is that weak scatterers lead to weak scattering. This can be understood by resorting to the Born approximation. In particular, consider the simple two-dimensional setting where particles are scattered from a circular potential of height V_0 and radius R. In the low energy (long wavelength) regime $kR < 1$ (with k being the wavevector), the Born approximation holds for weak scattering potential: $(m/\hbar^2)|V_0|R^2 \ll 1$. Likewise, in the high energy (short wavelength) regime characterized by $kR > 1$, the Born approximation still holds in the weak scattering regime: $(m/\hbar^2)|V_0|R^2 \ll kR$. In general, whether scattering is weak or strong can be quantified by the scattering cross section. For scalar waves governed by the Schrödinger equation, in the Born regime the scattering cross section can be expressed as polynomial functions of the effective potential strength and size [194]. For spinor waves governed by the Dirac equation (e.g., scattering in a graphene system), the two-dimensional transport cross section is given by [182] $\Sigma_{tr}/R \simeq (\pi^2/4)(V_0R)^2(kR)$ (under $\hbar v_F = 1$). In light scattering from spherically dielectric, "optically soft" scatterers with relative refractive index n near unity, i.e., $kR|n-1| \ll 1$, the Born approximation manifests itself as an exact analog of the Rayleigh-Gans approximation [195], which predicts that the scattering cross section behaves as $\Sigma/(\pi R^2) \sim |n-1|^2(kR)^4$ in the small scatterer size limit $kR \ll 1$. In wave scattering, the conventional understanding is then that a weak scatterer leads to a small cross section and, consequently, to weak scattering, and this holds regardless of nature of the scattering particle/wave, i.e., vector, scalar or spinor.

In this section, we report a counterintuitive phenomenon that defies the conventional wisdom that a weak scatterer always results in weak scattering. The phenomenon occurs in scattering of

higher spinor waves, such as pseudospin-1 particles that can arise in experimental synthetic photonic systems whose energy band structure consists of a pair of Dirac cones and a flat band through the conical intersection point [149, 151, 152, 154–158]. Theoretically, pseudospin-1 waves are effectively described by the generalized Dirac-Weyl equation [153, 154, 169]: $H_0\Psi = \boldsymbol{S}\cdot\boldsymbol{k}\Psi = E\Psi$ with $\Psi = [\Psi_1, \Psi_2, \Psi_3]^T$, $\boldsymbol{k} = (k_x, k_y)$ and $\boldsymbol{S} = (S_x, S_y)$ being the vector of 3×3 matrices for spin-1 particles. Investigating the general scattering of pseudospin-1 wave, we find the surprising and counterintuitive phenomenon that extraordinarily strong scattering, or superscattering, can emerge from arbitrarily weak scatterers at sufficiently low energies (i.e., in the deep subwavelength regime). Accompanying this phenomenon is a novel type of resonances that can persist at low energies for weak scatterers. We provide an analytic understanding of the resonance and derive formulas for the resulting cross section, with excellent agreement with results from direct numerical simulations. We also propose experimental verification schemes using photonic systems.

5.2.2. Results

We consider scattering of 2D pseudospin-1 particles from a circularly symmetric scalar potential barrier of height V_0 defined by $V(r) = V_0\Theta(R - r)$, where R is the scatterer radius and Θ denotes the Heaviside function. The band structure of pseudospin-1 particles can be illustrated using a 2D photonic lattice for transverse electromagnetic wave with the electric field along the z-axis. As demonstrated in previous works [149, 153], Dirac cones induced by accidental degeneracy can emerge at the center of the Brillouin zone for proper material parameters, about which three-component structured light wave emerges and is governed by the generalized Dirac-Weyl equation.

We consider the setting of photonic crystal to illustrate the pseudospin-1 band structure. 35(a) shows the band structure of lattices with a triangular configuration constructed by cylindrical alumina rods in air, where the rod radius is $r_0 = 0.203a$ (a is the lattice constant) and the rod dielectric

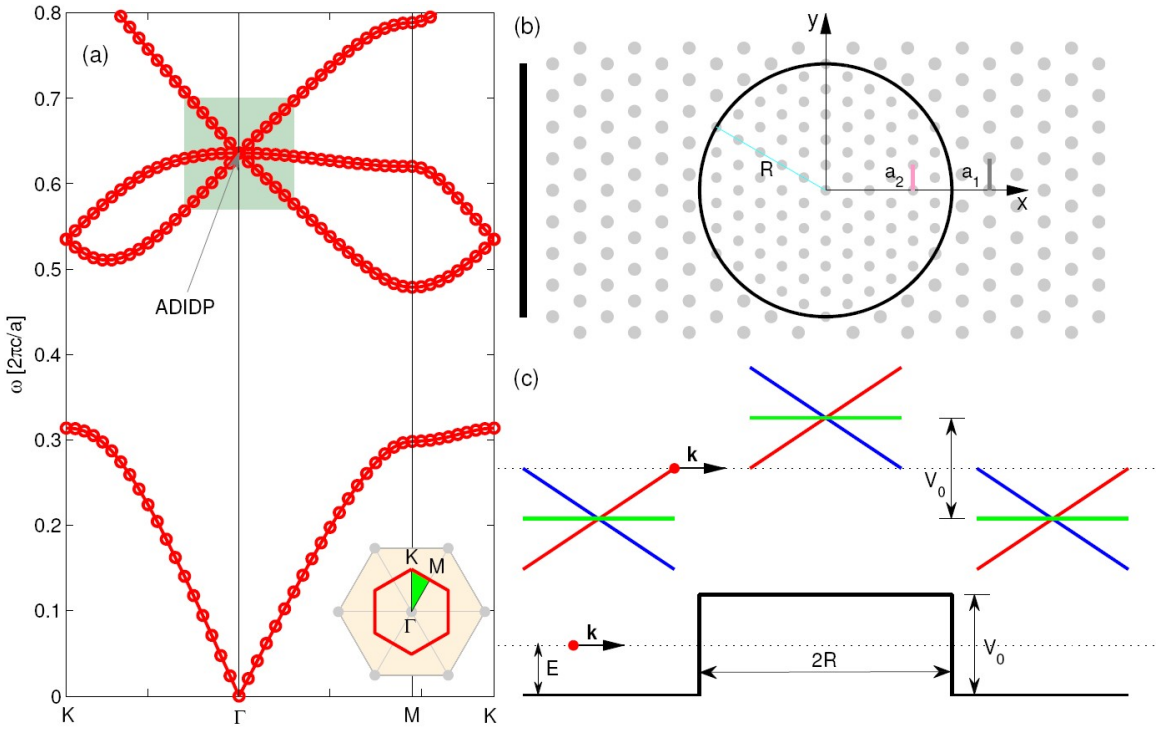

Fig. 35. Pseudospin-1 band structure and the underlying photonic lattice structure. The lattice has a triangular configuration constructed by cylindrical alumina rods in air. (a) The band structure with an accidental-degeneracy induced Dirac point at the center of the 1st Brillouin zone, (b) sketch of the physical lattice, and (c) band structures outside and inside of the scatterer. A possible experimental parameter setting is $a_1 = 17$mm, $r_1 = 0.203a_1$, $a_2 = 0.8a_1$, and $r_2 = 0.203a_2$. Dielectric constant of alumina rod is 8.8.

constant is 8.8 (Al_2O_3 : $9.3 - 11.5$). We obtain an accidental-degeneracy induced Dirac point at the center of the 1st Brillouin zone at the finite frequency of $0.6357 \cdot 2\pi \cdot c/r_0$. Following a general lattice scaling scheme of photonic gate potential [153], we obtain a sketch of the cross section of the lattice in the plane, as shown in 35(b), where the thick black bar denotes an applied exciter. For our scattering problem, the band structures outside and inside of the scatterer are shown in 35(c).

An analytic treatment of the scattering problem based on the Dirac-Weyl equation is provided in **Methods**. To demonstrate the phenomenon of superscattering, we use the transport cross section Σ_{tr} to characterize the scattering dynamics, which is defined in terms of the scattering coefficients A_l as: $\Sigma_{tr}/R = (4/x)\sum_{l=-\infty}^{\infty}\left\{|A_l|^2 - \Re\left[A_l(A_{l+1})^*\right]\right\}$, where A_l's can be obtained through the standard method of partial wave decomposition, as detailed in **Methods**. For convenience, we define $\rho \equiv V_0 R$ and $x \equiv kR$. At low energies, i.e., $x \ll 1$, scattering is dominated by the lowest angular momentum channels $l = 0, \pm 1$. To reveal the relativistic quantum nature of the scattering process, we focus on the under-barrier scattering regime, i.e., $x < \rho$, so that manifestations of phenomena such as Klein tunneling are pronounced. We define two subregimes of low energy scattering: $1 < \rho$ and $x < \rho < 1$, where the former corresponds to the case of a strong scatterer. The weak scatterer subregime, i.e., $x < \rho < 1$, is one in which the counterintuitive phenomenon of superscattering arises. Specifically, for $x < \rho < 1$, we obtain the leading coefficients as (see **Methods**) $A_0 \approx -P_0/(P_0 + iQ_0)$ and $A_{\pm 1} \approx -P_1/[P_1 + i(4 + Q_1)]$, where $P_0 = \pi x$ and $Q_0 = 2\left(x \ln\left(\gamma_E x/2\right) - J_0(\rho - x)/[J_1(\rho - x)]\right)$ with $\ln \gamma_E \approx 0.577\cdots$ being the Euler's constant and P_1, Q_1 given by relations $[P_1, Q_1] = x[P_0, Q_0]$. Using these relations, we obtain

$$\frac{\Sigma_{tr}}{R} = \frac{4P_0^2}{x(P_0^2 + Q_0^2)}\left\{1 - \frac{8Q_1}{P_1^2 + (4 + Q_1)^2}\right\}. \tag{5.73}$$

We first show that, in our scattering system, all the conventional resonances will disappear in the weak scatterer regime ($\rho < 1$). To make an argument, we examine the case of a strong scatterer:

$\rho > 1$ where the transport cross section as a function of x and ρ is given by

$$\begin{aligned} \frac{\Sigma_{tr}}{R} &\approx \frac{4}{x}\left(\frac{(\pi x)^2}{(\pi x)^2 + 4[\rho - \rho_0 + x\ln(\gamma_E x/2)]^2}\right) \\ &+ \frac{4}{x}\left(\frac{(\pi x^3)^2}{(\pi x^3)^2 + 4(\rho - \rho_1 - x)^2}\right), \end{aligned} \tag{5.74}$$

with $\rho_{0,1}$ denoting the zeros of the Bessel functions $J_{0,1}$, respectively. The resonances occur about $\rho \approx \rho_{0,1}$ for $x \ll 1$, and thus are well separated with a minimum position at $\rho \approx 2.4$. This indicates that the locations of all conventional resonances must satisfy $\rho > 2$, which are then not possible in the weak scatterer regime $\rho < 1$.

For sufficiently weak scatterer strength ($\rho \ll 1$), the prefactor in (6.41), i.e., $4P_0^2/[x(P_0^2 + Q_0^2)] \approx \pi^2 J_1^2(\rho - x)x/[J_0^2(\rho - x)] \to (\pi^2/4)(\rho - x)^2 x \ll 1$, is off-resonance. The remaining factor characterizes the emergence of a new type of (unconventional) revival resonances at $Q_1 + 4 = 0$, which are unexpected as the scatterers are sufficiently weak so, according to the conventional Born theory, no scattering resonances are possible. The resonant condition can be obtained explicitly from the constraint $Q_1 + 4 = 0 \Rightarrow xJ_0(\rho - x) = 2J_1(\rho - x)$. We obtain $\rho = 2x$ for $\rho \ll 1$. The surprising feature of revival resonance is that it persists no matter how weak the scatterer. As a result, superscattering can occur for arbitrarily weak scatterer strength. One example is shown in Fig. 36(a), where a good agreement between the theoretical prediction and numerical simulation is obtained. For comparison, results for the corresponding pseudospin-$1/2$ wave scattering system governed by the conventional massless Dirac equation are shown in Fig. 36(b), where scattering essentially diminishes for near zero scatterer strength, indicating complete absence of superscattering.

To characterize superscattering in a more quantitative manner, we obtain from Eq. (6.41) the associated resonance width as $\Gamma \sim \pi\rho^3/8$. In addition, at the resonance, we have

$$\left(\frac{\Sigma_{tr}}{R}\right)_{\max} \approx \left.\frac{\pi^2 J_1^2(x)}{J_0^2(x)}\frac{32}{\pi^2 x^4}\right|_{x=\rho/2} \simeq \frac{16}{\rho}. \tag{5.75}$$

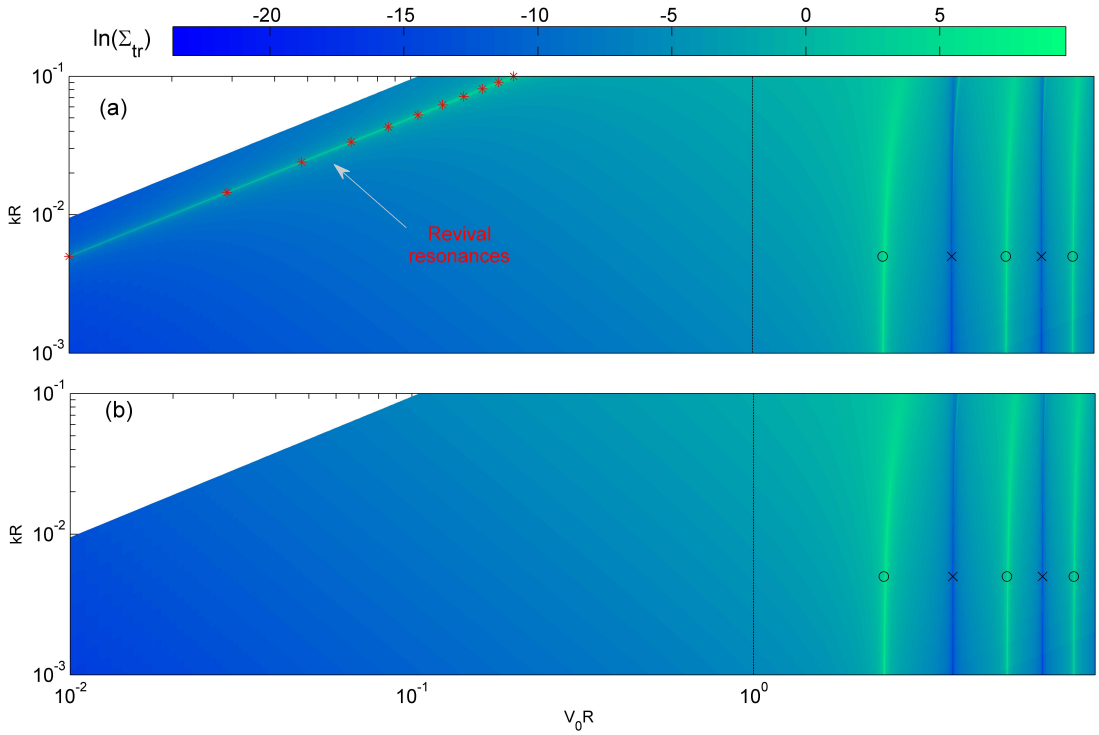

Fig. 36. Persistent revival resonances of pseudospin-1 particles from a weak circular scatterer at low energies. (a) Contour map of transport cross section (on a logarithmic scale) versus the scatterer strength $\rho = V_0 R$ and size $x = kR$ for relativistic quantum scattering of 2D massless pseudospin-1 particles. Revival resonances occur, which can lead to superscattering (see Fig. 37 below). (b) Similar plot for pseudospin-1/2 particles for comparison, where no resonances occur, implying total absence of superscattering. The scatterer is modeled as a circular step like potential $V(r) = V_0 \Theta(R - r)$, representing a finite size scalar impurity or an engineered scalar-type of scatterers. The markers correspond to the theoretical prediction, where the black circles ($\circ$) and crosses ($\times$) are from $\rho \approx \rho_{0,1}$ (for $x \ll 1$), and the red stars follow the revival resonant condition given by $\rho = 2x$ for $\rho \ll 1$.

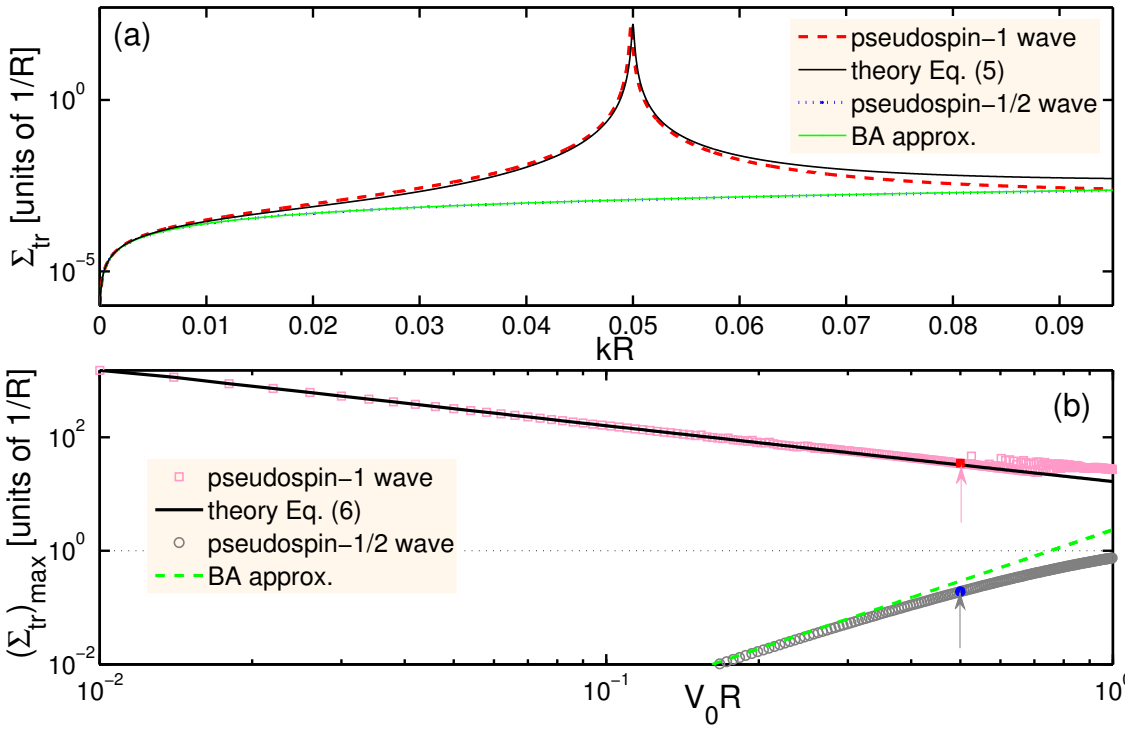

Fig. 37. Superscattering of pseudospin-1 wave. (a) Transport cross section as a function of $x \equiv kR$ for a weak scatterer of strength $\rho \equiv V_0R = 0.1$, and (b) dependence of the maximum transport cross section on V_0R.

A striking and counterintuitive consequence of (5.75) is that, the weaker the scatterer ($\rho \downarrow$), the larger the resulting maximum cross section ($(\Sigma_{tr}/R)_{\max} \uparrow$). This can be explained by noting that, due to the revival resonant scattering, an arbitrarily large cross section can be achieved for a sufficient weak scatterer with its radius R much smaller than the incident wavelength $2\pi/k$ (i.e., in deep-subwavelength regime $kR \ll 1$). In contrast, for a system hosting pseudospin-$1/2$ wave under the same condition of $x < \rho \ll 1$ where the ray optics and Born approximations apply, the maximum transport cross section is given by

$$\left(\frac{\Sigma_{tr}}{R}\right)_{\max}^{BA} \approx \frac{\pi^2}{4}\rho^3. \tag{5.76}$$

Comparing with pseudospin-$1/2$ particles, the scattering behavior revealed by Eq. (5.75) for pseudospin-1 particles is extraordinary and represents a fundamentally new phenomenon which, to our knowledge, has not been reported for any wave (especially matter wave) systems. The analytic predictions [Eqs. (5.75) and (5.76)] have been validated numerically, as shown in Fig. 37.

Further insights into superscattering can be obtained by examining the underlying wavefunction patterns, as shown in Fig. 38. In particular, Figs. 38(a,c) and 38(b,d) show the distributions of the real part of one component of the spinor wavefunction $\Re(\Psi_2)$ for pseudospin-$1/2$ and pseudospin-1 particles, respectively, where the parameters are $V_0R = 0.5$ and $kR = 0.2485$. The patterns in Figs. 38(b,d) correspond to the revival resonance indicated by the pink arrow in Fig. 37(b). We see that, even for such a weak scatterer, the incident pseudospin-1 wave of a much larger wavelength $\lambda = 2\pi/k \sim 25R$ is effectively blocked via trapping around the scatterer boundary, resulting in strong scattering. In contrast, for the conventional pseudospin-$1/2$ wave system, the weak scatterer results in only weak scattering, as shown in Figs. 38(a,c), which is anticipated from the Born theory.

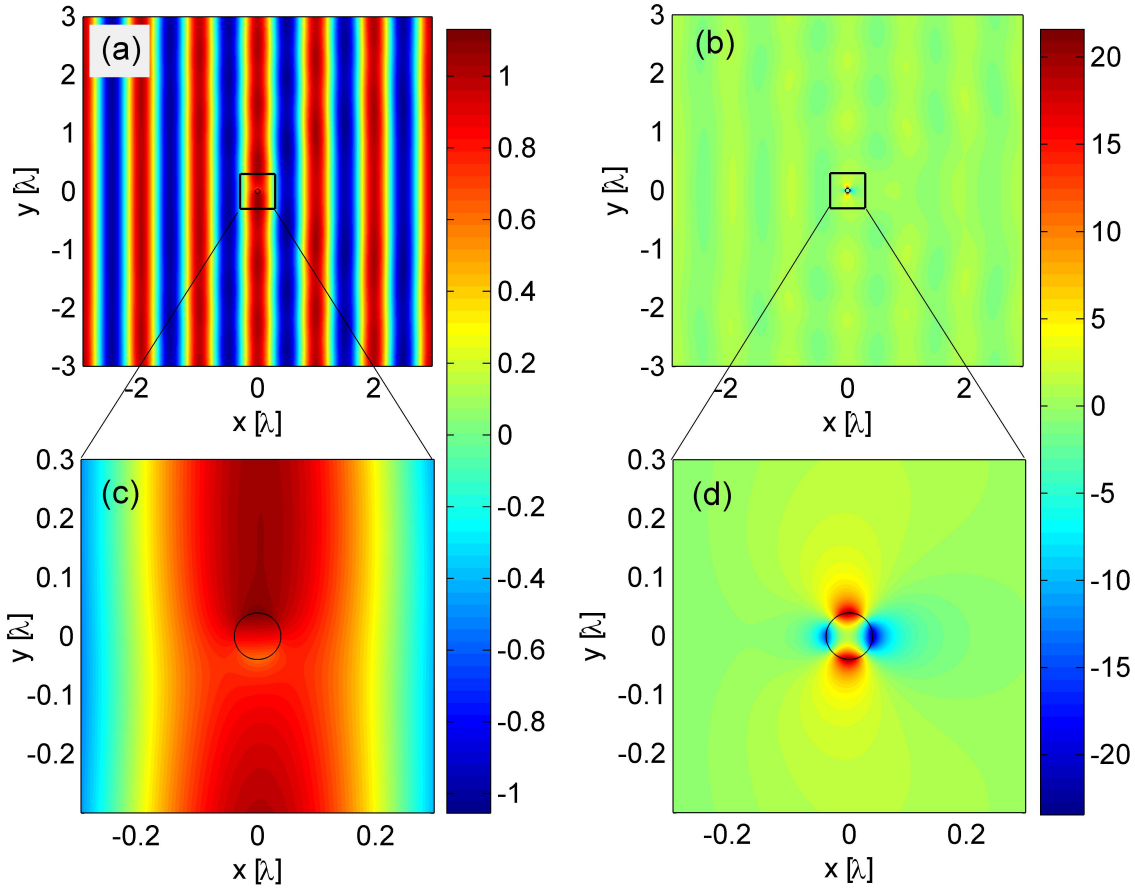

Fig. 38. Wavefunction patterns associated with superscattering. For $V_0R = 0.5$ and $kR = 0.2485$, distribution of the real part of one component of the spinor wavefunction $\Re(\Psi_2)$ for (a) pseudospin-$1/2$ and (b) pseudospin-1 wave. (c,d) Magnification of part of (a) and (b), respectively.

5.2.3. Experimental Test Proposal with Photonic Systems

It is possible to test superscattering in experimental optical systems. Recent realization of photonic Lieb lattices consisting of evanescently coupled optical waveguides implemented by femtosecond laser-writing technique [154–157] make them suitable for studying the physics of pseudospin-1 Dirac cones. Through a particular design of the refractive index profile across the lattice to realize the scattering configuration, the findings of this paper may be tested. Loading ultracold atoms into an optical Lieb lattice fabricated by interfering counter-propagating laser beams [158] provides another versatile platform to test our findings, where appropriate holographic masks can be used to implement the desired scattering potential barrier [162, 190]. Synthetic photonic crystal based 2D pseudospin-1 wave systems are also promising for feasible experimental validation. For example, it was demonstrated experimentally [149, 151, 152] and theoretically [150, 153] that a pseudospin-1 wave system can be realized in 2D dielectric photonic crystals via the principle of accidental degeneracy. Implementation of the scalar type of potential can be achieved by manipulating the length scale of the photonic crystals. From a recent work of "on-chip zero-index metamaterial" design [152] based on such a system, we note that the phenomenon of superscattering uncovered in this paper can be relevant to a novel on-chip superscatterer fabrication, which is not possible for conventional wave systems.

5.2.4. Conclusion

We uncover a superscattering phenomenon in a class of 2D wave systems that host massless pseudospin-1 particles described by the Dirac-Weyl equation, where extraordinarily strong scattering (characterized by an unusually large cross section) occurs for arbitrarily weak scatterer in the low energy regime. Physically, superscattering can be attributed to the emergence of persistent revival resonances for scatterers of weak strength, to which the cross section is inversely proportional.

These unusual features defy the prediction of the Born theory that is applicable but to conventional electronic or optical scattering systems. Superscattering of pseudospin-1 wave thus represents a fundamentally new scattering scenario, and it is possible to conduct experimental test using synthetic photonic systems.

An important issue is whether superscattering uncovered in this paper is due to the presence of a flat band that implies an infinite density of states. Our answer is negative, for the following reasons. Note that, measured from the three-band intersection point, the energy for the (dispersionless) flat band states is zero outside and V0 inside the scatterer, but for the two dispersion Dirac bands the energy is finite outside the scatterer and not equal to V0 inside. For elastic scattering considered in our work, the incident energy outside the scatterer is finite and less than V0 as well. As a result, only the states belonging to the conical dispersion bands are available both inside and outside the scatterer, and therefore are responsible for the superscattering phenomenon. Indeed, as demonstrated, superscattering is due to revival resonant scattering for states belonging to the conical dispersion bands that persist in the regime of arbitrarily weak scatterer strength. From another angle, if superscattering were due to the flat band, the phenomenon would arise in the conventional resonant scattering regime $V_0R > 1$, which has never been observed.

While the flat band itself is not directly relevant to the superscattering behavior, its presence makes the structure of the relevant states belonging to the conical bands different from those, e.g., in a two band Dirac cone system, giving rise to boundary conditions that permit discontinuities in the corresponding intensity distribution and tangent current at the interface. Interestingly, surface plasmon modes [c.f., 38(d)] are excited at the interface when revival resonant scattering occurs, which are strongly localized and can be excited for arbitrarily weak scatterer strength, leading to superscattering in the deep subwavelength regime. These modes are created from the particular

spinor structure of the photon states, which can be implemented by engineering light propagation in periodically modulated/arranged, conventional dielectric materials (e.g., alumina) rather than within the material itself. Our finding of the superscattering phenomenon is thus striking and represents a new scattering capability that goes beyond the Rayleigh-Gans limit or, equivalently, one defined by the Born approximation.

With respect to potential applications of the finding of this paper, it is worth emphasizing that the phenomenon of superscattering represents a novel way of controlling light behaviors beyond those associated with the conventional scattering scenario because, in our system [e.g., 35(b)], light is structured into three-component spinor states and behaves as relativistic spin-1 wave in the underlying photonic lattice. There have been extensive recent experimental works demonstrating that such lattice systems can actually be realized. Our theoretical prediction is based on a general setting that effectively characterizes the low-energy physics underlying the photonic lattices.

6 . GEOMETRIC VALLEY HALL EFFECT IN GAPLESS DIRAC-LIKE SYSTEMS

6.1. Background

In electronics and spintronics, information is encoded through charge and electronic spin, respectively. In addition to charge and spin, valley quantum numbers provide an alternative way to distinguish and designate quantum states, leading to the concept of valleytronics [196, 197], an area that has attracted much recent interest [198–204]. Take graphene as an example, where the crystalline structure stipulates that uncharged degrees of freedom such as isospin can emerge [205]. In the first Brillouin zone there are two nonequivalent Dirac points, $\mathbf{K}$ and $\mathbf{K}'$, which are associated with distinct momenta or valley quantum numbers. The two nonequivalent valleys act as an ideal two-state system (analogous to the isospin degree of freedom), which have a large momentum separation and are robust against external perturbations [206]. Electrons originated from the distinct valleys can be exploited for applications, e.g., in quantum information processing. Valley characteristics can also arise in other materials such as silicene and MoS_2 [201], and in graphene-inspired artificial crystals for classical waves, e.g., photonic graphene [207] that exhibits valley-polarized beams and sonic (phononic) crystals [204] in which valley vortex states can emerge.

In valleytronics, a fundamental issue is to separate the electrons with distinct valley quantum numbers, i.e., to create the so-called valley filters [196]. In graphene, due to its synthetic nature, the valley isospin can be manipulated for various valley filtering designs via mechanisms such as perfect zigzag edge confinements [196], staggered sublattice potentials [197], trigonal warping effect of the band structures [207], line defects [208], and strain engineering [209–211]. A viable mechanism to realize valley filtering is through the valley Hall effect (VHE) [197, 200, 202, 212–219], where electrons with different valley quantum numbers are separated and move in spatially distinct regions. Indeed, the Hall effect is one of the most fundamental phenomena in physics, and of particular

relevance to VHE are the anomalous Hall effect (AHE) [220] and the spin Hall effect (SHE) [221–226]. There exist two types of mechanism for AHE/SHE: intrinsic or extrinsic. The former in general has a topological origin, where the momentum space Berry curvatures, defined according to the band structure of the material, are linked, while the latter is typically caused by the skew (Mott) scattering or side-jump effect from the impurities and can be enhanced by resonant scattering [188, 227, 228]. SHE in fact opens an avenue for conversion between the electrical (charge) currents and the spin (uncharged) currents, which played a key role in spintronics for spin-current generators and detectors. Similar to SHE, associated with VHE, electrical currents can generate transverse valley currents and vice versa. In recent years there have been theoretical [197, 202, 212–215] and experimental [200, 216–219] studies of VHE. Due to the similarity between SHE and VHE, most existing theoretical proposals for the VHE are based on the same physics mechanism as for SHE [206, 229].

In this Letter, we report a singular Berry flux mediated VHE and demonstrate that it can lead to efficient valley filtering that is far stronger than that or the analogous one which can be achieved in metals or in graphene. Due to the geometric nature of the underlying mechanism, we name the phenomenon gVHE where, when the momentum-space Berry flux is fractional, charge neutral valley currents are generated from exceptional skew scattering from valley-independent, scalar type of impurities. To be concrete, we consider α-$\mathcal{T}_3$ lattices that host massless Dirac-like particles with variable singular Berry flux and show that there is a nonlinear dependence of the valley Hall angle on the Berry flux with asymmetrically resonant features. For the particular Berry flux of $\pi/2$, gVHE is considerably enhanced, which occurs near a resonance associated with skew scattering and can be electrically controlled. We develop a physical understanding of resonant skew scattering assisted valley filtering and show that gVHE is robust against thermal fluctuations and disorders, making it

promising for velleytronic applications.

6.2. Effective Hamiltonian for the α-$\mathcal{T}_3$ Model.

We consider a generalized lattice system interpolating between graphene and the so-called dice (or $\mathcal{T}_3$) lattice. The effective low-energy Hamiltonian is given by [5] $H_0 = \hbar v_F \left(\tau_3 \otimes S_x^\alpha k_x + \tau_0 \otimes S_y^\alpha k_y\right)$, where v_F is the Fermi velocity, $\boldsymbol{k} = (k_x, k_y)$ denotes the 2D wavevector measured about one of the two nonequivalent valleys (K or K') at a corner of the hexagonal Brillouin zone, and the Pauli matrices $\tau_{1,2,3}, \tau_0 = I_{2\times 2}$ act on the valley degree of freedom representing an emergent isospin. The matrices S_x^α and S_y^α (whose explicit form can be found in Supplementary Note 1) which are parameterized by $\alpha = \tan\phi$, identify the nonequivalent crystalline sublattices. The Hamiltonian H_0 acts on the six-component spinor $\Psi = (\Psi_A^\tau, \Psi_B^\tau, \Psi_C^\tau, \Psi_A^{\tau'}, \Psi_B^{\tau'}, \Psi_C^{\tau'})^T$. The energy spectrum consists of three bands: a dispersionless flat band $E_0(\boldsymbol{k}) = 0$ and two linearly dispersive bands $E_s(\boldsymbol{k}) = s\hbar v_F|\boldsymbol{k}|$ with $s = \pm 1$ being the band index, where the latter are identical to the low-energy bands of graphene that give rise to massless excitations.

Due to the $\alpha \to 1/\alpha$ (or $\phi \to \pi/2 - \phi$) duality of the model, we restrict our study to the regime $\alpha \in [0, 1]$. Note that the resulting zero-field spectrum is α-independent and features isotropic linear band crossings, while H_0 describes different low-energy excitations characterized by a α-dependent Berry phase upon widening of the band-touching point K or K'. In the related momentum space, the Berry phase underlying the nth energy band of the valley K is defined as $\Phi_n^\tau = \oint d\boldsymbol{k} \cdot \boldsymbol{\mathcal{A}}_n^\tau$ with $\boldsymbol{\mathcal{A}}_n^\tau = \langle \Psi_{n,\boldsymbol{k}}^\tau | i\nabla_{\boldsymbol{k}} | \Psi_{n,\boldsymbol{k}}^\tau \rangle$ being the Berry connection (potential). Quantitatively, we obtain $\Phi_s^\tau = \tau(1-\alpha^2)/(1+\alpha^2)\pi$ for the conical bands and and $\Phi_0^\tau = -2\tau(1-\alpha^2)/(1+\alpha^2)\pi$ for the flat band (Supplementary Note 2). Two particular cases arise for $\alpha = 0$ ($\phi = 0$) and $\alpha = 1$ ($\phi = \pi/4$). In the former case, the system corresponds to a graphene system with an extra inert flat band effectively

governed by a reduced Hamiltonian in the block diagonal form $H_0 = \hbar v_F(\tau_3 \otimes \sigma_x k_x + \tau_0 \otimes \sigma_y k_y) \oplus 0$, with the Pauli matrices $\sigma_{x,y}$ accounting for the effective sublattice degrees of freedom. In the latter case, the system is a dice lattice hosting massless pseudospin-1 quasiparticles with a vanishing Berry phase, where the matrices $S^{\alpha=1}_{x,y}$ satisfy the spin-1 algebra. From the point of view of symmetry, the two cases belong, respectively, to the classes SU(2)$\otimes$(SU(2)$\oplus$SU(1)) and SU(2)$\otimes$SO(3). In the intermediate regime $0 < \alpha < 1$, the matrices $S^{\alpha}_{x,y}$ in H_0 do not obey the algebra of angular momentum, nor any other closed algebra. As such, with more than a single pseudospin operator in general, H_0 cannot be reduced to any known case of relativistic particles (spin-1 or spin-$1/2$) but is an admixture (hybrid) of them with a non-π fractional Berry phase. Remarkably, the Berry phases associated with the two nonequivalent valleys are different except for the particular cases of $\alpha = 0, 1$. In addition, we note that the Berry curvature $\Omega^{\tau}_{\boldsymbol{k}} = \nabla_{\boldsymbol{k}} \times \boldsymbol{\mathcal{A}}^{\tau}_{\boldsymbol{k}}$ (acting as a "magnetic" field in the momentum space) is always zero away from the gapless point K or K' and hence makes the typical Hall effect of intrinsic type ruled out there.

6.3. Semiclassical Charge and Valley Transport.

To investigate the charge and valley transport properties, we analyze the semiclassical Boltzmann transport equation (BTE) which, in the presence of an applied uniform electric field $\boldsymbol{\mathcal{E}} = \mathcal{E}\boldsymbol{e}_x$, takes the form [193]

$$-e\boldsymbol{\mathcal{E}} \cdot \boldsymbol{v}_{\boldsymbol{k}} \frac{\partial n^0}{\partial E} = \sum_{\boldsymbol{k}',\tau'} \left[n_{\tau}(\boldsymbol{k}) - n_{\tau'}(\boldsymbol{k}') \right] W_{\tau'\tau}(\boldsymbol{k}', \boldsymbol{k}), \tag{6.1}$$

where $-e < 0$ is the electron charge, $\boldsymbol{v}_{\boldsymbol{k}} = (1/\hbar)\boldsymbol{\nabla}_{\boldsymbol{k}} E_{\boldsymbol{k}}$ is the band velocity, $n^0 = n^0(E) = 1/[\exp{(E-\mu)/k_B T} + 1]$ denotes the equilibrium Fermi-Dirac distribution, and $n_{\tau}(\boldsymbol{k})$ is the distribution function for carriers with momentum $\boldsymbol{k}$ and valley index τ. Impurities distributed at random positions of scattering centers $\boldsymbol{r}_i$ with a dilute concentration (areal density) n_{imp} are described by the disordered potential $V(\boldsymbol{r}) = \sum_i V(\boldsymbol{r} - \boldsymbol{r}_i)$, and the quantum scattering rate off the potential

from the state $|\boldsymbol{k},\tau\rangle$ to the state $|\boldsymbol{k}',\tau'\rangle$ is $W_{\tau'\tau}(\boldsymbol{k}',\boldsymbol{k}) = (4\pi^2\hbar v_g^2 n_{imp}/k)|f_{\tau\tau'}(\theta)|^2\delta(E_{\boldsymbol{k}} - E_{\boldsymbol{k}'})$, where $f_{\tau\tau'}(\theta)$ is the scattering amplitude at the angle $\theta = \arccos(\boldsymbol{k}\cdot\boldsymbol{k}'/k^2)$. Skew scattering means an asymmetry in the scattering amplitude $f_{\tau\tau'}(\theta) \neq f_{\tau\tau'}(-\theta)$, which leads to $W_{\tau\tau'}(\boldsymbol{k}',\boldsymbol{k}) \neq W_{\tau\tau'}(\boldsymbol{k},\boldsymbol{k}')$. Defining $\delta n_\tau(\boldsymbol{k}) = n_\tau(\boldsymbol{k}) - n^0$ as the deviation of the valley-dependent distribution function from its equilibrium value, in the linear response regime we impose the following ansatz for isotropic Fermi surfaces in the conduction (valence) band $s = 1$ ($s = -1$): $\delta n_\tau(\boldsymbol{k}) = s v_F\left[A_\tau\cos\varphi(\boldsymbol{k}) + B_\tau\sin\varphi(\boldsymbol{k})\right]$, where $\varphi(\boldsymbol{k})$ is the angle that the momentum vector $\boldsymbol{k}$ makes with the direction of the external electric field $\boldsymbol{\mathcal{E}}$. Substituting this ansatz into Eq. (6.1) and setting $\varphi(\boldsymbol{k}) = 0$ ($\varphi(\boldsymbol{k}) = \pi/2$) for the longitudinal (transverse) response, we obtain a closed form solution of the linearized BTE. The current due to the external driving electric field can be calculated explicitly as $\boldsymbol{j}_\tau = -egS/(2\pi)^2\int d^2\boldsymbol{k}'\delta n_\tau(\boldsymbol{k})\boldsymbol{v}_{\boldsymbol{k}}$ with $g = 2$ and S being the spin degeneracy and the given sample area, respectively. The steady state charge (longitudinal) and valley Hall (transverse) currents are then given by $j_x = \sum_\tau \boldsymbol{j}_\tau\cdot\boldsymbol{e}_x \equiv \sigma^{xx}|\boldsymbol{\mathcal{E}}|$ and $j_{vH} = \sum_\tau \tau\boldsymbol{j}_\tau\cdot\boldsymbol{e}_y \equiv \sigma_{vH}^{yx}|\boldsymbol{\mathcal{E}}|$, where the valley Hall conductivity

$$\sigma_{vH}^{yx} = -e^2\frac{g}{2\hbar}\sum_{\tau=\pm}\int dE|E|\frac{\partial n^0}{\partial E}\frac{\tau\xi_{sk}^\tau}{1+(\xi_{sk}^\tau/\xi_{tr}^\tau)^2}, \tag{6.2}$$

and the longitudinal conductivity

$$\sigma^{xx} = -e^2\frac{g}{2\hbar}\sum_{\tau=\pm}\int dE|E|\frac{\partial n^0}{\partial E}\frac{\xi_{tr}^\tau}{1+(\xi_{tr}^\tau/\xi_{sk}^\tau)^2}, \tag{6.3}$$

respectively, with the usual transport (longitudinal) relaxation time ξ_{tr}^τ and the skew (transverse) relaxation time ξ_{sk}^τ determined by $1/\xi_{tr}^\tau = (2\pi)^{-2}\int d^2\boldsymbol{k}'(1-\cos\theta)W_{\tau\tau}(\boldsymbol{k}',\boldsymbol{k})$ and $1/\xi_{sk}^\tau = (2\pi)^{-2}\int d^2\boldsymbol{k}'\sin\theta W_{\tau\tau}(\boldsymbol{k}',\boldsymbol{k})$, respectively. The valley Hall angle characterizing the efficiency of the charge current to valley current conversion is given by $\gamma = \sigma_{vH}^{yx}/\sigma^{xx}$, which at zero temperature reduces to the ratio $\xi_{tr}^\tau/\xi_{sk}^\tau$ and can be expressed in terms of the pertinent scattering cross sections

with respect to a single scattering event: $\gamma|_{T=0} = \Sigma^{\tau}_{sk}/\Sigma^{\tau}_{tr}$, where the skew and transport cross sections are given, respectively, by $\Sigma^{\tau}_{sk} = \int d\theta \sin\theta |f_{\tau\tau}(\theta)|^2$ and $\Sigma^{\tau}_{tr} = \int d\theta |f_{\tau\tau}(\theta)|^2(1-\cos\theta)$. From Eqs. (6.2) and (6.3), we see that valley skew scattering characterized by a finite ξ^{τ}_{sk} (or Σ^{τ}_{sk}) with opposite signs for different valleys ($\tau = \pm$) will give rise to nonzero valley Hall conductivity and hence a net transverse valley current but with vanishing charge current (i.e., long-range charge-neutral valley currents for weak intervalley scattering), as well as a modification to the standard longitudinal conductivity σ^{xx}. Such a skew scattering mechanism is more apparent from the closed form at zero temperature, i.e., $\gamma|_{T=0}$.

The impurities can be modeled as an ensemble of dilute disk scatterers of radius R with potential $V^i(\boldsymbol{r}) = \tau_0 \otimes \mathcal{I} V_0 \Theta(R - |\boldsymbol{r} - \boldsymbol{r}_i|)$. We have obtained an exact expression of the scattering amplitude $f_{\tau\tau'}(\theta)$ (Supplementary Note 3), from which a number of unusual phenomena are uncovered.

6.4. Results

6.4.1. Fractional Singular Berry Flux Defined Valley Hall Effect.

We first demonstrate the emergence of gVHE through the valley Hall angles (VHAs) originated from the non-π fractional singular Berry flux. The VHAs and hence gVHE are extrinsically induced by valley skew scattering from the scalar type of scatterers that are neither valley (isospin) nor sublattice (pseudopsin) dependent. We focus on the under-barrier scattering regime, where the conical energy dispersion is characteristic of that of massless Dirac-like excitations. From the closed form of VHA at zero temperature (i.e., $\gamma|_{T=0}$), we show its contour map versus the relative carrier energy E/V_0 and the normalized Berry flux Φ (via the convention of $\Phi \equiv \tau\Phi^{\tau}_s/\pi$) in Fig. 39(a). We see that there are finite VHAs ($\gamma \neq 0$) within the range $0 < \Phi < 1$, which corresponds to the fractional Berry flux, and $\gamma \to 0$ as $\Phi \to 0, 1$ which represent two typical limiting cases of dice lattice with massless pseudospin-1 low-energy excitations and graphene hosting massless pseudospin-$1/2$

quasiparticles, respectively. By definition, $\gamma = 0$ indicates that the Hall effect vanishes, and the larger the value of $|\gamma|$, the stronger the effect. In addition, at zero temperature, $\gamma|_{T=0}$ is effectively the transport skewness that characterizes the degree of asymmetry in the associated scattering events. As such, we obtain the case where gVHE emerges due to the fractional singular Berry flux that exceptionally permits valley skew scattering from valley independent, scalar type of scatterers. At low energies, i.e., $kR \ll 1$, for $E/V_0 \ll 1$, we obtain an analytic formula for the VHA versus the Berry flux (Supplementary Note 4):

$$\gamma(\Phi) \simeq \frac{\pi x^2 \frac{\Phi(1-\Phi)}{1+\Phi}}{(1+\eta)^2 \left[\Phi - (1-2\eta)\right]^2 + 4\eta \frac{\Phi(1-\Phi)}{1+\Phi}}, \tag{6.4}$$

where $\eta = E/V_0$ and $x = kR$. We see that the VHA exhibits a nonlinear dependence on the Berry flux and an asymmetric resonance profile. In particular, as Φ is increased from 0 to 1 monotonously, the VHA reaches a maximum at $\Phi_* \simeq (1 - 2\eta)$, followed by a decrease to zero. Asymptotic behaviors at the opposite limits of $\Phi \to 1$ and $\Phi \to 0$ derived from Eq. (6.46) are: $\gamma(\Phi) \sim (1 - \Phi)$ for $\Phi \to 1$ and $\gamma \sim \Phi$ for $\Phi \to 0$. We thus see that, for given parameters (e.g., $V_0R = 1$ and $E/V_0 = 0.1$), the resulting gVHE is induced by the fractional singular Berry flux through an asymmetric, nonlinear resonance. However, gVHE vanishes linearly as $\Phi \to 0, 1$, i.e., when π-quantized Berry phase is recovered. Relaxing the assumption of $E/V_0 \ll 1$, we obtain an estimation of the resonance positions for $E/V_0 > 1/2$ as $\Phi_* \simeq (2\eta - 1)$ [marked by the green dashed line in Fig. 39(a)].

Figure 39(b) reveals the effect of the scatterer strength V_0R on gVHE, where the averaged absolute VHA $\tilde{\gamma} \equiv \int |\gamma| dE / \int dE$ versus the Berry phase for three different values of V_0R (1, 10, 100) is shown, as indicated by the solid, dashed and dot-dashed lines, respectively. We see that, on average, weak scatterers favor phase-dependent VHAs, giving rise to pronounced gVHE, while strong scatterers do not. An intuitive picture can be obtained by resorting to

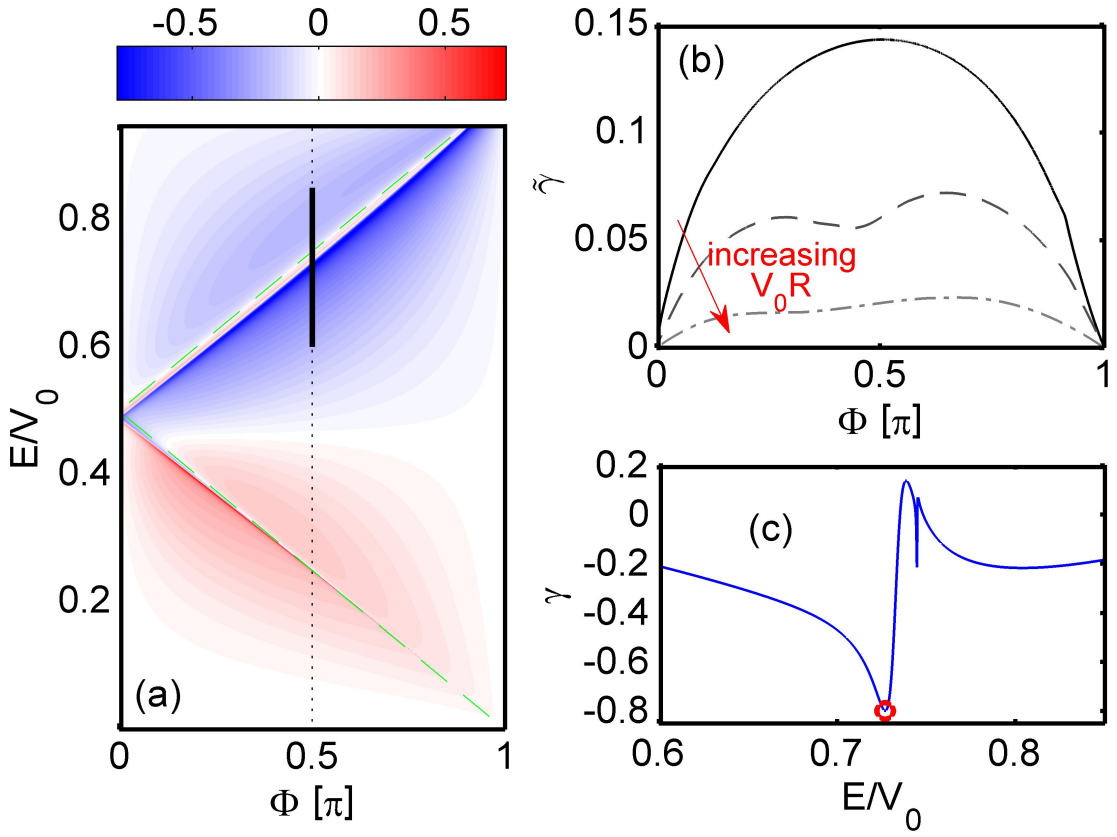

Fig. 39. Singular Berry flux defined valley Hall angle. (a) Contour map of valley Hall angle γ versus the Berry flux Φ and the relative energy E/V_0 for scatterer strength $V_0R = 1$. (b) Average valley Hall angle $\tilde{\gamma}$ over the Fermi energy versus the Berry flux for different values of the scatterer strength as represented by the thick line ($V_0R = 1$), the dashed line ($V_0R = 10$), and the dot-dashed line ($V_0R = 100$). (c) Enhancement of VHA due to resonant valley skew scattering occurring within the energy range indicated by the thick black line in (a) for $\Phi = \pi/2$ and $V_0R = 1$.

the general summation form of the skew cross section in terms of the scattering phase shift δ_l: $\Sigma^{\tau}_{sk} = 4/k \sum \sin\delta_l \sin\delta_{l+\tau} \sin(\delta_l - \delta_{l+\tau})$ where, for a given carrier energy value E/V_0, the larger V_0R, the more scattering channels with different phase shifts are excited. As a result, there are many sign changes in δ_l or $(\delta_l - \delta_{l+\tau})$, reducing significantly the summation and hence VHA. Interestingly, for a particular Berry flux, say $\Phi = 1/2$ (for $\alpha = 1/\sqrt{3}$), the VHA can be related to the massless Kane fermions observed in recent experiments (Supplementary Note 5). In particular, from Fig. 39(c), it can be seen that the VHA can be enhanced significantly due to the emergent resonant valley skew scattering in the energy domain that can be reached by controlling the Fermi energy.

6.4.2. Enhanced GVHE and Valley Filtering Through Resonant Skew Scattering.

Insights into resonant skew-scattering assisted valley filtering can be gained by investigating both the far-field and near-field behaviors in terms of the differential cross section (DCS) $d\Sigma^{\tau}/d\theta = |f_{\tau\tau}(\theta)|^2$ and the associated near-field patterns for different valleys, as illustrated in Figs. 40(a) and 40(b), respectively. There is an exact mirror symmetry with respect to the horizontal axis between the patterns associated with different valleys, which can be understood by referring to the formula for $\gamma|_{T=0}$: large VHAs imply a left-right asymmetry in the DCS and hence give rise to strong valley polarizations along the azimuthal direction, and vice versa. Demonstration using a polar plot of DCS is displayed in Fig. 40(a) with resonance parameters indicated by the red circle in Fig. 39(c). As a result, a remarkable valley filtering/polarization effect emerges together with VHA enhancement and gVHE. Furthermore, it can be seen from Fig. 40(b) that, at the given resonance, valley-contrasting spatial skew (asymmetric) trappings occur via the formation of unusual fusiform vortices around one side of the boundary. Consequently, the scatterer only blocks one of the valleys effectively at one side via valley-dependent skew trapping, makes the system an effective valley

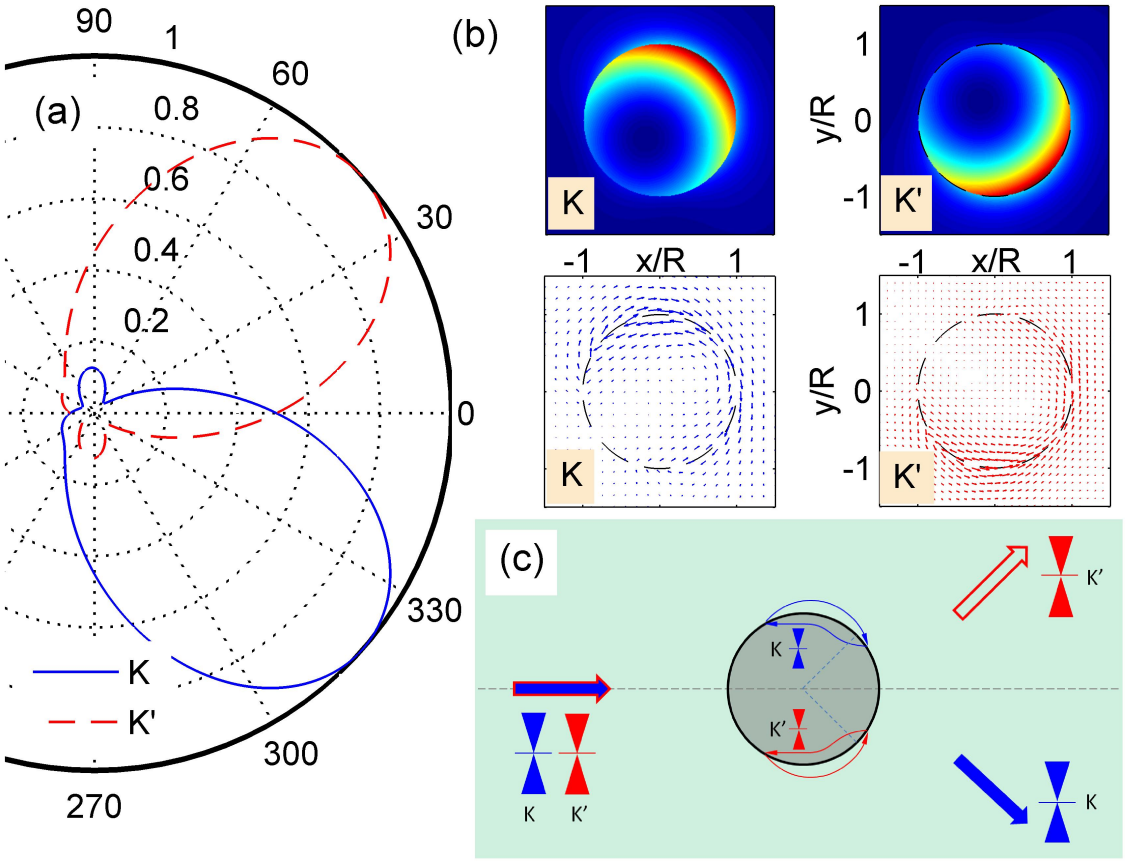

Fig. 40. Illustration of resonant skew scattering assisted valley filtering. For $\Phi = \pi/2$ with a resonance position indicated by the red circle in Fig. 39(c), (a) polar plot of normalized far-field scattering amplitude as a function of the scattering angle for different valleys: K (solid blue line) and K' (red dashed line), (b) associated near-field patterns of the local probability density belonging to different valleys (top two panels) and the corresponding current density plots (bottom ones), and (c) schematic illustration of gVHE associated with resonant valley skew scattering.

filter near the resonance. In Fig. 40(c), we sketch diagrammatically the valley filtering mechanism due to resonant skew scattering enhanced gVHE.

6.4.3. Exceptionally Large VHAs and Strong Valley Filtering.

Further analysis of the effect of scatterer strength reveals that gVHE enhancement induced by resonant skew scattering is significant for intermediate scatterer strength, say $V_0R \sim 2$, where large VHAs with the maximum absolute value $|\gamma|_{\max} \sim 0.8$ can arise, as shown in Fig. 41(a). The Hall angle values are much larger than those for metals [227, 230–233] ($|\gamma| \sim 0.01 - 0.1$) and for graphene [188, 234, 235] ($|\gamma| \sim 0.2$). This remarkable result holds in the presence of thermal fluctuations and disorder averaging, as shown in Fig. 41(b), rendering the phenomenon uncovered here promising for valleytronics applications.

6.5. Discussion

We uncover a momentum-space singular Berry flux mediated mechanism for VHE and show that it can lead to efficient electrically controllable valley filtering without hurting the carriers' high mobility, which is beyond typical ways of breaking their massless nature or deforming the underlying energy dispersion. In particular, when the Berry flux is fractional, charge neutral transverse valley currents can be generated from exceptional skew scattering from valley-independent, scalar type of impurities. We develop an analytic understanding of the phenomena of gVHE and valley filtering, for which further physical insights can be obtained by resorting to symmetry considerations (see Supplementary Note 6). We demonstrate that, respecting the carriers' high mobility simultaneously, gVHE and valley filtering are robust against thermal fluctuations and disorders, potentially opening a door to faster and more efficient valleytronics applications. While we have used α-$\mathcal{T}_3$ lattices to demonstrate our findings, we expect them to arise generally in physical systems hosting massless Dirac-like particles with variable Berry phase.

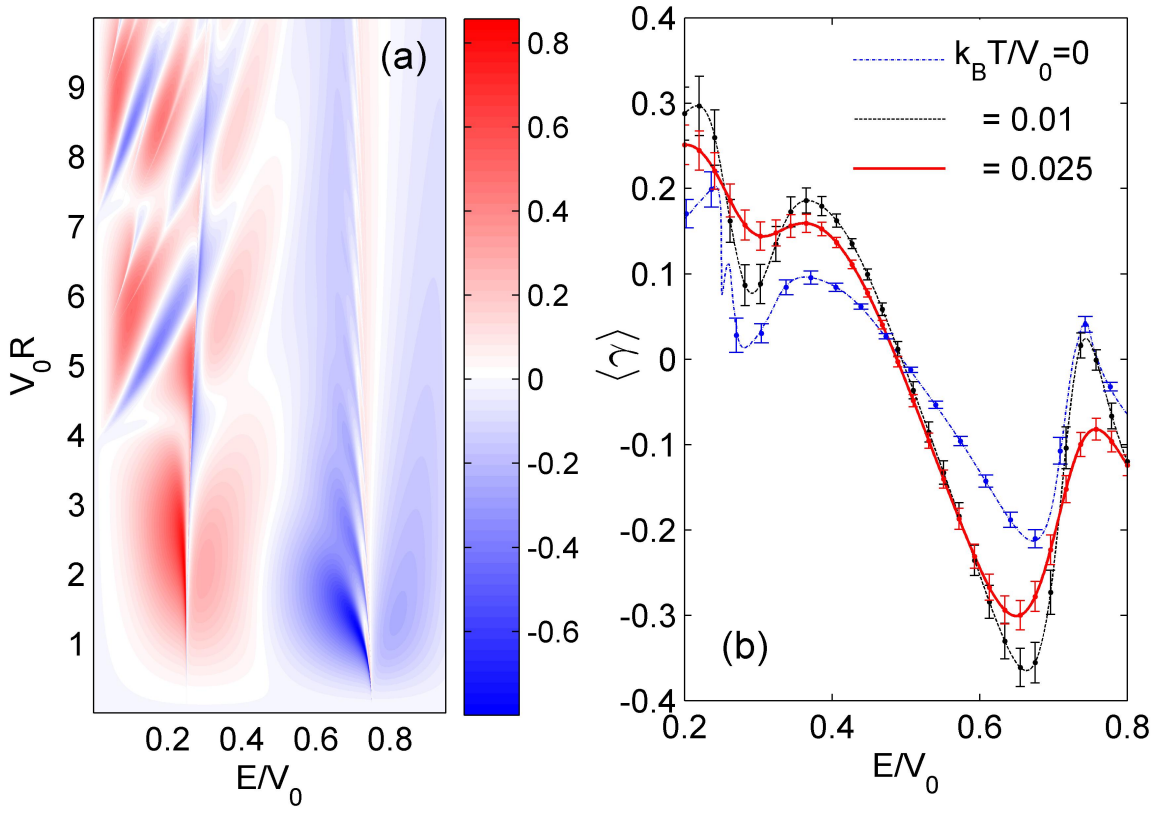

Fig. 41. Exceptionally large VHAs and effects of thermal fluctuations and disorder averaging. For $\Phi = \pi/2$, (a) contour plot of the VHA γ versus E/V_0 and the scatterer strength V_0R at zero temperature, and (b) ensemble averaged VHA over scatterers with randomly distributed strength $V_0R \in (0, 10]$ versus the reduced Fermi energy for different values of the normalized thermal temperature $k_BT/V_0 = 0, 0.01, 0.025$.

As noted in related works [236, 237] (see also Supplementary Note 5), there exists a correspondence between our model and *massless Kane fermion* (an exotic type of Dirac-like quasiparticle with the non-π fractional Berry flux) systems that can arise in 3D zinc-blende crystals, i.e., $Hg_{1-x}Cd_xTe$, at some critical doping concentration [238–240]. In particular, we have $\mathcal{H}_{Kane}(\boldsymbol{k}, k_z = 0) \equiv H_0(\alpha = 1/\sqrt{3})$. In this sense, the phenomenon of gVHE uncovered here would manifest itself as the *geometric* SHE (gSHE) in a massless Kane fermion system, which can be experimentally validated in the 3D zinc-blende crystals in the presence of spin-independent (scalar-type) cylindrical symmetric impurities (e.g., charged dislocation line defects along the [001] direction).

6.6. Supplementary Notes

6.6.1. Explicit form of matrices S_x^α and S_y^α

The matrices S_x^α and S_y^α are given by

$$S_x^\alpha = \begin{pmatrix} 0 & \cos\phi & 0 \\ \cos\phi & 0 & \sin\phi \\ 0 & \sin\phi & 0 \end{pmatrix}, \tag{6.5}$$

and

$$S_y^\alpha = \begin{pmatrix} 0 & -i\cos\phi & 0 \\ i\cos\phi & 0 & -i\sin\phi \\ 0 & i\sin\phi & 0 \end{pmatrix}, \tag{6.6}$$

which are parameterized by $\alpha = \tan\phi$. They identify the nonequivalent crystalline sublattices in the α-$\mathcal{T}_3$ lattice.

6.6.2. Berry Flux and Curvature Calculation

We follow the recent works [5, 236, 237] to carry out calculations to show that, in our α-$\mathcal{T}_3$ system, the Berry curvature and phase are not conventional in the sense that the phase can be a

fraction of π. The effective Hamiltonian in the main text is

$$H_0(\boldsymbol{k}) = \tilde{\boldsymbol{\alpha}} \cdot \boldsymbol{k}, \tag{6.7}$$

where $\boldsymbol{k} = (k_x, k_y, 0)$ and $\tilde{\boldsymbol{\alpha}} = (\tau_3 \otimes S_x^\alpha, \tau_0 \otimes S_y^\alpha, \tau_1 \otimes \tilde{S}_z)$ with $\tilde{S}_z = 0 \oplus \sigma_x$. The Hamiltonian H_0 has eigenvalues $E = n|\boldsymbol{k}|$ with $n = 0, \pm$ denoting the band index, and the associated eigenstates are given by

$$|\boldsymbol{k}, s\rangle|\tau\rangle = \frac{1}{\sqrt{2}} \begin{pmatrix} \tau \cos\phi e^{-i\tau\theta} \\ s \\ \tau \sin\phi e^{i\tau\theta} \end{pmatrix} |\tau\rangle, \tag{6.8a}$$

for $E = s|\boldsymbol{k}|$ with $s = \pm$, and

$$|\boldsymbol{k}, 0\rangle|\tau\rangle = \begin{pmatrix} \tau \sin\phi e^{-i\tau\theta} \\ 0 \\ -\tau \cos\phi e^{i\tau\theta} \end{pmatrix} |\tau\rangle, \tag{6.8b}$$

for $E = 0$, where $\tan\theta \equiv k_y/k_x$ and $\tau = \pm$ denotes the valley index. The Berry connection (field) of each band can be calculated from the definition $\boldsymbol{\mathcal{A}}^\tau_{n,\boldsymbol{k}} = \langle\tau|\langle\boldsymbol{k}, n|i\nabla_{\boldsymbol{k}}|\boldsymbol{k}, n\rangle|\tau\rangle$. We have

$$\boldsymbol{\mathcal{A}}^\tau_{0,\boldsymbol{k}} = -\tau\frac{1-\alpha^2}{1+\alpha^2}\nabla_{\boldsymbol{k}}\theta, \boldsymbol{\mathcal{A}}^\tau_{s,\boldsymbol{k}} = -\frac{1}{2}\boldsymbol{\mathcal{A}}^\tau_{0,\boldsymbol{k}}. \tag{6.9}$$

Consequently, the Berry curvature $\boldsymbol{\Omega}^\tau_{n,\boldsymbol{k}} = \nabla_{\boldsymbol{k}} \times \boldsymbol{\mathcal{A}}^\tau_{n,\boldsymbol{k}}$ is readily obtained as

$$\boldsymbol{\Omega}^\tau_{s,\boldsymbol{k}} = \frac{\tau}{2}\frac{1-\alpha^2}{1+\alpha^2}\nabla_{\boldsymbol{k}} \times \left(-\frac{k_y}{k_x^2+k_y^2}, \frac{k_x}{k_x^2+k_y^2}, 0\right) = \tau\frac{1-\alpha^2}{1+\alpha^2}\pi\delta(\boldsymbol{k})\hat{\boldsymbol{k}}_z, \tag{6.10}$$

for the conical bands and $\Omega^\tau_{0,\boldsymbol{k}} = -2\boldsymbol{\Omega}^\tau_{s,\boldsymbol{k}}$ for the flat band, while the Berry phase $\Phi^\tau_n = \oint d\boldsymbol{k} \cdot \boldsymbol{\mathcal{A}}^\tau_{n,\boldsymbol{k}}$ for any closed path $\mathcal{C}^\tau_{n,\boldsymbol{k}_d}$ encircling a degeneracy point $\boldsymbol{k}_d$ (i.e., a single valley center) in the momentum space is given by

$$\Phi^\tau_s = \tau\frac{1-\alpha^2}{1+\alpha^2}\pi, \text{ and } \Phi^\tau_0 = -2\Phi^\tau_s. \tag{6.11}$$

From Eqs. (6.10) and (6.11), we see that our α-$\mathcal{T}_3$ system possesses a vanishing Berry curvature and valley-contrasting Berry phases except for $\alpha = 0$ or 1. It should be noted that this argument holds for scalar type of perturbation assumed in our work, or more generally, any perturbation that preserves the gapless feature of the energy band.

6.6.3. Scattering Amplitude Formulas

Minimal model and partial wave expansion. As indicated in the main text, we use the following perturbed Hamiltonian

$$H = H_0 + V(\boldsymbol{r}), \tag{6.12}$$

to model the quantum scattering processes from the extrinsically controllable impurities such as randomly positioned antidots due to circularly symmetric vertical gates. The impurities are treated as an ensemble of finite-size scattering centers of radius R described by the disordered scalar potential $V(\boldsymbol{r}) = \sum_i \tau_0 \otimes \mathcal{I} V_0 \Theta(R - |\boldsymbol{r} - \boldsymbol{r}_i|)$, which are distributed at random positions $\boldsymbol{r}_i$ with V_0 being the potential height. The characteristic size R of each individual scatterer is assumed to be much larger than the lattice constant so that intervalley scattering is negligible. If the scatterers are sufficiently dilute so that multiple scattering effects can be ruled out, i.e., the density satisfies $n_{imp} \ll 1/R^2$, we can impose the single scattering-event approximation to obtain physically meaningful solutions for the far-field scattering amplitude $f_{\tau\tau'}(\theta)$ using the standard partial wave decomposition (PWD) scheme. In the following, we derive a formula for $f_{\tau\tau'}(\theta)$ for a single disk scatterer.

Far away from the scattering center (i.e., $r \gg R$), for an incoming flux along the x direction, the spinor wavefunction belonging to the valley τ with band index s takes the asymptotic form

$$|\Psi^{\gg}_{s,\tau}(\boldsymbol{r})\rangle = e^{ikx}|\boldsymbol{k}_0, s\rangle|\tau\rangle + \frac{f_{\tau\tau'}(\theta)}{\sqrt{-ir}} e^{ikr}|\boldsymbol{k}_\theta, s\rangle|\tau'\rangle, \tag{6.13}$$

where the Einstein summation convention is applied for the valley index τ', the ket $|\tau\rangle$ represents the valley state (analogous to the orientation of the isospin along the z axis), and the vector $|\boldsymbol{k}, s\rangle$ is

the spinor plane wave amplitude with wave vectors $\boldsymbol{k}_0 = (k, 0)$ and $\boldsymbol{k}_\theta = k(\cos\theta, \sin\theta)$ that define the directions of the incident and scattering waves, respectively. In our system, for the conical dispersion bands $s = \pm$, we have

$$|\boldsymbol{k}, s\rangle|\tau\rangle = \frac{1}{\sqrt{2}} \begin{pmatrix} \tau\cos\phi e^{-i\tau\theta} \\ s \\ \tau\sin\phi e^{i\tau\theta} \end{pmatrix} |\tau\rangle. \tag{6.14}$$

The current operator is defined as $\hat{\boldsymbol{J}} = (1/\hbar)\nabla_{\boldsymbol{k}} H(\boldsymbol{k}) = v_F(\tau_3 \otimes S_x^\phi, \tau_0 \otimes S_y^\phi)$. We thus obtain the scattered current as

$$J_{sc} = \frac{1}{r}\langle\tau'|\langle\boldsymbol{k}_\theta, s|f^*_{\tau\tau'}\hat{\boldsymbol{J}}\cdot\frac{\boldsymbol{k}_\theta}{k}f_{\tau\tau'}|\boldsymbol{k}_\theta, s\rangle|\tau'\rangle = \frac{\tau v_F}{r}\left[|f_{\tau\tau}(\theta)|^2 + |f_{\tau\bar{\tau}}(\theta)|^2\right], \tag{6.15}$$

while the incident current is

$$J_{in} = \langle\tau|\langle\boldsymbol{k}_0, s|\hat{\boldsymbol{J}}\cdot\boldsymbol{k}_0/k|\boldsymbol{k}_0, s\rangle|\tau\rangle = \tau v_F. \tag{6.16}$$

The differential cross section can be calculated from the scattering amplitudes $f_{\tau\tau'}(\theta)$ as

$$\frac{d\Sigma^\tau}{d\theta} = \frac{rJ_{sc}}{J_{in}} = |f_{\tau\tau}(\theta)|^2 + |f_{\tau\bar{\tau}}(\theta)|^2, \tag{6.17}$$

where $\bar{\tau} \equiv -\tau$, and $f_{\tau\bar{\tau}}(\theta)$ denotes the scattering amplitudes in the valley-flip channels, which vanishes in the absence of any inter-valley scattering. Other relevant cross sections can be calculated in a similar manner. In particular, the total cross section (TCS) is

$$\Sigma^\tau = \int_0^{2\pi} d\theta \frac{d\Sigma^\tau}{d\theta}, \tag{6.18}$$

the transport cross section (TrCS) is

$$\Sigma^\tau_{tr} = \int_0^{2\pi} d\theta(1 - \tau\tau'\cos\theta)|f_{\tau\tau'}(\theta)|^2, \tag{6.19}$$

and the skew cross section (SkCS) is given by

$$\Sigma_{sk}^{\tau} = \int_0^{2\pi} d\theta \tau\tau' \sin\theta |f_{\tau\tau'}(\theta)|^2. \tag{6.20}$$

To obtain an exact expression for $f_{\tau\tau'}(\theta)$, we expand the wavefunctions inside and outside the scatterer as a superposition of partial waves. In particular, for $r > R$ (outside the scatterer) and $r < R$ (inside the scatterer), we have

$$|\Psi_{s,\tau}^{>}(\boldsymbol{r})\rangle = \sum_l \psi_{l,s}^{>}(\boldsymbol{r})|\tau\rangle, \tag{6.21a}$$

and

$$|\Psi_{s,\tau}^{<}(\boldsymbol{r})\rangle = \sum_l \psi_{l,s}^{<}(\boldsymbol{r})|\tau\rangle, \tag{6.21b}$$

respectively, where $\psi_{l,s}^{>}|\tau\rangle$ and $\psi_{l,s}^{<}|\tau\rangle$ are the partial waves defined in terms of the cylindrical wave eigenfunctions of the reduced Hamiltonian $\mathcal{H}$, which in the polar coordinates $\boldsymbol{r} = (r, \theta)$ reads

$$\mathcal{H} = \hbar v_F \left(\begin{array}{ccc|ccc} 0 & \cos\phi\hat{L}_- & 0 & & & \\ \cos\phi\hat{L}_+ & 0 & \sin\phi\hat{L}_- & & \mathbf{0}_{3\times3} & \\ 0 & \sin\phi\hat{L}_+ & 0 & & & \\ \hline & & & 0 & -\cos\phi\hat{L}_+ & 0 \\ & \mathbf{0}_{3\times3} & & -\cos\phi\hat{L}_- & 0 & -\sin\phi\hat{L}_+ \\ & & & 0 & -\sin\phi\hat{L}_- & 0 \end{array}\right) + \mathcal{V}(r) \tag{6.22}$$

with the compact operator

$$\hat{L}_\tau = -ie^{i\tau\theta}\left(\partial_r + i\tau\frac{\partial_\theta}{r}\right),$$

and $\mathcal{V}(r) = \tau_0 \otimes \mathcal{I}V_0\Theta(R-r)$ being the circularly symmetric scalar type of scattering potential. Since the perturbation $\mathcal{V}$ is both valley and sublattice independent, it does not break any discrete symmetries and in fact preserves the rotational symmetry of the system. As a result, we have

$[\mathcal{H}, \hat{\mathcal{J}}_z] = 0$ with $\hat{\mathcal{J}}_z \equiv -i\hbar\partial_\theta + \tau_3 \otimes \hbar S_z$, analogous to the z component of the total "(pseudo) angular momentum." In addition, we have $[\tau_3 \otimes \mathcal{I}, \mathcal{H}] = 0$ (i.e., conservation of valley isospin) due to the absence of inter-valley coupling. Consequently, $\mathcal{H}$ acts on the spinor eigenfunctions of $\hat{\mathcal{J}}_z$, which yields

$$\mathcal{H}\varphi_{l,s}|\tau\rangle = E\varphi_{l,s}|\tau\rangle, \tag{6.23}$$

where the wavefunctions $\varphi_l|\tau\rangle$ simultaneously satisfy $\hat{\mathcal{J}}_z\varphi_l|\tau\rangle = \hbar\tau l\varphi_l|\tau\rangle$ with l being an integer. After some algebra, we obtain, for the conical bands (i.e., $s = \pm$),

$$\varphi_{l,s}^{(0,1)}(\boldsymbol{r})|\tau\rangle = \frac{1}{\sqrt{2\pi}} \begin{pmatrix} \cos\phi h_{l-\tau}^{(0,1)}(qr)e^{-i\tau\theta} \\ ish_l^{(0,1)}(qr) \\ -\sin\phi h_{l+\tau}^{(0,1)}(qr)e^{i\tau\theta} \end{pmatrix} e^{il\theta}|\tau\rangle, \tag{6.24}$$

where $q = |E - \mathcal{V}|/\hbar v_F$ and $s = \text{Sign}(E - \mathcal{V})$. The radial function $h_l^{(0)} = J_l$ is the Bessel function and $h_l^{(1)} = H_l^{(1)}$ is the Hankel function of the first kind. The partial waves outside ($r > R$) and inside ($r < R$) the scatterer are given by

$$\psi_{l,s}^{>}(\boldsymbol{r})|\tau\rangle = \sqrt{\pi}i^{l-1}\left[\varphi_{l,s}^{(0)}|\tau\rangle + A_l^{\tau\tau}\varphi_{l,s}^{(1)}|\tau\rangle + A_l^{\tau\overline{\tau}}\varphi_{l,s}^{(1)}|\overline{\tau}\rangle\right], \tag{6.25a}$$

and

$$\psi_{l,s}^{<}(\boldsymbol{r})|\tau\rangle = \sqrt{\pi}i^{l-1}\left[B_l^{\tau\tau}\varphi_{l,s'}^{(0)}|\tau\rangle + B_l^{\tau\overline{\tau}}\varphi_{l,s'}^{(0)}|\overline{\tau}\rangle\right], \tag{6.25b}$$

respectively, where $A_l^{\tau\tau}$ ($A_l^{\tau\overline{\tau}}$) and $B_l^{\tau\tau}$ ($B_l^{\tau\overline{\tau}}$) denote the elastic (valley-flip) partial wave reflection and transmission coefficients in the angular channel τl, respectively. To obtain explicit expressions of the partial wave coefficients, proper boundary conditions (BCs) are needed.

Boundary conditions. Recalling the commutation relations $[\hat{\mathcal{J}}_z, \mathcal{H}] = 0$ and $[\tau_3 \otimes \mathcal{I}, \mathcal{H}] = 0$, we define a spinor wavefunction in the polar coordinates as

$$\psi(r,\theta)|\tau\rangle = [\psi_1, \psi_2, \psi_3]^T|\tau\rangle = \begin{pmatrix} \mathcal{R}_1(r)e^{-i\tau\theta} \\ \mathcal{R}_2(r) \\ \mathcal{R}_3(r)e^{i\tau\theta} \end{pmatrix} e^{il\theta}|\tau\rangle, \tag{6.26}$$

which satisfies

$$\mathcal{H}\psi|\tau\rangle = E\psi|\tau\rangle. \tag{6.27}$$

Substituting Eq. (6.26) into Eq. (6.27) and eliminating the angular components, we obtain the following one-dimensional, first-order ordinary differential equation for the radial component:

$$\begin{aligned} &-i\tau \begin{pmatrix} 0 & \cos\phi\left[\frac{d}{dr} + \tau\frac{l}{r}\right] & 0 \\ \cos\phi\left[\frac{d}{dr} - \tau\frac{l-\tau}{r}\right] & 0 & \sin\phi\left[\frac{d}{dr} + \tau\frac{l+\tau}{r}\right] \\ 0 & \sin\phi\left[\frac{d}{dr} - \tau\frac{l}{r}\right] & 0 \end{pmatrix} \begin{pmatrix} \mathcal{R}_1(r) \\ \mathcal{R}_2(r) \\ \mathcal{R}_3(r) \end{pmatrix} \\ &= \frac{E - V(r)}{\hbar v_F} \begin{pmatrix} \mathcal{R}_1(r) \\ \mathcal{R}_2(r) \\ \mathcal{R}_3(r) \end{pmatrix}. \end{aligned} \tag{6.28}$$

Directly integrating the radial equation over a small interval $r \in [R-\eta, R+\eta]$ defined about the interface at $r = R$ and then taking the limit $\eta \to 0$, we obtain

$$\begin{aligned} \mathcal{R}_2(R-\eta) &= \mathcal{R}_2(R+\eta), \\ \cos\phi\mathcal{R}_1(R-\eta) + \sin\phi\mathcal{R}_3(R-\eta) &= \cos\phi\mathcal{R}_1(R+\eta) + \sin\phi\mathcal{R}_3(R+\eta), \end{aligned} \tag{6.29}$$

provided that the potential $V(r)$ and the radial function components $\mathcal{R}_{1,2,3}(r)$ are all finite. Reformulating such continuity conditions in terms of the corresponding wavefunction yields the desired

BCs:

$$\begin{aligned}\psi_2^<(R,\theta) &= \psi_2^>(R,\theta),\\ \cos\phi\psi_1^<(R,\theta)e^{i\tau\theta} + \sin\phi\psi_3^<(R,\theta)e^{-i\tau\theta} &= \cos\phi\psi_1^>(R,\theta)e^{i\tau\theta} + \sin\phi\psi_3^>(R,\theta)e^{-i\tau\theta}.\end{aligned} \tag{6.30}$$

Far-field solutions. Using the asymptotic form of the Hankel function,

$$H_l^{(1)}(kr) \sim \sqrt{2/\pi kr}e^{i(kr-l\pi/2-\pi/4)},$$

and evaluating the outside wavefunction given in Eq. (6.21a) in the far field region ($r \gg R$), we arrive at

$$|\Psi_{s,\tau}^{\gg}(\boldsymbol{r})\rangle = e^{ikx}|\boldsymbol{k}_0, s\rangle|\tau\rangle + \frac{-i\sqrt{2/\pi k}\sum_l A_l^{\tau\tau'}e^{il\theta}}{\sqrt{-ir}}e^{ikr}|\boldsymbol{k}_\theta, s\rangle|\tau'\rangle. \tag{6.31}$$

From Eqs. (6.31) and (6.13), we obtain

$$f_{\tau\tau'}(\theta) = -i\sqrt{\frac{2}{\pi k}}\sum_l A_l^{\tau\tau'}e^{il\theta}. \tag{6.32}$$

In our system, the valley-flip amplitudes $A_l^{\tau\bar{\tau}}$ and $B_l^{\tau\bar{\tau}}$ vanish due to the absence of intervalley coupling. Consequently, we have $f_{\tau\bar{\tau}} = 0$.

Imposing the BCs [Eq. (6.30)] on the total wavefunctions of both sides at the interface $r = R$, we have

$$\begin{cases} B_l^{\tau\tau}J_l(qR) = ss'\left[J_l(kR) + A_l^{\tau\tau}H_l^{(1)}(kR)\right], \\ B_l^{\tau\tau}X_{l,\tau}^{(0)}(qR) = X_{l,\tau}^{(0)}(kR) + A_l^{\tau\tau}X_{l,\tau}^{(1)}(kR), \end{cases} \tag{6.33}$$

where $X_{l,\tau}^{(0,1)} = h_{l-\tau}^{(0,1)}\cos^2\phi - h_{l+\tau}^{(0,1)}\sin^2\phi$. Solving Eq. (6.33), we obtain the unknown coefficients as

$$A_l^{\tau\tau} = -\frac{J_l(qR)X_{l,\tau}^{(0)}(kR) - ss'X_{l,\tau}^{(0)}(qR)J_l(kR)}{J_l(qR)X_{l,\tau}^{(1)}(kR) - ss'X_{l,\tau}^{(0)}(qR)H_l^{(1)}(kR)}, \tag{6.34}$$

and

$$B_l^{\tau\tau} = \frac{H_l^{(1)}(kR)X_{l,\tau}^{(0)}(kR) - X_{l,\tau}^{(1)}(kR)J_l(kR)}{H_l^{(1)}(kR)X_{l,\tau}^{(0)}(qR) - ss'X_{l,\tau}^{(1)}(kR)J_l(qR)}. \tag{6.35}$$

Using the basic relations $J_{-l} = (-)^l J_l$ and $H_{-l}^{(1)} = (-)^l H_l^{(1)}$, we obtain the following relations characterizing the inter-valley symmetries:

$$A_{-l}^{\tau\tau} = A_l^{\bar{\tau}\bar{\tau}}; B_{-l}^{\tau\tau} = B_l^{\bar{\tau}\bar{\tau}}. \tag{6.36}$$

However, there are no such symmetries for the coefficients belonging to the same valley, except for the particular cases of $\alpha = 0$ and $\alpha = 1$, where

$$A_{-l}^{\tau\tau} = A_l^{\tau\tau}; B_{-l}^{\tau\tau} = B_l^{\tau\tau}, \tag{6.37a}$$

for $\alpha = 1$ (dice lattice), and

$$A_{-l}^{\tau\tau} = A_{l+1}^{\tau\tau}; B_{-l}^{\tau\tau} = B_{l+1}^{\tau\tau}, \tag{6.37b}$$

for $\alpha = 0$ (graphene). The resulting probability density $\rho = \langle \Psi_{s,\tau}(\boldsymbol{r}) | \Psi_{s,\tau}(\boldsymbol{r}) \rangle$ and the local current density $\boldsymbol{j} = \langle \Psi_{s,\tau}(\boldsymbol{r}) | \hat{\boldsymbol{J}} | \Psi_{s,\tau}(\boldsymbol{r}) \rangle$ can be calculated accordingly. In addition, the exact scattering amplitudes $f_{\tau\tau}(\theta)$ can be obtained according to Eq. (6.32).

6.6.4. Low-Energy Scattering

It follows from the Eqs. (6.18)-(6.20) and Eq. (6.32) that the scattering cross sections have their summation forms given by

$$\Sigma^{\tau} = \frac{4}{k} \sum_{l=-\infty}^{\infty} |A_l^{\tau\tau}|^2, \tag{6.38a}$$

$$\Sigma_{tr}^{\tau} = \Sigma^{\tau} - \frac{4}{k} \sum_{l=-\infty}^{\infty} \Re\big[A_l^{\tau\tau} (A_{l+\tau}^{\tau\tau})^*\big], \tag{6.38b}$$

and

$$\Sigma_{sk}^{\tau} = \frac{4}{k} \sum_{l=-\infty}^{\infty} \Im\big[A_l^{\tau\tau} (A_{l+\tau}^{\tau\tau})^*\big]. \tag{6.38c}$$

Here we analyze the low energy scattering of the 2D massless Dirac-like particles as described by the Hamiltonian in Eq. (6.12). At low energies, i.e., $kR \ll 1$, the scattering is dominated by the lowest channels $l = 0, \pm\tau$. Defining $x \equiv kR$ and $\rho \equiv V_0 R$ and adopting the convention $\hbar v_F = 1$,

under the assumption of $x < \rho \ll 1$ (i.e., under-barrier scattering for weak scatterer/barrier), we obtain the coefficients as

$$A_0^{\tau\tau} = -\frac{P_0}{P_0 + iQ_0}, A_\tau^{\tau\tau} = -\frac{P_1}{P_1 + i(4\alpha^2 + Q_1)}, A_{-\tau}^{\tau\tau} = -\frac{P_1\alpha^2}{P_1 + i(4 + Q_1\alpha^2)}, \tag{6.39}$$

where $P_0 = \pi x$ and

$$Q_0 = 2\left(x \ln \frac{\gamma_E x}{2} - \frac{\tau J_0(\rho - x)}{J_\tau(\rho - x)}\right), \tag{6.40}$$

with $\ln \gamma_E \approx 0.577\cdots$ being the Euler's constant and P_1, Q_1 given by $[P_1, Q_1] = x[P_0, Q_0]$. Substituting these coefficients into Eq. (6.38), we obtain

$$\Sigma_{tr}^\tau / R = \frac{4P_0^2}{x(P_0^2 + Q_0^2)}\left\{1 - 4Q_1\alpha^2\left[\frac{1}{P_1^2 + (4\alpha^2 + Q_1)} + \frac{1}{P_1^2\alpha^4 + (4 + Q_1\alpha^2)^2}\right]\right\}, \tag{6.41}$$

and

$$\Sigma_{sk}^\tau / R = \frac{16P_0^2 P_1\alpha^2}{x(P_0^2 + Q_0^2)}\left\{\frac{1}{P_1^2 + (4\alpha^2 + Q_1)} - \frac{1}{P_1^2\alpha^4 + (4 + Q_1\alpha^2)^2}\right\}. \tag{6.42}$$

For the particular cases of $\alpha = 0$ (graphene) and $\alpha = 1$ (dice lattice), we have $\Sigma_{sk}^\tau / R = 0$, indicating absence of Hall effect. In the weak scattering regime ($\rho \ll 1$), the prefactor

$$\frac{P_0^2}{x(P_0^2 + Q_0^2)} \approx \frac{\pi^2 J_1^2(\rho - x)}{4J_0^2(\rho - x)} x \propto x \ll 1$$

is off-resonance. The other factors contain a dual resonance profile in general (except for $\alpha = 0, 1$). From Eq. (6.42), we obtain the resonant condition as

$$Q_1 + 4\alpha^2 = 0 \Rightarrow \frac{x}{\rho} = \frac{\alpha^2}{1 + \alpha^2}, \tag{6.43a}$$

or

$$Q_1\alpha^2 + 4 = 0 \Rightarrow \frac{x}{\rho} = \frac{1}{1 + \alpha^2}. \tag{6.43b}$$

Letting $\eta = x/\rho \equiv E/V_0$ and using the relation $\Phi \equiv \tau\Phi_s^\tau/\pi = (1 - \alpha^2)/(1 + \alpha^2)$, we reformulate the dual resonance condition in terms of the reduced Berry phase Φ explicitly given by

$$\eta_* = \frac{1 - \Phi_*}{2}, \tag{6.44a}$$

and

$$\eta_{**} = \frac{1+\Phi_*}{2} \equiv 1 - \eta_*. \tag{6.44b}$$

It can be seen that the first resonance occurs at $\eta \in (0, 1/2)$, while the second one lies within $\eta \in [1/2, 1)$. In addition, we note that the emergent dual resonances in the low-energy regime for weak scatterers can be utilized to detect/demarcate the unusual Berry phase of the particles in terms of their positions.

From Eqs. (6.41) and (6.42), we obtain the valley skewness (i.e., the valley Hall angle at zero temperature described in the main text) as

$$\gamma|_{T=0} \equiv \frac{\Sigma^{\tau}_{sk}}{\Sigma^{\tau}_{tr}} \approx \frac{4P_1(16 - P_1^2 - Q_1^2)\alpha^2(1-\alpha^2)(1+\alpha^2)}{(16^2 + Q_1^4)\alpha^4 + 16Q_1^2(1+\alpha^8) + 4Q_1\alpha^2(1+\alpha^4)(16+Q_1^2)}. \tag{6.45}$$

In the limit $\eta \ll 1$, Eq. (6.45) can be further simplified as (the subscript $T = 0$ is omitted hereafter for clarity)

$$\begin{aligned} \gamma(\Phi) &\approx \frac{4P_1\alpha^2(1-\alpha^2)(1+\alpha^2)}{Q_1^2 + 4Q_1\alpha^2(1+\alpha^4) + 16\alpha^4} \simeq \frac{\pi x^2 \frac{\Phi(1-\Phi)}{1+\Phi}}{(1+\eta)^2\left[\Phi - \frac{1-\eta}{1+\eta}\right]^2 + 4\eta\frac{\Phi(1-\Phi)}{1+\Phi}} \\ &\simeq \frac{\pi x^2 \frac{\Phi(1-\Phi)}{1+\Phi}}{(1+\eta)^2\left[\Phi - (1-2\eta)\right]^2 + 4\eta\frac{\Phi(1-\Phi)}{1+\Phi}}. \end{aligned} \tag{6.46}$$

We see that the valley Hall angle exhibits a nonlinear dependence on the carrier Berry phase Φ and an asymmetric resonance profile. In particular, as Φ is increased from 0 to 1 monotonously, the angle reaches a maximum $\gamma(\Phi_*) = \pi x^2/4\eta$ at $\Phi_* \simeq (1-2\eta)$, followed by a decrease to zero.

From Eq. (6.46), we obtain the asymptotic behaviors in the opposite limits of $\Phi \to 1$ (massless spin-$1/2$ particles occurring in, e.g., graphene or topological insulators) and $\Phi \to 0$ (massless spin-1 particles excited in dice lattices and various type synthetic photonic structures) as

$$\gamma(\Phi) \to \begin{cases} \frac{\pi x^2}{8\eta^2 + 4\eta(1-\Phi)}(1-\Phi), & \text{for } \Phi \to 1, \\ \frac{\pi x^2}{(1-\eta)^2 + 4\eta\Phi}\Phi, & \text{for } \Phi \to 0. \end{cases} \tag{6.47}$$

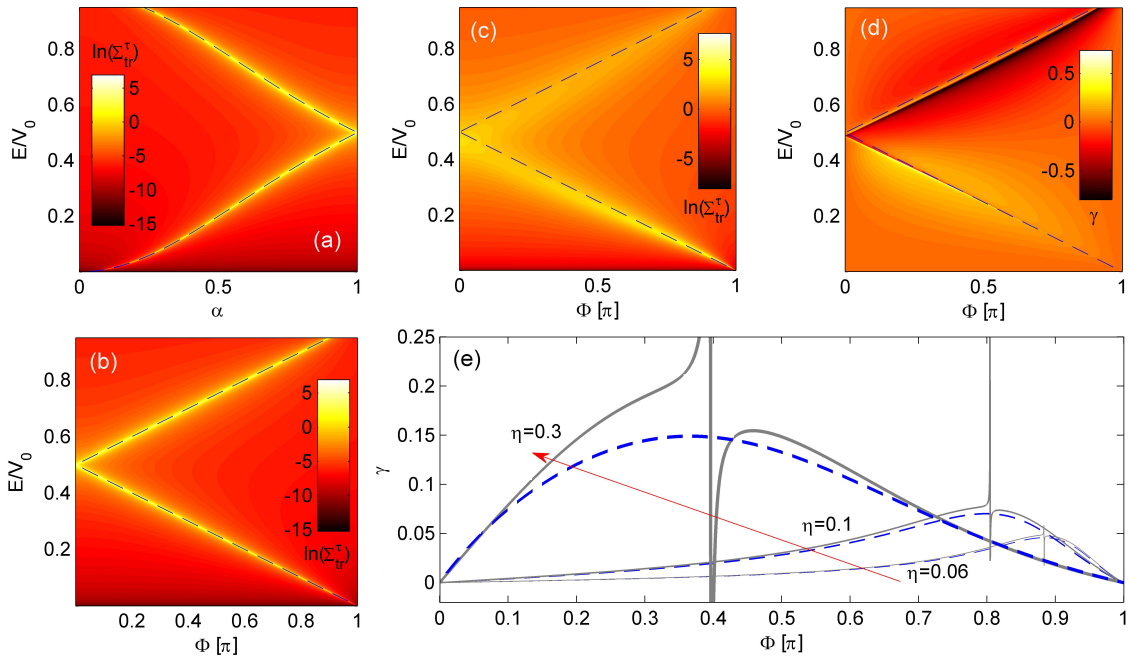

Fig. 42. Validity of analytic results in the low-energy scattering regime. For $x \ll 1$, (a,b) color coded natural logarithm of the transport cross section in the coordinates of (α, η) and (Φ, η), respectively, for scatterer strength $\rho = 0.1$. (c,d) Color coded $\ln(\Sigma^{\tau}_{tr})$ and zero temperature valley Hall angle γ as a function of the Berry flux Φ and η for $\rho = 1$. (e) Valley Hall angle γ versus the Berry flux Φ for different values of the reduced carrier energy $\eta = 0.06, 0.1, 0.3$ (along the red arrow). In all panels, the blue curves are calculated from the analytic formulae Eqs. (6.43) and (6.44) for the dual resonance condition [c.f., (a-d)] and Eq. (6.46) for the Berry flux dependence of the valley Hall angle [c.f., (e)], with the conventions $\{\hbar v_F = 1, x = kR, \rho = V_0 R, \eta = E/V_0\}$ (as in the main text).

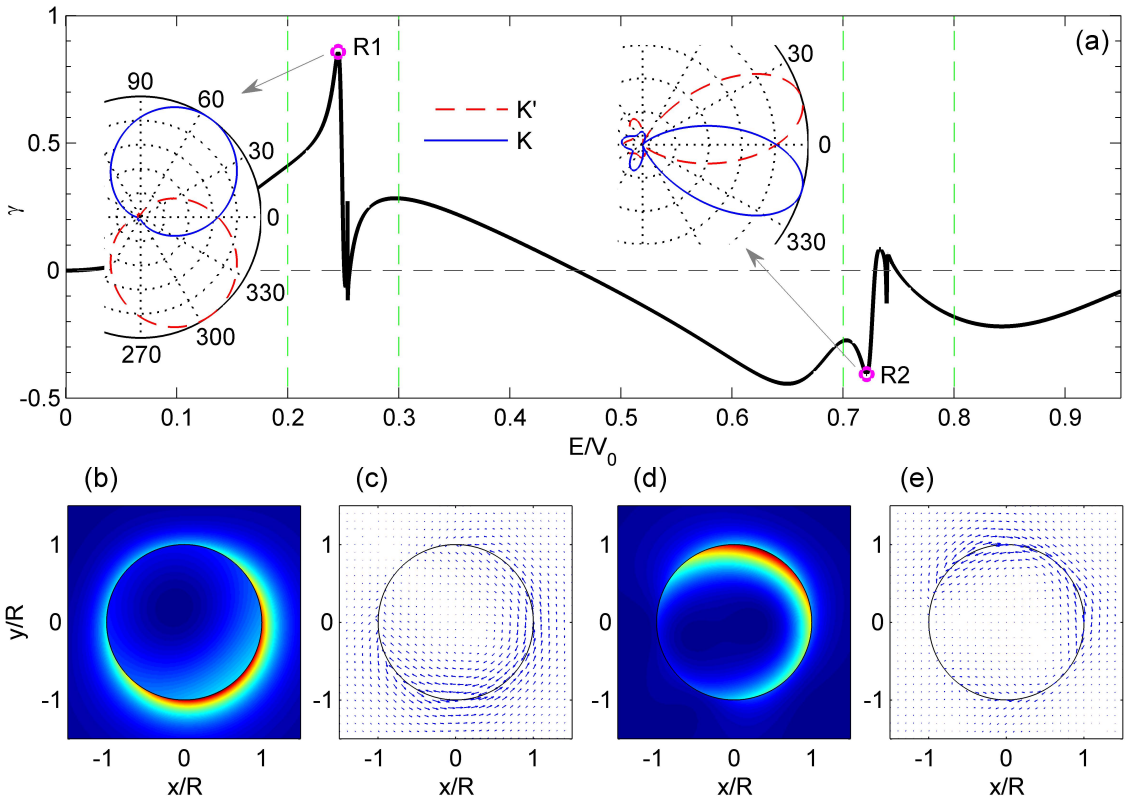

Fig. 43. Enhanced valley Hall angle and VHE by resonant skew scattering. (a) Valley Hall angle as a function of carrier energy normalized by the scattering potential height. (b,c) the near-field patterns of local probability and current density, respectively, associated with the valley K at the resonance indicated by the R1 pink circle in (a). (d,e) the corresponding near field patterns associated with another resonance as indicated by the R2 pink circle for the same valley. Insets of (a) are polar plots of the differential cross section for different valleys at two prominent valley Hall angles marked by the pink circles R1 and R2. For all panels, we set $\rho = 2$.

From the analysis above, we conclude that the valley Hall angle (and hence the valley Hall effect) is triggered by fractionally quantized (or non-π quantized) Berry flux in a nonlinear and asymmetrically resonant manner, but the angle approaches zero linearly as $\Phi \to 0, 1$ (i.e., π-quantized situations).

To validate the analytical results on resonance and the valley Hall angle, we compare them with those from direct numerical calculations. As shown in Fig. 42, there is an excellent agreement between the analytical results for the dual resonance condition in Eqs. (6.43) and (6.44) and the corresponding numerical results, and a similar agreement has been obtained for the Berry flux resolved valley Hall angle in Eq. (6.46).

For a particular value of the Berry flux, say $\Phi = 1/2$ (i.e., $\alpha = 1/\sqrt{3}$) that can be related to the massless Kane fermions observed in recent experiments (see Supplementary Note 5 below), we can infer from Eq. (6.42) that skew scattering will be enhanced due to the emergent dual resonances positioned at/around $\eta = (1 \pm \Phi)/2$, which can be reached by controlling the carrier energy E. Exact calculations show that such enhancements induced by the dual resonant skew scattering are significant and can lead to considerable valley Hall angles with the maximum absolute values $|\gamma|_{\max} \sim 0.8$ for intermediate scatterer strength, e.g., $\rho = 2$, as depicted in Fig. 43(a). These are much larger than the typical values for metals [227, 231–233] ($|\gamma| \sim 0.01 - 0.1$) as well as the "exceptionally" large values for graphene [188, 234, 235], which are about 0.2. As demonstrated in the main text, this conclusion holds in the presence of thermal fluctuations and disorder averaging, making our system promising for valleytronics applications.

An intuitive picture of resonant skew scattering assisted valley filtering can be obtained by investigating the associated near-field patterns, as illustrated in Figs. 43(b-e) for the valley K. (The patterns for the other valley K' are merely mirror images of those for K with respect to the hor-

izontal axis.) From the near-field patterns, we see that remarkable valley-contrasting spatial skew (asymmetric) trappings occur through the formation of unusual fusiform vortices around one side of the boundary. Consequently, the scattering effectively blocks one of the valleys at one side via the skew trapping, generating efficient valley filtering near/at the resonances. Our near-field argument is consistent with the (far-field) valley-contrasting angular distributions of the corresponding DCS as displayed in the insets of Fig. 43(a).

6.6.5. Map Onto Massless Kane Fermions

In recent experiments [238–240], exotic Dirac-like quasiparticles named massless Kane fermions have been observed in 3D zinc-blende crystals, i.e., $Hg_{1-x}Cd_xTe$, at some critical doping concentration. In the presence of strong spin-orbit interaction (e.g., $\sim$ 1eV), the fermions can be effectively described by the six-band Kane Hamiltonian [238] defined in the basis

$$\{|e\uparrow\rangle, |hh\uparrow\rangle, |lh\uparrow\rangle, |e\downarrow\rangle, |hh\downarrow\rangle, |lh\downarrow\rangle\},$$

that is arranged from the lowest electron conduction band $|e\lambda\rangle$, heavy hole valance band $|hh\lambda\rangle$ to the light hole valance band $|lh\lambda\rangle$ separated by the spin index $\lambda = \uparrow, \downarrow$ as

$$H_{Kane}(\boldsymbol{k}, k_z) = \left(\begin{array}{ccc|ccc} 0 & \frac{\sqrt{3}vk_+}{2} & -\frac{vk_-}{2} & 0 & 0 & -vk_z \\ \frac{\sqrt{3}vk_-}{2} & 0 & 0 & 0 & 0 & 0 \\ -\frac{vk_+}{2} & 0 & 0 & -vk_z & 0 & 0 \\ \hline 0 & 0 & -vk_z & 0 & -\frac{\sqrt{3}vk_-}{2} & \frac{vk_+}{2} \\ 0 & 0 & 0 & -\frac{\sqrt{3}vk_+}{2} & 0 & 0 \\ -vk_z & 0 & 0 & \frac{vk_-}{2} & 0 & 0 \end{array}\right), \tag{6.48}$$

where $k_\pm = k_x \pm ik_y$ and $v = \sqrt{3/2}P/m_0$ with P being the Kane's matrix element and m_0 being the free electron mass. Defining the following spin-independent unitary transformation:

$$\mathcal{S} = \tau_0 \otimes \begin{pmatrix} 0 & 1 & 0 \\ 1 & 0 & 0 \\ 0 & 0 & -1 \end{pmatrix},$$

we obtain

$$\mathcal{H}_{Kane}(\boldsymbol{k}, k_z) = \mathcal{S}^\dagger H_{Kane} \mathcal{S} = v\tilde{\alpha}_x k_x + v\tilde{\alpha}_y k_y + v\tilde{\alpha}_z k_z, \tag{6.49}$$

where the matrices $\tilde{\alpha}_{x,y,z}$ (resembling those for Dirac fermions) define the underlying symmetries of the quasiparticles and have the form

$$\tilde{\alpha}_x = \tau_3 \otimes \begin{pmatrix} 0 & \sqrt{3}/2 & 0 \\ \sqrt{3}/2 & 0 & 1/2 \\ 0 & 1/2 & 0 \end{pmatrix}, \tilde{\alpha}_y = \tau_0 \otimes \begin{pmatrix} 0 & -i\sqrt{3}/2 & 0 \\ i\sqrt{3}/2 & 0 & -i/2 \\ 0 & i/2 & 0 \end{pmatrix}, \tag{6.50a}$$

and

$$\tilde{\alpha}_z = \tau_1 \otimes \begin{pmatrix} 0 & 0 & 0 \\ 0 & 0 & 1 \\ 0 & 1 & 0 \end{pmatrix}. \tag{6.50b}$$

From Eq. (6.50a), we have $\tilde{\alpha}_x = \tau_3 \otimes S_x^{\alpha=1/\sqrt{3}}$ and $\tilde{\alpha}_y = \tau_0 \otimes S_y^{\alpha=1/\sqrt{3}}$. Since the subspace on which the Pauli matrices $\tau_{i=1,2,3}$ act hosts real spin instead of the valley isospin, there exists an exact map between the 2D sector of massless Kane fermion system and the generalized lattice model proposed in the main text:

$$\mathcal{H}_{Kane}(\boldsymbol{k}, k_z = 0) = H_0(\alpha = 1/\sqrt{3}). \tag{6.51}$$

In this sense, the extrinsic valley Hall effect uncovered in our work would manifest itself as an unusual extrinsic (geometric) spin Hall effect in the massless Kane fermion systems. Experimentally,

this can be validated in the 3D zinc-blende crystals in the presence of spin-independent (scalar-type) cylindrical symmetric impurities (e.g., charged dislocation line defects along the [001] direction).

6.6.6. Symmetry Considerations

The concept of symmetry breaking is fundamental and played an important role in the development of modern condensed matter physics. Various physical effects or phenomena can be attributed to the lack of certain discrete symmetries, e.g., the time reversal symmetry. Insights about our scattering system can be obtained from a symmetry analysis. To be general, we focus on the following perturbed Dirac-like Hamiltonian in two dimensions:

$$\mathcal{H}(\boldsymbol{k}) = \tilde{\alpha}_x k_x + \tilde{\alpha}_y k_y + \mathcal{V}, \tag{6.52}$$

where $(\tilde{\alpha}_x, \tilde{\alpha}_y) = (\tau_3 \otimes S_x^{\alpha}, \tau_0 \otimes S_y^{\alpha})$ and $\mathcal{V}$ denotes the external perturbed potential. The Hamiltonian $\mathcal{H}$ acts on the spinor wavefunction $\Psi = [\Psi_A^{\tau}, \Psi_B^{\tau}, \Psi_C^{\tau}, \Psi_A^{\bar{\tau}}, \Psi_B^{\bar{\tau}}, \Psi_C^{\bar{\tau}}]^T$ with $\bar{\tau} \equiv -\tau$ and satisfies $\mathcal{H}\Psi = E\Psi$. Following the work of Beenakker [241], we aim to obtain an explicit representation of the true time reversal operator given by

$$\mathcal{T} = \tau_1 \otimes \mathcal{I}K|_{\boldsymbol{k}\to-\boldsymbol{k}}, \tag{6.53}$$

where $\mathcal{I}$ is the 3×3 identity operator acting on the sublattice space and K denotes the complex conjugation operator. Note that the time reversal operation is of the orthogonal type, which leads to the transformations $\mathcal{T}\Psi = [\Psi_A^{\bar{\tau}*}, \Psi_B^{\bar{\tau}*}, \Psi_C^{\bar{\tau}*}, \Psi_A^{\tau*}, \Psi_B^{\tau*}, \Psi_C^{\tau*}]^T, \mathcal{T}\tilde{\alpha}_{x,y}\mathcal{T}^{-1} = -\tilde{\alpha}_{x,y}$ in the basis adopted and thus interchanges the valleys, consequently reversing the sign of the current $\boldsymbol{j} = \Psi^{\dagger}(\tilde{\alpha}_x, \tilde{\alpha}_y)\Psi$. For the Dirac-like Hamiltonian (6.52), there is another antiunitary operator defined independently

for each valley:

$$\mathcal{T}_e = \begin{cases} \tau_0 \otimes (i\sigma_y \oplus 0) K|_{\boldsymbol{k}\to-\boldsymbol{k}}, & \text{for } \alpha = 0, \\ \tau_0 \otimes \begin{pmatrix} 0 & 0 & -\alpha \\ 0 & 1 & 0 \\ -1/\alpha & 0 & 0 \end{pmatrix} K|_{\boldsymbol{k}\to-\boldsymbol{k}}, & \text{for } \alpha \in (0,1], \end{cases} \tag{6.54}$$

which by definition does not interchange the valleys but reverses the sign of the current associated with each valley. It thus acts as an effective time reversal operator for a single valley.

Distinct from the $\mathcal{T}$ symmetry, the $\mathcal{T}_e$ symmetry can be broken without a magnetic field. Conventionally, this occurs when sublattice/valley-dependent perturbations are present [241]. Due to the sublattice/valley-dependent nature, such perturbations will simultaneously induce additional symmetry breaking. For instance, a massive type of perturbation generated, e.g., by a sublattice-dependent (staggered) potential in the substrate, can lead to the breaking of the chiral (or sublattice) symmetry. Remarkably, in our system, we encounter a new scenario in which the $\mathcal{T}_e$ symmetry can be broken inherently but the $\mathcal{T}$ symmetry is preserved. In particular, for the scalar type of perturbation, i.e., $\mathcal{V} = \tau_0 \otimes \mathcal{I}V_0$ considered in our work, we have $\mathcal{T}\mathcal{V}\mathcal{T}^{-1} = \mathcal{V}, \mathcal{T}_e\mathcal{V}\mathcal{T}_e^{-1} = \mathcal{V}$ and thus $\mathcal{T}\mathcal{H}\mathcal{T}^{-1} = \mathcal{H}$ while $\mathcal{T}_e\mathcal{V}\mathcal{T}_e^{-1} \neq \mathcal{H}$ for $0 < \alpha < 1$, indicating that there is no $\mathcal{T}$ symmetry breaking as it should be (conventionally), but $\mathcal{T}_e$ is in general broken except for the particular cases of $\alpha = 0$ (graphene) and $\alpha = 1$ (dice lattice).

For scattering from a scalar type of scatterer, the breaking of the $\mathcal{T}_e$ symmetry imposes the following constrains on the scattering coefficients

$$A_l^{\tau\tau} \neq A_{-l}^{\tau\tau}, A_l^{\bar{\tau}\bar{\tau}} \neq A_{-l}^{\bar{\tau}\bar{\tau}}, A_l^{\tau\tau} = A_{-l}^{\bar{\tau}\bar{\tau}}. \tag{6.55}$$

Two relations then follow from Eq. (6.32): $|f_{\tau\tau}(\theta)| \neq |f_{\tau\tau}(-\theta)|$ and $|f_{\tau\tau}(\theta)| = |f_{\bar{\tau}\bar{\tau}}(-\theta)|$, where the former accounts for the breaking of the $\mathcal{T}_e$ symmetry and the latter signifies the preservation of the $\mathcal{T}$ symmetry. Consequently, the skew cross section defined in Eq. (6.20) is finite and has opposite signs for different valleys, leading to the emergence of a net charge-neutrality valley Hall current. We note that, when such an inherent $\mathcal{T}_e$ breaking (i.e., $0 < \alpha < 1$) occurs, the underlying Berry phase is fractionally quantized and can vary continuously as a function of α. We thus see that symmetry breaking provides an intuitive and physical picture for Berry phase rooted valley skew scattering and the gVHE uncovered in our work.

REFERENCES

[1] H. Zhang, *et al.*, Topological insulators in bi2se3, bi2te3 and sb2te3 with a single dirac cone on the surface. *Nat Phys* **5**, 438-442 (2009).

[2] M. I. Katsnelson, K. S. Novoselov, A. K. Geim, Chiral tunnelling and the klein paradox in graphene. *Nat. Phys.* **2**, 620-625 (2006).

[3] T. Wehling, A. Black-Schaffer, A. Balatsky, Dirac materials. *Adv. Phys.* **63**, 1-76 (2014).

[4] G.-H. Lee, G.-H. Park, H.-J. Lee, Observation of negative refraction of dirac fermions in graphene. *Nat. Phys* **11**, 925-929 (2015). Letter.

[5] A. Raoux, M. Morigi, J.-N. Fuchs, F. Piéchon, G. Montambaux, From dia- to paramagnetic orbital susceptibility of massless fermions. *Phys. Rev. Lett.* **112**, 026402 (2014).

[6] M. V. Berry, M. Robnik, Statistics of energy levels without time-reversal symmetry: Aharonov-bohm chaotic billiards. *J. Phys. A* **19**, 649 (1986).

[7] V. V. Cheianov, V. Fal'ko, B. L. Altshuler, The focusing of electron flow and a veselago lens in graphene p-n junctions. *Science* **315**, 1252-1255 (2007).

[8] M. Büttiker, Y. Imry, R. Landauer, Josephson behavior in small normal one-dimensional rings. *Physics Letters A* **96**, 365–367 (1983).

[9] Y. Aharonov, D. Bohm, Significance of electromagnetic potentials in the quantum theory. *Phys. Rev.* **115**, 485 (1959).

[10] L. P. Lévy, G. Dolan, J. Dunsmuir, H. Bouchiat, Magnetization of mesoscopic copper rings: Evidence for persistent currents. *Phys. Rev. Lett.* **64**, 2074–2077 (1990).

[11] V. Chandrasekhar, *et al.*, Magnetic response of a single, isolated gold loop. *Phys. Rev. Lett.* **67**, 3578–3581 (1991).

[12] A. C. Bleszynski-Jayich, *et al.*, Persistent currents in normal metal rings. *Science* **326**, 272–275 (2009).

[13] H. Bluhm, N. C. Koshnick, J. A. Bert, M. E. Huber, K. A. Moler, Persistent currents in normal metal rings. *Phys. Rev. Lett.* **102**, 136802 (2009).

[14] M. A. Castellanos-Beltran, D. Q. Ngo, W. E. Shanks, A. B. Jayich, J. G. E. Harris, Measurement of the full distribution of persistent current in normal-metal rings. *Phys. Rev. Lett.* **110**, 156801 (2013).

[15] D. Mailly, C. Chapelier, A. Benoit, Experimental observation of persistent currents in gaas-algaas single loop. *Phys. Rev. Lett.* **70**, 2020–2023 (1993).

[16] W. Rabaud, *et al.*, Persistent currents in mesoscopic connected rings. *Phys. Rev. Lett.* **86**, 3124–3127 (2001).

[17] N. A. J. M. Kleemans, *et al.*, Oscillatory persistent currents in self-assembled quantum rings. *Phys. Rev. Lett.* **99**, 146808 (2007).

[18] U. Sivan, Y. Imry, de haas-van alphen and aharonov-bohm-type persistent current oscillations in singly connected quantum dots. *Phys. Rev. Lett.* **61**, 1001–1004 (1988).

[19] H.-F. Cheung, E. K. Riedel, Y. Gefen, Persistent currents in mesoscopic rings and cylinders. *Phys. Rev. Lett.* **62**, 587–590 (1989).

[20] F. von Oppen, E. K. Riedel, Average persistent current in a mesoscopic ring. *Phys. Rev. Lett.* **66**, 84–87 (1991).

[21] V. Ambegaokar, U. Eckern, Coherence and persistent currents in mesoscopic rings. *Phys. Rev. Lett.* **65**, 381–384 (1990).

[22] A. Schmid, Persistent currents in mesoscopic rings by suppression of charge fluctuations. *Phys. Rev. Lett.* **66**, 80–83 (1991).

[23] R. Berkovits, Y. Avishai, Interacting electrons in disordered potentials: Conductance versus persistent currents. *Phys. Rev. Lett.* **76**, 291–294 (1996).

[24] J. Splettstoesser, M. Governale, U. Zülicke, Persistent current in ballistic mesoscopic rings with rashba spin-orbit coupling. *Phys. Rev. B* **68**, 165341 (2003).

[25] J. S. Sheng, K. Chang, Spin states and persistent currents in mesoscopic rings: Spin-orbit interactions. *Phys. Rev. B* **74**, 235315 (2006).

[26] V. Gudmundsson, C.-S. Tang, A. Manolescu, Nonadiabatic current generation in a finite width semiconductor ring. *Phys. Rev. B* **67**, 161301 (2003).

[27] A. Matos-Abiague, J. Berakdar, Photoinduced charge currents in mesoscopic rings. *Phys. Rev. Lett.* **94**, 166801 (2005).

[28] S. Datta, *Electronic Transport in Mesoscopic Systems* (Cambridge University Press, Cambridge, England, 1995).

[29] A. Fuhrer, *et al.*, Energy spectra of quantum rings. *Nature* **413**, 822–825 (2001).

[30] Ihn, Thomas, Fuhrer, Andreas, Meier, Lorenz, Sigrist, Martin, Ensslin, Klaus, Quantum physics in quantum rings. *Europhysics News* **36**, 78-81 (2005).

[31] D. Berman, O. Entin-Wohlman, M. Y. Azbel, Diamagnetic spectrum and oscillations in an elliptic shell. *Phys. Rev. B* **42**, 9299–9306 (1990).

[32] T. Chakraborty, P. Pietiläinen, Persistent currents in a quantum ring: Effects of impurities and interactions. *Phys. Rev. B* **52**, 1932–1935 (1995).

[33] D. V. Bulaev, V. A. Geyler, V. A. Margulis, Effect of surface curvature on magnetic moment and persistent currents in two-dimensional quantum rings and dots. *Phys. Rev. B* **69**, 195313 (2004).

[34] Y. V. Pershin, C. Piermarocchi, Persistent and radiation-induced currents in distorted quantum rings. *Phys. Rev. B* **72**, 125348 (2005).

[35] A. Bruno-Alfonso, A. Latgé, Aharonov-bohm oscillations in a quantum ring: Eccentricity and electric-field effects. *Phys. Rev. B* **71**, 125312 (2005).

[36] A. Bruno-Alfonso, A. Latgé, Quantum rings of arbitrary shape and non-uniform width in a threading magnetic field. *Phys. Rev. B* **77**, 205303 (2008).

[37] F. von Oppen, E. K. Riedel, Quantum persistent currents and classical periodic orbits. *Phys. Rev. B* **48**, 9170–9173 (1993).

[38] S. Kawabata, Persistent currents in quantum chaotic systems. *Phys. Rev. B* **59**, 12256–12259 (1999).

[39] A. H. C. Neto, K. Novoselov, Two-dimensional crystals: beyond graphene. *Mater. Exp.* **1**, 10-17 (2011).

[40] K. S. Novoselov, *et al.*, Electric field effect in atomically thin carbon films. *Science* **306**, 666-669 (2004).

[41] C. Berger, *et al.*, Ultrathin epitaxial graphite: 2d electron gas properties and a route toward graphenebased nanoelectronics. *J. Phys. Chem. B* **108**, 1991219916 (2004).

[42] K. S. Novoselov, *et al.*, Two-dimensional gas of massless dirac fermions in graphene. *Nature* **438**, 197200 (2005).

[43] T. Y. W. S. H. L. Zhang, Y. B., P. Kim, Experimental observation of the quantum hall effect and berrys phase in graphene. *Nature* **438**, 201-204 (2005).

[44] G. G. P. N. M. R. Neto, A. H. C., A. K. Geim, The electronic properties of graphene. *Rev. Mod. Phys.* **81**, 109-162 (2009).

[45] N. M. R. Peres, Colloquium: The transport properties of graphene: An introduction. *Rev. Mod. Phy.* **82**, 2673-2700 (2010).

[46] A. S. H. E. H. Sarma, S. D., E. Rossi, Electronic transport in two-dimensional graphene. *Rev. Mod. Phy.* **83**, 407-470 (2011).

[47] M. Z. Hasan, C. L. Kane, Colloquium. *Rev. Mod. Phys.* **82**, 3045–3067 (2010).

[48] R. A. B. J. G. V. Radisavljevic, B., A. Kis, Single-layer mos2 transistors. *Nat. Nanotech.* **6**, 147-150 (2011).

[49] K.-Z. K. K. A. C. J. N. Wang, Q. H., M. S. Strano, Electronics and optoelectronics of two-dimensional transition metal dichalcogenides. *Nat. Nanotech.* **7**, 699-712 (2012).

[50] D. Sheberla, *et al.*, High electrical conductivity in ni3(2,3,6,7,10,11-hexaiminotriphenylene)2 - a semiconducting metalorganic graphene analogue. *J. Am. Chem. Soc.* **136**, 88598862 (2014).

[51] Z. K. Liu, *et al.*, Discovery of a three-dimensional topological dirac semimetal na_3bi. *Science* **343**, 864867 (2014).

[52] Z. K. Liu, *et al.*, A stable three-dimensional topological dirac semimetal cd_3as_2. *Nature Materials* **13**, 677-681 (2014).

[53] A. H. Castro Neto, F. Guinea, N. M. R. Peres, Edge and surface states in the quantum hall effect in graphene. *Phys. Rev. B* **73**, 205408 (2006).

[54] D. S. L. Abergel, V. M. Apalkov, T. Chakraborty, Interplay between valley polarization and electron-electron interaction in a graphene ring. *Phys. Rev. B* **78**, 193405 (2008).

[55] C. W. J. Beenakker, A. R. Akhmerov, P. Recher, J. Tworzydło, Correspondence between andreev reflection and klein tunneling in bipolar graphene. *Phys. Rev. B* **77**, 075409 (2008).

[56] M. Zarenia, J. M. Pereira, F. M. Peeters, G. A. Farias, Electrostatically confined quantum rings in bilayer graphene. *Nano Letters* **9**, 4088-4092 (2009).

[57] R. Jackiw, A. I. Milstein, S.-Y. Pi, I. S. Terekhov, Induced current and aharonov-bohm effect in graphene. *Phys. Rev. B* **80**, 033413 (2009).

[58] M. M. Ma, J. W. Ding, N. Xu, Odd-even width effect on persistent current in zigzag hexagonal graphene rings. *Nanoscale* **1**, 387–390 (2009).

[59] M. Zarenia, J. M. Pereira, A. Chaves, F. M. Peeters, G. A. Farias, Simplified model for the energy levels of quantum rings in single layer and bilayer graphene. *Phys. Rev. B* **81**, 045431 (2010).

[60] D. Soriano, J. Fernández-Rossier, Spontaneous persistent currents in a quantum spin hall insulator. *Phys. Rev. B* **82**, 161302 (2010).

[61] D. Faria, A. Latgé, S. E. Ulloa, N. Sandler, Currents and pseudomagnetic fields in strained graphene rings. *Phys. Rev. B* **87**, 241403 (2013).

[62] N. Bolívar, E. Medina, B. Berche, Persistent charge and spin currents in the long-wavelength regime for graphene rings. *Phys. Rev. B* **89**, 125413 (2014).

[63] P. Michetti, P. Recher, Bound states and persistent currents in topological insulator rings. *Phys. Rev. B* **83**, 125420 (2011).

[64] D. Sticlet, B. Dóra, J. Cayssol, Persistent currents in dirac fermion rings. *Phys. Rev. B* **88**, 205401 (2013).

[65] S.-A. D. C. G. G. H. L. NÖckel, J. U., R. K. Chang, Directional emission from asymmetric resonant cavities. *Opt. Lett.* **21**, 1609-1611 (1996).

[66] C. Gmachl, *et al.*, High-power directional emission from microlasers with chaotic resonators. *Science* **280**, 1556-1564 (1998).

[67] K.-T. J. Spillane, S. M., K. J. Vahala, Ultralow-threshold raman laser using a spherical dielectric microcavity. *Nature* **415**, 621-623 (2002).

[68] K. J. Vahala, Optical microcavities. *Nature* **424**, 839-846 (2003).

[69] G. Reecht, *et al.*, Oligothiophene nanorings as electron resonators for whispering gallery modes. *Phys. Rev. Lett.* **110**, 056802 (2013).

[70] S. Russo, *et al.*, Observation of aharonov-bohm conductance oscillations in a graphene ring. *Phys. Rev. B* **77**, 085413 (2008).

[71] H. Peng, *et al.*, Aharonov-bohm interference in topological insulator nanoribbons. *Nature Mater.* **9**, 225-229 (2010).

[72] J. Dufouleur, *et al.*, Quasiballistic transport of dirac fermions in a bi2se3 nanowire. *Phys. Rev. Lett.* **110**, 186806 (2013).

[73] P. Recher, *et al.*, Aharonov-bohm effect and broken valley degeneracy in graphene rings. *Phys. Rev. B* **76**, 235404 (2007).

[74] E. K.-S. M. Schnez, S., T. Ihn, Analytic model of the energy spectrum of a graphene quantum dot in a perpendicular magnetic field. *Phys. Rev. B* **78** (2008).

[75] G. J. Ferreira, D. Loss, Magnetically defined qubits on 3d topological insulators. *Phys. Rev. Lett.* **111**, 106802 (2013).

[76] A. N. Redlich, Parity violation and gauge noninvariance of the effective gauge field action in three dimensions. *Phys. Rev. D* **29**, 23662374 (1984).

[77] B. M. J. K. D. Appelquist, T., L. C. R. Wijewardhana, Spontaneous breaking of parity in (2+1)-dimensional qed. *Phys. Rev. D* **33**, 37743776 (1986).

[78] M. V. Berry, R. J. Mondragon, Neutrino billiards: Time-reversal symmetry-breaking without magnetic fields. *Proc. Roy. Soc. Lond. A* **412**, 53-74 (1987).

[79] A. Chodos, R. L. Jaffe, K. Johnson, C. B. Thorn, V. F. Weisskopf, New extended model of hadrons. *Phys. Rev. D* **9**, 3471–3495 (1974).

[80] A. Hosaka, H. Toki, Chiral bag model for the nucleon. *Phys. Rep.* **277**, 65–188 (1996).

[81] G. Esposito, K. Kirsten, Chiral bag boundary conditions on the ball. *Phys. Rev. D* **66**, 085014 (2002).

[82] M. Robnik, Quantizing a generic family of billiards with analytic boundaries. *J. Phys. A* **17**, 1049 (1984).

[83] H. Xu, L. Huang, Y.-C. Lai, C. Grebogi, Chiral scars in chaotic dirac fermion systems. *Phys. Rev. Lett.* **110**, 064102 (2013).

[84] F. S. Nogueira, I. Eremin, Thermal screening at finite chemical potential on a topological surface and its interplay with proximity-induced ferromagnetism. *Phys. Rev. B* **90** (2014).

[85] X.-L. Qi, T. L. Hughes, S.-C. Zhang, Topological field theory of time-reversal invariant insulators. *Phys. Rev. B* **78**, 195424 (2008).

[86] M. G. Alford, F. Wilczek, Aharonov-bohm interaction of cosmic strings with matter. *Phys. Rev. Lett.* **62**, 1071-1074 (1989).

[87] P. d. S. Gerbert, Fermions in an aharonov-bohm field and cosmic strings. *Phys. Rev. D* **40**, 1346–1349 (1989).

[88] C. R. Hagen, Aharonov-bohm scattering of particles with spin. *Phys. Rev. Lett.* **64**, 503–506 (1990).

[89] C. Stelzer, W. Schweizer, Mesoscopic normal-metal rings in a magnetic field. *Phys. Rev. B* **62**, 7275–7282 (2000).

[90] H. J. Stöckmann, *Quantum chaos: an introduction* (Cambridge University Press, Cambridge, England, 1999).

[91] F. Haake, *Quantum Signatures of Chaos, 2nd Edition* (Springer, Berlin, 2001).

[92] L. Huang, Y.-C. Lai, C. Grebogi, Relativistic quantum level-spacing statistics in chaotic graphene billiards. *Phys. Rev. E* **81**, 055203 (2010).

[93] M. A. Nielsen, I. L. Chuang, *Quantum Computation and Quantum Information* (Cambridge University Press, Cambridge, UK, 2000).

[94] D. Loss, D. P. DiVincenzo, Quantum computation with quantum dots. *Phys. Rev. A* **57**, 120–126 (1998).

[95] J. Q. You, F. Nori, Superconducting circuits and quantum information. *Phys. Today* **58**, 42 (2005).

[96] J. Medford, *et al.*, Quantum-dot-based resonant exchange qubit. *Phys. Rev. Lett.* **111**, 050501 (2013).

[97] E. Paladino, Y. M. Galperin, G. Falci, B. L. Altshuler, 1/f noise: Implications for solid-state quantum information. *Rev. Mod. Phys.* **86**, 361-418 (2014).

[98] G. Casati, D. Shepelyansky, P. Zoller, G. Benenti, *Quantum Computers, Algorithms and Chaos* (IOS Press, Bologna, Italy, 2006).

[99] T. O. Wehlingab, A. M. Black-Schafferc, A. V. Balatskyd, Dirac materials. *Adv. Phys.* **63**, 1-76 (2014).

[100] P. Recher, *et al.*, Aharonov-bohm effect and broken valley degeneracy in graphene rings. *Phys. Rev. B* **76**, 235404 (2007).

[101] B. Trauzettel, D. V. Bulaev, D. Loss, G. Burkard, Spin qubits in graphene quantum dots. *Nat. Phys.* **3**, 192-196 (2007).

[102] A. Kormányos, V. Zólyomi, N. D. Drummond, G. Burkard, Spin-orbit coupling, quantum dots, and qubits in monolayer transition metal dichalcogenides. *Phys. Rev. X* **4**, 011034 (2014).

[103] P. Wei, *et al.*, Exchange-coupling-induced symmetry breaking in topological insulators. *Phys. Rev. Lett.* **110**, 186807 (2013).

[104] E. McCann, V. Fal'ko, Symmetry of boundary conditions of the dirac equation for electrons in carbon nanotubes. *J. Phys. Condens. Matter* **16**, 2371 (2004).

[105] H. Xu, L. Huang, Y.-C. Lai, C. Grebogi, Superpersistent currents and whispering gallery modes in relativistic quantum chaotic systems. *Sci. Rep.* **5** (2015).

[106] M. Büttiker, Y. Imry, R. Landauer, Josephson behavior in small normal one-dimensional rings. *Physics Letters A* **96**, 365-367 (1983).

[107] T. Hayashi, T. Fujisawa, H. D. Cheong, Y. H. Jeong, Y. Hirayama, Coherent manipulation of electronic states in a double quantum dot. *Phys. Rev. Lett.* **91**, 226804 (2003).

[108] E. Zipper, M. Kurpas, M. Szelág, J. Dajka, M. Szopa, Flux qubit on a mesoscopic nonsuperconducting ring. *Phys. Rev. B* **74**, 125426 (2006).

[109] Y. Yu, *et al.*, Energy relaxation time between macroscopic quantum levels in a superconducting persistent-current qubit. *Phys. Rev. Lett.* **92**, 117904 (2004).

[110] C. H. van der Wal, F. K. W. andl C. J. P. M. Harmans, J. E. Mooij, Engineering decoherence in josephson persistent-current qubits. *Eur. Phys. J. B* **31**, 111-124 (2003).

[111] Y. Makhlin, G. Schön, A. Shnirman, Quantum-state engineering with josephson-junction devices. *Rev. Mod. Phys.* **73**, 357–400 (2001).

[112] C. H. Bennett, D. P. DiVincenzo, Quantum information and computation. *Nature (London)* **404**, 247-255 (2000).

[113] D. Miller, Band-edge electroabsorption in quantum well structures: the quantum-confined stark effect. *Phys. Rev. Lett.* **53**, 2173-2176 (1984).

[114] E. Fradkin, *Field Theories of Condensed Matter Physics* (Cambridge University Press, New York, 2013), second edn.

[115] H. Zhang, *et al.*, Topological insulators in bi2se3, bi2te3 and sb2te3 with a single dirac cone on the surface. *Nature Physics* **5**, 438-442 (2009).

[116] A. M. Essin, J. E. Moore, D. Vanderbilt, Magnetoelectric polarizability and axion electrodynamics in crystalline insulators. *Phys. Rev. Lett.* **102**, 146805 (2009).

[117] X.-L. Qi, R. Li, J. Zang, S.-C. Zhang, Inducing a magnetic monopole with topological surface states. *Science* **323**, 1184-1187 (2009).

[118] R. Jackiw, C. Rebbi, Solitons with fermion number 1/2. *Phys. Rev. D* **13**, 3398–3409 (1976).

[119] Q. Liu, X. Zhang, L. B. Abdalla, A. Fazzio, A. Zunger, Switching a normal insulator into a topological insulator via electric field with application to phosphorene. *Nano Lett.* **15**, 1222-1228 (2015).

[120] X.-L. Qi, S.-C. Zhang, Topological insulators and superconductors. *Rev. Mod. Phys.* **83**, 1057–1110 (2011).

[121] A. Gutiérrez-Rubio, T. Stauber, Mass-profile quantum dots in graphene and artificial periodic structures. *Phys. Rev. B* **91**, 165415 (2015).

[122] A. De Martino, D. Klöpfer, D. Matrasulov, R. Egger, Electric-dipole-induced universality for dirac fermions in graphene. *Phys. Rev. Lett.* **112**, 186603 (2014).

[123] G. M. M. Wakker, R. P. Tiwari, M. Blaauboer, Localization and circulating currents in curved graphene devices. *Phys. Rev. B* **84**, 195427 (2011).

[124] T. Chakraborty, P. Pietiläinen, Optical signatures of spin-orbit interaction effects in a parabolic quantum dot. *Phys. Rev. Lett.* **95**, 136603 (2005).

[125] D. S. L. Abergel, V. M. Apalkov, T. Chakraborty, Interplay between valley polarization and electron-electron interaction in a graphene ring. *Phys. Rev. B* **78**, 193405 (2008).

[126] W. Sheng, J.-P. Leburton, Anomalous quantum-confined stark effects in stacked $\mathrm{InAs/GaAs}$ self-assembled quantum dots. *Phys. Rev. Lett.* **88**, 167401 (2002).

[127] J. G. Checkelsky, J. Ye, Y. Onose, Y. Iwasa, Y. Tokura, Dirac-fermion-mediated ferromagnetism in a topological insulator. *Nature Phys.* **8**, 729-733 (2012).

[128] A. Kandala, *et al.*, Growth and characterization of hybrid insulating ferromagnet-topological insulator heterostructure devices. *Applied Physics Letters* **103**, - (2013).

[129] L. D. Alegria, *et al.*, Large anomalous hall effect in ferromagnetic insulator-topological insulator heterostructures. *Applied Physics Letters* **105**, - (2014).

[130] M. Lang, *et al.*, Proximity induced high-temperature magnetic order in topological insulator - ferrimagnetic insulator heterostructure. *Nano Letters* **14**, 3459-3465 (2014). PMID: 24844837.

[131] M. Li, *et al.*, Proximity-driven enhanced magnetic order at ferromagnetic-insulator-magnetic-topological-insulator interface. *Phys. Rev. Lett.* **115**, 087201 (2015).

[132] H. Steinberg, J.-B. Laloë, V. Fatemi, J. S. Moodera, P. Jarillo-Herrero, Electrically tunable surface-to-bulk coherent coupling in topological insulator thin films. *Phys. Rev. B* **84**, 233101 (2011).

[133] S. Keuleyan, E. Lhuillier, P. Guyot-Sionnest, Synthesis of colloidal hgte quantum dots for narrow mid-ir emission and detection. *Journal of the American Chemical Society* **133**, 16422-16424 (2011). PMID: 21942339.

[134] J. Wang, S. Deng, Z. Liu, Z. Liu, The rare two-dimensional materials with dirac cones. *National Sci. Rev.* (2015).

[135] M. Z. Hasan, C. L. Kane, *Colloquium* : Topological insulators. *Rev. Mod. Phys.* **82**, 3045–3067 (2010).

[136] X.-L. Qi, S.-C. Zhang, Topological insulators and superconductors. *Rev. Mod. Phys.* **83**, 1057–1110 (2011).

[137] X.-L. Qi, T. L. Hughes, S.-C. Zhang, Topological field theory of time-reversal invariant insulators. *Phys. Rev. B* **78**, 195424 (2008).

[138] A. M. Essin, J. E. Moore, D. Vanderbilt, Magnetoelectric polarizability and axion electrodynamics in crystalline insulators. *Phys. Rev. Lett.* **102**, 146805 (2009).

[139] C.-Z. Chang, *et al.*, Zero-field dissipationless chiral edge transport and the nature of dissipation in the quantum anomalous hall state. *Phys. Rev. Lett.* **115**, 057206 (2015).

[140] Y. H. Wang, *et al.*, Observation of chiral currents at the magnetic domain boundary of a topological insulator. *Science* **349**, 948-952 (2015).

[141] M. C. Rechtsman, *et al.*, Topological creation and destruction of edge states in photonic graphene. *Phys. Rev. Lett.* **111**, 103901 (2013).

[142] Y. Plotnik, *et al.*, Observation of unconventional edge states in photonic graphene. *Nat. Mater.* **13**, 57-62 (2014). Article.

[143] Z. Wang, Y. D. Chong, J. D. Joannopoulos, M. Soljačić, Reflection-free one-way edge modes in a gyromagnetic photonic crystal. *Phys. Rev. Lett.* **100**, 013905 (2008).

[144] Z. Wang, Y. Chong, J. D. Joannopoulos, M. Soljacic, Observation of unidirectional backscattering-immune topological electromagnetic states. *Nature (London)* **461**, 772-U20 (2009).

[145] M. Hafezi, E. A. Demler, M. D. Lukin, J. M. Taylor, Robust optical delay lines with topological protection. *Nat. Phys.* **7**, 907-912 (2011).

[146] K. Fang, Z. Yu, S. Fan, Realizing effective magnetic field for photons by controlling the phase of dynamic modulation. *Nat. Photon.* **6**, 782-787 (2012).

[147] A. B. Khanikaev, *et al.*, Photonic topological insulators. *Nat. Mater.* **12**, 233-239 (2013).

[148] L. Lu, J. D. Joannopoulos, M. Soljaclc, Topological photonics. *Nat. Photon.* **8**, 821-829 (2014).

[149] X. Huang, Y. Lai, Z. H. Hang, H. Zheng, C. T. Chan, Dirac cones induced by accidental degeneracy in photonic crystals and zero-refractive-index materials. *Nat. Mater* **10**, 582-586 (2011).

[150] J. Mei, Y. Wu, C. T. Chan, Z.-Q. Zhang, First-principles study of dirac and dirac-like cones in phononic and photonic crystals. *Phys. Rev. B* **86**, 035141 (2012).

[151] P. Moitra, *et al.*, Realization of an all-dielectric zero-index optical metamaterial. *Nat Photon* **7**, 791-795 (2013). Letter.

[152] Y. Li, *et al.*, On-chip zero-index metamaterials. *Nat Photon* **9**, 738-742 (2015). Article.

[153] A. Fang, Z. Q. Zhang, S. G. Louie, C. T. Chan, Klein tunneling and supercollimation of pseudospin-1 electromagnetic waves. *Phys. Rev. B* **93**, 035422 (2016).

[154] D. Guzmán-Silva, *et al.*, Experimental observation of bulk and edge transport in photonic Lieb lattices. *New J. Phys.* **16**, 063061 (2014).

[155] S. Mukherjee, *et al.*, Observation of a localized flat-band state in a photonic lieb lattice. *Phys. Rev. Lett.* **114**, 245504 (2015).

[156] R. A. Vicencio, *et al.*, Observation of localized states in lieb photonic lattices. *Phys. Rev. Lett.* **114**, 245503 (2015).

[157] F. Diebel, D. Leykam, S. Kroesen, C. Denz, A. S. Desyatnikov, Conical diffraction and composite lieb bosons in photonic lattices. *Phys. Rev. Lett.* **116**, 183902 (2016).

[158] S. Taie, *et al.*, Coherent driving and freezing of bosonic matter wave in an optical lieb lattice. *Sci. Adv.* **1** (2015).

[159] M. Rizzi, V. Cataudella, R. Fazio, Phase diagram of the bose-hubbard model with $\sqcup_3$ symmetry. *Phys. Rev. B* **73**, 144511 (2006).

[160] A. A. Burkov, E. Demler, Vortex-peierls states in optical lattices. *Phys. Rev. Lett.* **96**, 180406 (2006).

[161] D. Bercioux, D. F. Urban, H. Grabert, W. Häusler, Massless dirac-weyl fermions in a T_3 optical lattice. *Phys. Rev. A* **80**, 063603 (2009).

[162] B. Dóra, J. Kailasvuori, R. Moessner, Lattice generalization of the dirac equation to general spin and the role of the flat band. *Phys. Rev. B* **84**, 195422 (2011).

[163] T. Andrijauskas, *et al.*, Three-level haldane-like model on a dice optical lattice. *Phys. Rev. A* **92**, 033617 (2015).

[164] F. Wang, Y. Ran, Nearly flat band with chern number $c = 2$ on the dice lattice. *Phys. Rev. B* **84**, 241103 (2011).

[165] J. Wang, H. Huang, W. Duan, Z. Liu, Identifying dirac cones in carbon allotropes with square symmetry. *The Journal of Chemical Physics* **139** (2013).

[166] W. Li, M. Guo, G. Zhang, Y.-W. Zhang, Gapless mos_2 allotrope possessing both massless dirac and heavy fermions. *Phys. Rev. B* **89**, 205402 (2014).

[167] J. Romhanyi, K. Penc, R. Ganesh, Hall effect of triplons in a dimerized quantum magnet. *Nat. Commun* **6** (2015). Article.

[168] G. Giovannetti, M. Capone, J. van den Brink, C. Ortix, Kekulé textures, pseudospin-one dirac cones, and quadratic band crossings in a graphene-hexagonal indium chalcogenide bilayer. *Phys. Rev. B* **91**, 121417 (2015).

[169] R. Shen, L. B. Shao, B. Wang, D. Y. Xing, Single dirac cone with a flat band touching on line-centered-square optical lattices. *Phys. Rev. B* **81**, 041410 (2010).

[170] D. F. Urban, D. Bercioux, M. Wimmer, W. Häusler, Barrier transmission of dirac-like pseudospin-one particles. *Phys. Rev. B* **84**, 115136 (2011).

[171] M. Vigh, *et al.*, Diverging dc conductivity due to a flat band in a disordered system of pseudospin-1 dirac-weyl fermions. *Phys. Rev. B* **88**, 161413 (2013).

[172] J. T. Chalker, T. S. Pickles, P. Shukla, Anderson localization in tight-binding models with flat bands. *Phys. Rev. B* **82**, 104209 (2010).

[173] J. D. Bodyfelt, D. Leykam, C. Danieli, X. Yu, S. Flach, Flatbands under correlated perturbations. *Phys. Rev. Lett.* **113**, 236403 (2014).

[174] E. H. Lieb, Two theorems on the hubbard model. *Phys. Rev. Lett.* **62**, 1201–1204 (1989).

[175] H. Tasaki, Ferromagnetism in the hubbard models with degenerate single-electron ground states. *Phys. Rev. Lett.* **69**, 1608–1611 (1992).

[176] H. Aoki, M. Ando, H. Matsumura, Hofstadter butterflies for flat bands. *Phys. Rev. B* **54**, R17296–R17299 (1996).

[177] C. Weeks, M. Franz, Topological insulators on the lieb and perovskite lattices. *Phys. Rev. B* **82**, 085310 (2010).

[178] N. Goldman, D. F. Urban, D. Bercioux, Topological phases for fermionic cold atoms on the lieb lattice. *Phys. Rev. A* **83**, 063601 (2011).

[179] J. Vidal, R. Mosseri, B. Douçot, Aharonov-bohm cages in two-dimensional structures. *Phys. Rev. Lett.* **81**, 5888–5891 (1998).

[180] D. S. Novikov, Elastic scattering theory and transport in graphene. *Phys. Rev. B* **76**, 245435 (2007).

[181] M. I. Katsnelson, F. Guinea, A. K. Geim, Scattering of electrons in graphene by clusters of impurities. *Phys. Rev. B* **79**, 195426 (2009).

[182] J.-S. Wu, M. M. Fogler, Scattering of two-dimensional massless dirac electrons by a circular potential barrier. *Phys. Rev. B* **90**, 235402 (2014).

[183] J. Cserti, A. Pályi, C. Péterfalvi, Caustics due to a negative refractive index in circular graphene p-n junctions. *Phys. Rev. Lett.* **99**, 246801 (2007).

[184] R. L. Heinisch, F. X. Bronold, H. Fehske, Mie scattering analog in graphene: Lensing, particle confinement, and depletion of klein tunneling. *Phys. Rev. B* **87**, 155409 (2013).

[185] M. M. Asmar, S. E. Ulloa, Rashba spin-orbit interaction and birefringent electron optics in graphene. *Phys. Rev. B* **87**, 075420 (2013).

[186] B. Liao, M. Zebarjadi, K. Esfarjani, G. Chen, Isotropic and energy-selective electron cloaks on graphene. *Phys. Rev. B* **88**, 155432 (2013).

[187] M. M. Asmar, S. E. Ulloa, Spin-orbit interaction and isotropic electronic transport in graphene. *Phys. Rev. Lett.* **112**, 136602 (2014).

[188] A. Ferreira, T. G. Rappoport, M. A. Cazalilla, A. H. Castro Neto, Extrinsic spin hall effect induced by resonant skew scattering in graphene. *Phys. Rev. Lett.* **112**, 066601 (2014).

[189] Y. Zhao, *et al.*, Creating and probing electron whispering-gallery modes in graphene. *Science* **348**, 672–675 (2015).

[190] W. S. Bakr, J. I. Gillen, A. Peng, S. Folling, M. Greiner, A quantum gas microscope for detecting single atoms in a hubbard-regime optical lattice. *Nature* **462**, 74-77 (2009).

[191] D. Jin, *et al.*, Topological magnetoplasmon. *arXiv:1602.00553* (2016).

[192] E. Illes, J. P. Carbotte, E. J. Nicol, Hall quantization and optical conductivity evolution with variable berry phase in the α-T_3 model. *Phys. Rev. B* **92**, 245410 (2015).

[193] J. Ziman, *Principles of the Theory of Solids* (Cambridge University Press, 1972).

[194] L. I. Schiff, *Quantum Mechanics* (McGraw-Hill, 1968), third edn.

[195] R. Newton, *Scattering Theory of Waves and Particles*, Dover Books on Physics (Dover Publications, 1982).

[196] A. Rycerz, J. Tworzydlo, C. W. J. Beenakker, Valley filter and valley valve in graphene. *Nat. Phys.* **3**, 172-175 (2007).

[197] D. Xiao, W. Yao, Q. Niu, Valley-contrasting physics in graphene: Magnetic moment and topological transport. *Phys. Rev. Lett.* **99**, 236809 (2007).

[198] K. Behnia, Polarized light boosts valleytronics. *Nat. Nanotech.* **7**, 488-489 (2012).

[199] C. E. Nebel, Electron dance in diamond. *Nat. Mater.* **12**, 690-692 (2013).

[200] R. V. Gorbachev, *et al.*, Detecting topological currents in graphene superlattices. *Science* **346**, 448-451 (2014).

[201] X. Xu, W. Yao, D. Xiao, T. F. Heinz, Spin and pseudospins in layered transition metal dichalcogenides. *Nat. Phys.* **10**, 343-350 (2014). Review.

[202] A. Kundu, H. A. Fertig, B. Seradjeh, Floquet-engineered valleytronics in dirac systems. *Phys. Rev. Lett.* **116**, 016802 (2016).

[203] Y. Ye, *et al.*, Electrical generation and control of valley carriers in a monolayer transition metal dichalcogenide. *Nat. Nanotech.* **11**, 598-602 (2016).

[204] J. Lu, C. Qiu, M. Ke, Z. Liu, Valley vortex states in sonic crystals. *Phys. Rev. Lett.* **116**, 093901 (2016).

[205] P. Michetti, P. Recher, Bound states and persistent currents in topological insulator rings. *Phys. Rev. B* **83**, 125420 (2011).

[206] M. Yamamoto, Y. Shimazaki, I. V. Borzenets, S. Tarucha, Valley hall effect in two-dimensional hexagonal lattices. *J. Phys. Soc. Japan* **84**, 121006 (2015).

[207] J. L. Garcia-Pomar, A. Cortijo, M. Nieto-Vesperinas, Fully valley-polarized electron beams in graphene. *Phys. Rev. Lett.* **100**, 236801 (2008).

[208] D. Gunlycke, C. T. White, Graphene valley filter using a line defect. *Phys. Rev. Lett.* **106**, 136806 (2011).

[209] A. Chaves, L. Covaci, K. Y. Rakhimov, G. A. Farias, F. M. Peeters, Wave-packet dynamics and valley filter in strained graphene. *Phys. Rev. B* **82**, 205430 (2010).

[210] Y. Jiang, T. Low, K. Chang, M. I. Katsnelson, F. Guinea, Generation of pure bulk valley current in graphene. *Phys. Rev. Lett.* **110**, 046601 (2013).

[211] M. M. Grujić, M. i. c. v. Tadić, F. m. c. M. Peeters, Spin-valley filtering in strained graphene structures with artificially induced carrier mass and spin-orbit coupling. *Phys. Rev. Lett.* **113**, 046601 (2014).

[212] M. Trushin, J. Schliemann, Pseudospin in optical and transport properties of graphene. *Phys. Rev. Lett.* **107**, 156801 (2011).

[213] D. Xiao, G.-B. Liu, W. Feng, X. Xu, W. Yao, Coupled spin and valley physics in monolayers of mos_2 and other group-vi dichalcogenides. *Phys. Rev. Lett.* **108**, 196802 (2012).

[214] Y. D. Lensky, J. C. W. Song, P. Samutpraphoot, L. S. Levitov, Topological valley currents in gapped dirac materials. *Phys. Rev. Lett.* **114**, 256601 (2015).

[215] J. C. W. Song, P. Samutpraphoot, L. S. Levitov, Topological bloch bands in graphene superlattices. *Proc. Nat. Acad. Sci. (USA)* **112**, 10879-10883 (2015).

[216] K. F. Mak, K. L. McGill, J. Park, P. L. McEuen, The valley hall effect in mos2 transistors. *Science* **344**, 1489–1492 (2014).

[217] M. Sui, *et al.*, Gate-tunable topological valley transport in bilayer graphene. *Nat. Phys.* **11**, 1027-1031 (2015).

[218] Y. Shimazaki, *et al.*, Generation and detection of pure valley current by electrically induced berry curvature in bilayer graphene. *Nat. Phys.* **11**, 1032-1036 (2015).

[219] J. Lee, K. F. Mak, J. Shan, Electrical control of the valley hall effect in bilayer mos2 transistors. *Nat. Nanotech.* **11**, 421-425 (2016).

[220] N. Nagaosa, J. Sinova, S. Onoda, A. H. MacDonald, N. P. Ong, Anomalous hall effect. *Rev. Mod. Phys.* **82**, 1539–1592 (2010).

[221] M. I. Dyakonov, V. I. Perel, Possibility of orientating electron spins with current. *Sov. Phys. JETP Lett.* **13**, 467-469 (1971).

[222] M. I. Dyakonov, V. I. Perel, Current-induced spin orientation of electrons in semiconductors. *Phys. Lett. A* **35**, 459-460 (1971).

[223] J. E. Hirsch, Spin hall effect. *Phys. Rev. Lett.* **83**, 1834-1837 (1999).

[224] Y. Kato, R. C. Myers, A. C. Gossard, D. D. Awschalom, Observation of the spin hall effect in semiconductors. *Science* **306**, 1910-1913 (2004).

[225] J. Wunderlich, B. Kaestner, J. Sinova, T. Jungwirth, Experimental observation of the spin-hall effect in a two-dimensional spin-orbit coupled semiconductor system. *Phys. Rev. Lett.* **94**, 047204 (2005).

[226] J. Sinova, S. O. Valenzuela, J. Wunderlich, C. H. Back, T. Jungwirth, Spin hall effects. *Rev. Mod. Phys.* **87**, 1213–1260 (2015).

[227] G.-Y. Guo, S. Maekawa, N. Nagaosa, Enhanced spin hall effect by resonant skew scattering in the orbital-dependent kondo effect. *Phys. Rev. Lett.* **102**, 036401 (2009).

[228] A. Fert, P. M. Levy, Spin hall effect induced by resonant scattering on impurities in metals. *Phys. Rev. Lett.* **106**, 157208 (2011).

[229] T. Ando, Theory of valley hall conductivity in graphene with gap. *J. Phys. Soc. Japan* **84**, 114705 (2015).

[230] Y. Niimi, *et al.*, Extrinsic spin hall effect induced by iridium impurities in copper. *Phys. Rev. Lett.* **106**, 126601 (2011).

[231] M. Morota, *et al.*, Indication of intrinsic spin hall effect in $4d$ and $5d$ transition metals. *Phys. Rev. B* **83**, 174405 (2011).

[232] L. Liu, *et al.*, Spin-torque switching with the giant spin hall effect of tantalum. *Science* **336**, 555–558 (2012).

[233] T. Seki, *et al.*, Giant spin hall effect in perpendicularly spin-polarized fept/au devices. *Nat. Mater.* **7**, 125-129 (2008).

[234] J. Balakrishnan, *et al.*, Giant spin hall effect in graphene grown by chemical vapour deposition. *Nat. Commun.* **5**, 4748 (2014).

[235] H.-Y. Yang, C. Huang, H. Ochoa, M. A. Cazalilla, Extrinsic spin hall effect from anisotropic rashba spin-orbit coupling in graphene. *Phys. Rev. B* **93**, 085418 (2016).

[236] E. Illes, J. P. Carbotte, E. J. Nicol, Hall quantization and optical conductivity evolution with variable berry phase in the α-T_3 model. *Phys. Rev. B* **92**, 245410 (2015).

[237] T. Louvet, P. Delplace, A. A. Fedorenko, D. Carpentier, On the origin of minimal conductivity at a band crossing. *Phys. Rev. B* **92**, 155116 (2015).

[238] M. Orlita, *et al.*, Observation of three-dimensional massless kane fermions in a zinc-blende crystal. *Nat. Phys.* **10**, 233-238 (2014).

[239] J. D. Malcolm, E. J. Nicol, Magneto-optics of massless kane fermions: Role of the flat band and unusual berry phase. *Phys. Rev. B* **92**, 035118 (2015).

[240] F. Teppe, *et al.*, Temperature-driven massless kane fermions in hgcdte crystals. *Nat. Commun.* **7**, 12576 (2016).

[241] C. W. J. Beenakker, *Colloquium* : Andreev reflection and klein tunneling in graphene. *Rev. Mod. Phys.* **80**, 1337–1354 (2008).

A

ACHIEVEMENTS DURING PHD STUDIES

Following are the relevant publications on the topics presented in this dissertation

1. H.-Y. Xu, L. Huang, Y.-C. Lai, and C. Grebogi, "Superpersistent currents and whispering gallery modes in relativistic quantum chaotic systems," *Scientific Reports* **5**, 8963 (2015). [Chapter 2]

2. H.-Y. Xu, L. Huang, and Y.-C. Lai, "A robust relativistic quantum two-level system with edge-dependent currents and spin polarization," *Europhysics Letters* **115**, 20005 (2016). (**Editor's Choice**) [Chapter 3]

3. H.-Y. Xu and Y.-C. Lai, "Reverse Stark effect, anomalous optical transitions, and control of spin in topological insulator quantum dots," *Physical Review B* **92**, 195120 (2015). [Chapter 4]

4. H.-Y. Xu and Y.-C. Lai, "Revival resonant scattering, perfect caustics, and isotropic transport of pseudospin-1 particles," *Physical Review B* **94**, 165405 (2016). [Chapter 5]

5. H.-Y. Xu and Y.-C. Lai, "Superscattering of a pseudospin-1 wave in a photonic lattice," *Physical Review A* **95**, 012119 (2017). [Chapter 5]

6. H.-Y. Xu, L. Huang, and Y.-C. Lai, "Geometric valley Hall effect and filtering with singular Berry flux," *submitted.* [Chapter 6]